Diss. ETH No. 18576

Inhomogeneous deformation of Zr-based bulk metallic glasses

A dissertation submitted to the

ETH ZURICH

for the degree of

DOCTOR OF SCIENCES

presented by

ALBAN DUBACH

Dipl. Ing., ETH Zurich
born December 14th, 1979
citizen of Switzerland

accepted on the recommendation of

Prof. Dr. Jörg F. Löffler, examiner

Prof. Dr. A. Lindsay Greer, co-examiner

Dr. Johann Michler, co-examiner

Dr. Florian H. Dalla Torre, co-examiner

2009

Acknowledgements

First I would like to thank my supervisor, Professor Jörg F. Löffler, for introducing me to the fascinating field of metallic glasses, and for his guidance and the scientifically fruitful discussions during my thesis work. I also appreciate the freedom he gave me to explore novel approaches to tackling the problem of deformation in metallic glasses.

I am deeply grateful to Dr. Florian Dalla Torre for his constant support and advice, for all the scientific and technical discussions, encouraging words and jocular chats, and for acting as co-referee of this thesis. Special thanks go to Dr. Johann Michler and Dr. Benedikt Moser, who helped me a lot with micromechanical and indentation testing. As my "primary contact persons" at EMPA Thun, they always found time to discuss scientific, technical and organisational problems with me. Prof. A. Lindsay Greer is gratefully acknowledged for acting as external co-referee of this thesis. I warmly thank Prof. Upadrasta Ramamurty from the Indian Institute of Science for contributing his expertise in the field of the mechanical properties of metallic glasses, and for his enthusiasm, which let to a very productive collaboration; and Dr. Rejin Raghavan, who recently found his way from India to Switzerland, for his scientific input.

I wish to thank all my colleagues for making the LMPT a comfortable place to work! Special thanks go to Marco Siegrist and Edward Arata for introducing me to metallic glass processing; Bruno Zberg and David Klaumünzer for stimulating discussions; Niklaus Koch and Markus "Bio" Müller for their help with sample preparation; Katherine Hahn for proof-reading my manuscripts; and Christian Wegmann, who always found the right solution when there was a technical problem.

The work of Yannick Santschi, Fabian Amstad, Adrienne Nelson, Roman Kontic, Henri Brunisholz and Martina Frischherz, whom I had the pleasure to supervise during student research projects and who contributed many experiments and ideas to this thesis, is gratefully acknowledged. I also thank Lorenz Bonderer for his supervision on the scanning electron microscope, Karolina Rzepiejewska for her help with the nanopillar compression tests, and Dr. Rudy Ghisleni, Frederik Oestlund and Gerhard Bürki for their technical support with the nanoindenter, the focused-ion beam instrument and the microcompression equipment.

This doctoral thesis would not have been possible without the support of colleagues and friends outside my work, who helped me to keep my life balanced! Special thanks go to Thomas Wüthrich, Patric Martin and Daniel Schober, coaches and team-mates from FC Hermrigen (I know my attendance at training is rather poor …), my Zurich housemate Andreas Buser, and the “kebab buddies”.

I am deeply grateful to my parents for their thorough support during my life, which enabled me to get where I am now. Coming home at weekends during my academic education was always like a holiday! Finally, I would like to thank Anick for all her support, patience and love.

Contents

Summary

Amorphous metals, commonly referred to as “metallic glasses”, are a relatively new class of materials. In contrast to ordinary metallic materials, which have a crystalline structure consisting of a highly-ordered arrangement of atoms, metallic glasses are non-crystalline and exhibit a disordered atomic-scale structure without long-range order. They can among other techniques be produced by rapid cooling from the liquid state and thus be frozen as vitreous solids. Due to their lack of crystalline defects such as grain boundaries and dislocations, metallic glasses generally exhibit extraordinary mechanical properties such as high strength and elastic strain limit, as well as good fracture toughness or corrosion resistance. Unfortunately, they intrinsically suffer from highly localised and hence limited plastic deformation prior to catastrophic failure. So far, this brittle behaviour has limited the possible structural applications of this class of materials. The primary aim of this thesis project was to investigate the mechanical properties and relate them to different amorphous states. Specifically, the project aimed to provide a fundamental understanding of the micromechanisms of (inhomogeneous) deformation of bulk metallic glasses (BMGs).

Detailed mechanical investigations on Zr-based BMGs (mainly $Zr_{52.5}Ti_5Cu_{17.9}Ni_{14.6}Al_{10}$, i.e. Vit105) were performed by means of uniaxial compression tests at various temperatures and strain rates. Serrated flow, which is commonly observed at room temperature, disappears below a critical temperature and above a critical strain rate, respectively, in accordance with a change in the strain rate sensitivity from negative to positive values. These observations, together with an increase in the magnitude of stress drops with increasing strain and their decrease with increasing strain rate, indicate phenomenologically close similarities to the dynamic strain aging effect or Portevin-LeChâtelier mechanism known for certain crystalline metals.

The results suggest a micromechanical deformation mechanism based on two processes: shear displacement through the formation and operation of shear transformation zones (STZs), and diffusive relaxation of the distorted structure. The latter vanishes below a critical temperature (or above a critical strain rate), resulting in the measured change in the strain-rate sensitivity and the disappearance of serrated flow. The crucial factor determining serrated flow in BMGs is the ratio between the cooperative shearing of STZs and the rate of adjacent diffusive relaxation processes.

Based on the phenomenological observations and derived kinetic parameters, such as activated shear deformation volumes and energies, a thermally-activated constitutive deformation model for metallic glasses was developed. Since shear band formation is related to a stress-driven structural disordering process, the temporal evolution of the deformation (and consequently also the strain rate sensitivity) is quantitatively assessed by introducing a structural state variable into the classical, thermally-activated shear rate equations. The structural state variable accounts for the degree of structural relaxation after a shear event and hence governs the temperature and strain-rate dependence of the inhomogeneous deformation characteristics of BMGs. That means it reflects a strain-, strain-rate and temperature-dependent energetic quantity for the appearance and disappearance of serrated flow.

Additionally, the thesis describes detailed micro-pillar compression experiments and instrumented indentation tests carried out on a Zr-based BMG in different structural states (as-cast, structurally-relaxed and shot-peened). In the range of the tested sample dimensions (300 nm–3 μm) the microcompression tests show a yield strength and deformation mode that is independent of sample size, surface-area-to-volume ratio and material condition. However, hardness and shear band morphology around indents changes depending on the structural state of the BMG. The differing behaviour can be rationalised in terms of free-volume-dependent pressure sensitivity, quantified by the constraint factor (i.e. hardness-to-yield strength ratio) and the intersection angle of shear bands emanating at the edge of conical indents. While structural relaxation generates enhanced pressure sensitivity compared to the as-cast state, pre-deformation by means of shot-peening results in a pressure-insensitive deformation response in the BMG. The microscopic origin of this behaviour is the ease of STZ activation, which requires local dilatation and is hence promoted in less dense glassy structures. Similarly, enhanced pressure sensitivity with decreasing temperature is observed, in conjunction with a decrease in the determined STZ volume.

Zusammenfassung

Amorphe Metalle, üblicherweise auch als “metallische Gläser” bezeichnet, sind eine relative neue Klasse von Werkstoffen. Im Gegensatz zu herkömmlichen metallischen Materialien, die eine kristalline Struktur mit regelmässiger Anordnung der Atome aufweisen, sind metallische Gläser nicht kristallin und besitzen eine ungeordnete atomare Struktur ohne langreichweitige Ordnung. Sie lassen sich unter anderem durch rasches Abschrecken aus der flüssigen Phase herstellen, wobei die Schmelze glasartig erstarrt. Durch das Fehlen von Kristallbaufehlern (z.B. Krongrenzen und Versetzungen) haben metallische Gläser meist sehr gute mechanische Eigenschaften, wie hohe Festigkeit, elastische Dehngrenze, Bruchzähigkeit und Korrosionsbeständigkeit. Leider haben metallische Gläser aber die Tendenz zu einer starken Lokalisierung der Verformung in dünnen Scherbändern, was üblicherweise zu einer geringen Bruchverformung führt. Bis anhin hat diese fehlende Duktilität mögliche strukturelle Anwendungen von metallischen Gläsern stark eingeschränkt. Das Hauptziel dieser Arbeit war die Untersuchung der mechanischen Eigenschaften und deren Beeinflussung durch verschiedene Materialzustände. Ein besonderes Augenmerk der Arbeit lag auf der Verbesserung des Verständnisses der (inhomogenen) Verformungsmechanismen in metallischen Gläsern.

Die mechanischen Eigenschaften von Zr-basierten metallischen Massivgläsern (hauptsächlich $Zr_{52.5}Ti_5Cu_{17.9}Ni_{14.6}Al_{10}$, d.h. Vit105) wurden mittels einachsigen Druckversuchen bei verschiedenen Temperaturen und angelegten Dehnraten untersucht. Die inhomogene Verformung zeigt sich bei Raumtemperatur üblicherweise durch sägezahnartige Sprünge in der Spannungs-Dehnungs-Kurve. Diese Instabilitäten verschwinden jedoch unterhalb einer kritischen Temperatur bzw. oberhalb einer kritischen Dehnrate, in Übereinstimmung mit einem Wechsel der Dehnratenabhängigkeit von negativen zu positiven Werten. Zusätzlich konnte gezeigt werden, dass die Grösse der Spannungsabfälle mit zunehmender Dehnung und abnehmender Dehnrate zunehmen. Interessanterweise zeigt dieses Deformationsverhalten grosse Ähnlichkeiten mit der dynamischen Reckalterung und dem Portevin-LeChâtelier-Effekt, die unter gewissen Voraussetzungen in kristallinen Metallen auftreten können.

Die erhaltenen Resultate deuten auf einen zweistufigen Deformationsmechanismus hin: Scherung durch die Aktivierung von „Scher-Transformationszonen“ (STZ) und diffusive

Relaxationsvorgänge der verformten Struktur. Letztere finden unterhalb einer kritischen Temperatur (oder oberhalb einer kritischen Dehnrate) nicht mehr genügend schnell statt, was zu der gemessenen Änderung der Dehnratenabhängigkeit und dem Verschwinden der sägezahnartigen Sprünge im Spannungs-Dehnungs-Diagramm führt. Der ausschlaggebende Faktor für das Auftreten der Spannungsinstabilitäten in metallischen Massivgläsern ist das Verhältnis von Scherrate, gegeben durch das Zusammenwirken von vielen STZ, und Geschwindigkeit der anschliessenden diffusiven Relaxationssvorgänge.

Anhand der gemachten Beobachtungen und abgeleiteten kinetischen Parametern, wie Aktivierungsenergien und -volumina, wurde ein thermisch aktiviertes Verformungsmodell für metallische Gläser entwickelt. Die durch die Bildung von Scherbändern eingebrachte strukturelle Unordnung und die zeitliche Entwicklung der Verformung werden dabei quantitativ durch eine Struktur-Zustandsvariable bestimmt. Sie berücksichtigt das Ausmass der strukturellen Relaxation nach einem Schervorgang und bestimmt so die Temperatur- und Dehnratenabhängigkeit des inhomogenen Verformungsverhaltens von metallischen Massivgläsern, d.h. sie widerspiegelt eine dehnungs-, dehnraten- und temperaturabhängige Energie für das Auftreten von instabilem Fliessen.

Des Weiteren wurden einachsige Druckversuche auf Mikrosäulen und Eindrücktests auf Zr-basierten metallischen Massivgläsern in verschiedenen Zuständen (im Gusszustand, relaxiert und kugelgestrahlt) durchgeführt. Für Säulen mit einem Durchmesser zwischen 300 nm und 3 μm ist die Fliessgrenze unabhängig von Probengrösse, Oberfläche-zu-Volumen-Verhältnis und Materialzustand. Die Härte und Scherbandmorphologie hingegen ändern sich mit dem strukturellen Zustand des Glases. Das unterschiedliche Verhalten lässt sich mit einer vom freien Volumen abhängigen Druckempfindlichkeit erklären, die sich durch den plastischen Zwängungsfaktor (d.h. Verhältnis von Härte zu Fliessspannung) oder den Schnittwinkel von Scherbändern um einen konischen Eindruck quantitativ bestimmen lässt. Im Vergleich zum Gusszustand führt strukturelle Relaxation zu einer erhöhten Druckempfindlichkeit, während Kugelstrahlen zu einer Druckunempfindlichkeit führt. Die Ursache für das unterschiedliche Verhalten hängt davon ab, wie leicht STZ aktiviert werden können. Da STZ lokal eine gewisse Aufweitung der Struktur benötigen, werden sie bevorzugt in weniger dichtgepackten Glasstrukturen aktiviert. Eine erhöhte Druckempfindlichkeit, in Verbindung mit einer Abnahme des ermittelten Volumens von STZ, wird auch mit abnehmender Temperatur beobachtet.

1 General introduction

Metallic glasses are a relatively young class of materials. Their amorphous structure gives rise to exciting mechanical behaviour and other interesting microstructure-property relationships. This chapter gives a general introduction to metallic glasses and their development over the five decades since their discovery, and briefly outlines their unique mechanical properties with particular emphasis on microstructural aspects and potential applications.

1.1 Metallic glasses

"What, they are not transparent?" This is often the surprised reaction of people outside the "metallic glass community" when they hear about metallic glasses for the first time. The reason for this mistaken idea is that the expression "glass" is commonly used as a synonym for "window glass", whose main applications derive from its transparency. Generally, however, a glass is defined as a non-crystalline, amorphous[1] solid in which the atoms are arranged randomly with no topological long-range order. Or in the words of M.L. Falk: "To a large extent, a glass is defined by what it is not: a well-ordered crystal" [1]. Per definition, it is manufactured by undercooling a liquid to temperatures below its glass transition temperature, T_g, where it solidifies without crystallisation. Therefore it can be regarded as a "frozen liquid", in which the structure of the liquid is preserved. While a glass is always amorphous, not all amorphous solids are glasses, i.e. an amorphous solid really refers to a wider spectrum of materials than just glasses. However, in this thesis the terms "glassy" and "amorphous" will be used interchangeably. In contrast to liquids, which can be regarded as fluid, solidified liquids show higher resistance to shear stresses, i.e. display a higher viscosity. Therefore T_g is often arbitrarily defined as the temperature at which viscosity exceeds a certain value (e.g. $\sim 10^{13}$ Pa s for metallic glasses).

Making amorphous solids is not new: many common materials, including oxide glasses (such as ordinary window glass) and various polymers, are amorphous and have been produced for centuries. Metallic alloys, however, are not usually amorphous. The reasons for this are the non-directional nature of their metallic bonds and their "spherical" building-blocks (i.e., atoms), which contrast with those of e.g. silicon oxide glasses, whose building-blocks are larger SiO_2 tetrahedrons with directional covalent bonds. Consequently, the fabrication of metallic glasses requires either very high cooling rates or sluggish crystallisation kinetics. Additionally, possible heterogeneous nucleation sites must be avoided, which generally involves the use of high-purity elements and vacuum processing techniques, making the fabrication processes rather cost-intensive.

An amorphous metallic solid can basically be produced either by vapour-, chemical- or electro-deposition techniques [2,3,4,5], mechanical amorphisation (e.g. milling or severe plastic deformation) or rapid quenching from the liquid phase (e.g. [6,7] and references

[1] from Greek 'ámorphos', meaning without shape, i.e. shapeless/formless

therein). However, today the most common way to fabricate larger quantities of metallic amorphous alloys is the rapid quenching route. Here, depending on the glass-forming ability of the alloy, various techniques such as splat quenching (very high cooling rates), melt spinning (high cooling rates) or copper-mould casting techniques (moderate to low cooling rates) may be used [8]. In metallic glasses produced by melt processing, the glass-forming ability of an alloy is generally described by either the critical cooling rate or the critical casting thickness. The critical cooling rate is the cooling rate which is necessary to bypass crystallisation, whereas the critical casting thickness is the maximum thickness of the minimum dimension that an alloy can be cast to without crystallising. The amorphous phase possesses a higher intrinsic energy than the crystalline phase, which generally represents the thermodynamic equilibrium state of the system (Fig. 1.1). Therefore, metallic glasses are considered to be metastable. As discussed in further detail in Section 1.3, alloys displaying good glass-forming ability typically have a small energy difference between the amorphous and crystalline solid phases, leading to a smaller driving force for crystallisation. Further, good glass-formers generally have high melt viscosities, which hinder diffusion of atoms and thus slow down crystallisation [9,10].

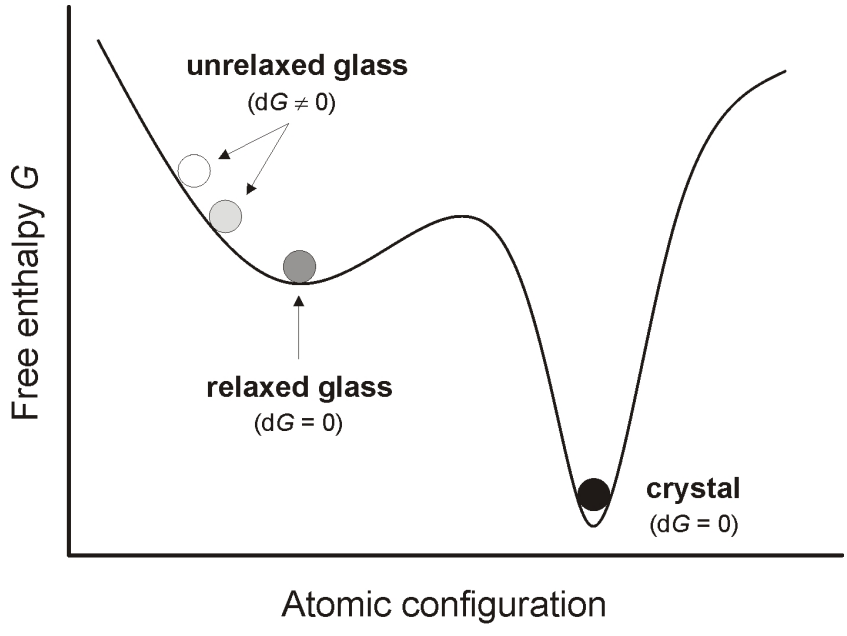

Fig. 1.1: Schematic diagram of the free enthalpy (i.e. "potential energy landscape") of unrelaxed (unstable) and relaxed (metastable) glass, and a crystalline (stable) phase.

1.2 Discovery and development of bulk metallic glasses

The first successful preparation of an amorphous metallic alloy was reported in 1960 [11]. The glassy alloy was obtained by rapid quenching of the low-melting eutectic in the binary Au–Si system at a cooling rate on the order of 10^6 K/s. Its stability, however, was rather poor; and it crystallised at room temperature within a few hours. In the following years, rapid solidification techniques for the production of amorphous wires and ribbons were much improved. The early metallic glasses, however, had inferior glass-forming ability and required cooling rates on the order of 10^5–10^6 K/s, which limited their critical casting thickness to a few tens of microns. At the same time the first specific efforts were made to slow down crystallisation kinetics by exploring new alloy compositions, with consequent increases in the critical casting thickness. This led to the discovery of novel amorphous alloys such as ternary Pd-, Au- or La-based alloys [12,13,14], and in the early 1990s resulted in the development of bulk metallic glasses[2] (BMGs), e.g. in the form of a quinary Zr-based alloy ($Zr_{41.2}Ti_{13.8}Cu_{12.5}Ni_{10}Be_{22.5}$) [15] or La- and Mg-based multicomponent alloys [16]. An important success in this context was also the development of fluxing techniques (for Pd-based glasses), which help to inhibit crystallisation by eliminating heterogeneous nucleation sites [17].

The significant improvement of glass-forming ability stimulated intense global research activity, not only in terms of further alloy development, but also regarding systematic characterisation of the properties of bulk metallic glasses.

Nowadays, a wide variety of bulk metallic glass-forming alloys are known which can be classified as either nonferrous alloy systems (among which the most important are based on zirconium, copper, titanium, magnesium, aluminium, palladium or platinum) or ferrous alloy systems (iron-, nickel- and cobalt-based systems). A detailed overview of existing bulk glassy alloy systems can, for example, be found in Refs. [18,19] (an overview of BMGs with critical size $\geq$ 10 mm is given in Ref. [20]). They always consist of two or more components. Good glass-forming alloys (cf. Table 1.1) have critical cooling rates on the order of 1–10 K/s (or even below, e.g. [21]), which allows them to be fabricated under inert atmosphere by means of conventional copper-casting methods (e.g. drop casting, suction/squeeze casting, injection moulding, etc.) from the liquid state.

[2] Here "bulk" is arbitrarily defined as having a critical casting thickness in the millimeter range.

Table 1.1: Critical casting thickness (t_c) and critical cooling rate (R_c) for particular bulk metallic glasses [22]

Alloy system	t_c (mm)	R_c (K/s)
Fe–(Al,Ga)–(P,C,B,Si)	~3	~400
Fe–(Co,Ni)–(Zr,Hf,Nb)–B	~6	~200
Ti–Ni–Cu–Sn	~6	~200
Mg–Al–(Cu,Ni)	~10	~200
Zr–Ti–Al–(Cu,Ni)	~30	1–5
Zr–Ti–Al–(Cu,Ni)-Be	~30	1–5
Pd–Cu–Ni–P	~75	~0.1

1.3 Glass-forming ability of metallic glasses

Generally, a glass has such low crystal nucleation rates and growth kinetics that the liquid can be undercooled far below its melting point and glass transition is reached before crystallisation starts. This, of course, ideally also implies the absence of any impurities (e.g. oxides or high-melting intermetallic phases) in the melt which might act as nucleation sites upon cooling. A common way of visualising crystallisation behaviour is the so-called time-temperature-transformation (TTT) diagram. Fig. 1.2 gives an example of a TTT diagram for a $Zr_{52.5}Ti_5Cu_{17.9}Ni_{14.6}Al_{10}$ BMG, where the onset times for isothermal crystallisation are plotted as a function of temperature. The typical “C-shape” or “nose” originates from the competition between the increasing driving force for crystallisation and the slowing down of the kinetics of the atomic movements with increasing undercooling, i.e. decreasing temperature. Note that the TTT diagram is only valid for isothermal transformations and is in principle not adaptable to dynamic or continuous processes, such as rapid cooling. In this case, a continuous-cooling transformation diagram would be necessary, which experimentally, however, is much more difficult to measure. Nonetheless, the TTT diagram gives a rough estimate of the processing time available for the fabrication of an amorphous solid.

A simple approximation relating the critical cooling rate R_c and the critical casting thickness t_c was provided by Lin and Johnson [23]: By making a few assumptions regarding the thermal conductivity and heat capacity of the alloy one obtains

$$R_c(\mathrm{K/s}) \approx \frac{10}{[t_c(\mathrm{cm})]^2}. \tag{1.1}$$

A melt-spun ribbon with a thickness of 30 µm is therefore cooled at a rate of approximately 10^6 K/s. On the other hand, an alloy with a critical cooling rate $R_c = 10$ K/s can be produced with a dimension of 1 cm.

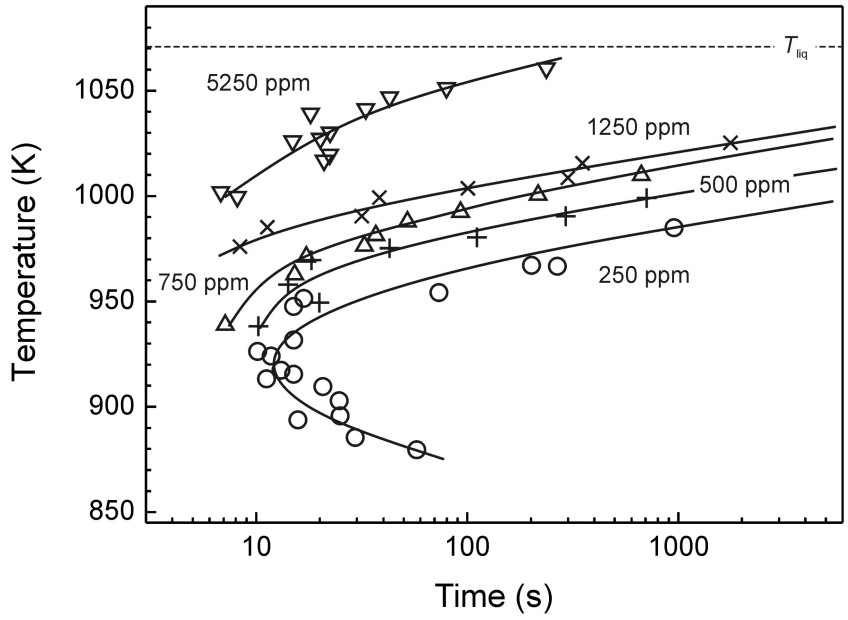

Fig. 1.2: Time-temperature-transformation (TTT) diagram for $Zr_{52.5}Ti_5Cu_{17.9}Ni_{14.6}Al_{10}$ (Vit105) with different oxygen contents in atomic ppm (adapted from Ref. [24]). Obviously, an increased oxygen content leads to a drastic reduction of the crystallisation time and consequently a higher critical cooling rate.

If we refer to classical nucleation theory, several guidelines can be deduced for predicting the glass-forming ability of a liquid. When a liquid is cooled below its melting temperature the free energy difference $\Delta G_{l-s} = G_l - G_s$ between liquid (G_l) and crystal phase (G_s) provides a driving force for crystal nucleation. At the same time, the formation of a liquid-solid interface creates an energy barrier that has to be overcome to form a nucleus of critical size. The growth of such a nucleus, on the other hand, requires atomic

rearrangements in the liquid, which are hindered increasingly the higher the viscosity, $\eta(T)$, of the liquid is. The nucleation rate, I_v, per unit volume is then determined as the product of these thermodynamic and kinetic factors [10,19] as

$$I_v = \frac{A_v}{\eta(T)} \exp\left(-\frac{\Delta G^*}{k_B T}\right), \tag{1.2}$$

where A_v is a constant and k_B is the Boltzmann constant; ΔG^* is the activation energy that has to be overcome for the formation of a stable nucleus and can (for a spherical nucleus) be expressed as $\Delta G^* = 16\pi\sigma^3 / 3(\Delta G_{l\text{-}s})^2$, where σ is the interfacial energy between the nucleus and the liquid phase. Based on an analysis of the temperature dependence of Eq. 1.2, as early as the 1960s Turnbull [25] suggested a useful rule of thumb for predicting glass-forming ability which states that the homogeneous nucleation rate in the undercooled liquid is negligibly small if the reduced glass transition temperature (i.e. ratio of glass transition temperature, T_g, to melting point, T_m) $T_{rg} \geq 2/3$. In consequence, alloy compositions lying close to deep eutectics typically exhibit better glass-forming ability. This criterion has recently been extended by proposing a parameter that depends on T_{rg} and the fragility index m [26]. The concept builds on the observation that good glass-forming alloys generally show strong liquid behaviour with high viscosity (i.e. low m), while marginal glass-formers are more fragile liquids (i.e. have high m) [27]. Besides T_{rg}, other criteria characterising glass-forming ability have been proposed over the last few years, such as the supercooled liquid region ΔT_x ($= T_x - T_g$), which is equal to the difference between the onset temperature of crystallisation, T_x, and the glass transition temperature [28], or $\gamma = T_x/(T_g + T_m)$ [29]. Other criteria that are not based on the characteristic temperatures for glass formation have also been proposed, such as the correlation between volumetric change and glass-forming ability [30], or, for binary alloys, a combined parameter based on topological instability and the average electronegativity difference of the constituent elements [31].

Inoue summarised the results of glass-forming in multicomponent alloys and proposed three empirical criteria for stabilising the supercooled liquid state and good glass-forming ability [18,22]: (1) the use of multicomponent alloys of three or more elements increases the complexity and size of the crystal unit cell and lowers the energetic advantage of forming an ordered structure; (2) an atomic radius mismatch larger than 12 % increases the packing density and impedes crystallisation; and (3) negative heats of mixing among the

main elements decrease the atomic diffusivity and hence increase the equilibrium melt viscosity. Exceptions are a few binary (e.g. CuZr, CuHf, PdSi, CaAl) and Pd-based alloys which do not satisfy the three empirical rules, pointing to the complexity of glass-forming and its underlying mechanism(s). The empirical criteria were expanded by the "confusion" principle [32] or the role of "frustration" [33]. These concepts state that the more diverse the atomic species, the less likely the system will be to find a crystal structure that is able to incorporate the various elements. The crystal structure is "confused" or "frustrated" by chemical disorder, resulting in a deeper, more complex eutectic structure.

Despite these empirical rules for good glass-forming ability, the fundamental aspects influencing glass-forming ability have not yet been completely revealed. Consequently, the alloy development of multicomponent BMGs has mainly involved trial and error, which is obviously a very tedious and costly approach. There exist only a few recent exceptions where the number of required samples has been systematically reduced, e.g. by tracing liquidus lines via differential scanning calorimetry to the eutectic [34], by tracing the composition of maximal casting thickness by systematically examining a few consecutive compositional planes (i.e. varying the ratio of two constituent elements while keeping the ratio of the others constant) [35], or by applying an (idealised) binary eutectic cluster model [36]. However, these approaches are often limited to specific alloy systems or involve other strict restrictions. Therefore, establishing general strategies in multi-dimensional composition space to locate the best glass-forming composition remains an ongoing task. An alternative approach to reducing the labour-intensive alloy development endeavour is to use ultrahigh gravitational acceleration processing, which due to effective separation of solid and liquid phases allows the straightforward identification of deep eutectics in multicomponent alloys when applied during the cooling of compositionally off-eutectic melts [37,38].

1.4 Microstructural aspects of metallic glasses

Microstructure determines the properties of materials. A fundamental understanding of the microstructure and the availability of basic structural models is therefore highly desirable for any class of materials. In oxide glasses covalent angle constraints helped to establish structural models (e.g. Ref. [39]), but the situation in metallic glasses is more complicated due to the non-directional nature of metallic bonds and gets even more complex when the dynamics of metallic glass structures (such as diffusion, relaxation or deformation) are considered.

Metallic glasses are non-crystalline solids without long-range order of their constituent atoms. Interestingly, density measurements show that the difference between a metallic glass and its corresponding fully-crystallised state is only in the range of 0.3–1.0 % [22,40]. At first sight, the constituent atoms of a metallic glass can be considered randomly arranged, but at the same time homogeneously distributed on a macroscopic level. Early models of metallic glass structures were described as a high degree of dense random packing of hard spheres with equal [41] and unequal sizes [42]. The atomic arrangement was considered from a purely geometrical perspective, simply using ratios of atomic radii. These models, however, suffered from the conflict between efficient packing and randomness, since the densest packing of atoms can be achieved only with well-developed order (i.e. crystalline structure) and the models failed to explain the observation that most stable metallic glasses have three or more constituents. Further, they were unable to provide insight into the short- and medium-range order (SRO and MRO[3], respectively) that develops to a certain extent upon cooling as the atoms seek energetically-favourable positions. SRO typically develops over a few coordination shells (< 0.5 nm), beyond which MRO may extend up to 1–2 nm [43].

Nonetheless, it seems that efficient packing is an important principle in the description of metallic glass structures, and it recently inspired the development of the efficient cluster packing (EPC) model [44]. A knowledge of SRO is not enough to determine the overall structure of metallic glasses, and thus dense atomic-scale packing has to be extended beyond the SRO to the macroscopic scale. The local structural elements consist of efficiently packed solute-centred atomic clusters. An extended structure (i.e., MRO) is then

[3] SRO and MRO comprise all kinds of inherent local structures/clusters in the glassy matrix, including quenched-in crystalline phases whose formation was not fully suppressed during solidification.

produced by idealising these clusters as spheres and efficiently packing these sphere-like clusters in a face-centred cubic (fcc) or hexagonal closed packed (hcp) configuration to fill space. Internal strains and packing frustration, however, impede the regular arrangement of the clusters on a long-range scale and the disordered structure of metallic glasses is retained beyond a few cluster diameters on the nanoscale. Although structure can be rationalised, the EPC model does not directly account for chemical contributions, internal strains and structural relaxation processes to the stability of the glass. Subsequent experimental and atomistic simulation studies suggested icosahedral packing of the clusters [45]. While these models give very helpful insights into the static structures of metallic glasses and it is expected that it is short- and medium-range order which mainly control their properties, a description of structural dynamics is much more complicated because various types of atomic motion (plastic deformation and diffusion) and thermal history have to be included.

Since it is not easy to characterise the three-dimensional structure and its dynamics straightforwardly, phenomenological concepts are often used to describe atomic transport and deformation in metallic glasses. One of the most frequently used concepts here is free-volume model [46,47]. Regardless of the packing model, the total volume of a metallic glass can be divided into a certain volume fraction occupied by dense atomic clusters and the space remaining in between, where the local density is slightly reduced due to packing frustrations. This additional volume in excess of an ideally packed reference amorphous state is often referred to as “free volume”. Any site in the structure at which the amount of free volume is increased represents a particular site with enhanced atomic mobility. As will be shown in Section 2.4, the free volume has been shown to be very useful as a (semiquantitative) intrinsic state variable that triggers plastic deformation, and consequently for describing the mechanical properties of metallic glasses. Contrasting with this description is Egami’s theory of local topological fluctuations based on atomic level stresses [48,49], where structural dynamics (e.g. diffusion or shear deformation) are viewed as bond-exchange processes.

An alternative description of the structure of metallic glasses was brought forward by Bakai [50], who used a polycluster model which consists of polyatomic chemically ordered non-crystalline nanoclusters separated by disordered intercluster boundaries. Plastic deformation, for example, is then described by moving dislocation-like defects along the intercluster boundaries. Based on neutron scattering measurements and Reverse Monte Carlo simulations, Fan *et al*. proposed a similar model [51 and references therein]. Their

atomistic structure model essentially contains three parts: tight-bond (bcc- or icosahedral-like) clusters, free-volume regions between the clusters, and loosely-bonded interconnecting zones. According to this model the stability of BMGs lies in the formation and impingement of stable clusters of low internal energy, and crystallisation is hindered by the tight intracluster bonds which would need to be broken prior to forming long-range ordered structures. The weakly-bond free-volume zones provide room for cooperative sliding and rotation of the clusters under an applied force, resulting in shear-band formation and plastic deformation of BMGs.

At present, it is difficult to judge which of the various existing models is closest to reality. The real atomic structure of metallic glasses remains unsolved, and extensive research is currently attempting to reveal and describe the structure of metallic glasses, understand the glass transition and characterise the various structure-property relationships.

1.5 Mechanical properties of bulk metallic glasses

The absence of long-range order, crystal defects and grain boundaries in metallic glasses makes their mechanical properties and behaviour fundamentally different from those of crystalline alloys. In the absence of the well-defined dislocation defects ubiquitous in crystalline alloys, metallic glasses consequently exhibit room-temperature strength much closer to the theoretical strength of the material and significantly higher elastic strain limit than their crystalline counterparts.

The average specific strength of metallic glasses is about 340 MPa/(g/cm^3) and hence more than twice as high as that of their crystalline counterparts, which display ~150 MPa/(g/cm^3) [52]. As shown in Fig. 1.3, the highest fracture strengths can be found in Fe- and Co-based BMGs, where even values above 5 GPa have been reported (see e.g. [53]).

The Hookean elastic strain, ε_{el}, of roughly 2 % that a metallic glass can support in tension, compression or bending is approximately four times higher than that of a

corresponding crystalline alloy of similar density, resulting in a storage density of elastic energy E_{el} ca. 10–20 times higher, since $E_{el} \sim \varepsilon_{el}^2$.

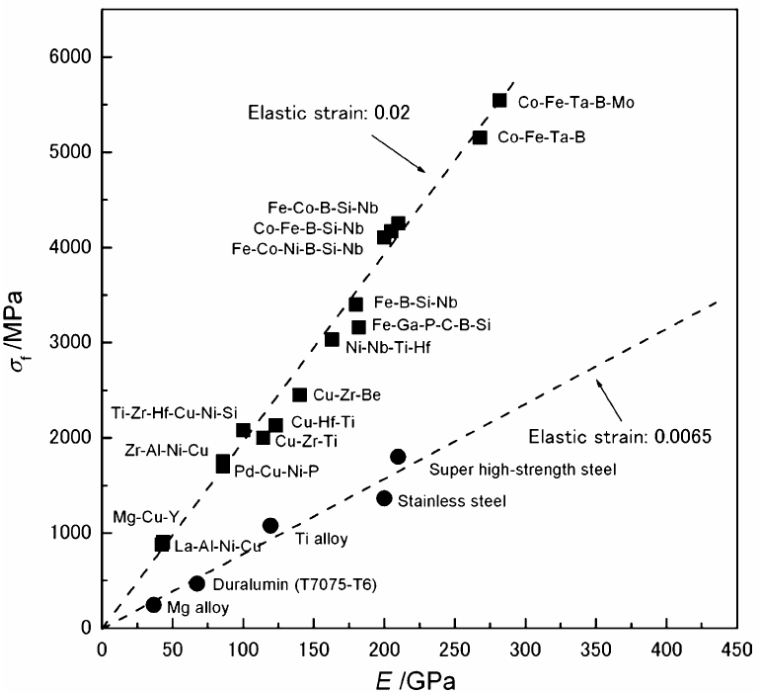

Fig. 1.3: Relationship between fracture strength and Young's modulus for a variety of bulk metallic glasses. The data for several commercialised crystalline alloys are indicated for comparison (from Ref. [54]).

Due to their high yield strength and hardness metallic glasses have promising tribological and wear-resistant properties, which in special cases can be even superior to those of conventional crystalline alloys (for a detailed review see e.g. [55] and references therein). In contrast to those of crystalline alloys, which depend strongly on their microstructure, the mechanical properties of amorphous metals are well correlated with each other. For example, fracture stress, σ_f, and yield stress show a strong linear dependency on Young's modulus (see Fig. 1.3) and shear modulus [56], respectively. Similarly, in metallic glasses there exists an approximately linear relationship between hardness, H, and Young's modulus due to the fact that $H/\sigma_f \approx 2.8$–3.2 [57].

Further, the glass transition temperature often provides a suitable basis for normalising various properties when comparing different glassy alloys, such as shown in Fig. 1.4 using the example of fracture strength.

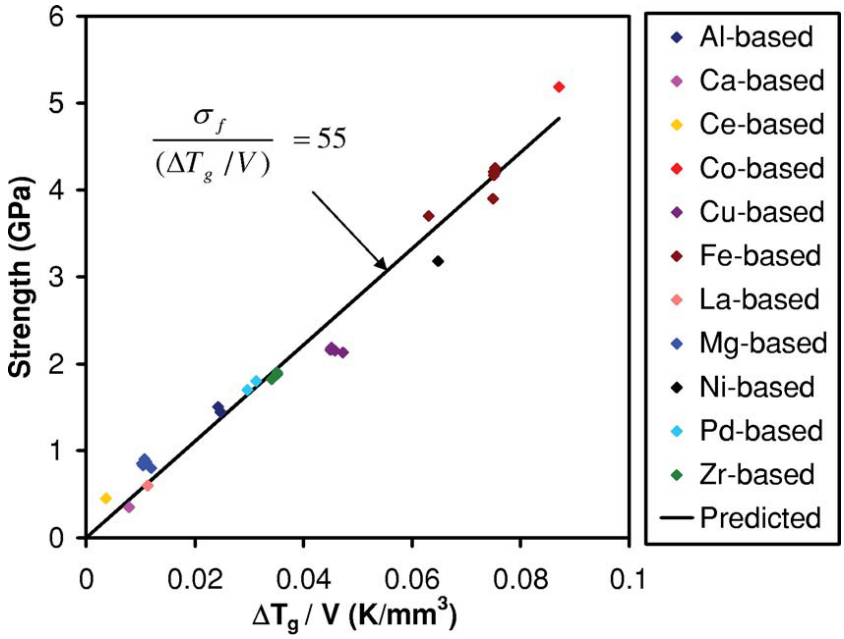

Fig. 1.4: Relationship between room-temperature fracture strength (σ_f), and the ratio $\Delta T_g = T_g - T_0$ (where T_g is the glass transition temperature and T_0 is taken as room temperature) to molar volume (V) for a variety of bulk metallic glasses (from Ref. [58]).

The Achilles' heel of BMGs at room temperature is their limited plastic deformation prior to catastrophic failure. Especially if tested under unconfined tensile conditions, they usually fail with little (i.e. almost zero) macroscopic plastic deformation. Their stress-strain curves resemble those of conventional brittle materials, such as ceramics and oxide glasses, and so BMGs are often referred to as "brittle", or at least "macroscopically brittle". The cause of this limited macroscopic plasticity in BMGs is the absence of grain structure and an extreme localisation of plastic flow into narrow shear bands that initiate strain-softening. Deformation strains inside the shear bands, however, can range from 100–1000 %, showing that BMGs are not intrinsically brittle and do posses inherent mechanisms for plastic flow on a microscopic scale.

There is considerable difference (and also scattering) of the reported compressive plasticity of (monolithic) BMGs, ranging from very limited (< 1 %) to large plastic strains (>> 20 %) [59]. The origin of this difference in behaviour is not fully understood. Purely geometrical reasons (e.g. specimen misalignment [60] and low aspect ratio [61]) or mechanical interlocking of cracks [62] are among the many explanations for enhanced plasticity of (monolithic) BMGs to be found in literature. Other prominent examples are the presence of chemical inhomogeneities [63], structural ordering on the scale of 1–2 nm (e.g.

nanocrystallisation [64] during deformation), the presence of nanocrystals [65] or quenched-in icosahedral nuclei [66] in the amorphous matrix, amorphous (nanoscale) phase separation [67,68], and excessive free-volume content [69]. Basically, they all lead to the formation of multiple shear bands and/or their deflection/intersection, resulting in the higher plastic strain to failure measured. Similarly, it was shown that even small changes in the chemical composition of an alloy can generate significant increases/decreases in the compressive plasticity [59]. A possible explanation for this behaviour was proposed in Ref. [70] for CuZr-based BMGs, where a correlation between the measured plastic strain and the activation energy for crystallisation was found. The mechanical properties of many BMGs are also highly sensitive to variations in oxygen content. The presence of low oxygen traces during the synthesis of Zr-based BMGs, for example, causes an embrittlement of the material [71] and a drastic reduction in its fracture toughness [72].

At present it seems that intrinsic relationships exist between the plasticity of BMGs and their Poisson's ratio (ν), and between fracture energy/toughness and shear-to-bulk modulus ratio (G/B) [73]. The idea emerged from the observation that a monolithic $Pt_{57.5}Cu_{14.7}Ni_{5.3}P_{22.5}$ BMG displaying a high Poisson's ratio ($\nu = 0.42$) shows up to 20 % plasticity under compression [74]. For a Poisson's ratio larger than ~0.32 (or, equivalently $G/B < 0.40$) shear-band tips tend to extend rather than induce crack initiation, allowing the formation of multiple shear bands and generating higher plasticity and toughness. The correlation applies equally to as-cast metallic glasses of different compositions [73] and for the embrittlement of glasses upon annealing [75]. There is also significant evidence that the plastic zone size ahead of a crack can be estimated as

$$R_{\mathrm{p}} \approx \frac{1}{6\pi}\left(\frac{K_{\mathrm{I}}}{\sigma_{\mathrm{y}}}\right)^2, \tag{1.3}$$

where K_{I} is the fracture toughness [76]. The high (yield) strength, σ_{y}, of metallic glasses makes the process zone small (between e.g. ~0.1 μm for Mg-based BMGs and ~100 μm for Zr-based BMGs, see Fig. 1.5), suggesting that macroscopically brittle fracture is to be expected in specimens that exceed this size. However, it may be possible to overcome this limitation, for example by increasing the process zone size (via the fabrication of composite materials) or by effectively decreasing the sample dimensions below the limiting size (see also Section 2.3.3 for further details).

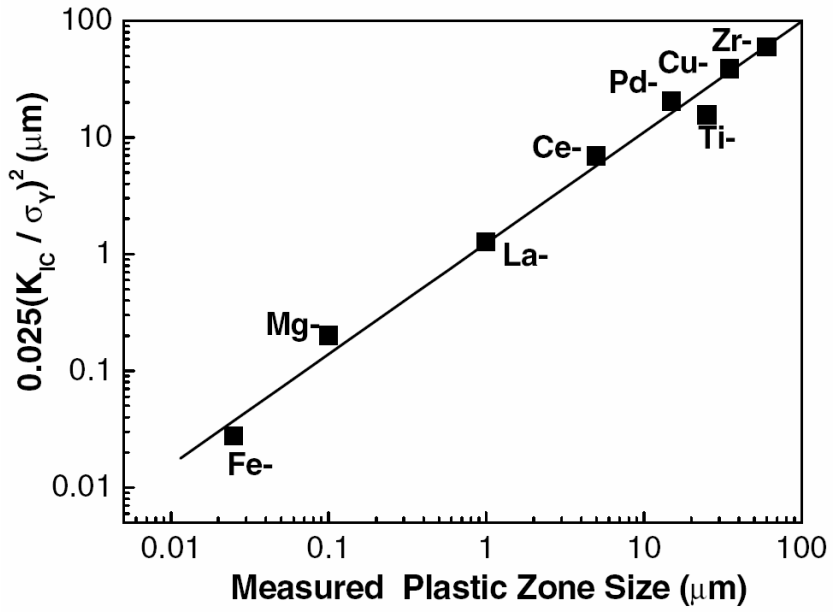

Fig. 1.5: Correlation between fracture toughness, yield strength and plastic zone size for a variety of bulk metallic glasses (from Ref. [76]).

1.6 Application potential

The lack of room-temperature plasticity in BMGs obviously limits industrial and structural applications, where reliability is crucial. Nevertheless, their unique properties make them attractive for many potential applications where very specific functionalities are required and/or components are small. For recent reviews of (potential) applications of metallic glasses and further references about the examples given in the following see Refs. [8,77,78].

Metallic glasses display very soft magnetic properties (i.e. high permeability and low coercivity) due to their lack of magnetocrystalline anisotropy and grain boundaries (i.e. domain pinning). In addition, the magnetic properties of metallic glasses can be tailored by inducing nanocrystallisation and adjusting the grain size. This led to the first large-scale application of Fe-based ribbons as low-loss magnetic cores in transformers, magnetic read-heads or as components in electronic article surveillance systems.

Due to their excellent mechanical properties BMGs have also found application in sports equipment, where they were first exploited commercially in golf club heads, then parts of tennis rackets, baseball bats, skis and bicycles. Their ability to store high densities of elastic energy turns metallic glass into the "premier" spring material. A newly developed application utilising their efficient energy transfer characteristics is the use of BMG spheres for shot-peening purposes. The high elastic strain limit of metallic glasses led to the development of coriolis mass flowmeters, pressure sensors and strain gauges with properties superior to conventional crystalline parts. The generally good hardness and peculiar tribological properties of metallic glasses make them attractive as coating materials. And indeed, there have been efforts to fabricate amorphous coatings, for example by low-temperature spraying or radio-frequency magneton sputtering. Another area of commercial interest is the field of biocompatible BMGs suitable for medical components such as implants and surgical instruments. The self-sharpening effect known in metallic glasses has already led to their first medical application as surgical scalpel blades.

A big advantage in fabricating amorphous metallic components is that metallic glasses can be processed in the supercooled liquid region above the glass transition temperature and below the onset temperature of crystallisation. This superplastic forming involves heating the material and forming it under an applied pressure, similar to the processing of thermoplastics. Conventional net-shape manufacturing processes, such as die/injection casting or blow moulding, can be applied. The cast glassy alloys exhibit a high surface quality and maintain dimensional accuracy due to their lack of crystallisation shrinkage. This has led to the market introduction of structural parts, such as casings for electronic components, cell phone hinges, and (by using precious BMGs) jewellery and watch applications. BMGs' superplastic net-shape forming makes them attractive for microstructure fabrication (e.g. microgears) and applications for microelectromechanical systems (MEMS). Additionally, the recent development of nano- and microscale process techniques using focused ion beam, electron beam and LIGA (i.e. X-ray lithography, electroforming, and plastic moulding) processes has increased the importance of materials with homogeneous structures on the nanometre scale, and consequently created a new field for potential applications of BMGs and nanocrystalline alloys.

More critical than the limited plasticity at room temperature, which to some extent hampers their structural application, the production costs of BMGs are generally much higher than those of conventional crystalline alloys. This is because their fabrication often

requires high-purity elements and expensive vacuum-processing techniques. Therefore, the most prominent future applications of BMGs might be microcomponents produced in large quantities; products with high added value, such as medical devices, luxury goods and leisure equipment; or those with very specific functionality.

1.7 Outline of the thesis

After the general overview of metallic glasses with an emphasis on glass-forming ability, microstructure and mechanical properties presented in this chapter, the thesis is structured as follows. Chapter 2 describes the deformation characteristics and the existing deformation models of metallic glasses, and Chapter 3 defines the aims of the thesis. Chapter 4 summarises the experimental investigations into the temperature dependence and strain-rate effects (i.e. strain-rate sensitivity) of inhomogeneous flow in Zr-based BMGs, and presents high-resolution SEM observations of shear surfaces. Based on these experimental findings, additional kinetic parameters of flow are deduced in Chapter 5 and a constitutive model for (inhomogeneous) deformation in metallic glasses is developed and its implications and validation discussed. In Chapter 6 the influence of sample size and varying free-volume content on the deformation behaviour are addressed by means of microcompression and instrumented indentation tests, and discussed with regard to the pressure sensitivity of metallic glasses. Chapter 7 concludes the study, with a general summary of the thesis and an outlook for possible future work.

1.8 References

[1] M.L Falk, Science 318 (2007) 1880.
[2] J. Kramer, Ann. Phys. 19 (1934) 37.
[3] A. Brenner, J. Res. Nat. Bur. Stand. 44 (1950) 109.
[4] W. Buckel, R. Hilsch, Z. Phys. 128 (1950) 324.
[5] W. Buckel, R. Hilsch, Z. Phys. 132 (1952) 420.
[6] D. Turnbull, Metall. Trans. A 12 (1981) 695.
[7] A.L. Greer, Science 267 (1995) 1947.
[8] J.F. Löffler, A.A. Kündig, F.H. Dalla Torre in *Materials Processing Handbook*, edited by J.R. Groza, J.F. Shackelford, E.L. Lavernia, and M.T. Powers, (CRC Press, Taylor & Francis Group 2007), chap. 17.
[9] R. Busch, Ann. Chim. Sci. Mat. 27 (2002) 3.
[10] J.F. Löffler, Intermetallics 11 (2003) 529.
[11] W. Klement, R.H. Willens, P. Duwez, Nature 187 (1960) 869.
[12] H.S. Chen, Acta Metall. 22 (1974) 1505.
[13] M.C. Lee, J.M. Kendall, W.L. Johnson, Appl. Phys. Lett. 40 (1982) 382.
[14] A. Inoue, T. Zhang, T. Masumoto, Mater. Trans. JIM 31 (1990) 425.
[15] A. Peker, W.L.Johnson, Appl. Phys. Lett. 63 (1993) 2342.
[16] A. Inoue, T. Zhang, T. Masumoto, J. Non-Cryst. Solids 156 (1993) 473.
[17] H.W. Kui, A.L. Greer, D. Turnbull, Appl. Phys. Lett. 45 (1984) 615.
[18] A. Inoue, A. Takeuchi, Mat. Sci. Eng. A 375 (2004) 16.
[19] W.H. Wang, C. Dong, C.H. Shek, Mater. Sci. Eng. R 44 (2004) 45.
[20] Y. Li, S.J. Poon, G.J. Shiflet, J. Xu, D.H. Kim, J.F. Löffler, MRS Bull. 32 (2007) 624.
[21] J.F. Löffler, J. Schroers, W.L. Johnson, Appl. Phys. Lett. 77 (2000) 681.
[22] A. Inoue, Acta Mater 48 (2000) 279.
[23] X.H. Lin, W.L. Johnson, J. Appl. Phys. 78 (1995) 6514.
[24] X.H. Lin, W.L. Johnson, W.K. Rhim, Mater. Trans. JIM 38 (1997) 473.
[25] D. Turnbull, Contemp. Phys. 10 (1969) 473.
[26] O.N. Senkov, Phys. Rev. B, 76, (2007) 104202.
[27] E.S. Park, J.H. Na, D.H. Kim, Appl. Phys. Lett. 91 (2007) 031907.
[28] M. Marcus, D. Turnbull, Mat. Sci. Eng. 23 (1976) 211.
[29] Z.P. Lu, C.T. Liu, Acta Mater. 50 (2002) 3501.
[30] E.S. Park, D.H. Kim, Appl. Phys. Lett. 92 (2008), 091915.
[31] W.J. Botta, F.S. Pereira, C. Bolfarini, C.S. Kiminami, M.F. de Oliveira, Philos. Mag. Lett. 88 (2008), 785.
[32] A.L. Greer, Nature 366 (1999) 303.
[33] W.L. Johnson, MRS Bull. 24 (1999) 42.
[34] H. Tan, Z.P. Lu, H.B. Yao, B. Yao, Y.P. Feng, Y. Li, Mater. Trans. JIM 42 (2001) 551.
[35] H. Ma, L.L. Shi, J. Xu, Y. Li, E. Ma, Appl. Phys. Lett. 87 (2005) 181915.
[36] Z.P. Lu, J. Shen, D.W. Xing, J.F. Sun, C.T. Lu, Appl. Phys. Lett. 89 (2006) 071910.
[37] J.F. Löffler ,W.L. Johnson, Intermetallics 10 (2002) 1167.
[38] E.R. Arata, F.H. Dalla Torre, J.F. Löffler, Acta Mater. 56 (2008) 651.
[39] P.K .Gupta, J. Am. Ceram. Soc. 76 (1993) 1088.

[40] A. Inoue, T. Negishi, H.M. Kimura, T. Zhang, A.R. Yavari, Mater. Trans. JIM 39 (1998) 318.
[41] J.D. Bernal, Nature 185 (1960) 68.
[42] H.J. Frost, R. Raj, J. Am. Ceram. Soc. 95 (1982) C19.
[43] T.C. Hufnagel, S. Brennan, Phys. Rev. B 67 (2003) 014203.
[44] D.B. Miracle, Nat. Mater. 3 (2004) 697.
[45] H.W. Sheng, W.K. Luo, F.M. Alamgir, J.M. Bai, E. Ma, Nature 439 (2006) 419.
[46] M.H. Cohen, D. Turnbull, J. Chem. Phys. 31 (1959) 1164.
[47] F. Spaepen, Acta Metall. 25 (1977) 407.
[48] T. Egami, K. Maeda, V. Vitek, Philos. Mag. A 41 (1980) 883.
[49] T. Egami, Intermetallics 14 (2006) 882.
[50] A.S. Bakai, in *Topics in Applied Physics – Galssy Metals III*, edited by H. Beck and H.J. Gunterodt, Vol. 72 (Springer, Berlin, 1994), p. 209.
[51] C. Fan, P.K. Liaw, C.T. Liu, Intermetallics 17 (2008) 46.
[52] J.F. Löffler, Z. Metallkd. 97 (2006) 225.
[53] A. Inoue, B.L. Shen, H. Koshiba, H. Kato, A.R. Yavari, Nat. Mater. 2 (2003) 661.
[54] A. Inoue, B.L. Shen, C.T. Chang, Intermetallics 14 (2006) 936.
[55] A.L. Greer, K.L. Rutherford, I.M. Hutchings, Int. Mater. Rev. 47 (2002) 87.
[56] M.D. Demetriou, J.S. Harmon, M. Tao, G. Duan, K. Samwer, W.L. Johnson, Phys. Rev. Lett. 97 (2006) 065502.
[57] H.W. Zhang, G. Subhash, X.N. Jing, L.J. Kecskes, R.J. Dowding, Philos. Mag. Lett. 86 (2006) 333.
[58] B. Yang, C.T. Liu, T.G. Nieh, Appl. Phys. Lett. 88 (2006) 221911.
[59] Y.H. Liu, G. Wang, R.J. Wang, D.Q. Zhao, M.X.Pan, W.H. Wang, Science 315 (2007) 1385.
[60] W.F. Wu, Y. Li, C.A. Schuh, Philos. Mag. 88 (2008) 71.
[61] Z.F. Zhang, H. Zhang, X.F. Pan, J. Das, J. Eckert, Philos. Mag. Lett. 85 (2005) 513.
[62] K. Mondal, G. Kumar, T. Ohkubo, K. Oishi, T. Mukai, K. Hono, Philos. Mag. Lett. 87 (2007) 625.
[63] J. Das, M.B. Tang, K.B. Kim, R. Theissmann, F. Baier. W.H. Wang, J. Eckert, Phys. Rev. Lett. 94 (2005) 205501.
[64] M.W. Chen, A. Inoue, W. Zhang, T. Sakurai, Phys. Rev. Lett. 96 (2006) 245502.
[65] A. Inoue, W. Zhang, T. Tsurui, A.R. Yavari, A.L. Greer, Philos. Mag. Lett 85 (2005) 221.
[66] J.M. Park, H.J. Chang, K.H. Han, W.T. Kim, D.H. Kim, Scr. Mater. 53 (2005) 1.
[67] J.C. Oh, T. Ohkubo, Y.C. Kim, E. Fleury, K. Hono, Scr. Mater. 53 (2005) 165.
[68] X.H. Du, J.C. Huang, K.C. Hsieh, Y.H. Lai, H.M. Chen, J.S.C. Jang, P.K. Liaw, Appl. Phys. Lett. 91 (2007) 131901.
[69] L.Y. Chen, Z.D. Fu, G.Q. Zhang, X.P. Hao, Q.K. Jiang, X.D. Wang, Q.P. Cao, H. Franz, Y.G. Liu, H.S. Xie, S.L. Zhang, B.Y. Wang, Y.W. Zeng, J. Z. Jiang, Phys. Rev. Lett. 100 (2008) 075501.
[70] S.W. Lee, M.Y. Huh, E. Fleury, J.C. Lee, Acta Mater. 54 (2006) 349.
[71] Z.P. Lu, H. Bei, Y. Wu, G.L. Chen, E.P. George, C.T. Liu, Appl. Phys. Lett. 92 (2008) 011915.
[72] V. Keryvin, C. Bernard, J.C. Sangleboeuf, Y. Yokoyama, T. Rouxel, J. Non-Cryst. Solids 352 (2006) 2863.
[73] J.J. Lewandowski, W.H. Wang, A.L. Greer, Philos. Mag. Lett. 85 (2005) 77.
[74] J. Schroers, W.L. Johnson, Phys. Rev. Lett. 93 (2004) 155506.

[75] A. Castellero, D.I. Uhlenhaut, B. Moser, J.F. Löffler, Philos. Mag. Lett. 87 (2007) 383.
[76] X.K. Xi, D.Q. Zhao, M.X. Pan, W.H. Wang, Y. Wu, J.J. Lewandowski, Phys. Rev. Lett. 94 (2005) 125510.
[77] M.F. Ashby, A.L. Greer, Scr. Mater. 54 (2006) 321.
[78] A. Inoue, N. Nishiyama, MRS Bull. 32 (2007) 651.

2 Deformation of metallic glasses

When a solid is plastically deformed, it can exhibit either homogeneous or inhomogeneous deformation. While during homogeneous deformation plastic strain is uniformly distributed throughout the specimen, during inhomogeneous deformation plastic strain is localised and confined in thin regions called shear bands. This strain localisation phenomenon is observed not only in metallic glasses but also in a wide variety of material systems, such as polymers, fine-grained alloys, foams, granular media and colloids.

In this chapter the most prominent phenomenological influences of temperature and strain rate on the (homogeneous and inhomogeneous) deformation behaviour of metallic glasses are summarised. Emphasis is placed on strain localisation and shear-band characteristics which limit plasticity at low temperatures, and on strategies for improving plasticity through suitable microstructural design or geometrical adjustment (e.g. “sample size effects”). Finally, the last section gives an overview of existing deformation models and their recent refinement. It also provides a basis for the discussion and constitutive modelling of our results in Chapters 4 and 5.

2.1 Introduction

Based on phenomenological observation of the deformation behaviour of metallic glasses, as early as 1977 Spaepen constructed a "deformation (mechanism) map" classifying deformation behaviour as a function of temperature and stress state (Fig. 2.1). Basically, there exist two modes of deformation: homogeneous flow at high temperature and low stress, where each volume element undergoes the same strain; and inhomogeneous flow at low temperature and high stress, where strain is concentrated in a few thin shear bands. The map loses its proper significance at temperatures above the crystallisation temperature (T_x), where crystallisation processes strongly influence the deformation behaviour.

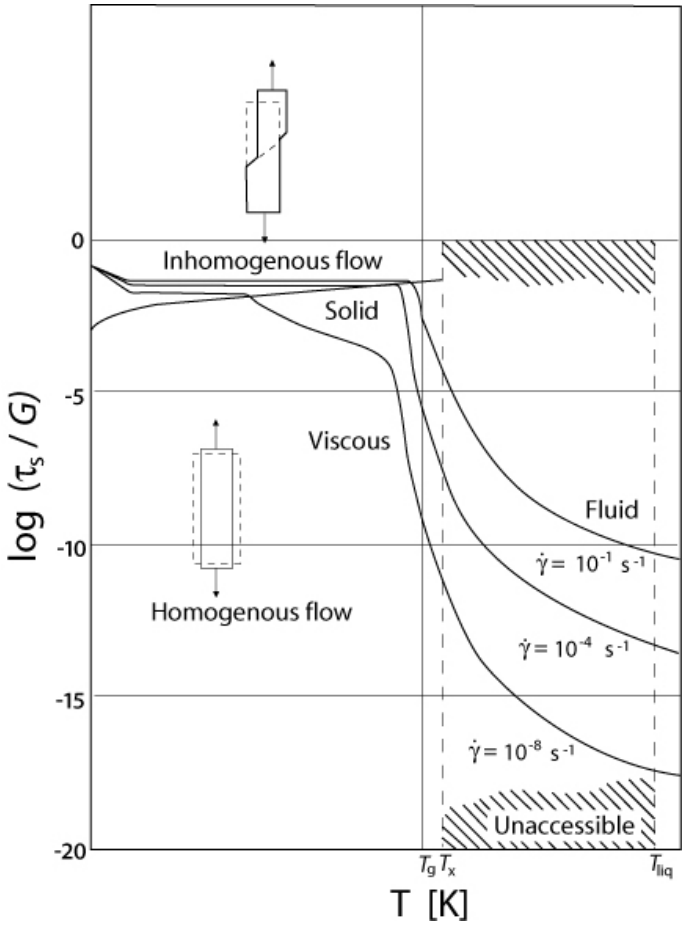

Fig. 2.1: Characteristic deformation map for metallic glasses. Plotted is the shear stress normalised by the shear modulus as a function of temperature. The solid lines indicate constant strain rates (reproduced from [1]).

Above the liquidus temperature (T_{liq}) metallic glasses have viscosities on the order of $\eta \approx 1$ Pa s and behave like Newtonian liquids. The viscosity increases drastically with cooling of the liquid and by definition reaches a value of $\eta \approx 10^{13}$ Pa s at the glass transition temperature (T_g). In the temperature region between T_x and T_g ("undercooled liquid region") deformation is strongly dependent on th applied strain rate, as shown in Fig. 2.1.

2.2 Homogeneous deformation

Homogeneous deformation of metallic glasses usually takes place at high temperatures close to the glass transition temperature or above the latter in the undercooled liquid region. In this temperature range, metallic glasses are extremely ductile and a considerable degree of plastic deformation in tension and compression can be achieved. As shown in Fig. 2.2, the deformation behaviour is very sensitive to temperature and imposed strain rate. At a given strain rate an increase in the temperature leads to a transition from inhomogeneous flow (shear localisation) to homogeneous flow (non-Newtonian or Newtonian). The transition from inhomogeneous to homogeneous deformation is also characterised by a sharp change in the temperature dependence of the peak stress. While its temperature dependence in the inhomogeneous flow regime is only small, the peak stress drastically decreases in the homogeneous flow regime with increasing temperature, as shown in Fig. 2.2 for two different strain rates. As shown in Ref. [2] the transition from inhomogeneous to homogeneous flow approximately follows

$$\ln \dot{\gamma} \propto \frac{\mu(T)}{T}, \tag{2.1}$$

where $\dot{\gamma}$ is the shear strain rate, $\mu(T)$ is the temperature-dependent shear modulus and T the testing temperature.

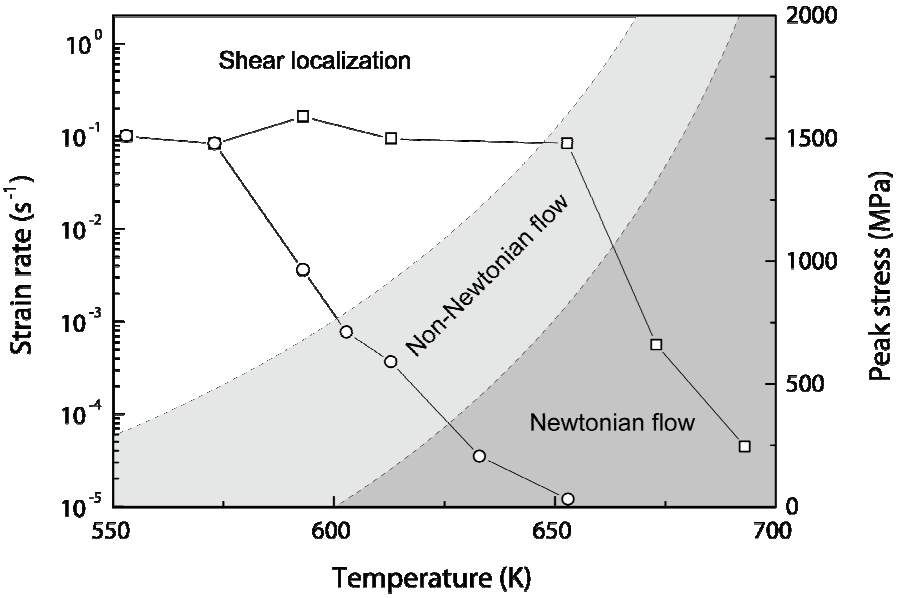

Fig. 2.2: Transition between homogeneous (non-Newtonian or Newtonian) and inhomogeneous flow (shear localisation) for amorphous $Zr_{41.2}Ti_{13.8}Cu_{12.5}Ni_{10}Be_{22.5}$ (Vitreloy 1) at temperatures around $T_g \cong 625$K. The symbols indicate measured peak stresses for various temperatures at strain rates of 10^{-4} s^{-1} (circles) and 10^{-1} s^{-1} (squares). Data is taken from [3].

At low strain rates the homogeneous flow can be characterised as Newtonian. The viscosity depends solely on temperature and scales with the ratio between shear stress and strain rate, i.e. $\eta = \tau/\dot{\gamma}$. At higher strain rates and/or lower temperatures deformation becomes non-Newtonian and viscosity strongly depends on both temperature and strain rate. From a microscopic point of view it is not fully clear what causes the transition from Newtonian to non-Newtonian flow in metallic glasses. While some studies associate the non-Newtonian behaviour with the concurrent crystallisation of the amorphous structure during deformation [4], others suggest that the non-Newtonian behaviour is associated with the existence of a transient stress-strain phenomenon ("stress overshoot", Fig. 2.3) [5], which cannot be explained by a change in sample shape, such as necking, because it is observed under tensile and compressive loading. The softening of metallic glasses (steady-state viscosity) following the stress overshoot can be attributed to a transformation of the glass from its original structure to a dynamically different structure of higher atomic mobility and lower viscosity. The dynamic structure is determined by defect creation (i.e. stress-driven disordering) and annihilation (i.e. structural relaxation) in competition, and hence deformation history plays an important role. The observed stress overshoot increases with decreasing temperature, increasing strain rate and increasing fraction of stress

relaxation [5]. It is worth noting that both structural relaxation and defect creation are kinetic processes which are temperature- and strain-rate-dependent. Therefore it is not surprising to find both Newtonian and non-Newtonian flows in the same materials but at different temperature and strain rate regimes.

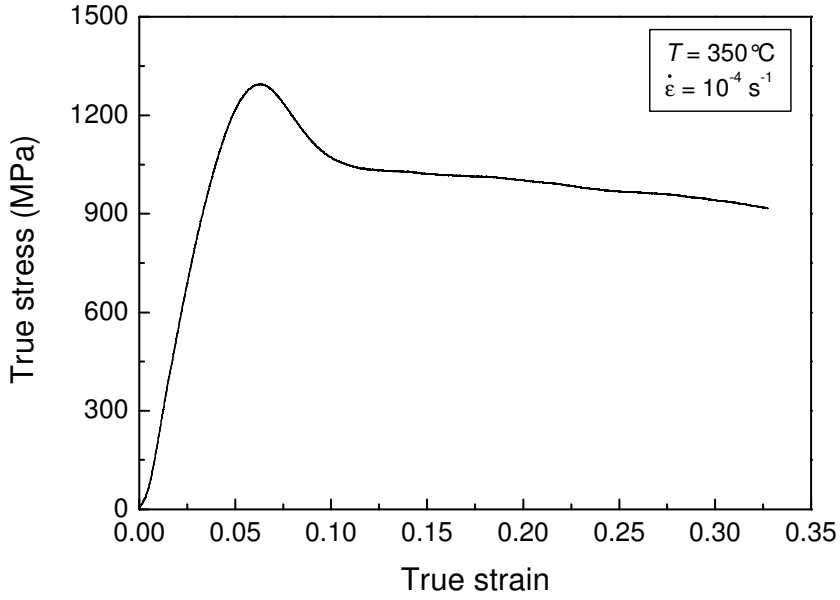

Fig. 2.3: Uniaxial compression test on $Zr_{52.5}Ti_5Cu_{17.9}Ni_{14.6}Al_{10}$ (Vit105) at $T = 350°C \cong 0.93\,T_g$ and an initial strain rate of 10^{-4} s^{-1} revealing a stress overshoot phenomenon.

Generally, both peak and steady-state flow stress in the homogeneous deformation regime show a positive strain-rate sensitivity,

$$m = \frac{\partial \ln \sigma}{\partial \ln \dot{\varepsilon}} > 0, \tag{2.2}$$

i.e. an increase in the imposed strain rate leads to an increase in the stress. The strain-rate sensitivity (m) for Newtonian flow is $m \approx 1$, which allows very large (tensile) deformation on the order of several thousand percent ("superplastic deformation") [6]. The transition to non-Newtonian flow generates a deviation from the linearity in the strain rate–stress relation and a decrease of the value of m to values far smaller than one.

The significant drop in flow stress and viscosity and the large plastic strains that can be achieved at temperatures above the glass transition temperature offer the possibility of superplastic forming of many BMGs via conventional net-shape manufacturing processes.

This, of course, requires that the BMGs possess adequate thermal stability against crystallisation.

2.3 Inhomogeneous deformation

2.3.1 Deformation characteristics

At temperatures significantly lower than T_g plastic deformation is spatially and temporally inhomogeneous and carried by highly localised, narrow shear bands, limiting macroscopic plasticity. Particularly in tension, plastic deformation is often so low that only a single dominant shear band develops, which instantly leads to fracture of the specimen. However, extensive shear banding can be observed in compression, bending or indentation tests. Here, as shown in Fig. 2.4, the shear bands can easily be observed because of the associated formation of sharp surface steps.

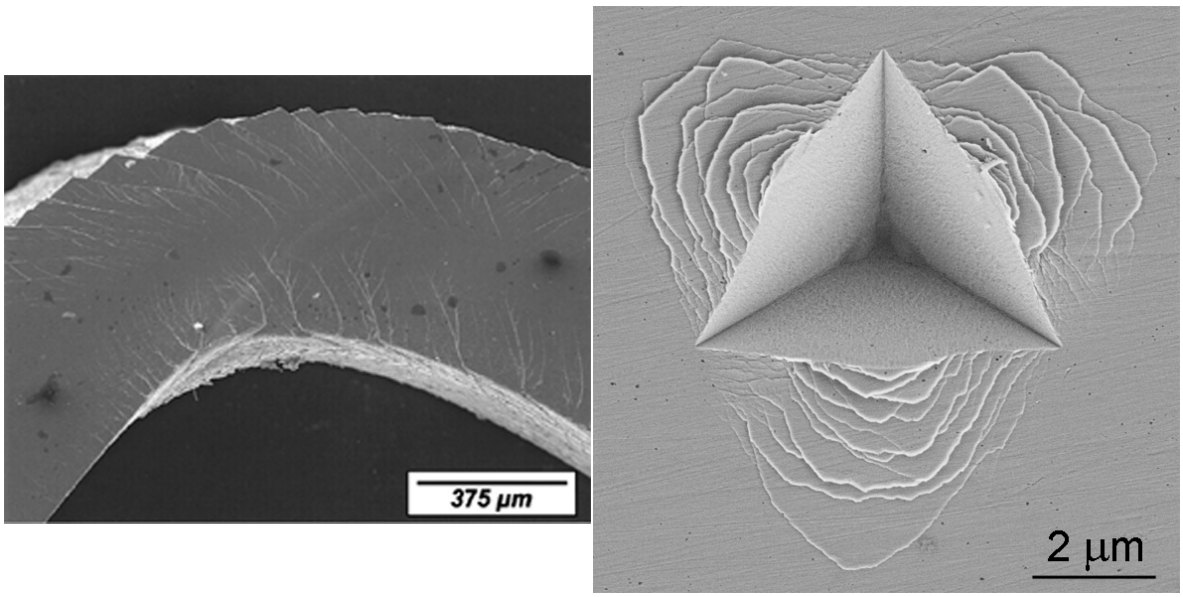

Fig. 2.4: Shear band and surface step formation after bending [7] (left) and cube-corner indentation test (right) in Zr-based BMGs.

The spatially and temporally inhomogeneous deformation is characterised by the activation and propagation of individual shear bands. The work softening associated with shear localisation is expected to make the propagation stress of a shear band less than the stress required to initiate it. This gives rise to serrated flow, which manifests itself as small displacement bursts or stress drops during plastic deformation in a (macroscopic) stress-strain curve, as shown in Fig. 2.5. The magnitude of the stress drop during compression, however, also depends on the stiffness of the testing machine in the displacement control loading mode [8]. The appearance of new surface steps (shear bands) has recently been correlated with displacement bursts ("pop-ins") in the load displacement curve during nanoindentation testing [9,10].

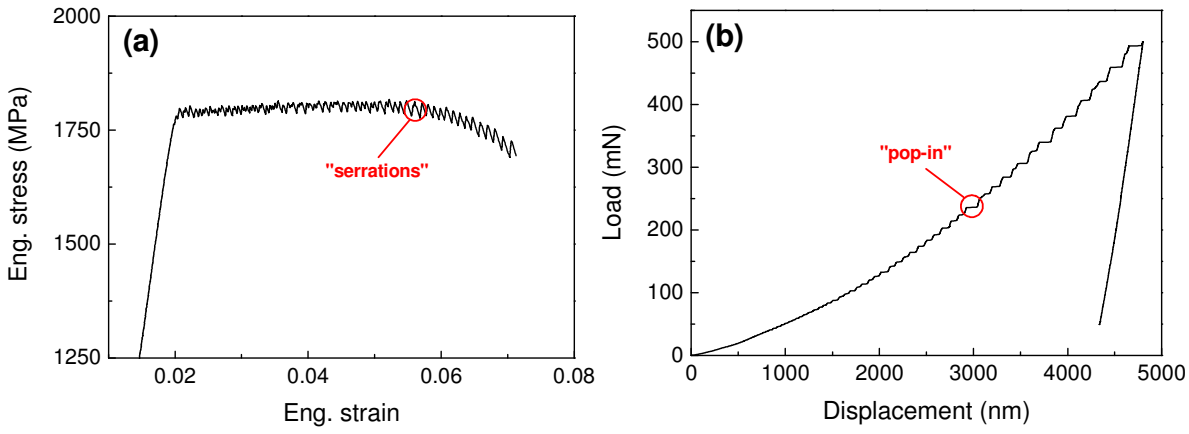

Fig. 2.5: (a) Magnified view of a stress-strain compression test (performed at an initial strain rate of 10^{-3} s^{-1}) and (b) instrumented indentation test (using a cube-corner tip and a loading rate of 1.67 mN/s) on amorphous $Zr_{52.5}Ti_5Cu_{17.9}Ni_{14.6}Al_{10}$ (Vit105) at room temperature showing serrated flow and "pop-ins", respectively.

The inhomogeneous deformation behaviour of BMGs is strongly influenced by the imposed strain rate. As shown in Fig. 2.6, mechanical tests at room temperature have shown a slight decrease in fracture strength with increasing strain rate (negative strain-rate dependence) [11,12,13,14,15,16,17], in agreement with the results presented in this thesis. Insensitivity to the strain rate [3,18,19,20] and, at high strain rate, contrasting behaviour (positive strain-rate dependence) have also recently been observed [21,22], however, as also shown in Fig. 2.6. It should be noted that in all these studies the strain rate-sensitivity was determined via fracture/yield strength measured on different samples, where due to

scattering the data is only vague, and not by more accurate strain rate change tests. In addition, the strain rate's influence on plastic strain to failure is also controversial: both an enhancement [23] and a reduction [14] upon an increase in the strain rate have been reported. However, there is strong experimental evidence that the temporal intervals and the load variations in the flow serrations and "pop-ins" diminish with increasing compressive strain rate [14,22,24,25,26,27] and nanoindentation load rate [2,9,10,28,29]. Strain rate also exerts a significant influence on the formation of shear bands in BMGs. Jiang et al. [24-27] recently reported that the number of shear bands in a Zr-based BMG observed ex-situ on uniaxially compressed specimens decreases with increasing strain rate. This trend contrasts with previous indentation studies which indicate that higher strain rates promote more shear bands [9,29,30,31]. Based on the observations of diminishing "pop-ins" at increasing strain rate Schuh *et al*. [2,29] proposed a "homogeneous II" regime in the deformation map of BMGs, where the deformation rate exceeds the characteristic rate of shear-band nucleation. Consequently, the simultaneous operation of multiple shear bands (i.e. homogenisation in time) leads to macroscopically more homogeneous flow (disappearance of "pop-ins"). These nanoindentation experiments led to the development of a thermo-viscoplastic model which describes the dependency of an increasing shear-band density on increasing strain rate [32]. Here it is, however, important to highlight the differences between uniaxial compression and nanoindentation tests: the deformation in nanoindentation is complex due to the fact that the strain gradient constantly changes during penetration, so that re-activation of the same shear band is for geometrical reasons less likely than in uniaxial compression. Thus an increase in shear-band density with increasing strain rate is not expected in uniaxial compression tests. Despite this discrepancy the various studies agree on an apparent homogenisation in time at higher strain rates. Similarly, it has been shown that a decrease in testing temperature leads to a decrease in the magnitude of stress drops and the associated time intervals between two serrations [8,26,33], and at the same time to an increase in strength (without loss of ductility) [34,35], in agreement with the results shown in Chapter 4.

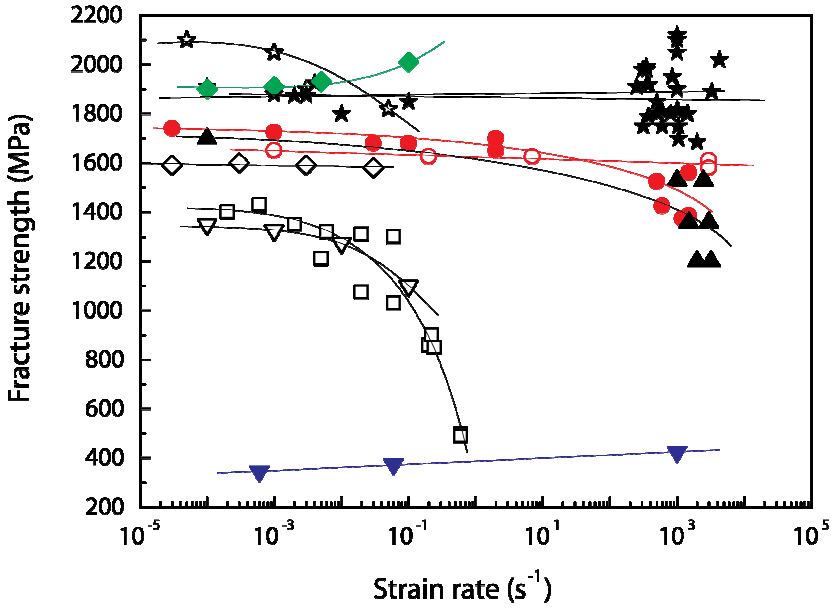

Fig. 2.6: Fracture strength as a function of strain rate in various BMGs: ★,☆ $Zr_{41.25}Ti_{13.75}Cu_{12.5}Ni_{10}Be_{22.5}$ [3,17,18,19,], ▲ $Zr_{57}Ti_5Cu_{20}Ni_8Al_{10}$ [12], ◇ $Zr_{59}Cu_{20}Al_{10}Ni_8Ti_3$ [20], □ $Zr_{65}Al_{10}Ni_{10}Cu_{15}$ [12], ▽ Dy_3Al_2 [23], ●,○ $Pd_{40}Ni_{40}P_{20}$ [14,15], ◆ $Ti_{45}Zr_{16}Ni_9Cu_{10}Be_{20}$ [22], and ▼ $Nd_{60}Fe_{20}Co_{10}Al_{10}$ [21]. Filled and unfilled symbols indicate compression and tension tests, respectively.

Inhomogeneous flow in metallic glasses also depends on the applied stress state, which can affect the formation and propagation of shear bands and cracks, respectively. For example, the fracture toughness of a Zr-based BMG is about 4 times lower in mode I deformation (crack opening) than in mode II (shearing) [36]. Many studies have also shown asymmetric behaviour in uniaxial tension and compression. The shear and fracture planes are often seen at 50–60° to the loading axis in tension and at 40–45° to the loading axis in compression [20,37]. This yield asymmetry reveals the importance of normal or hydrostatic stress components in the deformation process (i.e. pressure sensitivity), which can be incorporated via e.g. the Mohr-Coulomb criterion [38]. The physical origin of this asymmetry lies in the principle of "atomic friction" and the flow stress is assumed to be influenced by the local normal stress: $\tau = k_0 \pm \alpha\sigma_n$, where τ is the shear stress at yielding, k_0 is a constant and α is the effective coefficient of friction that quantifies the strength of the stress component normal to the shear plane (σ_n). The plus sign applies for compression and the minus for tension.

As shown in Fig. 2.7, the fracture surfaces of metallic glasses typically show vein patterns arising from viscous flow at the moment of failure due to the sudden relief of stress energy and its (partial) conversion into heat. The presence of re-solidified droplets on fracture surfaces indicate that even (local) melting of the material may take place. The vein morphology resembles the features that are formed when two rigid surfaces which are held together by a viscous film (e.g. oil or grease) are separated. This observation prompted the suggestion [39] that fracture in metallic glasses can be rationalised in terms of the Taylor instability [40], which is associated with the moving boundary between two immiscible fluids: a fluid meniscus that propagates in the direction of its convex curvature tends to break up into a series of fingers which penetrate the fluid meniscus. Thus, the vein morphology observed in metallic glasses is thought to be generated as the viscous material between the fingers necks down to failure.

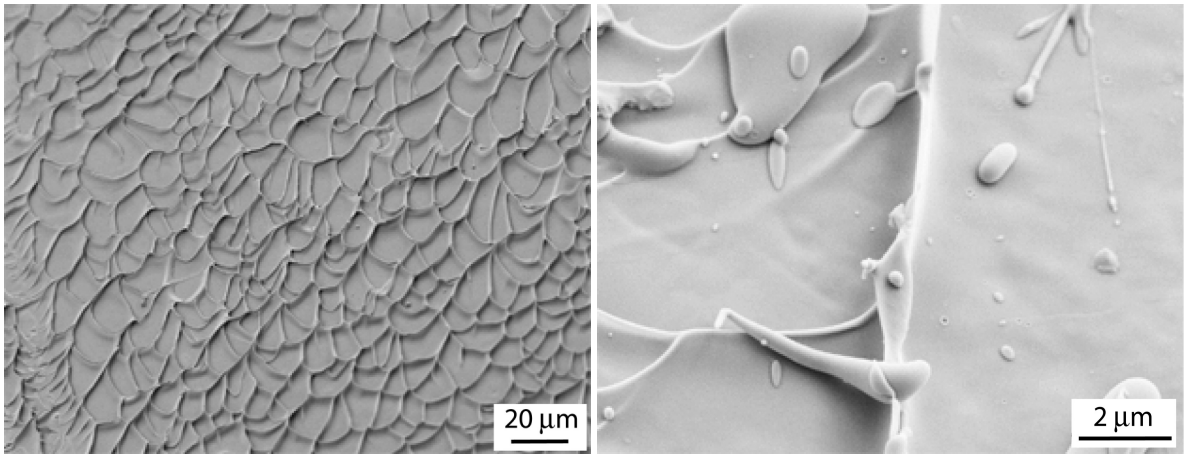

Fig. 2.7: Scanning electron micrograph of a compressive fracture surface of a $Zr_{52.5}Ti_5Cu_{17.9}Ni_{14.6}Al_{10}$ BMG showing characteristic "vein pattern" (left) and re-solidified droplets (right) arising from viscous flow at the moment of failure.

2.3.2 Shear-band characteristics

At high stresses and/or low temperatures deformation is confined to a discrete number of narrow shear bands with a characteristic thickness on the order of 10–20 nm [41]. They are the result of progressive deformation-induced softening (i.e. "strain-softening") of the material in the band. Extremely high strain up 100 is accommodated in a shear band [42],

and the local structure can alter significantly as a result. The structural change is commonly assumed to be an increase in the free volume in the glassy structure, associated with a dilatation, the lowered density being presumed to lower the stress for maintaining shear on the bands. Some dilatation is preserved after shear, such that deformed materials, upon reloading, tend to shear on existing bands. Preferential etching at shear bands also provides evidence of a structural change. It has been known for some time that shear bands in BMGs are susceptible to preferential etching [43], indicating a structural change in the deformed material such as an increased free-volume content and/or chemical reordering. Over the last few years new insights into this structural evolution during shear banding have underlined the importance of the formation and coalescence of free volume. Higher free-volume contents have been suggested after deformation, for example by positron annihilation spectroscopy (PAS) [44,45,46] where longer lifetimes were measured, and X-ray diffraction (XRD) and differential scanning calorimetry (DSC), where larger interatomic volumes and relaxation enthalpies were determined [47,48]. The PAS investigations also indicate that the content of certain alloying elements around free-volume sites is significantly enhanced at the expense of the other, remaining constituents of the BMG. The coalescence and spontaneous formation of nanometer-scale voids during deformation has also been experimentally observed [49] via high-resolution transmission electron microscopy, and confirmed according to thermodynamic considerations [50]. Depending on the stress state and composition of the metallic glass, even nanocrystallisation in shear bands has been seen in aluminium-based amorphous alloys [51,52] and in $Cu_{50}Zr_{50}$ BMG [53], and explained by dynamic flow dilatation and the attendant enhancement in atomic diffusional mobility [52].

Shear banding is not unique to metallic glasses, but is also observed in various materials classes, such as polymers, fine-grained alloys, foams, colloids and granular media. The creation of excess free volume in metallic glasses is very similar to that in granular materials (e.g. sand), in which the shear deformation of dense, randomly close-packed grains requires (local) dilatation and leads to the formation of voids within the shear bands [54]. A direct consequence of this dilatation can for example be observed when a person walks on a wet beach: the water disappears underneath the foot because of the shear-induced dilatation of the sand grains [55]. In addition, a wide variety of experimental studies on granular materials have shown that strain is localised in shear bands that are 6–20 mean particles wide (see e.g. [56] and references therein). Therefore it can be wondered

whether a similar relationship is present in metallic glasses. Here, the shear-band thickness (10–20 nm) is typically about 10 times the size of the medium-range ordered clusters (1–2 nm).

The localised deformation within shear bands (i.e. local release of stress) in metallic glasses is accompanied by emission of an acoustic signal. Acoustic emission (AE) measurements, therefore, provide an opportunity to acquire real-time information about shear-band formation and propagation (see e.g. Ref. [57]).

Finally, significant attention has been paid to how adiabatic heating contributes to the viscosity decrease in shear bands (e.g. [58,59,60,61,62]). In-situ thermographic investigations by means of (high-speed) infrared cameras during mechanical testing showed a temperature rise associated with shear banding. The spatial localisation and the short time intervals of heat generation, however, make quantification difficult and the estimated temperature rises in shear bands range from ~0.1 to a few thousand Kelvin (see e.g. references in [62]). By applying a fusible coating it has recently been shown that the heat content in shear bands corresponds to a maximum temperature rise of several thousand Kelvin [62]. Since the observed shear-band thicknesses are less than can be explained by thermal diffusion lengths, however, the authors concluded that the temperature rises are a consequence of shear-band localisation or frictional effects and not their origin. This observation is corroborated by adiabatic estimates of the time (Δt) elapsed during the unloading segment of a single stress drop: by balancing the heat generated through plastic deformation and the heat lost due to thermal conduction the thickness of an adiabatic shear band, δ_{SB}, can be estimated as [59]

$$\delta_{SB} = \sqrt{\frac{\lambda T_{SB}}{\beta \tau_{SB} \dot{\gamma}_{SB}}}, \tag{2.3}$$

where λ is the thermal conductivity, and T_{SB}, τ_{SB}, and $\dot{\gamma}_{SB}$ are the temperature, the shear stress and the shear strain rate, respectively, within the shear band. $\beta \approx 0.9$ is the fraction of plastic work converted to heat. With $\dot{\gamma}_{SB} = \Delta\gamma_{SB}/\Delta t$, where γ_{SB} is the shear strain in the shear band, Eq. 2.3 can be rewritten as

$$T_{SB}\Delta t = \frac{\delta_{SB}^2 \beta \tau_{SB} \Delta\gamma}{\lambda}. \tag{2.4}$$

Using characteristic values of $\delta_{SB} = 20$ nm [41], $\tau_{SB} = 1$ GPa, $\lambda = 15$ W/mK (at T_g [63]) for Zr-based BMGs, and estimated shear strains in the shear band of 100–1000, one obtains $T_{SB}\Delta t = 2.4\times10^{-6} - 2.4\times10^{-5}$ Ks, and consequently time periods in the range of nanoseconds (i.e. $\Delta t = 4 - 36$ ns) to reach temperatures close to T_g. This is substantially shorter than time periods of shear-band propagation measured in quasi-static compression tests that typically are on the order of milliseconds [58,59,64] (in agreement with our results). These results demonstrate that although fully adiabatic heating conditions might not be fulfilled, thermal conduction has a significant effect on temperature in shear bands and high temperatures (even above T_g) may result from very localised deformation, especially at the moment of fracture.

2.3.3 Approaches for improving plasticity at low homologous temperature

Shear localisation at low temperatures (e.g. room temperature) limits stable plastic flow, and the concentration of deformation in shear bands promotes early fracture initiation. Therefore, understanding and controlling shear localisation is crucial if BMGs are to be deployed as structural parts. Basically there exist two possibilities for improving the plasticity: either the development of monolithic metallic glasses with a less severe tendency towards shear localisation, or the fabrication of metallic-glass-matrix composites where a second phase promotes shear-band initiation/splitting.

Observation of conventional crystalline alloys has shown that good toughness/plasticity is associated with a low resistance to shear deformation (quantified by the shear modulus, μ) coupled with a high resistance to dilatation near crack tips (quantified by the bulk modulus, B). Similar considerations have led to the conclusion that intrinsically tough glasses should have low μ/B [65]. A low value of μ/B (typically < 0.40) facilitates the distribution of strain on multiple shear bands, giving these glasses the ability to support large(r) plastic strains. Using the relationships among the elastic constants, the correlation can also be expressed in terms of the Poisson's ratio, ν, as $\mu/B = 3(1-2\nu)/2(1+\nu)$ for isotropic systems, indicating that metallic glasses with higher ν (larger than ~0.32) show greater plasticity. And indeed, experimental measurements on various glasses (ranging from tough Pt- and Pd-based BMGs to very brittle oxide glasses) [65] and metallic glasses

in different annealing states [66] confirm this correlation. However, our preliminary investigations on $Au_{49}Ag_{5.5}Pd_{2.3}Cu_{26.9}Si_{16.3}$ ($\mu = 26.5$ GPa, $B = 132.3$ GPa) with a low ratio of $\mu/B = 0.20$ and a high Poisson's ratio of $\nu = 0.406$ [67] show a "macroscopically brittle" behaviour: Compression tests on cylindrical Au-based BMG samples with 2 mm in diameter show no or very limited plastic deformation before failure. Detailed investigations are currently underway to clarify the reasons for this behaviour [68].

Plasticity can, to a certain extent, also be changed by tailoring the amount of free volume: experimental investigations on various BMGs showed that an increased free-volume content (e.g. via high cooling rates [69], elastostatic and plastic pre-compression [70,71], high-pressure pre-treatment [72] or cold rolling [73]) has a positive influence on the (compressive or bending) plasticity. Sub-T_g annealing, on the other hand, leads to embrittlement in metallic glasses, and a virtually complete loss of toughness [74]. Similarly, an increased oxygen content can drastically reduce the toughness of many BMGs, as shown using the example of Zr-based glasses in Ref. [73]. Further, the (compressive) plasticity of metallic glasses can also be enhanced by inducing compressive residual stresses on sample surfaces via shot peening [75]. The formation of shear bands in the deformed surface layer during shot peening combined with the suppression of cracking by the compressive residual stress leads to a more uniform deformation on multiple shear bands and therefore greater plasticity. Analogously, it was shown that residual stresses introduced due to temperature gradients during casting can increase the toughness of metallic glasses [76]. Other approaches use geometrical effects to tailor the stress distribution or induce specific stress gradients [77], generating a less harsh tendency towards shear localisation. Prominent examples which illustrate these concepts are the use of compression samples with low aspect ratio (i.e. height/diameter < 1), where a single shear band cannot result in failure due to geometrical constraints, producing an enhanced apparent plasticity [78]; or reduction of the specimen size (e.g. thin ribbons), showing that the spacing of shear bands and offsets scales with sample thickness [7]. Further, it seems that there is a sample size effect in the plastic flow of metallic glasses. Experiments on small-volume specimens (e.g., the compression/tension of nanopillars [79,80] or nanolaminates [81]) showed that shear localisation can be avoided and that homogeneous deformation tends to become the dominant mode when the deforming sample volume decreases to approach that of a typical shear band. Numerous studies on micrometer-sized pillars also showed that, in contrast to macroscopic compression samples with identical

composition, no catastrophic failure occurs during inhomogeneous deformation and very great apparent plasticity can be achieved. (For further discussion of the effect of sample size on plasticity, see Chapter 6).

An additional influence on plasticity in BMGs also stems from composition. It has been shown that slight compositional changes or the minor addition of an additional alloying element can result in considerable changes in the deformation behaviour [82,83,84]. A promising approach to improving plasticity is the fabrication of BMGs with two glassy phases [85]. Often, however, a negative correlation between plasticity and yield strength exists: enhanced plasticity can only be achieved at the expense of lowered yield strength and vice versa. Nevertheless, it seems that the plasticity of monolithic BMGs can be improved by tailoring the microstructure through the appropriate choice of composition and thermal processing.

In metallic-glass-matrix composites (MGMCs) a second phase (i.e. chemical or structural inhomogeneity) is deliberately introduced into the amorphous matrix with the goal of promoting multiple shear-band initiation and hindering shear-band propagation by arrest, deflection and split-up. The second-phase particles in MGMCs are usually more ductile than the matrix, which is precisely the opposite of the situation in conventional metal-matrix composites, where the introduced particles generally act as strengthening phase. MGMCs are split into two categories: foreign-particle-reinforced composites and in-situ-formed composites. Foreign-particle-reinforced BMGs are reinforced with particles or fibres and can be produced either by powder consolidation techniques or by melt processing. Prominent examples here are the use of tungsten fibres, ductile crystalline particles (W, Ta, Nb and Cu) [86] or soft graphite particles [87]. In the latter case, a combination of enhanced plasticity and high yield strength was achieved. As shown in Fig. 2.8, preliminary investigations also showed that it is possible to produce fibre-reinforced BMG composites with rather low fibre content (< 5 vol.%) and homogeneous distribution via the injection technique [88]. Further work with alternative reinforcement materials, however, is necessary to specifically improve the mechanical properties of these composites. Positive effects on plasticity can also be expected by introducing (micrometer-sized) pores [89] and fabricating of foams [90,91]. Here, pores basically act as very soft second particles with a shear modulus of zero, and as stress concentrators which force the initiation of shear bands, without significantly degrading other mechanical properties. At the same time, the interaction of a shear band with pores reduces the stress concentration at

the tip of the shear band. However, in the case of a very high volume content of pores (i.e. foams) the yield strength is drastically reduced.

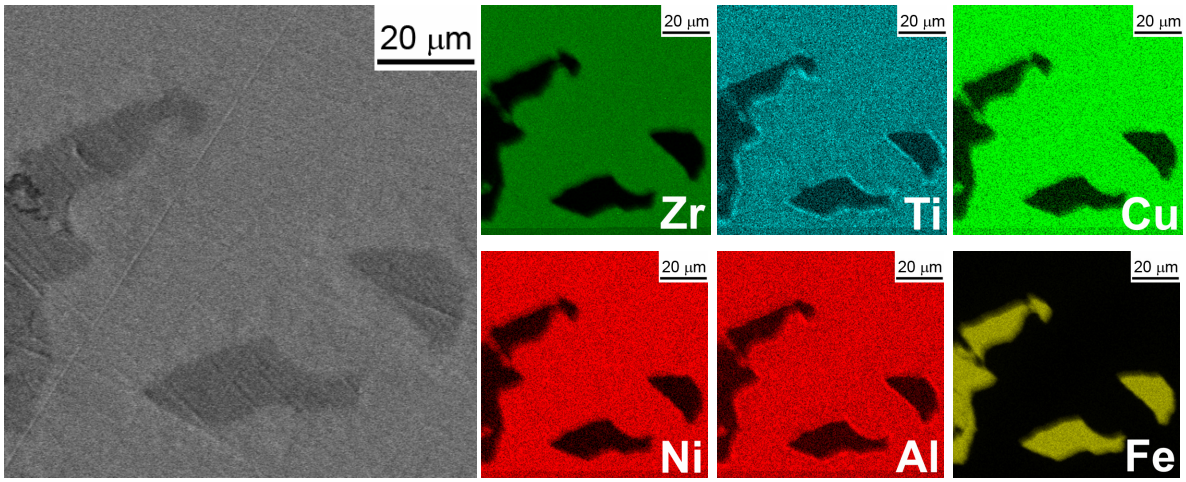

Fig. 2.8: Cross-sectional scanning electron microscopy (SEM) image (left) and energy dispersive x-ray (EDX) mapping (right) of a steel-fibre-reinforced Zr-based BMG. The EDX analysis reveals a thin Ti- and Al-enriched interface layer between fibre and matrix. The BMG composite was produced by infiltration of commercial steel wool with the metallic melt in an injection moulding system which allows rapid cooling of the composite to obtain an amorphous matrix.

In-situ formed BMG composites are produced by partial devitrification of the BMG upon heating [92] or by adding a substance to the matrix that reacts with one or more of the matrix components to form a crystalline phase in the amorphous matrix during processing. Obviously, in the latter case the composites can only be produced by melt processing, and their microstructure is strongly dependent on the cooling conditions. Generally these composites are manufactured by precipitating a ductile dendritic phase from the melt [93]. By matching the microstructural length scales (i.e. size, spacing and volume fraction) of the dendrites to the characteristic length scales of deformation (e.g. plastic zone size), both fracture toughness and tensile ductility ($\varepsilon_p \approx 12\%$) could be significantly improved in Zr- and Ti-based metallic glass composites [94,95].

Common for foreign-particle-reinforced and in-situ-formed BMG composites is the difficulty of controlling size and (homogeneous) distribution of the second particles in the amorphous matrix during processing. For the in-situ-formed composites this implies a very

controlled temperature profile during fabrication, whereas for the foreign-particle reinforced composites homogeneous mixing is the crucial step.

2.4 Deformation models

Establishing models for structure-property relationships is a central task of materials science. In metallic glasses, however, just how internal structure influences mechanical properties is unclear and a thorough picture of the deformation kinetics is not yet available. The lack of long-range order in amorphous alloys makes their plastic deformation fundamentally different from that of crystalline solids, where deformation can generally be described in terms of the underlying dislocation dynamics. While at low temperatures crystal dislocations allow changes in the atomic neighbourhood at low energy and stress, the atomic rearrangement in amorphous metals represents a relatively high-energy/stress process. Since the discovery of metallic glasses in the 1960s a number of theories to describe their deformation behaviour have been developed. This section briefly summarises the most prominent deformation models and, at the same time, provides a basis for the constitutive modelling of our results in Chapter 5.

At elevated temperatures (typically in the undercooled liquid region) where homogeneous and steady-state Newtonian flow prevails, the viscosity of a metallic glass can be described by the Vogel-Fulcher-Tammann (VFT) equation, $\eta = \eta_0 \exp[D^* T_0 / (T - T_0)]$, where T_0 is the VFT-temperature (at which $\eta \to \infty$), η_0 is a constant, and D^* is called the "strength" parameter of the liquid [96,97]. The change in viscosity of a liquid as a function of undercooling can be used to classify different liquids, because the temperature dependence varies significantly among the glass-forming liquids. A simple graphic visualisation of the differences is the so-called Angell plot, where $\log(\eta)$ vs. T_g/T is shown. Liquids that show strong variation above T_g in this plot are called "fragile", while those that do not are called "strong".

For the description of the homogeneous deformation at elevated temperatures Khonik [98] suggested a directional structural relaxation model that quantitatively explains the

homogeneous plastic flow of metallic glasses as a result of thermally activated structural relaxation oriented by external stress. The flow behaviour is then determined by the kinetics of irreversible structural relaxation during testing following a continuous activation energy spectrum, and homogeneous deformation basically takes place if the characteristic structural relaxation time is significantly smaller than the characteristic loading time (i.e., inverse strain rate). Other models using rate theory and rheological approaches that average the operation of many local atomic-scale events (e.g. free-volume and shear transformation model) discussed in the following were initially developed to describe the characteristics of homogeneous flow. Although they are mainly discussed in the context of inhomogeneous deformation, in their generalised form they can naturally also be used to describe homogeneous flow.

While the homogeneous flow of metallic glasses is understood and described relatively well, a fundamental description of inhomogeneous flow is so far lacking. Phenomenologically, shear-band formation in amorphous alloys is a strain localisation phenomenon and can be related to a local change of viscosity in narrow bands near planes of maximum shear stress. Many authors have discussed the possibility of adiabatic temperature rise during shear-band propagation. However, as discussed in Ref. [62], the local heating and the temperature rise, respectively, cannot be the origin of yielding and shear localisation, but are most likely the result of intense localised deformation. It seems therefore that shear-band initiation is triggered by a thermally-activated and stress-assisted process. Apart from the temperature increase during localised shearing, shear dilatation models, such as the shear transformation model [99] and the free-volume or diffusive-jump like model [1], have found wide acceptance in explaining the drop in viscosity. These models share the basic idea that the viscosity of a metallic glass at the atomic scale is governed by the presence of particular sites where, under an applied stress and thermal activation, the atoms can be rearranged to produce local shear. These shear events require local mechanical dilatation and consequently, due to the additional dilatational volume, trigger the formation of other local shear processes. It is assumed that the local dilatation is not purely elastic such that it would be eliminated immediately, but is (partially) retained in the post-activation state (as excess free volume) and might only be eliminated by diffusional processes on a longer time scale. The viscosity drop in the shear band is then the result of an increased number of such atomic rearrangement sites.

Early approaches tried alternatively to explain plasticity in metallic glasses in the framework of dislocation theory [100]. Shear is seen as the result of the glide of discrete microscopic dislocation lines with local variations in the magnitude and direction of the Burgers vector ("Somigliana dislocations"). Resistance to glide results from the work of dilatation normal to the glide plane. The description of the energy needed to cause dilatation and consequently allow motion of the dislocation over the energy barrier is derived by treating the dilatation as point defects. Despite the difference in describing the structure and motion of the flow defect, similar thermally-activated rate equations have been derived as in the shear transformation and free-volume model. One must be careful, however, in drawing analogies with dislocations in crystalline alloys. In particular, interactions between dislocations and microstructure do not determine the mechanical properties of amorphous alloys in the manner common to crystalline solids. An obvious example is that metallic glasses do not strain-harden, even at high shear-band densities. An increase in the free-volume content or entropy in BMGs generates a decrease of the hardness, whereas an increase of the defect density in crystalline alloys generally increases their hardness. This indicates that the description of plastic behaviour of metallic glasses based on discrete dislocations may not be appropriate.

The free-volume model, developed by Cohen and Turnbull [101] and adapted to metallic glass deformation by Spaepen [1], considers the "free volume" as a simple state or order variable to the deformation of metallic glasses. Here, free volume is defined as the atomic volume in excess of an ideally packed reference amorphous state[1]. Statistically, the higher the free volume of an atom, the higher the possibility of a diffusive jump-like motion. Macroscopic flow then occurs as a result of a number of discrete atomic jumps across an activation barrier, ΔG_0, as shown in Fig. 2.9. Note that this is modelled as an uncooperative process of individual atoms. If no external stress is present the activation energy is provided by thermal fluctuations. (Basically this situation is identical to the microscopic mechanism of diffusion). Under an applied force the atomic jumps are biased,

[1] It must be noted that although free volume has been shown to be very useful as an intrinsic state variable for describing plastic flow, it is not a tangible physical entity that can be determined quantitatively. One can measure molar volume and its changes and sense excess volume from positron lifetime in positron annihilation measurements, but to quantify the absolute value of free volume one would need an ideal reference state with predefined zero free volume (which in experiments cannot usually be achieved). Further, free volume does not contain information about (local) topological symmetry and chemical order. The enthalpy release during structural relaxation measured in calorimetric scans is often used as an indirect measure of the free volume in the metallic glass. The calorimetric enthalpy release, however, is much greater than the energy reduction expected from the annihilation of excess free volume.

which results in a net macroscopic deformation. The strain rate is then defined as the product of the fraction of such potential jump sites (*f*) times the number of jumps on each of those sites per time interval (ν_0) times the strain (ε_0) produced at each site $\dot{\varepsilon} = f\nu_0\varepsilon_0$. The structural parameter in the flow equation that governs the viscosity is the average free volume. The lowered viscosity in shear bands, however, indicates an increase in free volume. Therefore it is proposed that free volume can be created at high stresses by squeezing an atom into a neighbouring hole which possesses a volume smaller than the hard-sphere volume of the atom itself (Fig. 2.9). Similar to free-volume creation (disordering), free volume can also be annihilated (diffusional reordering) by a series of atomic jumps. Consequently, plastic flow is modelled based on the competition between stress-biased creation and diffusional annihilation of excess free volume via discrete atomic jumps. The macroscopic shear strain rate under an applied shear stress τ can then be written as [1]

$$\dot{\gamma} = 2f\nu_0 \exp\left(-\frac{\alpha v^*}{v_f} - \frac{\Delta G_0}{k_B T}\right)\sinh\left(\frac{\tau\Omega}{2k_B T}\right), \tag{2.5}$$

where *f* is the fraction of shearing volume, ν_0 is frequency of atomic vibration, α is a geometrical factor of order unity, v_f is the average free volume per atom, v^* is the effective hard-sphere size of the atoms, ΔG_0 is the activation energy, Ω is the atomic volume, k_B and T are the Boltzmann constant and absolute temperature, respectively. At high stresses, where backward atomic jumps are negligible, the hyperbolic function becomes exponential. In the case of homogeneous deformation ($f = 1$) and low stresses (i.e. $\sinh(\tau\Omega/2k_B T) \approx \tau\Omega/2k_B T$) Eq. 2.5 recovers the Newtonian viscous behaviour where viscosity depends solely on temperature and scales as $\eta = \tau/\dot{\gamma}$. On the other hand, strain localisation can be initiated by introducing small fluctuations in the initial free-volume distribution [102], and adopting free volume as an order parameter that can be changed by diffusion, annihilation and stress-driven creation [103,104].

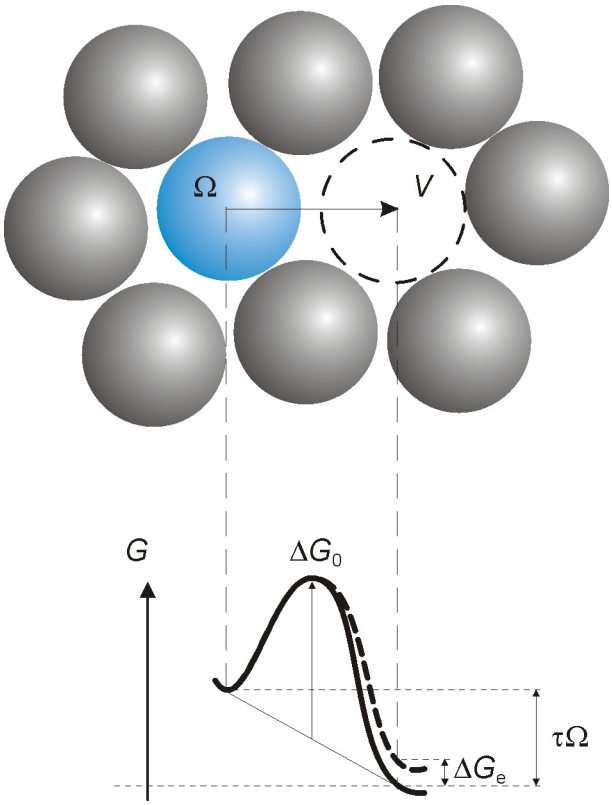

Fig. 2.9: Schematic illustration of a thermally-activated and stress-assisted atomic jump from one local free energy minima to another by passing an energy barrier ΔG_0. The applied shear force, τ, results in a biasing of the atomic jumps in the direction of the force, i.e. the free energy G is lowered by the work $\tau\Omega$, where Ω is the atomic volume (full line). If the atom is squeezed in a volume $V<\Omega$ the free energy after the jump is increased by the elastic distortion energy ΔG_e (dotted line). Adapted from [1].

The original work of Argon [99] extended the free-volume model by introducing the concept of local shear transformations to the deformation mechanism of metallic glasses. Here, plastic strain is produced by local shear transformations (i.e. cooperative movement of numerous atoms) nucleated under an applied stress and with the assistance of thermal fluctuations in regions around free-volume sites. The kinetics of those shear transformations are treated in the common framework of transition state theory [105]. The transition from homogeneous to inhomogeneous deformation (localisation as a consequence of local strain softening from free-volume accumulation or transformation dilatation) is modelled by introducing a perturbation in the local strain rate and the consequent growth of this perturbation with applied strain until a new stable redistribution

of shear flow is reached between a band (covering a volume fraction f) and the remaining matrix $(1-f)$. The work of Argon was later extended by introducing the concept of "shear transformation zones" (STZs) to the deformation mechanism of BMGs [106]. There, a STZ is described as a basic shear unit in amorphous metals which consists of a zone with slightly lowered density or increased free-volume content. Consequently, this zone corresponds to an atomic configuration that is more susceptible to plastic rearrangements than the surrounding matrix. It is worth noting that a STZ is not seen as a structural defect per se, which for example can be visualised in a transmission electron microscope as a dislocation, but is understood rather as a local event defined by its transience. These atomic scale STZs (several tens of atoms) deform collectively under an applied shear stress and thermal fluctuation to produce macroscopic shear deformation, as shown in Fig. 2.10. Topologically, such shear motions require a local increase in free volume (a dilatation) and produce an elastic strain field that autocatalytically initiates similar shear transformations in neighbouring volume elements and may result in the formation of a macroscopic shear band. Molecular dynamics (MD) simulations indicate that STZs typically consist of ~100 atoms, i.e. have a diameter in the range of 1–2 nm [107,108]. Interestingly, their size coincides approximately to the length scale up to which dense structures without appreciable translational symmetry can be formed within the scheme of cluster-cluster packing, i.e. medium-range order (MRO, cf. Section 1.4). Alternatively to free volume, the STZ density and deformation rate was described with an "effective disorder temperature" taken as a dynamic state variable [109]. The effective disorder temperature characterises the state of configurational disorder of the system and consequently also accounts for the local disorder due to plastic deformation. At the same time, this suggests a mechanism for strain localisation because a region with higher disorder is more susceptible to flow under an applied stress. Seemingly, the effective disorder temperature is related to the free volume (a more disordered glass can be obtained by moving the constituent atoms away from their equilibrium positions, e.g. by introducing excess free volume) but provides a more generalised state variable in plasticity theory.

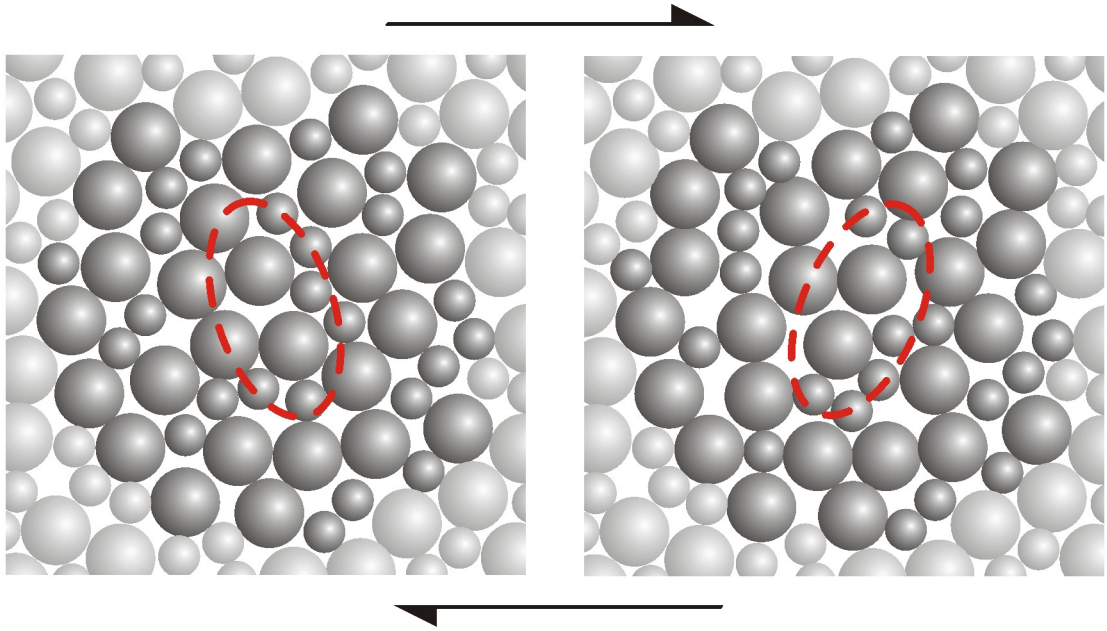

Fig. 2.10: Schematic illustration of a shear transformation zone (STZ) before and after operation under an applied shear force. The darker colour indicates which atoms are involved in the inelastic rearrangement from one low energy configuration to a second such configuration by passing an activated configuration of higher energy and volume. The red dashes visualise the strain at the core of the STZ.

Given that a STZ has a volume Ω_0 which sustains a shear strain γ_0, Argon calculated the free energy for the activation (i.e. Helmholtz activation free energy) of a shear transformation as [110]

$$\Delta G_0 = \left[\frac{7-5\nu}{30(1-\nu)} + \frac{2(1+\nu)}{9(1-\nu)}\beta^2 + \frac{\hat{\tau}}{2\gamma_0\mu(T)} \right] \mu(T)\gamma_0^2\Omega_0 , \tag{2.6}$$

where ν is the Poisson ratio, $\hat{\tau}$ is the ideal shear resistance of a STZ, $\mu(T)$ is the temperature-dependent shear modulus and γ_0 is the characteristic strain of a STZ on the order of ~0.1. The parameter β describes the ratio of volumetric dilatation to the shear strain, and is about equal to unity for metallic glasses. The first and second terms in Eq. 2.6 represent the increment of elastic shear strain energy and volumetric dilatational energy, respectively, and the third term accounts for the interatomic shear resistance. Ascribing each net forward STZ operation a characteristic strain γ_0, the (steady-state) shear rate yields

$$\dot{\gamma} = \alpha\nu_0\gamma_0 \exp\left(-\frac{\Delta G_0}{k_B T}\right) \sinh\left(-\frac{\tau\gamma_0\Omega_0}{k_B T}\right), \tag{2.7}$$

where α is a numerical factor that incorporates the fraction of deforming material. In the STZ framework the activation volume V is the product of the characteristic STZ volume Ω_0 and shear strain γ_0, $\gamma_0\Omega_0$. Typical values of Ω_0, obtained by computer simulations, are in the range of ~100 atoms [106,107,108]. At low stresses Eq. 2.7 reduces to a Newtonian flow form, at high stresses the bias for forward STZ operation becomes very large and the influence of back-transformations can be neglected, i.e.

$$\dot{\gamma} = \frac{\alpha}{2} \nu_0 \gamma_0 \exp\left(-\frac{\Delta G_0 - \tau \gamma_0 \Omega_0}{k_B T} \right). \tag{2.8}$$

The validity of the STZ theory has recently been demonstrated experimentally via the visualisation of structural rearrangements in colloidal glasses in real time under shear [111]. The observation showed that STZs are characterised as irreversible transformations with a spatial extent of a few particle diameters that can be induced by thermal fluctuations. Note however, that the activation volume of about 4 particle sizes determined in Ref. [111] is somewhat smaller than activation volumes derived for metallic glasses (~6–8 atoms, e.g. [104]). Typical strains of $\gamma_0 \sim 0.1$ are produced in the centre of a STZ and the resulting (long-range) elastic strain field facilitates the formation of new zones in its vicinity.

Johnson and Samwer merged the STZ theory with the concepts of the potential energy landscape[2] (PEL) and inherent states (e.g. [112]) and proposed a cooperative shearing model (CSM) as a simple scaling law to predict the temperature-dependent critical shear stress of BMGs [113]. The thermodynamic state variable controlling flow in this concept is identified as the isoconfigurational shear modulus μ (i.e. the curvature of the potential energy density function). As shown in Fig. 2.11, they observed that the critical shear strain (i.e. the ratio between yield stress to shear modulus, $\gamma_c = \tau_c/\mu$) of metallic glasses at room temperature is typically 2.67 %, and derived a universal law which shows that the shear strength scales with $(T/T_g)^{2/3}$, revealing a universal shear strain limit of $\gamma_{c0} = 0.036$ at $T = 0$ K. Following Frenkel's approach to calculate the theoretical shear strength of a

[2] The potential energy landscape of a glass assigns a potential energy to any possible atomic configuration. The energetic landscape comprises a population of inherent states ("basins") associated with local energy minima that are the stable configurational states of the glass. These are separated by saddle points that constitute the barriers for changes between different configurations. Transitions within these minima may be identified with anelastic reversible excitations (fast β-processes) while inter-basin transitions may be ascribed to irreversible STZs (slow α-processes).

dislocation-free crystal [114] the total potential energy barrier for an unstressed STZ in metallic glasses can be expressed as $\Delta G_0 = (8/\pi^2)\mu\gamma_c^2\zeta\Omega_0$, where $\zeta \sim 2$–4 is a correction factor and Ω_0 is the STZ volume [113]. According to the CSM this potential energy barrier is biased by an applied shear stress and approaches zero at yielding. Incorporating the temperature dependence of the yield stress the energy barrier at finite stress ($0 < \tau < \tau_c$) can be written as

$$\Delta G_\tau \approx \mu\gamma_c^2(1-\tau/\tau_c)^{3/2}\zeta\Omega_0, \tag{2.9}$$

where μ and τ_c are the shear modulus of the unstressed system and the threshold shear stress of the metallic glass at a given temperature. Consequently, the inelastic shear strain rate can be expressed as $\dot{\gamma} = \dot{\gamma}_0 \exp(-\Delta G_\tau / k_B T)$, with a characteristic strain rate $\dot{\gamma}_0$ that depends on an attempt frequency.

Following the CSM, energetic considerations and molecular dynamics simulation have quantitatively evaluated the activation energy barrier and size of STZs [107,108,115]. The results suggest that a STZ contains approximately tens to hundreds of atoms, i.e. a spatial size of 1-2 nm in diameter, and an activation energy of ~0.3 eV.

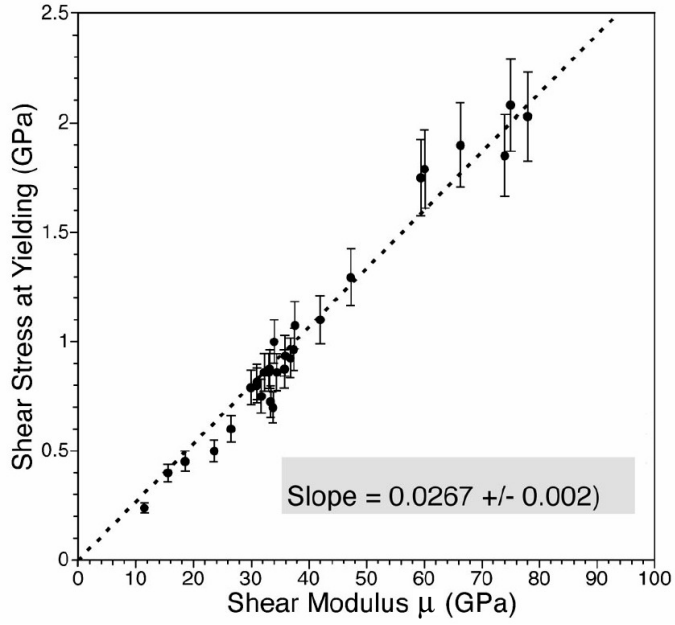

Fig. 2.11: Experimental shear stress at yielding as a function of shear modulus for various bulk metallic glasses at room temperature (taken from Ref. [113].

Finally, it is worth noting that at present it seems that in metallic glasses there is only one single mechanism of plastic flow irrespective of the experimental conditions. This mechanism (whether one sees it as shear transformation or as diffusive-jump-like mechanism) may occur homogeneously throughout the entire volume or may occur localised as during shear banding. The different macroscopic responses only arise because of different spatial distributions, frequencies, sizes, and temporal evolutions of the "basic" flow events. This contrasts with (poly-)crystalline solids, where various distinct mechanisms of deformation (e.g. dislocation glide/climb, diffusional creep, or grain-boundary sliding) are present. In this case, deformation is viewed as a competition of these mechanisms, and whichever mechanism is dominant depends on microstructure, temperature and stress state.

2.5 References

[1] F. Spaepen, Acta Metall. 25 (1977) 407.
[2] C.A. Schuh, A. C. Lund, T.G. Nieh, Acta Mater. 52 (2004), 5879.
[3] J. Lu, G. Ravichandran, W.L. Johnson, Acta Mater. 51 (2003) 3429.
[4] T.G. Nieh, J. Wadsworth, C.T. Liu, T. Ohkubo, Y. Hirotsu, Acta mater. 49 (2001) 2887.
[5] Y. Kawamura, T. Shibata, A. Inoue, Appl. Phys. Lett. 71 (1997) 779.
[6] Y. Kawamura, T. Shibata, A. Inoue, T. Masumoto, Scr. Mater. 37 (1997) 431.
[7] R.D. Conner, W.L .Johnson, N.E. Paton, W.D. Nix, J. Appl. Phys. 94 (2003) 904.
[8] H. Kimura, T. Masumoto, Acta Metall. 31 (1983) 231.
[9] B. Moser, J. Kuebler, H. Meinhard, W. Muster, J. Michler, Adv. Eng. Mater. 7 (2005) 388.
[10] B. Moser, J.F. Löffler, J. Michler, Philos. Mag. 86 (2006) 5715.
[11] T. Masumoto, R. Maddin, Acta Metall. 19 (1971) 725.
[12] Y. Kawamura, T. Shibata, A. Inoue, T. Masumoto, Appl. Phys. Lett. 69 (1996) 1208.
[13] T.C. Hufnagel, T. Jiao, Y. Li, L.Q. Xing, K.T. Ramesh, J. Mater. Res. 17 (2002) 1441.
[14] T. Mukai, T.G. Nieh, Y. Kawamura, A. Inoue, K. Higashi, Intermetallics 10 (2002) 1071.
[15] T. Mukai, T.G. Nieh, Y. Kawamura, A. Inoue, K. Higashi, Scr. Mater. 46 (2002) 43.
[16] H. Li, G. Subhash, X.L. Gao, L.J. Keckes, R.J. Dowding, Scr. Mater. 49 (2003) 1087.

[17] A.V. Sergueeva, N.A. Mara, J.D. Kuntz, D.J. Branagan, A.K. Mukherjee, Mater. Sci. Eng. A 383 (2004) 219.
[18] H.A. Bruck, A.J. Rosakis, W.L. Johnson, J. Mater. Res. 11 (1996) 503.
[19] G. Subhash, R.J. Dowding, L.J. Kecskes, Mater. Sci. Eng. A 334 (2002) 33.
[20] Z.F. Zhang, J. Eckert, L. Schultz, Acta Mater. 51 (2003) 1167.
[21] L.F. Liu, L.H. Dai, Y.L. Bai, B.C Wei, G.S. Yu, Intermetallics 13 (2005) 827.
[22] J. Zhang, J.M. Park, D.H. Kim, H.S. Kim, Mater. Sci. Eng. A 449 (2007) 290.
[23] A.V. Sergueeva, N.A. Mara, D.J. Branagan, A.K. Mukherjee, Scr. Mater. 50 (2004) 1303.
[24] W.H. Jiang, G.J. Fan, F.X. Liu, G.Y. Wang, H. Choo, P.K. Liaw, J. Mater. Res. 21 (2006) 2164.
[25] W.H. Jiang, F. Liu, D.C. Qiao, H. Choo, P.K. Liaw, J. Mater. Res. 21 (2006) 1570.
[26] W.H. Jiang, F. Jiang, F.X. Liu, H. Choo, P.K. Liaw, K.Q. Qiu, Appl. Phys. Lett. 89 (2006) 261909.
[27] W.H. Jiang, G.J. Fan, F.X. Liu, G.Y. Wang, H. Choo, P.K. Liaw, Int. J. Plast. 24 (2008) 1.
[28] T.G. Nieh, C.A. Schuh, J. Wadsworth, Y. Li, Intermetallics 10 (2002) 1177.
[29] C.A. Schuh, T.G. Nieh, Acta Mater 51 (2003) 87.
[30] W.H. Jiang, M. Atzmon. J. Mater. Res. 18 (2003) 755.
[31] L.F. Liu, L.H. Dai, Y.L. Bai, B.C. Wei, J. Eckert, J. Mater. Res. 21 (2006) 153.
[32] Y.F. Gao, B. Yang, T.G. Nieh, Acta Mater. 55 (2007) 2319.
[33] H. Kimura, T. Masumoto, Acta Metall. 31 (1983) 231.
[34] H.Q. Li, C. Fan, K.X. Tao, H. Choo, P.K. Liaw, Adv. Mater. 18 (2006) 752.
[35] A. Kawashima, T. Okuno, H. Kurishita, W. Zhang, H. Kimura, A. Inoue, Mater. Trans. 48 (2007) 2787.
[36] K.M. Flores, R.H. Dauskardt, J. Mech. Phys. Solids 54 (2006) 2418.
[37] Z.F. Zhang, G. He, J. Eckert, L. Schultz, Phys. Rev. Lett. 91 (2003) 045505.
[38] C.A. Schuh, A.C. Lund, Nat. Mater. 2 (2003) 449.
[39] C.A. Pampillo, A.C. Reimschuessel, J. Mater. Sci. 9 (1974) 718.
[40] G.I. Taylor, Proc. Roy. Soc. (Lond.) A 201 (1950) 192.
[41] Y. Zhang, A.L. Greer, Appl. Phys. Lett. 89 (2006) 071907.
[42] W.H. Jiang, F.X. Liu, P.K. Liaw, H. Choo, Appl. Phys. Lett. 90 (2007) 181903.
[43] C.A. Pampillo, Scr. Mater. 6 (1972) 915.
[44] P. Asoka-Kumar, J. Hartley, R. Howell, P.A. Sterne, T.G. Nieh, Appl. Phys. Lett. 77 (2000) 1973.
[45] K.M Flores, D. Suh, R.H. Dauskardt, P. Asoka-Kumar, P.A. Sterne, R.H. Howell, J. Mater. Res. 17 (2002) 1153.
[46] K.M. Flores, B.P. Kanungo, S.C. Glade, P. Asoka-Kumar, J. Non-Cryst. Solids 353 (2007) 1201.
[47] A.R. Yavari, A. Le Moulec, A. Inoue, N. Nishiyama, N. Lupu, E. Matsubara, W.J. Botta, G. Vaughan, M. Di Michiel, A. Kvick, Acta Mater. 53 (2005) 1611.
[48] R.T. Ott, M.J. Kramer, M.F. Besser, D.J. Sordelet, Acta Mater. 54 (2006) 2463.
[49] J. Li, Z.L. Wang, T.C. Hufnagel, Phys. Rev. B 65 (2002) 144201.
[50] W.J. Wright, T.C. Hufnagel, W.D. Nix, J. Appl. Phys. 93 (2003) 1432.
[51] H. Chen, Y. He, G.J. Shiflet, S.J. Poon, Nature 367 (1994) 541.
[52] J.J. Kim, Y. Choi, S. Suresh, A.S. Argon, Science 295 (2002) 654.
[53] M.W. Chen A. Inoue, W. Zhang, T. Sakurai, Phys. Rev. Lett. 96 (2006) 245502.
[54] M. Oda, H. Kazama, Géotechnique 48 (1998) 465.

[55] F. Spaepen, Nat. Mater. 5 (2006) 7.
[56] C.M. Gourlay, A.K. Dahle, Nature 445 (2007) 70.
[57] A.Y. Vinogradov, V.A. Khonik, Philos. Mag. 84 (2004) 2147.
[58] W.J. Wright, R.B. Schwarz, W.D. Nix, Mater. Sci. Eng. A 319 (2001) 229.
[59] T.C. Hufnagel, T. Jiao, Y. Li, L.Q. Xing, K.T. Ramesh, J. Mater. Res. 17 (2002) 1441.
[60] K.M. Flores, R.H. Dauskardt, J. Mech. Phys. Sol. 54 (2006) 2418.
[61] B. Yang, C.T. Liu, T. G. Nieh, M.L. Morrison, P.K. Liaw, R.A. Buchanan, J. Mater. Res. 21 (2006) 915.
[62] J.J. Lewandowski, A.L. Greer, Nat. Mater. 5 (2006) 15.
[63] M. Yamasaki, S. Kagao, Y. Kawamura, Scr. Mater. 53 (2005) 63.
[64] S.X. Song. T.G. Nieh, Intermetallics 17 (2009) 762.
[65] J.J. Lewandowski, W.H. Wang, A.L. Greer, Philos. Mag. Lett. 85 (2005) 77.
[66] A. Castellero, D.I. Uhlenhaut, B. Moser, J.F. Löffler, Philos. Mag. Lett. 87 (2007) 383.
[67] J. Schroers, B. Lohwongwatana, W.L. Johnson, A. Peker, Appl. Phys. Lett. 87 (2005) 061912.
[68] D. Klaumünzer, PhD thesis, ETH Zürich (work in progress).
[69] Y.J. Huang, J. Shen, J.F. Sun, Appl. Phys. Lett. 90 (2007) 081919.
[70] S.C. Lee. C.M. Lee, J.W. Yang, J.C. Lee, Scr. Mater. 58 (2008) 591.
[71] L. He, M.B. Zhong, Z.H. Han, Q. Zhao, F. Jiang, J. Sun, Mater. Sci. Eng. A 496 (2008) 285.
[72] P. Yu, H.Y. Bai, J.G. Zhao, C.Q. Jin, W.H. Wang, Appl. Phys. Lett. 90 (2007) 051906.
[73] Y. Yokoyama, J. Non-Cryst. Solids 316 (2003) 104.
[74] P. Murali, U. Ramamurty, Acta Mater. 53 (2005) 1467.
[75] Y. Zhang, W.H. Wang, A.L. Greer, Nat. Mater. 5 (2006) 857.
[76] C.J. Gilbert, V. Schroeder, R.O. Ritchie, Metall. Mater. Trans. A 30 (1999) 1739.
[77] W.F. Wu, C.Y. Zhang, Y.W. Zhang, K.Y. Zeng, Y. Li, Intermetallics 16 (2008) 1190.
[78] Z. F. Zhang, H. Zhang, X.F. Pan, J. Das, J. Eckert, Philos. Mag. Lett. 85 (2005) 513.
[79] Z.W. Shan, J. Li, Y.Q. Cheng, A.M. Minor, S.A. Syed Asif, O.L. Warren, E. Ma, Phys. Rev. B 77 (2008) 155419.
[80] H. Guo, P.F. Yan, Y.B. Wang, J. Tan, Z.F. Zhang, M.L. Sui, E. Ma, Nat. Mater. 6 (2007) 735
[81] Y.M. Wang, J. Li, A.V. Hamza, T.W. Barbee, Proc. Natl. Acad. Sci. USA 104 (2007) 11155.
[82] X.J. Gu, A.G. McDermott, S.J. Poon, G.J. Shiflet, Appl. Phys. Lett. 88 (2006) 211905.
[83] Y.Q. Cheng, A.J. Cao, H.W. Sheng, E. Ma, Acta Mater. 56 (2008) 5263.
[84] S. Nowak, P. Ochin, A. Pasko, O. Maciejak, P. Aubert, Y. Champion, J. Alloys Compd. 483 (2009) 139.
[85] X.H. Du, J.C. Huang, K.C. Hsieh, Y.H. Lai, H.M. Chen, J.S.C. Jang, P.K. Liaw, Appl. Phys. Lett. 91 (2007) 131901.
[86] R.D. Conner, R.B. Dandliker, W.L. Johnson, Acta Mater. 46 (1998) 6089.
[87] M.E. Siegrist, J.F. Löffler, Scr. Mater. 56 (2007) 1079.
[88] Y. Santschi, Diploma thesis, ETH Zürich (2007).
[89] T. Wada, A. Inoue, A.L. Greer, Appl. Phys. Lett. 86 (2005) 251907.

[90] J. Schroers, C. Veazey, M.D. Demetriou, W.L. Johnson, J. Appl. Phys. 96 (2004) 7723.
[91] A.H. Brothers, D.C. Dunand, Adv. Mater. 17 (2005) 484.
[92] J.F. Löffler, S. Bossuyt, S.C. Glade, W.L. Johnson, W. Wagner, P. Thiyagarajan, Appl. Phys. Lett. 77 (2000) 525.
[93] C.C. Hays, C.P. Kim, W.L. Johnson, Phys. Rev. Lett. 84 (2000) 2901.
[94] D.C. Hofmann, J.Y. Suh, A. Wiest, G. Duan, M.L. Lind, M.D. Demetriou, W.L. Johnson, Nature 451 (2008) 1085.
[95] D.C: Hofmann, J.Y. Suh, A. Wiest, M.L. Lind, M.D. Demetriou, W.L. Johnson, Proc. Natl. Acad. Sci. USA 105 (2008) 20136.
[96] C.A. Angell, Science 267 (1995) 1924.
[97] P.G. Debenedetti, F.H. Stillinger, Nature 410 (2001) 259.
[98] V.A. Khonik, Phys. Stat. Sol. A 117 (2000) 173.
[99] A.S Argon, Acta Metall. 27 (1979) 47.
[100] J.J. Gilman, J. Appl. Phys. 46 (1975) 1625.
[101] M.H. Cohen, D. Turnbull, J. Chem. Phys. 31 (1959) 1164.
[102] P.S. Steif, F. Spaepen, J. W. Hutchinson, Acta Metall. 30 (1982) 447.
[103] R. Huang, Z. Suo, J.H. Prevost, W.D. Nix, J. Mech. Phys. Solids 50 (2002) 1011.
[104] M. Heggen, F. Spaepen, M. Feuerbacher, J. Appl. Phys. 97 (2005) 033506.
[105] H. Eyring, J. Chem. Phys. 4 (1936) 283.
[106] M.L. Falk, J.S. Langer, Phys. Rev. E 57 (1998) 7192.
[107] S.G. Mayr, Phys. Rev. Lett. 97 (2006) 195501.
[108] M. Zink, K. Samwer, W.L. Johnson, S.G. Mayr, Phys. Rev. B 73 (2006) 172203.
[109] J.S. Langer, Phys. Rev. E 70 (2004) 041502.
[110] A.S. Argon, L.T. Shi, Acta Metall. 31 (1983) 499.
[111] P. Schall, D.A. Weitz, F. Spaepen, Science 318 (2007) 1895.
[112] F.H. Stillinger, Science 267 (1995) 1935.
[113] W.L. Johnson, K. Samwer, Phys. Rev. Lett. 95 (2005) 195501.
[114] J. Frenkel, Z. Phys. 37 (1926) 572.
[115] F. Delogu, Intermetallics 16 (2008) 658.

3 Aim of the thesis

The goal of this thesis project was to deepen the understanding of the inhomogeneous deformation characteristics of bulk metallic glasses by deploying compression tests over a wide range of temperatures and strain rates. Based on the experimental observations, basic parameters of plastic deformation such as activation volume and energy, were deduced, and a general constitutive framework describing the deformation kinetics was developed. Finally, the issues of possible size effects and the influence of varying free-volume content on the deformation behaviour were addressed by means of micropillar compression tests and instrumented indentation.

3.1 Specific objectives

3.1.1 Influence of temperature and strain rate on inhomogeneous flow

Due to the lack of significant plasticity in many bulk metallic glasses at low temperatures systematic investigations of their inhomogeneous deformation characteristics are scarce. Only the recent development of novel BMGs with increased (compressive) plasticity has offered the possibility to carry out such detailed experimental investigations.

Using the example of “ductile” Zr-based BMGs, we wanted to study in detail the role of thermomechanical loading on uniaxial compression deformation behaviour. The main objective was to experimentally obtain the stress-strain relationship over a broad range of temperatures and strain rates. For this purpose uniaxial compression tests at constant strain rates and changing strain rates were performed. The strain rate change tests (i.e. transient tests) allow an evaluation of the strain rate sensitivity and provide activation parameters (such as activation volumes and energies) so far not accessible for inhomogeneous flow. The aim was also, by means of e.g. high-resolution scanning electron microscopy (SEM) observations on shear surfaces, to elaborate a fundamental understanding of structural change during deformation and its influence on shear band formation/propagation.

3.1.2 Constitutive modelling of deformation behaviour

In addition to the phenomenological description of the relationship between microstructure and mechanical properties, the investigations also aimed to develop a constitutive physical model of the deformation of BMGs. Besides being of scientific interest, understanding how atomic-scale mechanisms of deformation lead to shear localisation may also pave the way for the design of new alloys with less tendency towards shear localisation and therefore with enhanced plasticity.

Based on our experimental findings, and adapting certain concepts used to describe the inhomogeneous deformation behaviour of crystalline solids showing dynamic strain aging, a constitutive framework was developed. The implications of the model were discussed and cross-checked via measurements of the temperature- and strain-rate-dependent shear band densitiy and comparison with recent findings in literature.

3.1.3 Deformation size effects and influence of free volume on plasticity

In macroscopic samples it is commonly observed that during inhomogeneous BMG deformation different length scales exist or develop, such as shear offsets on the sample surface (typically hundreds of nanometers to micrometers), shear band spacing (on the order of micrometers) and shear band thickness (~10–20 nm). Consequently, the question emerged of possible size effects in the deformation behaviour of metallic glasses when sample dimensions are decreased down to these length scales. It is also known that the structural state of a metallic glass can significantly influence its mechanical properties. A prominent example here is the embrittlement (i.e., loss of toughness) of metallic glasses with time/annealing. Less, however, is known about the influence of the material conditions (e.g. variation of free volume content) on the atomic-scale mechanisms of deformation.

We chose to address these questions by performing in-situ SEM compression tests on micropillars of different sizes, geometries and free volume contents. Complementary instrumented indentation tests on the material in its different conditions might reveal further information, such as pressure sensitivity, and thus shed further light on the underlying processes governing plastic deformation in metallic glasses.

4 Temperature and strain-rate effects on the inhomogeneous flow behaviour

This chapter summarises the experimental investigations of this study, with a focus on the mechanical characterisation via temperature and strain-rate-change tests performed on various Zr-based bulk metallic glasses. The investigations show that serrated flow disappears below a critical temperature and above a critical strain rate, in accordance with a change in the strain-rate sensitivity from negative to positive values. Possible micromechanical reasons for this behaviour are discussed.

The results presented provide a basis for the constitutive modelling of the deformation behaviour in Chapter 5. Some of the findings presented in this chapter have, in slightly modified versions, been published separately in various journals[1].

[1] 1) F.H. Dalla Torre, A. Dubach, M.E. Siegrist, J.F. Löffler, *Applied Physics Letters* **89** (2006) 091918.
2) A. Dubach, F. H. Dalla Torre, J.F. Löffler, *Philosophical Magazine Letters* **87** (2007) 695.
3) F.H. Dalla Torre, A. Dubach, A. Nelson, J.F. Löffler, *Materials Transactions* **48** (2007) 1774.
4) F.H. Dalla Torre, A. Dubach, J. Schällibaum, J.F. Löffler, *Acta Materialia* **56** (2008) 4635.
5) A. Dubach, F.H. Dalla Torre, J.F. Löffler, *Acta Materialia* **57** (2009) 881.

4.1 Introduction

Ever since their development the mechanical properties of metallic glasses have attracted great scientific interest. Their frequent lack of plasticity at temperatures substantially below T_g, however, has prevented systematic experimental investigations into their inhomogeneous flow behaviour and the precise effects of temperature and strain rate. Consequently, mechanical examinations have concentrated mainly on homogeneous deformation at elevated temperatures (i.e., the supercooled liquid regime) or constraint geometries, such as during instrumented indentation tests. Only with the discovery of monolithic BMGs, which reveal a certain (compressive) plasticity or malleability, have detailed investigations of the deformation kinetics become possible. At present there is a general consensus that the basic unit process underlying deformation must be a local rearrangement of atoms that can accommodate shear strain. Following the seminal work of Argon [1], these local rearrangements are generally referred to as "shear transformations" or "shear transformation zones" (STZs) [2]. Important insights into the deformation behaviour of metallic glasses have also been gleaned from recent computer simulations, where parameters such as activation energy and volume of a STZ or strain-rate sensitivity (SRS) have been derived [3,4,5,6,7]. Generally, the SRS characterises the kinetically-driven response of the stress (σ) for a material at a given strain (ε) upon a change in the applied strain rate $\dot{\varepsilon}$. It can be quantified by the strain-rate sensitivity parameter, *m*, by

$$m = \left(\frac{\partial \ln \sigma}{\partial \ln \dot{\varepsilon}} \right)_{\varepsilon} . \tag{4.1}$$

Materials exhibiting values of *m* close to zero are not rate-sensitive (this is e.g. typical for athermal deformation mechanisms such as twinning in crystalline materials), while a value of unity corresponds to perfect Newtonian flow where the stress is directly proportional to the strain rate (i.e. purely thermally activated).

Despite these recent developments a detailed microscopic, kinetic and thermodynamic interpretation of the shear process is still lacking, and none of the existing constitutive equations for inhomogeneous plastic flow addresses the serrated flow as a kinetic phenomenon sufficiently well.

So far only a few literature reports have paid attention to the surface morphology of shear planes in bulk amorphous metals [8,9]. This is mainly because of the generally small amount of plastic strain occurring before failure, which would otherwise result in large enough shear offsets and thus allow more detailed microscopic examination. The observation of the surface morphology of shear planes, however, provides information important for the description of possible deformation mechanisms in metallic glasses. Fracture surfaces of metallic glasses, on the other hand, are well known and described by their typical river, vein or other flow patterns [10,11]. These flow features suggest that temperatures well above the glass transition temperature are reached at the moment of fracture. Since their first observation, several thermographic experiments have supported the idea of these high-temperature bursts at fracture [12,13,14,15]. Some ambiguity with respect to adiabatic heating and the amount of temperature rise associated with shearing before fracture, however, remains, and has stimulated recent debate as to whether the temperature might be high enough to instigate a localised drop in viscosity and thus promote easy glide along this softened shear zone [16,17,18,19].

4.2 Material & methods

4.2.1 Material

The bulk metallic glass commonly referred to as Vit105 ($Zr_{52.5}Ti_5Cu_{17.9}Ni_{14.6}Al_{10}$, composition given in atomic percent[2]) serves as "model material" for the investigations in this project. The reason for studying this material is because extensive research has been performed on Vit105 and many of its physical, thermodynamical and mechanical properties are readily available in literature (cf. Table 4.1). Further, it does not contain any toxic or hazardous elements, such as beryllium, and it is reasonably straightforward in its production, which is not the case for other alloys (e.g. Pd-based BMGs, which require fluxing).

[2] All the chemical compositions mentioned in this work are indicated in atomic percent.

Table 4.1: Selected properties of Vit105 from literature [20,21,22].

Critical cooling rate (Ks^{-1})	~10
T_g (K) at heating rate 40 K/min	675
Supercooled liquid region (K)	52
Reduced glass transition temperature (T_g/T_m)	0.63
Density (g/cm^3)	6.73
Young's modulus (GPa)	88.6
Shear modulus (GPa)	32.3
Bulk modulus (GPa)	114.1
Poisson's ratio	0.37
Vicker's hardness (HV0.2)	579

Complementary tests were also performed on $Cu_{50}Zr_{50}$ and $Zr_{57.9}Cu_{22}Fe_8Al_{12}Pd_{0.1}$ BMGs. Prealloys of the compositions mentioned were prepared by arc melting the pure elements in a Zr-gettered high-purity argon atmosphere (99.9999 % purity) in an 18-litre Bühler arc melter equipped with an LSG400 power supply (Edmund Bühler GmbH, Tübingen, Germany). To guarantee homogeneity the prealloys were re-melted several times. The purity of the elements used ranged from 99.9 % to 99.999 % (see Table 4.2). They were cleaned with ethanol in an ultrasonic cleaning unit before use.

Table 4.2: Purity, form and supplier of elements used.

Element	Purity	Form	Supplier
Zr	99.9 %	crystal bar	MMA
Ti	99.995 %	pellets	Cerac
Cu	99.998 %	VP rod*	Praxair MRC
Ni	99.99 %	VP rod*	Praxair MRC
Al	99.999 %	pellets	Cerac
Fe	99.97 %	pieces	Alfa Aesar
Pd	99.95 %	bar	UBS

* vacuum-processed, low oxygen content (< 10 ppm)

From the prealloys smaller cylindrical rods were suction-cast in a Bühler MAM-1 system (200 mbar argon atmosphere) into a copper mould with a length of ~30 mm and a diameter of 3 mm (and 2 mm for the $Cu_{50}Zr_{50}$ samples), as shown in Fig. 4.1. Compression test specimens with a length-to-diameter ratio of 5/3 = 1.7 were cut from these rods and subsequently polished to ensure parallelism with the loading plates during compression testing.

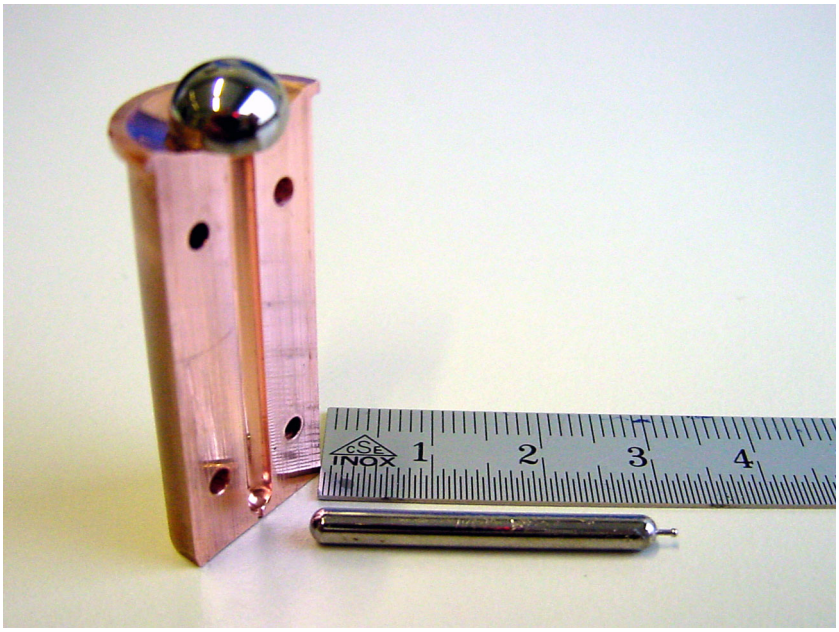

Fig. 4.1: Suction-cast Vit105 rod and corresponding copper mould.

4.2.2 Experimental characterisation

By default, the amorphous structure of the specimens was confirmed by X-ray diffraction (XRD) using a PANalytical X'pert diffractometer using Cu–K_α radiation, and by differential scanning calorimetry (DSC) using a Seteram Labsys DSC (at a heating rate of 20°C/min). Complementarily, the microstructure of selected, polished cross-sections was qualitatively analysed by optical microscopy to check the presence of large impurities and crystallites. Both shear-band appearance and shear surfaces of deformed specimens (fractured and unfractured) were investigated by means of scanning electron microscopy (SEM) using a LEO 1530 equipped with a field-emission gun.

The microstructure of some samples was investigated by transmission electron microscopy (TEM). The experiments were performed with a Philips CM20 microscope operating at 200 kV. TEM samples were prepared by mechanical dimpling for ~30 min followed by ion milling with a 3 keV argon beam.

Oxygen content was analysed by hot-extraction using a LECO TC-436 with high-purity Ni as the bath metal. The equipment was calibrated for oxygen using a zirconium standard (LECO 1280 ppm oxygen, where ppm values refer to mass parts).

The elastic modulus was measured at 10 Hz by dynamic mechanical analysis (DMA) with a Mettler DMA Messmodul apparatus in a temperature range from 130 to 360 K at a heating rate of 1 K/min. Constant cross-head displacement tests and strain-rate-change tests in compression were performed on a screw-driven four-column Schenck Trebel machine (equipped with a 100 kN load cell) over a temperature range of 77 to 673 K, where strain and strain rate were measured from the crosshead displacement and speed, respectively. In order to ensure confidence in the measured crosshead displacement, a clip gauge was additionally mounted on the pistons directly above and below the specimens. Various crosshead velocities ranging from 0.01 to 60 mm/min were applied, resulting in initial strain rates of 3.3×10^{-5} to 0.2 s^{-1}. The samples were cooled to the desired temperature of between 77 K (liquid nitrogen) and room temperature (RT) by immersing them in various cooling mixtures with ethanol and liquid nitrogen or dry ice (CO_2) during testing. Some recent tests were also performed in an EC2043 climate chamber with a CU2007 control unit by Severn Thermal Solutions Ltd, Bristol, UK. Temperature was measured using a thermocouple mounted on the disc piston next to the specimen, and held constant at ± 2 K during testing. The cyclic strain-rate-change tests were performed by alternating the crosshead speed between two distinct values (generating corresponding strain rates $\dot{\varepsilon}_1$ and $\dot{\varepsilon}_2$, respectively). A ratio of $\dot{\varepsilon}_2 / \dot{\varepsilon}_1 = 10$ and $\dot{\varepsilon}_2 / \dot{\varepsilon}_1 = 2$ was chosen for temperatures below 600 K and above 600 K, respectively. To clearly differentiate the stress drops from the background noise of the load cell (with a resolution of ~2–3 MPa) a value of 5 MPa was chosen as the lower limit of the serration amplitude. Acquisition rates from 20 to 300 Hz were used to provide information on the duration of the shear events.

Finally, shear-band appearances and densities on the surfaces of samples deformed to a plastic strain of ~1 % at different temperatures and strain rates were characterised by optical

microscopy. The shear offsets were quantified using a non-contact scanning laser profilometer (UBM telefocus measurement system).

4.3 Results

4.3.1 Microstructural and thermophysical properties of Vit105

Figure 4.1 shows an example of an as-cast Vit105 rod with a diameter of 3 mm. Generally, the as-cast samples exhibit very good and shiny surface quality, and the optical microscopy investigations on polished cross-sections reveal no impurities or crystallites, suggesting a macroscopically homogeneous, amorphous sample structure, as also confirmed by TEM observations (Fig. 4.2a). Partially crystalline specimens, such as those shown on the example of failed cast plates in Fig. 4.2b, are not generally observed under proper standard casting conditions.

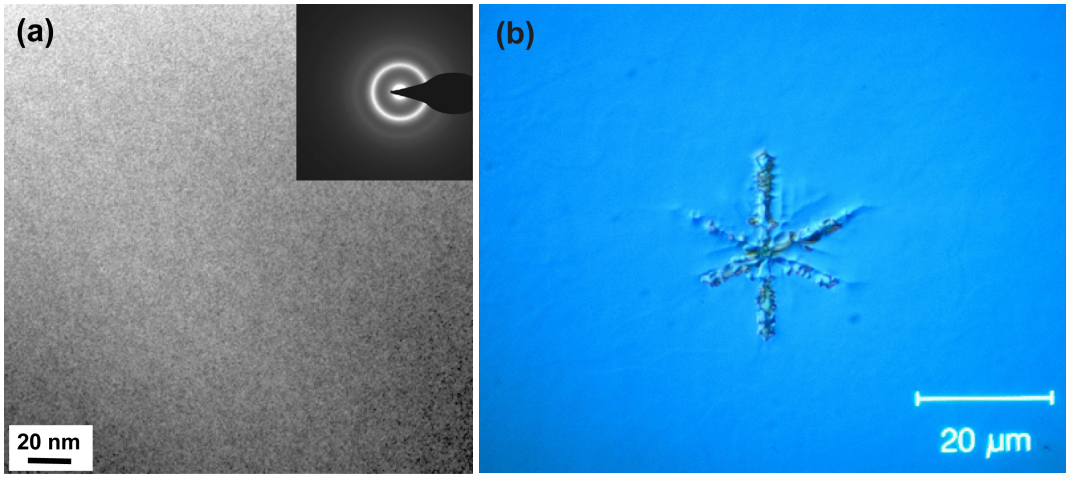

Fig. 4.2: (a) Bright field TEM image with selected area diffraction pattern of an as-cast Vit105 sample; and (b) optical microscopy image (using a polariser) of a polished cross-sections of a failed cast Vit105 plate, revealing the presence of crystallites, i.e. dendrites, of ~20 µm in diameter. The cross-section was etched in a solution of 45 % H_2O, 45 % HNO_3 (65 %), 10 % HF (40 %) for 30 s.

Further analysis by means of XRD and DSC confirmed the amorphous structure of the suction-cast cylindrical Vit105 specimens and correspondingly the reproducibility of the process. As shown in Fig. 4.3a, a typical XRD scan of an as-cast Vit105 specimen reveals no distinct (crystalline) peaks but only characteristic amorphous "humps" with the main one at $2\theta \approx 37.5°$. As shown in Fig. 4.3b, DSC scans at a heating rate of 20°C/min reveal a glass transition temperature T_g of 400°C, an onset temperature of crystallisation $T_{x,onset}$ of 458°C and a crystallisation enthalpy of 61 J/g. These results are similar to values in literature, e.g. Ref. [21]. The measured oxygen content of the as-cast cylindrical rods typically lies in the range of 190 ± 20 ppm.

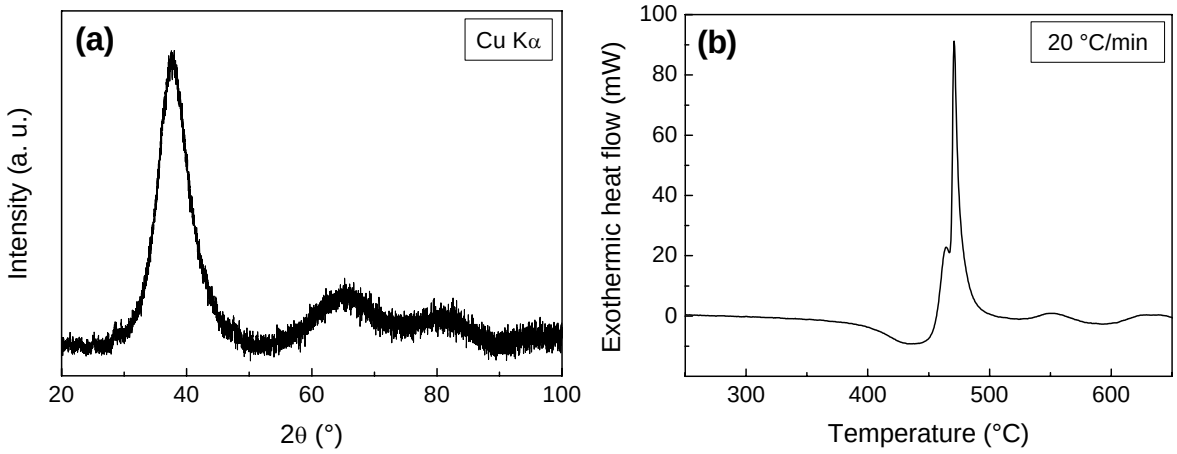

Fig. 4.3: Characteristic (a) XRD and (b) DSC scan of as-cast Vit105.

4.3.2 Deformation behaviour at room temperature

Figure 4.4 shows characteristic stress-strain curves for Vit105 tested under compressive and tensile loading at constant strain rates. The yield or fracture stress at the elastic strain limit of 0.02 are 1890 MPa (compression) and 1780 MPa (tension), revealing a slight strength asymmetry which also manifests itself in the different fracture angles of ~42° (compression) and ~55° (tension), indicating Mohr-Coulomb failure criterion, $\tau = k_0 - \alpha\sigma_n$, where τ is the effective shear stress, k_0 is a constant and α is a system-specific coefficient that controls the strength of the normal stress σ_n [23]. (Note that in crystalline alloys mainly pressure-insensitive criteria such as the Tresca or the von Mises yield criterion are applied,

i.e. $\alpha = 0$.) While under tensile conditions fracture occurs without any significant plastic deformation, several percent of deformation are achieved under compressive loading. This is surprising because the vast majority of monolithic BMGs shows no significant compression plasticity under comparable test conditions.

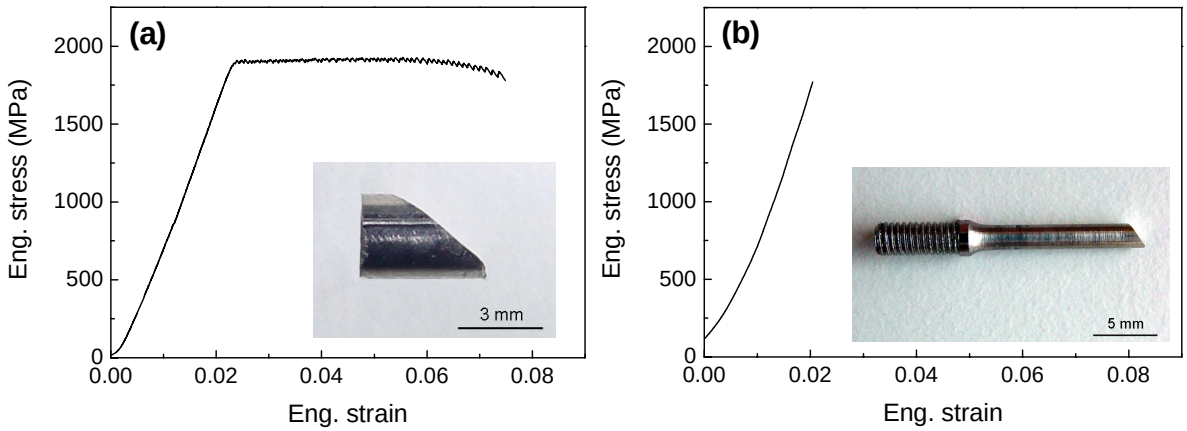

Fig. 4.4: Characteristic (a) compressive and (b) tensile stress-strain curves for Vit105 specimens tested at room temperature and a strain rate of 10^{-3} s^{-1}; the insets show the fractured specimens with fracture angles of ~42° (compression) and ~55° (tension).

In addition, under confined loading conditions (i.e. aspect ratio < 1) high compressive plastic strains can be achieved. As shown in Fig. 4.5, the initial thickness of 1 mm of an as-cast Vit105 specimen can be reduced by 80 % by rolling, without catastrophic failure. (Rolling was performed at room temperature on a Duo-Walzwerk EW105/106 by Bühler, Germany in multiple cycles, while thickness was reduced by ~1.5 % in each cycle.) This shows that depending on the loading conditions BMGs can be plastically deformed to an extremely large extent. Such behaviour, for example, is relevant for potential industrial applications of BMGs.

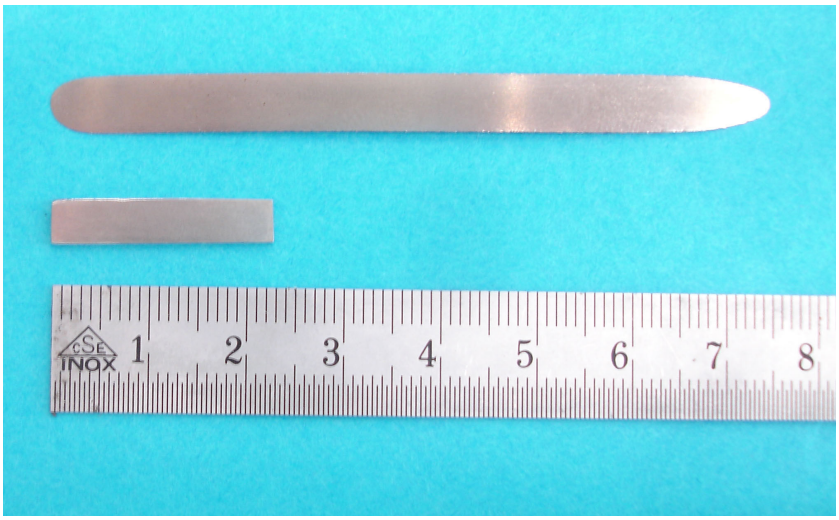

Fig. 4.5: Rolled Vit105 sample with a thickness reduction from 1 mm to 0.2 mm.

Plastic deformation at room temperature is inhomogeneous and localised in narrow shear bands. The activation and propagation of individual shear bands gives rise to serrated flow behaviour (Fig. 4.4) which manifests itself as stress drops and small displacement bursts during plastic deformation at constant crosshead speed. Zooming in on the serrations it becomes obvious that after a successful shear event stress builds up again elastically until the next shear event takes place, leading to a stress drop and corresponding plastic strain. Generally, an increase in the stress drops with increasing strain is observed. The average magnitude increases approximately linearly with increasing strain, as shown in Fig. 4.6a. A steady occurrence of smaller stress drops along with increasing strain is commonly observed up to intermediate strain levels.

As shown in Fig. 4.6b, tests on numerous monolithic samples reveal a decrease in the amplitude of the stress drops per average shear event with increasing strain rate. The same trend was observed previously in nanoindentation and compression tests on BMGs, e.g. in Refs. [24,25,26,]. The time needed for a stress drop occurrence increases with increasing stress drops from 10–40 ms at low stress drops (5–10 MPa) to ~100 ms at the highest stress drops (~40 MPa). Along with a decrease in the average stress drop per shear event, an increase in the average strain produced by a single shear event has been observed with increasing strain rate such that they balance each other out. This results in a roughly constant product of stress times strain per shear event.

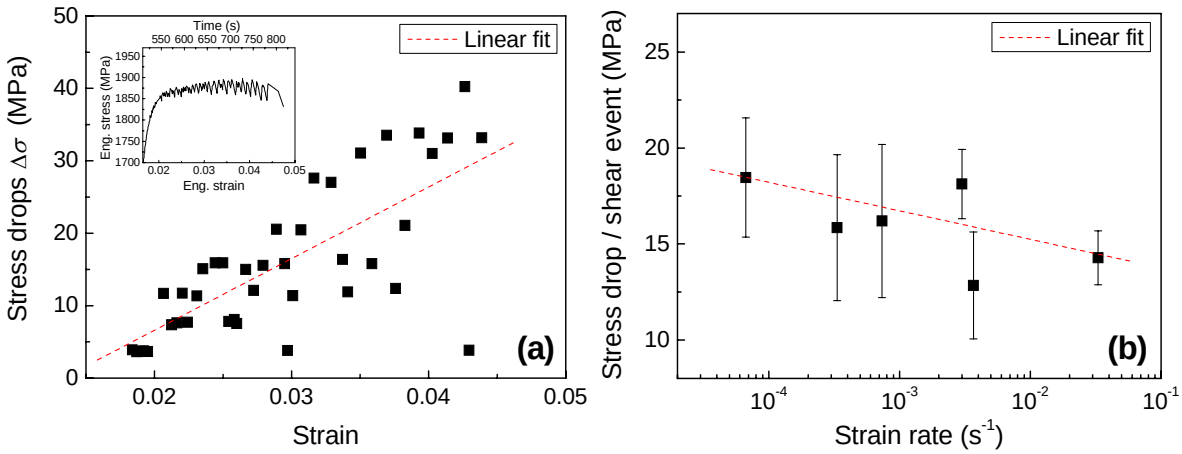

Fig. 4.6: (a) Stress drops as a function of strain tested on a single Vit105 specimen at a strain rate of 10^{-3} s^{-1} (the inset shows the corresponding stress-strain curve with the time scale for the duration of the test). (b) Mean stress drop per shear event versus strain rate for a series of Vit105 samples.

Figure 4.7a shows a stress-strain curve from a Vit105 specimen, where the strain rate was cycled between 3.7×10^{-3} s^{-1} and 3.3×10^{-4} s^{-1}, starting with the higher strain rate and achieving 2.5 cycles. The flow stresses reach slightly higher values at the lower strain rate, indicating a small but negative strain-rate sensitivity. Systematic investigations at different strain rates showed that the strain-rate sensitivity is negative over the whole range of tested strain rates. The strain-rate sensitivities determined are shown in Fig. 4.7b, plotted as a function of the mean strain rate (which is the average of the two strain rates applied during the strain-rate-change tests). Due to small changes in stress upon changes in strain rate compared to the significantly higher stress drops (at constant deformation speed), the estimation of the strain-rate sensitivity is obscured, resulting in relatively large error bars.

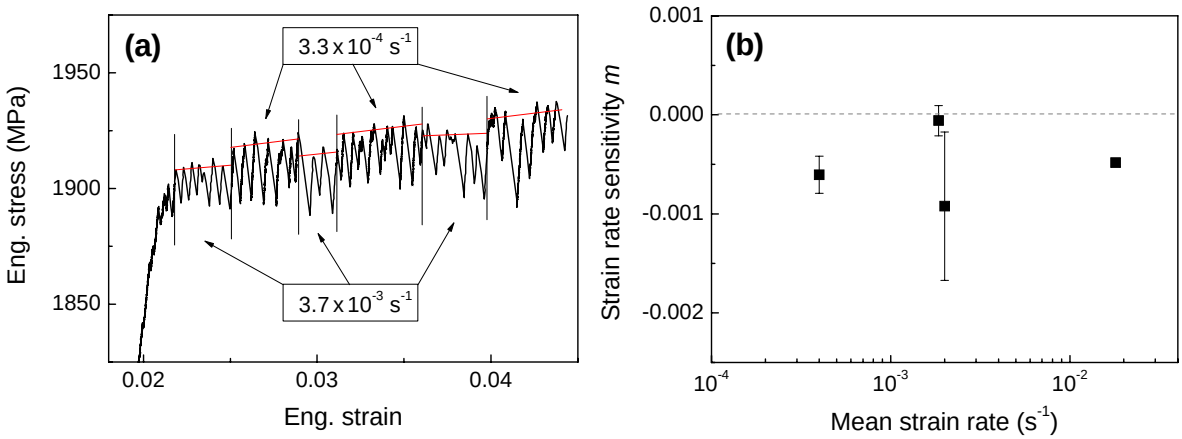

Fig. 4.7: (a) Characteristic compressive stress-strain curve for a Vit105 specimen tested at oscillating strain rates of 3.7×10^{-3} s^{-1} and 3.3×10^{-4} s^{-1}; the red lines indicate the average (maximum) flow stress. (b) Room-temperature strain-rate sensitivity as a function of the applied mean strain rate.

4.3.3 Deformation behaviour as a function of temperature and strain rate

Figure 4.8a shows the stress-strain behaviour of two Vit105 specimens tested at room temperature and 77 K at a strain rate of 10^{-4} s^{-1}. The samples exhibit nearly elastic-perfectly plastic behaviour, and show high strains to failure of 7 % and 11 %, respectively. The samples are X-ray amorphous, but as reported in Refs. [27,28] their (relatively) high strain to failure may be ascribed to the presence of a small volume fraction of nanocrystals homogeneously distributed in the amorphous matrix (see also Section 4.5). Nevertheless, further experimental investigations are necessary to clarify the exact reasons for the compressive plasticity obtained. Statistically, greater strains to failure are measured at lower temperatures. The flow stress at 77 K is about 320 MPa higher than at room temperature, in rough accordance with the increase in the elastic modulus. Fig. 4.8b shows the temperature dependence of the elastic modulus (E') measured by DMA and the flow stress. The elastic modulus decreases linearly with increasing temperature, whereas the flow stress decreases with increasing temperature following a power law with a temperature exponent less than unity. The data may be fitted by a $T^{2/3}$-law, as derived in Ref. [29]. However, as discussed in Section 5.3.1, a refined analysis of the temperature dependence of the flow stress over a larger temperature range reveals a deviation from this $T^{2/3}$ law.

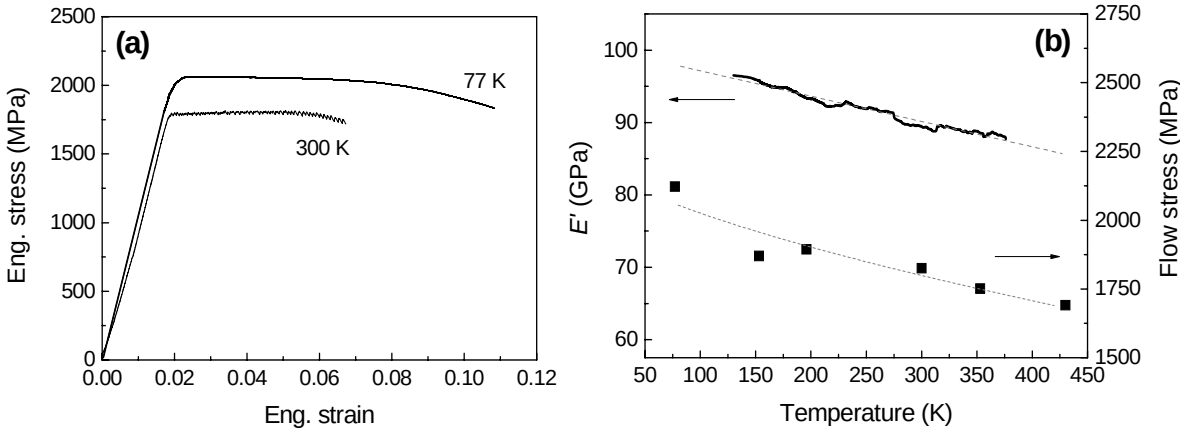

Fig. 4.8: (a) Characteristic stress-strain curve of Vit105 tested at RT ($T = 300$ K) and liquid nitrogen temperature ($T = 77$ K) at a strain rate of 10^{-4} s^{-1}. (b) Elastic modulus E' (measured by DMA) and compressive flow stress (at a strain rate of 3.33×10^{-4} s^{-1}) of Vit105 as functions of temperature. The elastic modulus decreases linearly with temperature while the flow stress appears to follow a $T^{2/3}$-dependence (dashed lines).

Plastic flow at room temperature proceeds in a jerky way, as reflected in the serrated flow curves in Figs. 4.6a and 4.8a (see Section 4.4.2 for further details on the micromechanical origins of serrated flow). In contrast to room temperature measurements, no serrated flow is present at 77 K and the stress-strain curve becomes smooth. At the same time, statistically larger plastic strains to failure are measured in the non-serrated flow regime at low temperatures, as shown in more detail in Section 5.3.1. Although the deformation at low temperature appears macroscopically to be homogeneous, it is spatially inhomogeneous: optical micrographs still reveal the presence of individual shear bands in the form of slip steps on the surface of the tested specimens, as shown in Fig. 4.9a. Similarly, the fracture surfaces of the specimens tested at 77 K in Fig. 4.9b exhibit typical vein patterns with a few liquid droplets which are attributable to the adiabatic heating caused by the dissipation of elastic strain energy within the shear band at the moment of failure.

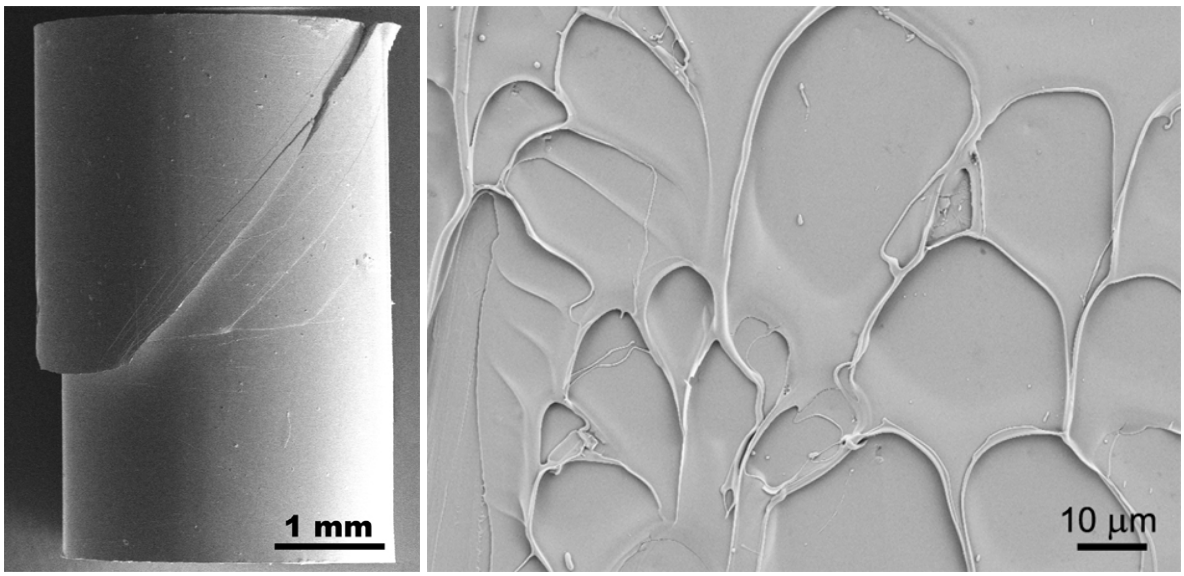

Fig. 4.9: Shear bands on the surface of a tested sample (left) and SEM image of a fracture surface (right) after compression testing at $T = 77$ K.

Figure 4.10a shows the compressive stress-strain behaviour of two Vit105 specimens tested at room temperature and 77 K while alternating the applied strain rate between $\dot{\varepsilon} = 7.33 \times 10^{-4}$ s^{-1} and $\dot{\varepsilon} = 6.67 \times 10^{-5}$ s^{-1}. Increasing the strain rate during deformation at 77 K generates an increase in the flow stress (positive strain-rate sensitivity) which contrasts with the behaviour measured at room temperature, where an increase in the strain rate produces a decrease in the flow stress (negative strain-rate sensitivity).

The observed disappearance of serrated flow at low temperatures (cf. Fig. 4.8a) is highlighted in Fig. 4.10b: at a temperature of 195 K the deformation behaviour changes from serrated to non-serrated flow upon a change in the strain rate. Early work on $Pd_{78}Cu_6Si_{16}$ (which has T_g and mechanical properties comparable to those of Vit105) has shown a disappearance of serrated flow below a critical temperature of ~200 K [10], which is in good agreement with our results. Obviously the appearance/disappearance of serrated flow is reversible: at the higher strain rate $\dot{\varepsilon}_1 = 7.33 \times 10^{-4}$ s^{-1} no serrations are present, whereas at the lower rate $\dot{\varepsilon}_2 = 6.67 \times 10^{-5}$ s^{-1} serrations are clearly visible. Systematic investigations of the transition from discrete to continuous yielding showed that temperature and strain rate are interrelated: for each given temperature there exists a critical strain rate $\dot{\varepsilon}_c$ at which the transition takes place, or, correspondingly, for each strain rate there is a critical temperature T_c at which the transition occurs.

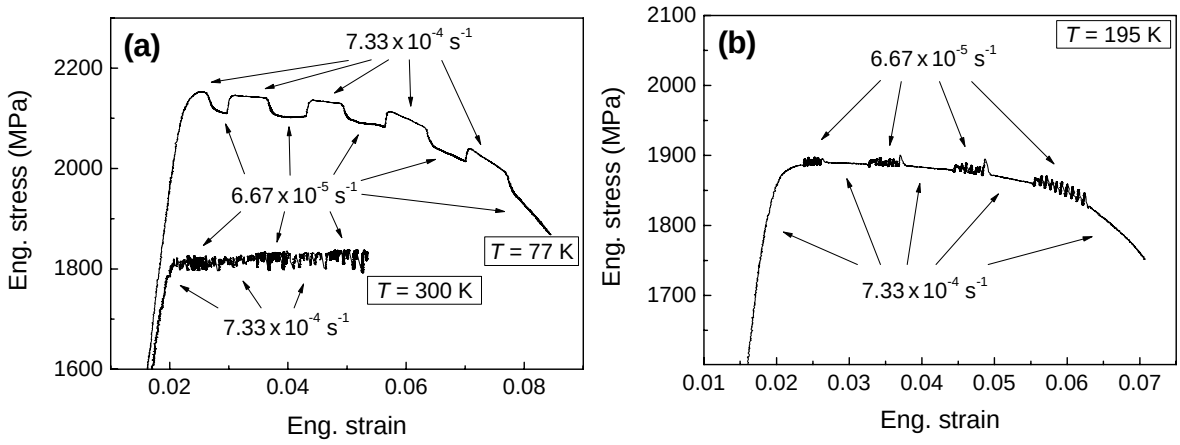

Fig. 4.10: Compressive stress-strain curves for Vit105 obtained while alternating the applied strain rate between $\dot{\varepsilon}_1 = 7.33 \times 10^{-4}$ s^{-1} s^{-1} and $\dot{\varepsilon}_2 = 6.67 \times 10^{-5}$ s^{-1} (a) measured at room temperature and 77 K and (b) at 195 K.

Complementary strain-rate-change tests were also performed at elevated temperatures. Fig 4.11 shows the true stress-strain behaviour of three samples tested at different temperatures close to T_g and alternating applied strain rates ($\dot{\varepsilon}_1 = 1.33 \times 10^{-4}$ s^{-1} and $\dot{\varepsilon}_2 = 6.67 \times 10^{-5}$ s^{-1}). Apparently, no serrations can be identified. In contrast to that at low temperatures, the plastic deformation here is homogeneous both in space and time and significant plastic strains (> 25 %) are achieved without failure. The maximum flow stress decreases drastically with an increase in the temperature from 623 K to 673 K. A clear stress overshoot at yielding and upon increasing the strain rate (and a stress undershoot upon decreasing the strain rate) is visible in the stress-strain curves, characterising a transient state where the material adjusts to the new strain-rate condition. Its magnitude, however, significantly decreases with increasing temperature, as similarly observed in Ref. [30]. The steady-state flow stress is higher at higher strain rate, i.e. it displays a positive strain-rate sensitivity.

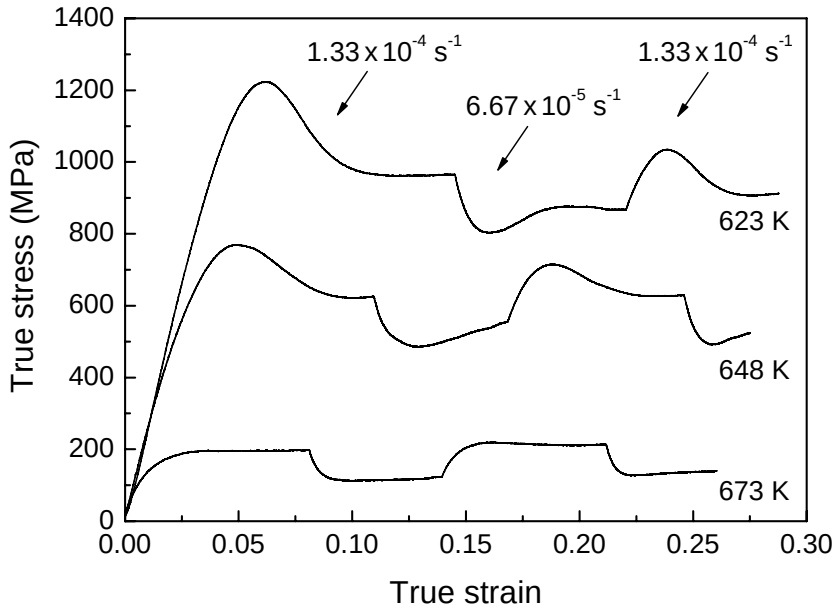

Fig. 4.11: Strain-rate-change tests between $\dot{\varepsilon}_1 = 1.33 \times 10^{-4}\ \mathrm{s}^{-1}$ and $\dot{\varepsilon}_2 = 6.67 \times 10^{-5}\ \mathrm{s}^{-1}$ and in the homogeneous deformation regime at elevated temperatures, starting with the higher strain rate. A clear stress overshoot/undershoot is visible at 623 K and 648 K after an increase/decrease in the strain rate.

4.4 Discussion

4.4.1 Temperature and strain-rate dependence of serrated flow and strain-rate sensitivity

The results of the systematic investigation of the transition from discrete to continuous yielding are summarised in Fig. 4.12 for temperatures between 77 K and 380 K and strain rates between $3.3 \times 10^{-5}\ \mathrm{s}^{-1}$ and $0.2\ \mathrm{s}^{-1}$ in an Arrhenius plot. The boundary between appearance and disappearance of serrated flow is plotted by fitting the critical strain rate $\dot{\varepsilon}_\mathrm{c}$ for the transition from serrated to non-serrated flow according to

$$\dot{\varepsilon}_\mathrm{c} = A \exp\left(-\frac{Q}{k_\mathrm{B} T}\right), \tag{4.2}$$

where A is a constant and Q is the apparent activation energy, determined to be $Q = 0.37$ eV (see dashed line in Fig. 4.12). It should be noted that this schematically-drawn line reflects a physical change in the deformation behaviour as a function of the different testing conditions: in one case ($T > T_c$, $\dot{\varepsilon} < \dot{\varepsilon}_c$) it is characterised by a strongly non-uniform shear deformation (serrated flow), whereas in the other case ($T < T_c$, $\dot{\varepsilon} > \dot{\varepsilon}_c$) a temporally uniform flow behaviour prevails. The boundary represents the lower energy limit for the onset of serrated flow, which is governed by a diffusional relaxation process where the strain rate matches the rate of diffusional relaxation (explained in detail in Chapter 5). In this respect, at the boundary the free energy for STZ activation ΔG changes as a function of temperature.

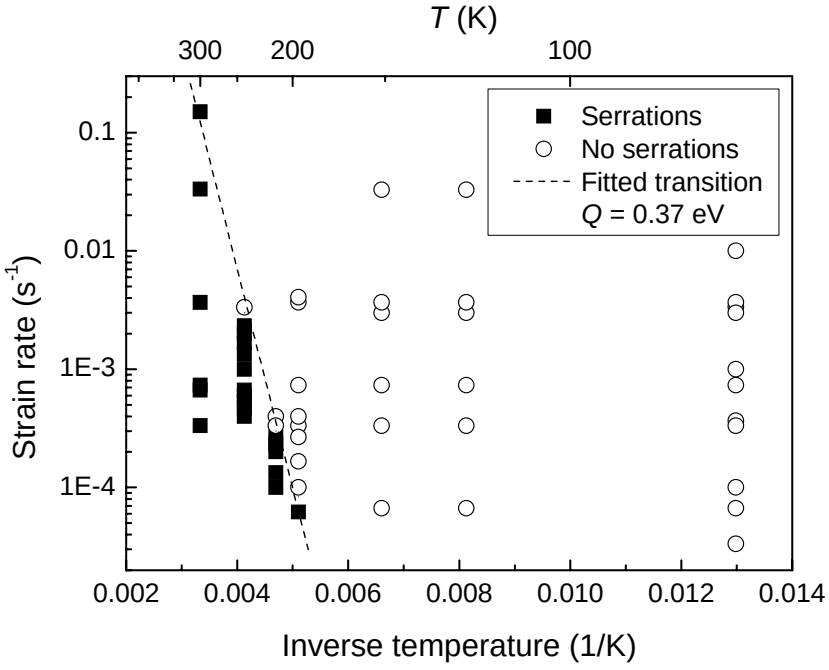

Fig. 4.12: Arrhenius plot illustrating the appearance and disappearance of serrated flow in Vit105. The dashed line, describing the transition from serrated to non-serrated flow, is a fit according to Eq. 4.2.

It should be noted that the magnitude of the stress drops depends on various parameters. On the one hand, it is dominated by the material's instability mechanism, which here depends on microstructure, binding energy, elastic constants and T_g, i.e. material-dependent parameters. On the other, external parameters such as machine stiffness, compliance of the

load cell, sample geometry and possible sample imperfections may interfere with the slope of the transition from serrated to non-serrated flow. However, it is reasonable to assume that the instability mechanism remains the same for the transition, i.e. the change of the viscosity within the shear band remains approximately constant when changing temperature and strain rate in a reversible manner. In literature only a few data exists regarding the temperature-dependent inhomogeneous flow behaviour of BMGs. (Some work on this topic was done already in the 1970s and 1980s by Pampillo and Chen or Masumoto, Maddin and co-workers, e.g. [10,11].) Compression and bending experiments conducted by Kimura and Masumoto on an amorphous $Pd_{78}Cu_6Si_{16}$ sample (which has T_g and elastic moduli comparable to the material we use) revealed an activation energy for the transition of 0.35 eV [31,32], in close agreement with our value. Tearing experiments on amorphous $Fe_8Ni_{70}Si_{10}B_{12}$ and $Co_{78}Si_{10}B_{12}$ ribbons revealed activation energies for the transition of 0.46 eV and 0.48 eV, respectively [33]. However, no further interpretation of the determined activation energies was given in these early studies. Finally, the activation energy of STZs in simulations were recently determined to be 0.34 eV [4] and 0.31 eV [7] for a CuTi and a NiZr model glass, respectively. These values are close to the activation energy for the transition from serrated to non-serrated flow, $Q = 0.37$ eV, obtained from the fit in Fig. 4.12. Therefore, it might be speculated if the experimentally determined activation energy Q for the transition, which is characterized by the absence and presence of structural relaxation, reflects the activation energy of STZ operation in this respect?

As shown in the following, a change in the strain-rate dependence of the stress (strain-rate sensitivity) accompanies the change from serrated to non-serrated flow. The strain-rate-change tests enable us to determine the macroscopic strain-rate sensitivity. In this context a distinction can be made between the instantaneous and the asymptotic SRS (see Fig. 4.13 for (a) positive and (b) negative SRS). The instantaneous SRS (m_i) of the flow stress, which is an intrinsically positive parameter of a viscoelastic solid (Maxwell body), describes the instantaneous change in the flow stress (σ_i) upon a change of the strain rate ($\dot{\varepsilon}$) and is in infinitesimal notation defined as [34,35]

$$m_i = \left(\frac{\partial \ln \sigma_i}{\partial \ln \dot{\varepsilon}} \right)_{\varepsilon} . \tag{4.3}$$

In contrast, the asymptotic SRS (m_∞) characterises the steady-state change after a (possibly existing) transient of the flow stress according to

$$m_{\mathrm{i}} = \left(\frac{\partial \ln \sigma_{\mathrm{s}}}{\partial \ln \dot{\varepsilon}} \right)_{\varepsilon}, \tag{4.4}$$

where σ_{s} is the flow stress levelled-off at the steady-state value after a characteristic time-lag t_{ϕ} [35].

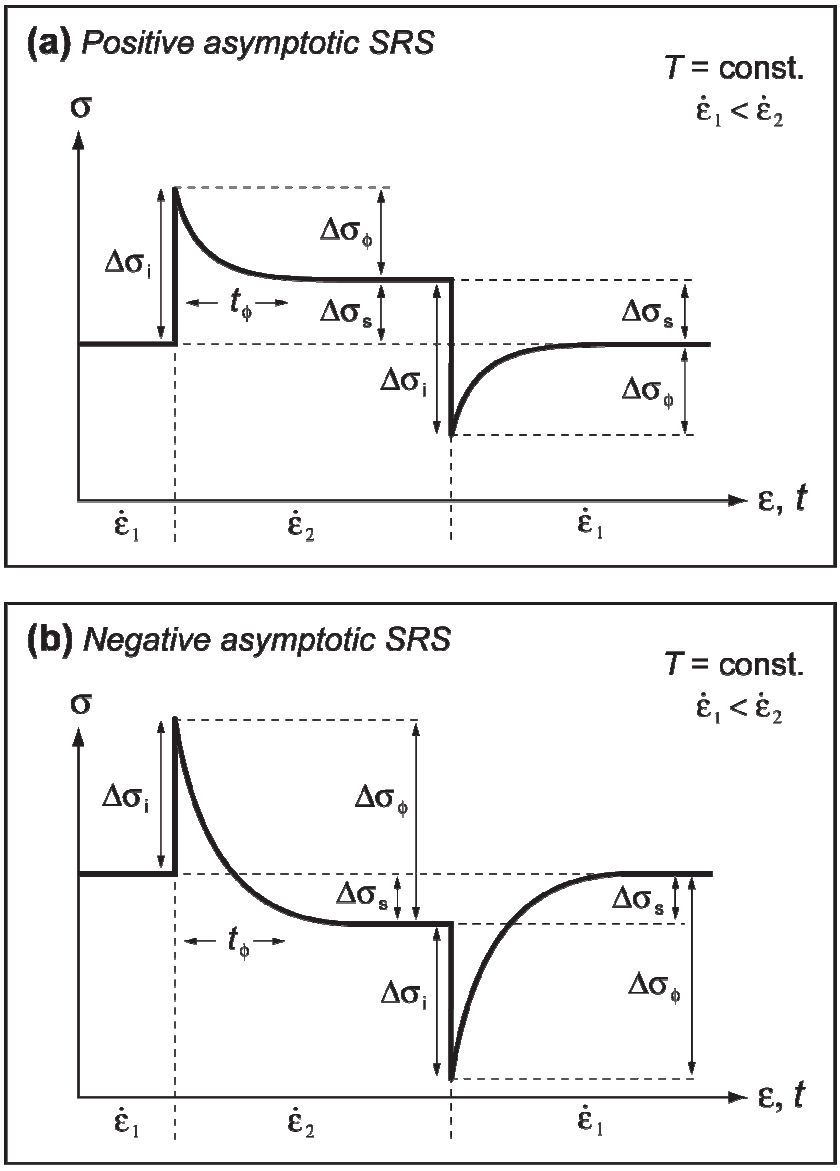

Fig. 4.13: Schematic illustration of the stress response to a strain-rate change ($\dot{\varepsilon}_1 < \dot{\varepsilon}_2$) in the case of (a) a positive asymptotic SRS ($m_{\infty} > 0$) and (b) a negative asymptotic SRS ($m_{\infty} < 0$), modified after Refs. [34,37].

It should be noted that the concepts used here to derive macroscopic values for the strain-rate sensitivity are taken from constitutive laws commonly applied to homogeneous deformation. Nonetheless, this concept has shown its usefulness in describing deformation kinetics in crystalline metals deforming inhomogeneously, e.g. via the dynamic strain aging (DSA) mechanism [35,36,37]. Facing the difficulty of measuring the effective strain rate within a shear band during deformation on a microscopic level, our model has some limitations. A straightforward way of dealing with this issue is to introduce a fraction of shearing volume in the macroscopic shear strain rate, as did e.g. Argon [38]. In the non-serrated flow regime at low temperatures a rough estimation of the effective shear strain rate in the shear band during uniaxial compression can be made based on geometrical considerations, i.e.

$$\dot{\gamma} = \frac{\dot{\varepsilon} l_0}{nh\cos\theta}, \tag{4.5}$$

where $\dot{\varepsilon}$ is the applied (uniaxial) strain rate, l_0 is the initial height of the specimen, n is the number of simultaneously active shear bands, h is the thickness of a shear band and θ is the angle between shear band and loading axis. Assuming that only one shear band is active (i.e. $n = 1$) and using $l_0 = 5$ mm, $h = 20$ nm and $\theta = 45°$ yields $\dot{\gamma} \approx 3.5 \times 10^5 \dot{\varepsilon}$. This estimation points out that even if several shear bands operate simultaneously the local shear strain rate is orders of magnitude higher than the global, applied strain rate. In the serrated flow regime even higher local shear strain rates can be expected due to the strong temporal localisation of the shear banding events.

Figure 4.14 summarises the asymptotic SRS as a function of the testing temperature for different mean strain rates, $\dot{\varepsilon}_{\text{mean}} = (\dot{\varepsilon}_1 + \dot{\varepsilon}_2)/2$. Due to the completely brittle behaviour of the specimens between 400 K and 600 K the SRS in this temperature range could not be determined by strain-rate-change tests. The asymptotic SRS is negative when serrated flow prevails and positive when serrations are absent. Three different temperature regimes can be distinguished. (I) At very low temperatures (below ~200 K for our tested strain-rate range) the SRS is positive and deformation proceeds in a smooth manner (i.e. with no serrations). The presence of shear bands on the deformed specimens, however, indicates that deformation is still inhomogeneous in space. (II) In the intermediate temperature range (200–380 K) the SRS is negative and deformation proceeds by shear banding in a jerky

manner. (III) At elevated temperatures the SRS is again positive and deformation is homogeneous in space and time.

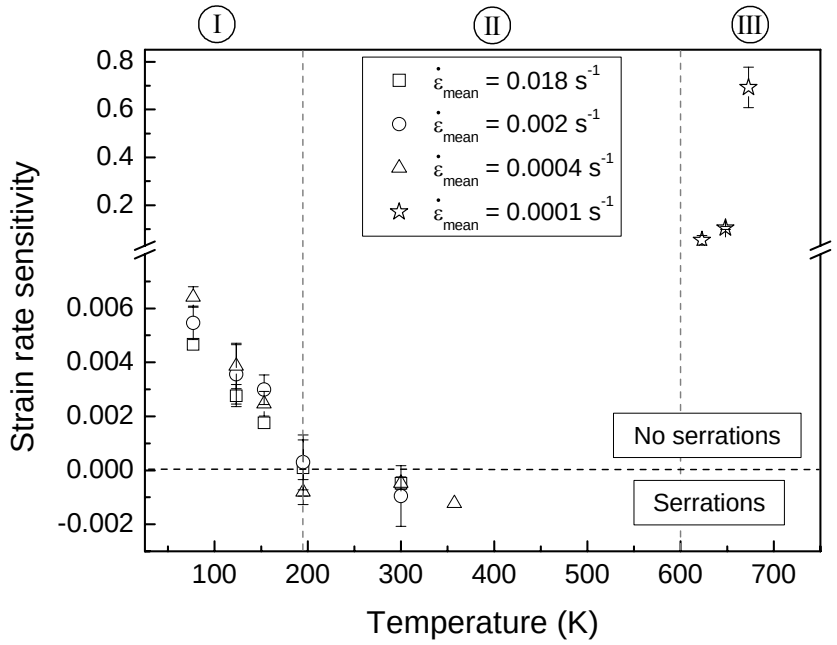

Fig. 4.14: Asymptotic strain-rate sensitivity of Vit105 as a function of temperature and mean strain rate.

The change in the SRS from positive ($T < 195$ K) to negative values ($T > 195$ K) indicates a change in the micromechanism of flow, despite the fact that deformation still proceeds by shear banding. It also provides evidence that the disappearance of serrations at low temperatures or high strain rates is a true material response and does not result from instrumental artefacts (i.e. lack of resolution). As pointed out in Ref. [39], other instrumental effects arising from the lateral and longitudinal constraints of tested samples may play a role in the arrest of shear bands. When a sample is deformed along a shear band the lateral movement of the two half-parts may be hindered by the friction between sample top/bottom surfaces and the compression pistons so that further slip along the shear band would not be possible. However, because of the narrowness of the shear band (~10–20 nm) the lateral movement is generally very small and it is questionable whether the lateral constraint effect is significant for the shear-band arrest. Further, large plastic deformation is achieved in specific metallic glasses only. At exactly the same compression conditions, the vast majority of monolithic BMGs do not show significant compressive plasticity, which

suggests that the shear-band arrest is most likely an intrinsic material property of "ductile" (or malleable) metallic glasses (which may to a certain extent contain structural inhomogeneities).

Systematic mechanical investigation of other BMGs ($Zr_{57.9}Cu_{22}Fe_8Al_{12}Pd_{0.1}$ and $Cu_{50}Zr_{50}$) confirmed the phenomenological observation made regarding Vit105 (e.g., the increase in the magnitude of the stress drops with increasing strain and decreasing strain rate) and the correlation between the disappearance/appearance of serrated flow and the change in the strain-rate sensitivity (see Table 4.3). Similar to Vit105, the transition from serrated to non-serrated flow for these alloys takes place at a critical temperature of around $T_c \approx 200$ K (for a strain rate of 10^{-4} s^{-1}), as also reported earlier for a Pd-based BMG [31,40]. This analogy is not surprising because all these glass-forming alloys possess comparable elastic constants and glass transition temperatures of around 675 K. However, recent results by Huang *et al*. [41] on a $Ti_{40}Zr_{25}Ni_3Cu_{12}Be_{20}$ BMG with a lower T_g of about 590 K (but with comparable Young's modulus, $E = 89$ GPa) showed that the disappearance of serrated flow for a strain rate of 4×10^{-4} s^{-1} takes places at a temperature below 193 K. Further, the serrated flow characteristics are strongly dependent on the chemical composition of the metallic glass. For example, the serrations of $Cu_{50}Zr_{50}$ BMG are less pronounced than for Vit105, and different metallic glasses exhibit at room temperature different critical strain rates, where serrations cease (e.g. as shown in nanoindentation experiments [25]). This compositional dependence illustrates the importance of local atomic rearrangements in shear bands and may be taken into account by scaling to the homologous temperature, resulting in a generalised deformation map, as in Ref. [26].

Table 4.3: Strain-rate sensitivity values of different BMGs measured at various temperatures at a mean strain rate of 2×10^{-3} s^{-1}.

BMG composition	Strain-rate sensitivity			
	$T = 300$ K	$T = 195$ K	$T = 153$ K	$T = 77$ K
$Zr_{52.5}Ti_5Cu_{17.9}Ni_{14.6}Al_{10}$	-0.001 ± 0.001	0.0003 ± 0.001	0.0030 ± 0.0005	0.0055 ± 0.0005
$Zr_{57.9}Cu_{22}Fe_8Al_{12}Pd_{0.1}$	-0.002 ± 0.0002	n.m.	n.m.	0.0035 ± 0.0005
$Cu_{50}Zr_{50}$	-0.001 ± 0.0002	0.000 ± 0.001	0.001 ± 0.001	0.004 ± 0.001

The errors result from variations of the measured values. The abbreviation n.m. stands for "not measured".

Finally, it should be noted that the mechanical behaviour of the $Cu_{50}Zr_{50}$ alloy is greatly affected by the fraction of (nano-)crystals embedded in the amorphous matrix. It is known that bulk $Cu_{50}Zr_{50}$ samples with diameters of 1–2 mm consist of an amorphous matrix containing fine crystalline particles with a size of about 5 nm [27]. This inhomogeneity in the microstructure reflects their sensitivity to the glass-forming ability, critical casting thickness and processing history of the binary alloy. Our investigations show that completely X-ray-amorphous samples show a sharp elastic/plastic transition, no strain hardening (i.e. elastic-perfectly plastic behaviour) and clear serrations. On the other hand, samples with a higher fraction of crystallites, which appear as small peaks overlaying the amorphous hump in the XRD spectra, show a lower yield point, significant strain hardening and no or very limited serrated flow. In this respect, only $Cu_{50}Zr_{50}$ samples which showed compressive behaviour similar to the former were considered for the analysis of strain-rate sensitivity.

4.4.2 Micromechanical origins of serrated flow and negative SRS

The micromechanical source of our phenomenological observations may be regarded as a local diffusive type of atomic rearrangement during a successful shear event. The inhomogeneous deformation in metallic glasses is localised in “flow defects” or “shear transformation zones” comprising small groups of atoms which generate a local rearrangement of the surrounding atomic structure and trigger the formation of macroscopic planar shear bands. For these shear events to be irreversible (plastic deformation) there must be a change in displacement of at least a few atomic neighbours at the core of the STZ, which corresponds to a local shear strain on the order of unity. (Note that the characteristic, global strain of a STZ is assumed to be ~0.1.) The percolation of such activated STZs, occurring within a narrow time span of a few milliseconds, is assumed to lead to the formation of shear bands which are macroscopically detected as stress drops (serrations) in a stress-strain curve. Such shear processes induce volume dilatations (e.g. increased free-volume content [42] generates local “softening” in shear bands [43,44,45]) and are believed to locally destroy the short-range order of the BMG, which makes them susceptible to preferential etching [10].

Assuming that the basic deformation mechanism of shear banding at room temperature is comparable to that at lower temperatures, the disappearance of serrated flow, the change in the SRS value and the change in its temperature dependence can be explained by incorporating a thermally-activated relaxation process in the cooperative shearing of STZs. At sufficiently high temperatures (e.g. room temperature) and low strain rates, where serrated flow prevails, atoms located in a STZ and adjacent areas which have undergone stress-driven atomic shearing and were moved away from their original positions can now structurally relax towards a lower state of energy via collective, diffusive processes. This generates a higher resistance to shear banding and thus higher stress amplitude (stress drop $\Delta\sigma$). An increase in the strain rate leaves less time for structural relaxation processes, leading to a decrease in $\Delta\sigma$. Above T_c (or, respectively, below $\dot{\varepsilon}_c$) the diffusive relaxation processes keep up with the shear transformations and deformation becomes serrated. This structural relaxation may counteract the increase in free volume during a shear event, such that the net free volume in the shear band after relaxation is lower than at the moment of shearing. This higher atomic density in turn causes a strengthening of the shear band, which is experimentally observed by higher yield strength for lower strain rates (or greater relaxation times). This results in a deformation regime with a negative SRS. The extent of structural relaxation, however, is limited by the time span between two local, adjacent STZ operations and the temperature. Below a critical temperature T_c (or above $\dot{\varepsilon}_c$) the atomic mobility is not sufficient to rearrange or relax the configuration of the STZ after a successful shear event and deformation becomes macroscopically smooth. In this case, an increase in the strain rate generates an increase in the yield strength and therefore a positive SRS. Thus, in contrast to the explanation for the disappearance of pop-ins at high indentation rates given in Ref. [26] we believe that the absence of serrated flow is caused by the inability of a shear band to structurally relax rather than by the simultaneous operation of many shear bands.

4.5 SEM analysis of shear surfaces

Figure 4.15a shows a stress-strain curve and the corresponding deformed $Zr_{57.9}Cu_{22}Fe_8Al_{12}Pd_{0.1}$ specimen. It was compressed without fracture to more than 20 %. The change in the slope of the engineering stress-strain curve is associated with the geometrical changes in the cross-sectional area during shearing. Due to the frictional forces between the sample and the compression plates, cohesion of the sample is additionally supported once its top part makes contact with the lower compression plate (i.e. constraint plasticity). At this moment the stress increases again and fracture of the sample becomes less critical due to the continuously decreasing aspect ratio (i.e. length/diameter) of the specimen. The peculiarly high plastic strain (of ~15 %) in the unconstrained part may be attributed to the pre-existence of nano-sized crystals dispersed in the amorphous matrix which have been nucleated during solidification (Fig. 4.15b). The positive influence of nano-sized crystals embedded in an amorphous matrix on the plastic strain has been reported previously by various authors [46,47].

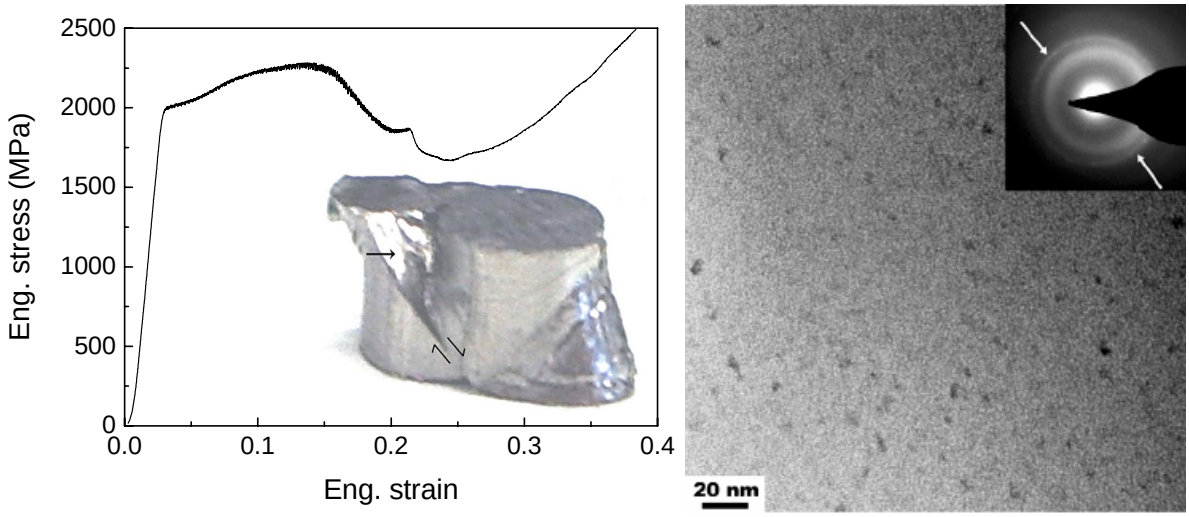

Fig. 4.15: (Left) Stress-strain curve of a $Zr_{57.9}Cu_{22}Fe_8Al_{12}Pd_{0.1}$ sample deformed at room temperature and at an initial strain rate of 10^{-4} s^{-1}. Note that the stress-strain curve above a strain of ~15 % looses its proper physical significance due highly constraint conditions and frictional forces between sample and loading plats. The inset shows the corresponding specimen after deformation; the vector arrows indicate the shear direction, while the single arrow indicates the shear surface examined by SEM. (Right) Bright-field TEM image with selected area diffraction (SAD) pattern indicating the presence of nano-sized crystals embedded in the amorphous matrix. The second ring in the SAD pattern, indicated by the arrows, confirms the crystallinity of the darker nano-sized contrasts shown in the bright-field image.

The left side of Fig. 4.16 shows the linear shear striations that cover 90 % of the totally sheared and revealed shear surface. These shear striations bear similarities in appearance to those known in ductile shear zones of rock-forming minerals (mylonites), which form as a consequence of shear softening towards a semi-fluid state that allows for quasi-viscous flow [48,49]. The big arrows in the figures indicate the direction of shear on the surface made by the top part of the compression specimen. Detailed examination of the major shear-band plane indicates that it is laterally separated into many smaller shear surfaces. They are separated by vertical steps facing the opposite direction of the shear, i.e. they form a gentle ascending staircase structure. The exact mechanism of heir formation is not clear, however, the same orientation of topological shear steps has recently been observed on the shear surface of a Pd-based BMG which was deformed during micropillar compression experiments [50]. Closer inspection of these shear step surfaces indicates that the majority shows a brittle fracture mechanism where a high density of shear bands or microcracks intersect, being roughly 100 nm or less apart. On the surfaces of the shear steps only a few areas indicate a viscous fracture type, where onsets/nucleations of vein patterns are visible (smaller arrows in Fig. 4.16 left). Interestingly, these vein patterns occur at the foot of the steps, where shearing along the lower plane is assumed to be more pronounced. Some areas indicate a very narrow separation of shear steps. This indicates that the major shear plane, or more generally speaking a macroscopically visible major shear band of a deformed sample, is not sheared solely on one plane, but is sheared along a whole shear zone consisting of many parallel spaced, smaller shear planes. The spacing of these smaller shear planes can be as close as several tens of nanometres, which is of the same order of magnitude as the nano-sized crystals embedded in the amorphous matrix shown in Fig. 4.15. It is not clear from this observation whether the magnitude of the shear-band spacing is dictated by the nano-sized crystals; this might, however, explain the increased plasticity in the sample [46,47].

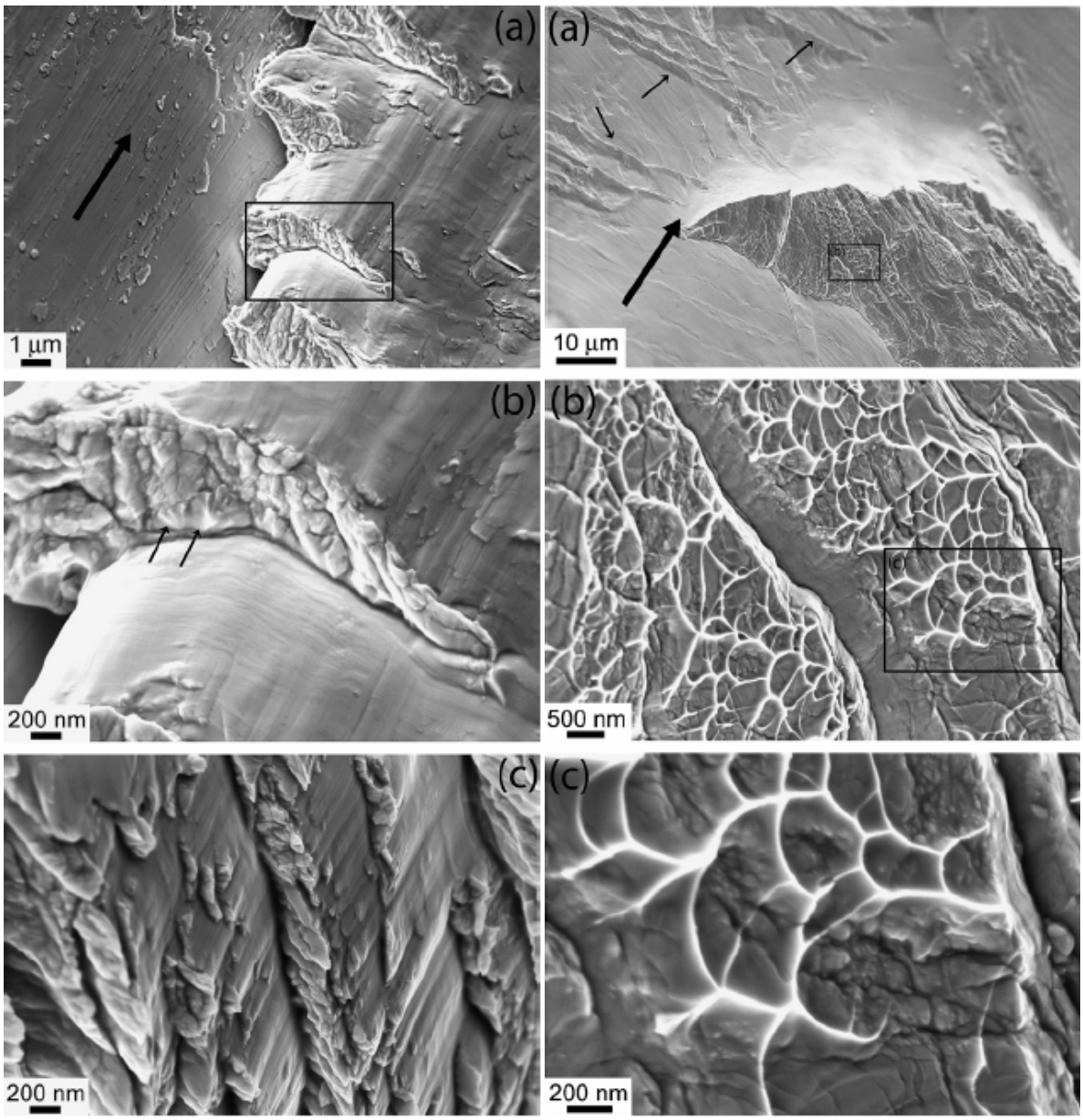

Fig. 4.16: SEM images of the shear surface of the sample shown in Fig. 4.14. (Left) Shear striations indicating the direction of shear (big arrow) together with shear step surfaces oriented perpendicularly to the shear plane. The close-up (b) of one of the shear step surfaces (see square in (a)) shows a brittle fracture mechanism with microcracks and a ductile fracture mechanism indicated by the vein pattern (see arrows in (b)). The spacing of single shear planes can be as narrow as tens to a few hundreds of nanometres (c). (Right) The small arrows in (a) indicate the intersection of the major shear plane with a minor one; the large arrow indicates the direction of shear of the major shear plane. The vein pattern observed on the triangular feature is of shallow depth and reveals a more brittle mode lying underneath (b), closeup shown in (c).

The right-hand image in Fig. 4.16 shows a set of SEM pictures taken from another shear step on the shear plane, which (compared to the shear steps shown on the left) does not

have a 90° orientation but stands at a greater angle to the shear plane surface in front of it. The triangular feature highlighted by a square and shown in greater detail in (b) and (c) is to a large extent covered with vein patterns otherwise seen only on fracture surfaces. Closer inspection of these vein patterns, however, indicates an important contrast to the fracture surfaces of metallic glasses. Here the vein pattern is very thin and reveals a dense network of shear bands or microcracks underneath, which suggests localised brittle behaviour superimposed by a viscous mechanism. Fractured surfaces, in contrast, are smooth throughout their entire visible depth of a few micrometers (see Fig. 2.7 or Fig. 4.9). Moreover, the veins seem to be localised by shear bands, acting either as the source of these viscous flow patterns or as a barrier.

Only a few areas on the shear surface were found which exhibit vein patterns and shear striations near each other and have the same planar orientation (Fig. 4.17). This resemblance between the patterns suggests that the thermal histories of both structures are similar. Thus the shear striations can be explained as smeared-out, viscous-like features, which compared to the vein patterns have experienced a more intensive compressive shear stress component before being exposed to the surface. Note that similar features are also generated in tribological wear resistance tests performed on BMGs [51].

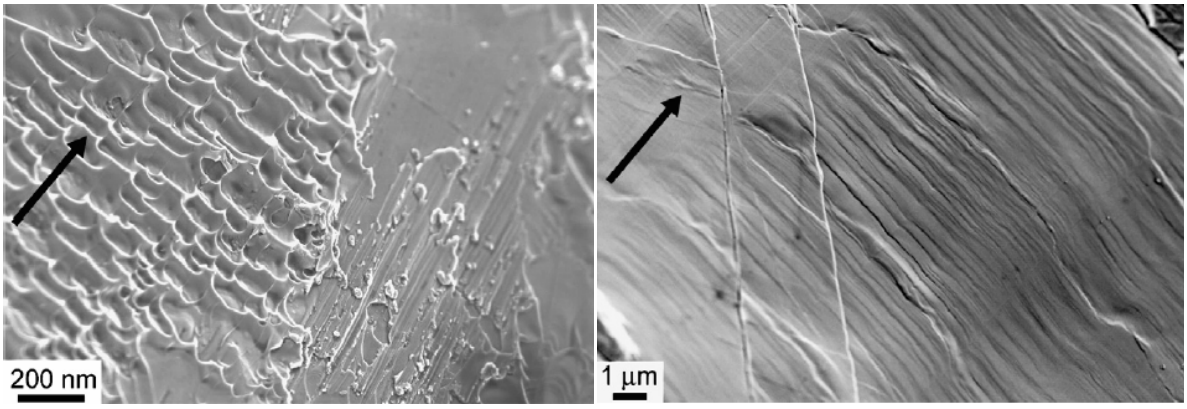

Fig. 4.17: (Left) Area showing viscous flow features in the near neighbourhood of shear striations, which have the same shear plane surface as in Fig. 4.15. (Right) Signature of discrete shear slip events on the shear surface oriented perpendicular to the shear direction (arrow). These slip marks are proof of the reactivation of a pre-existing shear band. The distances of the slip marks have the same dimension as the displacement measured from a stress drop in the deformation curve.

In order to evaluate whether the stress drops microscopically observed on stress-strain curves (see Fig. 4.15) represent single shear events on an existing shear band, or rather a sum of instantaneously released, newly nucleated shear bands, the shear surface was closely inspected. As shown in Fig. 4.17, slight but distinct slips perpendicular to the shear striations on the shear surface (direction of shear indicated by the arrow) are present, suggesting that they arise from temporally separated reactivation of the same shear band by single shear off-sets or events. Here we refer to single shear events as the stress drops recordable during compression testing. Measuring the distance between these marks reveals values of 200 nm–2 μm, which are of the same order of magnitude as the shear displacements measured from stress-strain curves. This observation confirms that spatially and temporally the stress drops can be taken as single shear events occurring along one single shear band. To the knowledge of the author such a correlation between the details of a stress-strain diagram and microscopic shear slips seen on shear surfaces of metallic glasses has not been previously observed.

The observed stress drops and their increase in magnitude with strain (see Fig. 4.6 a) can therefore be approximately associated with the continuous reactivation of the same shear band. (Strictly speaking this assumption is only valid in a small strain interval where the stress state remains roughly constant. For geometrical reasons, large deformations lead to changes of the stress state and consequently to the activation of new shear bands). The energy release (ΔE) in a single stress drop can be estimated by

$$\Delta E = \int \Delta F dx \cong \frac{1}{2} \Delta F x , \tag{4.6}$$

where ΔF is the load drop and x the axial displacement. The conversion from the displacement measured parallel to the loading direction to that of a shear plane oriented ~45° with respect to the compression direction is obtained by simple geometric relationships. Consequently, an energy release of $\sim 10^{-4}$ J is obtained at the beginning of plastic deformation. The steady increase of the stress drop magnitude with increasing plastic strain leads to an increase of ΔE to $\sim 10^{-3}$ J before fracture. Correcting for machine stiffness and the effect of damping on the load cell values, a factor ~2 higher may be expected [31]. (Further discussions of the energy release are given later in Chapter 6). At the moment of fracture, however, the energy release is about three orders of magnitude larger and reaches values close to 1 J. Comparing these values with the appearance of fracture surfaces (micrometer-thick river patterns throughout the entire surface) and shear

planes (a few areas with much thinner vein pattern) suggests that the heat release during fracture is high enough to melt the entire fracture surface, whereas the temperatures during shearing before fracture are significantly lower and thus might cause no or far less local melting. As shown in Section 2.3.2, fully adiabatic heating conditions may not be fulfilled during shearing, but other non-adiabatic effects, such as friction and its release via stress drops, causing an energy burst, may be responsible for local temperature increases and consequently for the observed viscous structures on shear surfaces.

4.6 Conclusions

Detailed micromechanical investigations of Zr-based BMGs at various temperatures and strain rates revealed accurate information on their inhomogeneous flow kinetics. Serrated flow in conjunction with a negative strain-rate sensitivity was observed at room temperature. The disappearance of serrated flow below a critical temperature and/or above a critical strain rate correlates with a transition of the strain-rate sensitivity to positive values and exhibits an activation energy of 0.37 eV. These observations, together with an increase in stress drops with increasing strain and their decrease with increasing strain rate, indicate phenomenologically close similarities with the dynamic strain aging deformation mechanism known for crystalline solids, as will be discussed in greater detail in the following chapter. The results suggest a micromechanical deformation mechanism based on two processes: shear displacement through the formation and operation of STZs, and diffusive relaxation processes of the distorted structure. The latter vanishes below a critical temperature (or above a critical strain rate), resulting in the change measured in the SRS and the disappearance of serrated flow. The crucial factor determining serrated flow in BMGs is the ratio between the cooperative shearing of STZs and the rate of adjacent diffusive relaxations.

Detailed high-resolution SEM observations of the shear surface morphology of deformed, but unbroken, BMG specimens enabled a thorough interpretation of the deformation kinetics and temperature influence during shearing before fracture. Apart from closely-spaced shear striations, only a few areas reveal typical vein pattern structures, but

less thick than those resulting at the moment of fracture. These observations, combined with estimates of the energy release, suggest that the heat release during plastic deformation is not sufficient to melt the entire surface. Melting only takes place locally due to friction and stress drops causing a local burst in energy release.

4.7 References

[1] A.S. Argon, H.Y. Kuo, Mater. Sci. Eng. 39 (1979) 101.
[2] M.L. Falk, J.S. Langer, Phys. Rev. E 57 (1998) 7192.
[3] Y.F. Shi, M.L. Falk, Phys. Rev. B 73 (2006) 214201.
[4] S.G. Mayr, Phys. Rev. Lett. 97 (2006) 195501.
[5] N.P. Bailey, J. Schiøtz, K.W. Jacobsen, Phys. Rev. B 73 (2006) 064108.
[6] M. Zink, K. Samwer, W.L. Johnson, S.G. Mayr, Phys. Rev. B 73 (2006) 172203.
[7] F. Delogu, Intermetallics 16 (2008) 658.
[8] W.J. Wright, R. Saha, W.D. Nix, Mater. Trans. JIM 42 (2001) 642.
[9] S.X. Song, H. Bei, J. Wadsworth, T.G. Nieh, Intermetallics 16 (2008) 813.
[10] C.A. Pampillo, H.S. Chen, Mater. Sci. Eng. 13 (1974) 181.
[11] T. Masumoto, M. Maddin, Mater. Sci. Eng. 19 (1975) 1.
[12] H.A. Bruck, A.J. Rosakis, W.L. Johnson, J. Mater. Res. 11 (1996) 503.
[13] K.M. Flores, R.H. Dauskardt, J. Mater. Res. 14 (1999) 638.
[14] T.H. Hufnagel, T. Jaiao, Y. Li, L.Q. Xing, K.T. Ramesh J. Mater. Res. 17 (2002) 1441.
[15] B. Yang, M.L. Morrison, P.K. Liaw, R.A. Buchanan, G. Wang, C.T. Liu, M. Denda, Appl. Phys. Lett. 86 (2005) 141904.
[16] C. J. Gilbert, J.W. Ager, V. Schroeder, R.O. Ritchie, J.P. Lloyd, J.R. Graham, Appl. Phys. Lett. 74 (1999) 3809.
[17] W.J. Wright, R.B. Schwarz, W.D. Nix, Mater. Sci. Eng. A 319 (2001) 229.
[18] J.J. Lewandowski, A.L. Greer, Nat. Mater. 5 (2006) 15.
[19] B. Yang, C.T. Liu, T.G. Nieh, M.L. Morrison, P.K. Liaw, R.A. Buchanan, J.Mater. Res. 21 (2006) 915.
[20] X.H. Lin, W.L. Johnson, W.K. Rhim, Mater. Trans. JIM 5 (1997) 473.
[21] S.C. Glade, R. Busch, D.S. Lee, W.L. Johnson, R.K. Wunderlich, H. J. Fecht, J. Appl. Phys. 87 (2000) 7242.
[22] Z. Bian, M.X. Pan, Y. Zhang, W.H. Wang, Appl. Phys. Lett. 81 (2002) 4739.
[23] C.A. Schuh, A.C. Lund, Nat. Mater. 2 (2003) 449.
[24] T. Mukai, T.G. Nieh, Y. Kawamura, A. Inoue K. Higashi, Intermetallics 10 (2002) 1071.
[25] C.A. Schuh, T.G.Nieh, Acta Mater. 51 (2003) 87.
[26] C.A. Schuh, A.C. Lund, T.G. Nieh, Acta Mater. 52 (2004) 5879.

[27] A. Inoue, W. Zhang, T. Tsurui, A.R. Yavari, A.L. Greer, Philos. Mag. Lett. 85 (2005) 221.
[28] W. Dong, H. Zhang, J. Cai, W. Sun, A. Wang, H. Li, Z. Hu, J. Alloys Comp. 425 (2006) L1.
[29] W.L. Johnson, K. Samwer, Phys. Rev. Lett. 95 (2005) 195501.
[30] Y. Kawamura, T. Shibata, A. Inoue, T. Masumoto, Appl. Phys. Lett. 69 (1996) 1208.
[31] H. Kimura, T. Masumoto, Acta Metall. 31 (1983) 231.
[32] H. Kimura, T. Masumoto, Acta Metall. 28 (1980) 1663.
[33] H. Kimura, T. Masumoto, Philos. Mag. A 44 (1981) 1021.
[34] P.G. McCormick, Acta Metall. 36 (1988) 3061.
[35] M. Zaiser, P. Hähner, Phys. Stat. Sol. B 199 (1997) 267.
[36] T. Wutzke, C. Schwink, Phys. Stat. Sol. A 137 (1993) 337.
[37] F. Springer, A. Nortmann, C. Schwink, Phys. Stat. Sol. A 170 (1998) 63.
[38] A.S. Argon, Acta Metall. 27 (1979) 47.
[39] M.W. Chen, Annu. Rev. Mater. Res. 38 (2008) 445.
[40] C.A. Pampillo, J. Mater. Sci. 10 (1975) 1194.
[41] Y.J. Huang, J. Shen, J.F. Sun, Z.F. Zhang, Mater. Sci. Eng. A 498 (2008) 203.
[42] K.M. Flores, D. Suh, R.H. Dauskardt, P. Asoka-Kumar, P.A. Sterne, R.H. Howell, J. Mater. Res. 17 (2002) 1153.
[43] F. Spaepen, Acta Metall. 25 (1977), 407.
[44] A. Concustell, J. Sort, G. Alcalá, S. Mato, A. Gebert, J. Eckert, M.D. Baró, J. Mater Res. 20 (2005) 2719.
[45] R. Bhowmick, R. Raghavan, K. Chattopadhyay, U. Ramamurty, Acta Mater. 54 (2006) 4221.
[46] A. Inoue, W. Zhang, T. Tsurui, A.R. Yavari, A.L. Greer, Philos. Mag. Lett. 85 (2005) 221.
[47] J. Das, M.B. Tang, K.B. Kim, R. Theissmann, F. Baier, W.H. Wang, J. Eckert, Phys. Rev. Lett. 94 (2005) 205501.
[48] C.W. Passchier, R.A. Trouw, Microtectonics, Berlin: Springer Verlag (1996), p. 289.
[49] S.H. White, S.E. Burrows, J. Carreras, N.D. Shaw, F.J. Humphreys. J. Struct. Geol. 2 (1980) 175.
[50] B.E. Schuster, Q. Wei, M.H. Ervin, S.O. Hruszkewycz, M.K. Miller, T.C Hufnagel, K.T. Ramesh, Scr. Mater. 57 (2007) 517.
[51] M.E. Siegrist, E.D. Amstad, J.F. Löffler, Intermetallics 15 (2007) 1228.

5 Deformation kinetics and their constitutive modelling

Based on the experimental findings presented in Chapter 4 and additional kinetic parameters such as activated shear deformation volumes and energies derived in Section 5.2, a thermally-activated constitutive deformation model for metallic glasses was developed and is presented in Section 5.3[1]. Despite the absence of dislocation-based deformation mechanisms, amorphous metals show close phenomenological similarities to the dynamic strain aging effect known for crystalline solids. In this respect the constitutive model described below follows certain concepts originally developed in the framework of dynamic strain aging. Section 5.4, finally, discusses the implications and experimental validation of the newly-developed deformation model.

[1] 1) A. Dubach, F. H. Dalla Torre, J.F. Löffler, *Philosophical Magazine Letters* **87** (2007) 695.
2) A. Dubach, F.H. Dalla Torre, J.F. Löffler, *Acta Materialia* **57** (2009) 881.

5.1 Introduction

Many early investigations on metallic glasses provided important information for the characterisation of inhomogeneous flow behaviour in amorphous metals [1,2,3,4]. One of the first experiments to tackle the inhomogeneous flow kinetics in metallic glasses showed preferential etching of shear bands in deformed samples and demonstrated that pre-existing shear bands are reactivated more easily than new ones are formed – a clear indication of a modification of the atomic structure during deformation [2]. In addition, a change in the serration amplitude with increasing strain was observed and associated with different stages of deformation [1]. The temperature dependence of the appearance and the disappearance of serrations observed in a stress-strain diagram were explained with an adiabatic shear model proposed by Chen and Leamy [1,5]. In this model a sufficiently high temperature is needed for the shear event to initiate a local decrease in viscosity and result in an overall drop in the stress, i.e. serrated flow. Today, however, pure adiabatic shear is regarded as rather unlikely.

More recent studies on the plastic deformation behaviour of metallic glasses have mainly been performed by nanoindentation, where instabilities and early failure are not as critical as in compression or bending [6,7,8,9,10]. These investigations reveal a decrease in the serration amplitude ("pop-ins") with increasing indentation rate. The tests indicate that shear-band formation not only causes a sudden decrease in the load, i.e. a local stress drop, but actively contributes to plastic deformation by a shear offset of up to several tens of nanometres. Based on the observed disappearance of "pop-ins", which implies a transition from discrete to continuous shearing, Schuh *et al*. [11] proposed a new homogeneous deformation regime which is kinetically driven by the superior rate of deformation compared to the rate of shear-band nucleation. This simultaneous operation of multiple shear bands at higher rates leads to a spatially more homogeneous flow. In contrast to Ref. [1] the load drop/displacement burst which occurs during shear-band formation has been rationalised by STZs, which percolate to a fast-running shear band once a critical number of nuclei have been activated [11].

Our work basically builds on the early experiments undertaken in Refs. [1,2,3,4], but it also benefits from existing knowledge and theories of dislocation-mediated plasticity in crystalline materials (e.g. [12,13,14,15]). As briefly touched upon in Chapter 4, the

inhomogeneous deformation behaviour of metallic glasses shows close phenomenological similarities to the inhomogeneous deformation characteristics of crystalline solid solution metals undergoing strain aging effects (DSA). Note that despite the highly inhomogeneous flow associated with DSA, constitutive laws of thermal activation can be used to characterise the deformation kinetics. In dislocation theories the shear stress, τ, which arises when applying a force on a specimen, is generally regarded as the sum of two sources by

$$\tau = \tau_{\mathrm{at}} + \tau_{\mathrm{eff}}\,, \tag{5.1}$$

with τ_{at} being the athermal long-range internal stress caused by grain boundaries and other obstacles and τ_{eff} being the effective thermal stress. The thermal stress contribution arises when glide dislocations overcome short-range obstacles by a thermal activation process involving only a small number of atoms. Although τ_{eff} is usually a (small) fraction of τ it entirely accounts for the strain-rate and temperature dependency of τ. If ΔG is the free activation energy needed to overcome these obstacles, the shear strain rate $\dot{\gamma}$ can be written as

$$\dot{\gamma} = \dot{\gamma}_0 \exp\left(-\frac{\Delta G}{k_{\mathrm{B}} T}\right) = \dot{\gamma}_0 \exp\left(-\frac{\Delta G_0 - V\tau_{\mathrm{eff}}}{k_{\mathrm{B}} T}\right), \tag{5.2}$$

where $\dot{\gamma}_0$ is a characteristic strain rate depending on the attempt frequency of the process. The free activation energy is equal to the difference between the total energy barrier ΔG_0 and the work performed by the effective stress τ_{eff} on a volume V. In order to gain information about the rate-controlling process, ΔG is often not considered, but instead its derivate with respect to τ_{eff}, i.e. the activation volume V.

In the framework of shear transformation zone (STZ) mediated deformation in metallic glasses similar thermally-activated expressions for the plastic shear rate are widely used. Given that a STZ has a volume Ω_0, Argon [16,17] calculated the total energy barrier for the activation of a shear transformation as

$$\Delta G_0 = \left[\frac{7-5\nu}{30(1-\nu)} + \frac{2(1+\nu)}{9(1-\nu)}\beta^2 + \frac{\hat{\tau}}{2\gamma_0 \mu(T)}\right]\mu(T)\gamma_0^2\Omega_0\,, \tag{5.3}$$

where ν is the Poisson's ratio, $\hat{\tau}$ is the ideal shear resistance of a STZ (i.e. the shear stress that has to be overcome without thermal activation at $T = 0$ K), $\mu(T)$ is the temperature-dependent shear modulus and γ_0 is the characteristic strain of a STZ on the order of ~0.1.

The parameter β describes the ratio of volumetric dilatation to the shear strain, and is about equal to unity for metallic glasses. Based on the work of Eshelby [18] and Argon [16], and merging the STZ picture with the concept of potential energy landscapes [19], a cooperative shear model was recently developed to describe the plastic yielding in metallic glasses as a function of temperature [20]. There the total energy barrier ΔG_0 of the unstrained system that must be surmounted in order to activate a STZ was given by

$$\Delta G_0 = (8/\pi^2)\gamma_c^2 \zeta \Omega_0 \mu , \tag{5.4}$$

where μ is the shear modulus (of the unstressed material), γ_c the critical yield strain, Ω_0 the actual volume of the STZ and ζ a correction factor (≈ 3). This total energy barrier implies the material's dependence on temperature and configurational state via the variables μ and Ω_0 and scales with the yield stress via $\tau_y = \gamma_c \mu$ (i.e., Hooke's law).

In this respect Eqs. 5.3 and 5.4 allow a description of the total energy barrier (and consequentially of the flow stress), but do not account for the flow characteristics after yielding (serrated and non-serrated) and the observed negative strain-rate sensitivity, as described in Chapter 4. Irrespective of the model chosen, it is expected that the mechanical behaviour of BMGs is intrinsically dependant on the actual STZ volume Ω_0. Assessment of the sizes of STZs is thus of key importance in understanding the plastic deformation of BMGs. Recent molecular dynamics (MD) simulations [21,22,23] have quantitatively evaluated the number of atoms in a STZ of glassy materials. However, with the single exception of Ref. [24], experimental quantitative measurements of STZ volumes at temperatures significantly below the glass transition temperature are missing. In this chapter a constitutive framework of inhomogeneous flow is developed and kinetic state variables, such as activation volume, STZ volume and strain-rate sensitivity, are determined. Finally, the implications and validation of the newly-developed model are discussed in light of additional experimental findings and data from very recent literature reports.

5.2 Strain-rate sensitivity and activation volume

Provided that the strain rate follows an Arrhenius-type law, as given in Eq. 5.2 and also assumed by Argon [16], the thermally activated component of plastic deformation is generally expressed in terms of the (effective) activation volume

$$V = -\frac{\partial \Delta G(\tau_{\text{eff}})}{\partial \tau_{\text{eff}}}, \tag{5.5}$$

where ΔG is the minimum Gibbs free energy that has to be supplied to operate a STZ at a given temperature, and τ_{eff} is the thermal (or effective stress) component of the applied stress τ. It should be noted that in the framework of rate theory the activation volume is a measure for overcoming an "obstacle" (i.e., energy barrier) for a certain strain rate and time, so that it depends solely on the effective stress. Using the stress change $\Delta\sigma$ upon a change of the strain rate $\dot{\varepsilon}$ in a strain-rate jump test, an apparent activation volume can be calculated according to

$$V_{\text{ap}} = \alpha k_{\text{B}} T \frac{\Delta \ln \dot{\varepsilon}}{\Delta \sigma}, \tag{5.6}$$

where α is a constant accounting for the conversion from shear (τ) to normal stress (σ) and k_{B} is the Boltzmann constant. For a shear angle of ~42° for Vit105 [25], $\alpha = 2.01$. The apparent activation volume V_{ap}, determined by strain-rate change tests, only coincides with the effective activation volume V if the stress dependence of the pre-exponential term $\dot{\gamma}_0$ in Eq. 5.2 is negligible and the applied stress change entirely reflects the change in the effective stress τ_{eff} [26] (this is further discussed in Section 5.2.1). Difficulties in determining the apparent activation volume arise if there is a transient behaviour of the stress subsequent to the strain-rate change (cf. Fig. 4.13). In this case, two apparent activation volumes may be computed according to Eq. 5.6 which correspond to the instantaneous change in the flow stress ($\Delta\sigma_{\text{i}}$) and the change in the steady-state stress ($\Delta\sigma_{\text{s}}$), respectively. In this work the apparent activation volume is calculated using $\Delta\sigma_{\text{i}}$ (i.e. peak stress) as it more closely reflects the change in stress as a function of strain rate without changing the internal structure, which is a prerequisite for a valid evaluation of V_{ap} [26]. At temperatures below 200 K, however, the instantaneous stress change is nearly the same as the change in the steady-state stress, and therefore either may be used to calculate the apparent activation volume at $T < 200$ K.

The SRS and the apparent activation volume at 77 K are shown in Fig. 5.1 as a function of the mean strain rate ($\dot{\varepsilon}_{mean} = (\dot{\varepsilon}_1 + \dot{\varepsilon}_2)/2$). The SRS at 77 K decreases logarithmically with increasing mean strain rate, while the apparent activation volume correspondingly increases logarithmically with increasing mean strain rate. The calculated apparent activation volumes are on the order of 0.13–0.23 nm^3 in the strain-rate range of 5×10^{-5} – 5×10^{-2} s^{-1}. Assuming a characteristic STZ strain γ_0 of ~0.1 yields a characteristic STZ volume on the order of 1.3–2.3 nm^3, corresponding to about 70–130 atoms, when using an average Goldschmidt radius of 0.16 nm.

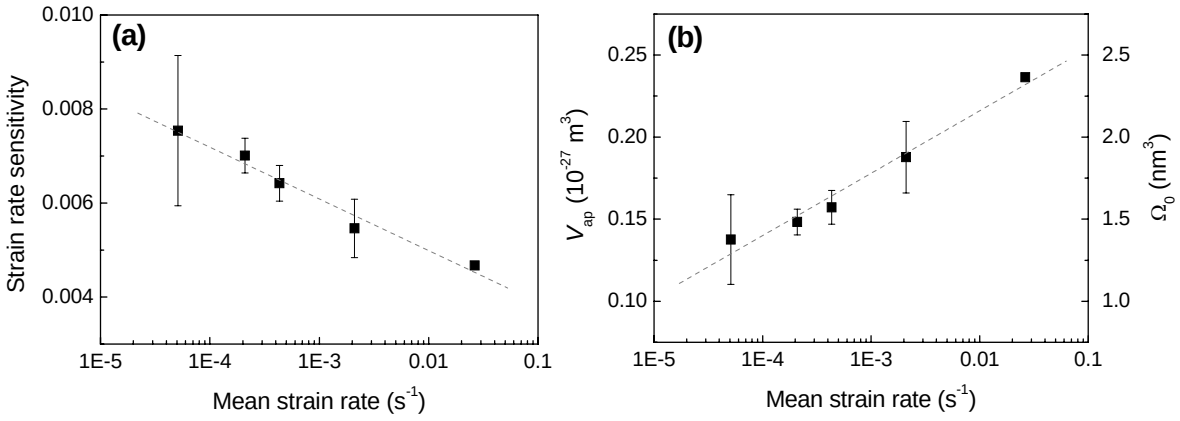

Fig. 5.1: (a) Strain-rate sensitivity and (b) apparent activation volume V_{ap} and characteristic STZ size Ω_0 for Vit105 as functions of mean strain rate at $T = 77$ K (using $\gamma_0 = 0.1$).

Figure 5.2 shows the apparent activation volumes for Vit105 as a function of the testing temperature, calculated from strain-rate jump tests with $\dot{\varepsilon}_1 = 7.33 \times 10^{-4}$ s^{-1} and $\dot{\varepsilon}_2 = 6.67 \times 10^{-5}$ s^{-1} (the values at temperatures above 600 K are derived from strain-rate jump tests with $\dot{\varepsilon}_1 = 1.33 \times 10^{-4}$ s^{-1} and $\dot{\varepsilon}_2 = 6.67 \times 10^{-5}$ s^{-1}). In the spatially inhomogeneous flow regime below 195 K the activation volume appears to increase exponentially from about 0.15 nm^3 at 77 K to 3.6 nm^3 at the transition temperature of 195 K (corresponding to a STZ volume of about 2000 atoms). In the spatially and temporally inhomogeneous flow regime (195 K < T < 600 K) an accurate calculation of the activation volume via strain-rate change tests is hindered due to either the presence of serrations, which impede accurate determination of the instantaneous stress change (resulting in a large error bar at 300 K), or the absence of any significant plastic deformation (between 350 K and 600 K).

Nonetheless, the results reveal that the relaxation processes present in this deformation regime generate a significant increase in the apparent activation volume. Interestingly, the activation volumes in the homogeneous flow regime at temperatures above 600 K are again on the order of 0.1 nm^3, comparable to the value determined at 77 K. The order of magnitude of the derived apparent activation volumes indicates clearly that deformation is not governed by a single hopping (diffusion) process but by the collective motion of several tens/hundreds of atoms as proposed in the framework of the STZ theory [16].

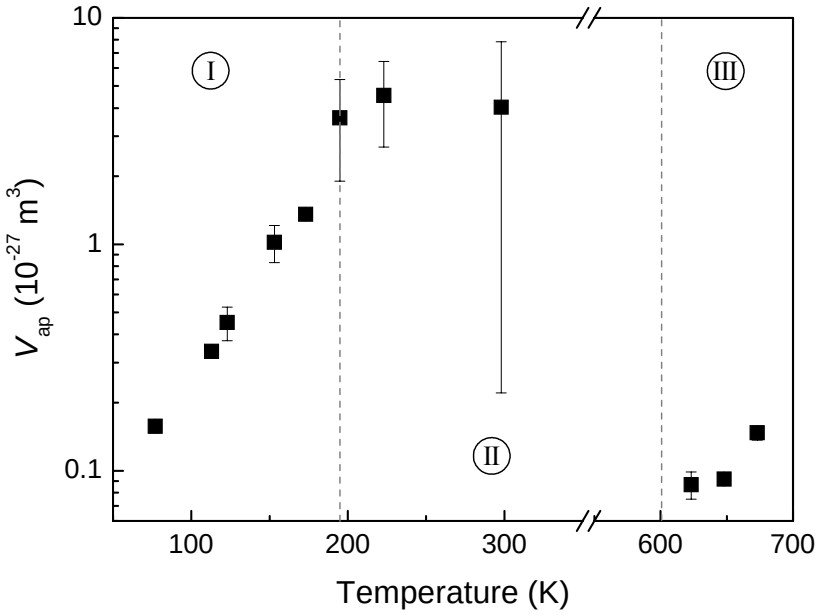

Fig. 5.2: Apparent activation volumes for Vit105 as a function of temperature, calculated from strain-rate jump tests with $\dot{\varepsilon}_1 = 7.33 \times 10^{-4}$ s^{-1} and $\dot{\varepsilon}_2 = 6.67 \times 10^{-5}$ s^{-1} (and $\dot{\varepsilon}_1 = 1.33 \times 10^{-4}$ s^{-1} and $\dot{\varepsilon}_2 = 6.67 \times 10^{-5}$ s^{-1} at temperatures above 600 K, respectively). I: spatially inhomogeneous deformation (non-serrated) and positive SRS; II: spatially and temporally inhomogeneous flow (serrated) and negative SRS; III: homogeneous deformation and positive SRS.

5.2.1 Apparent and effective activation volume

This sub-section briefly discusses the relationship between effective and apparent activation volume and the coherency of our analysis. The quantitative investigation of the implications is restricted to our experimental results obtained at liquid nitrogen temperatures, because of the extensive amount of data measured at this temperature and the relative ease of the analysis due to the absence of serrations and structural relaxation.

From Eq. 5.2, the free activation energy can be deduced as $\Delta G = -k_B T \ln(\dot{\varepsilon}/\dot{\varepsilon}_0)$. With the general definition of the effective activation volume $V = -\frac{\partial \Delta G(\tau_{eff})}{\partial \tau_{eff}}$ and the conversion from shear to normal stress (i.e. $\tau = \sigma/\alpha$) this yields for a given temperature

$$V = \alpha k_B T \left(\frac{\partial \ln(\dot{\varepsilon}/\dot{\varepsilon}_0)}{\partial \sigma_{eff}} \right) = \alpha k_B T \left(\frac{\partial \ln \dot{\varepsilon}}{\partial \sigma} - \frac{\partial \ln \dot{\varepsilon}_0}{\partial \sigma} \right) \frac{\partial \sigma}{\partial \sigma_{eff}} . \tag{5.7}$$

Assuming that an applied stress change entirely reflects the change in the effective stress (i.e. $\partial\sigma / \partial\sigma_{eff} = 1$), only the first term of Eq. 5.8 is accessible by strain-rate change tests. This term is commonly taken as the apparent activation volume, $V_{ap} = \alpha k_B T \frac{\partial \ln \dot{\varepsilon}}{\partial \sigma}$. From Eq. 5.7 it also becomes evident that effective and apparent activation volume only coincide if the stress dependence of the pre-exponential term $\dot{\varepsilon}_0$ is negligible (i.e. $\partial \ln \dot{\varepsilon}_0 / \partial \sigma = 0$).

By using the definition of the strain-rate sensitivity (m) and $\partial \sigma = \sigma \partial \ln \sigma$ one obtains

$$V_{ap} = \frac{\alpha k_B T}{m \sigma} , \tag{5.8}$$

i.e. the apparent activation volume is inversely proportional to the strain-rate sensitivity and the (flow) stress. As shown in Fig. 5.3, re-plotting of the liquid-nitrogen temperature data of Fig. 5.1 confirms the relationship derived in Eq. 5.8. The obtained slope of the linear fit (2.09×10^{-21} Nm) is in excellent agreement with the value of $\alpha k_B T = 2.13 \times 10^{-21}$ Nm, emphasising the inherent consistency of our analysis, and indicating that an Arrhenius-type law of deformation, on which V_{ap} is based, is justified.

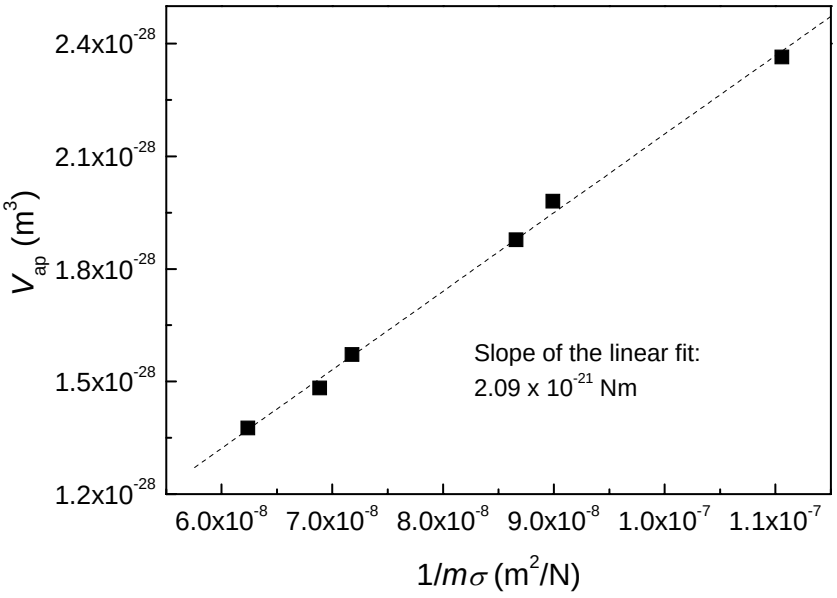

Fig. 5.3: Apparent activation volumes (V_{ap}) at 77 K as a function of the inverse product of strain-rate sensitivity (m) times flow stress (σ) for Vit105. The dashed line is a linear fit of the data.

As an alternative to strain-rate change tests the apparent activation volume can also be obtained by stress relaxation tests. If the relaxation curves exhibit a logarithmic decrease in the stress with time (as in our case it evidently does, as shown in Fig. 5.4) it can be fitted according to [27]

$$\Delta\sigma = -\frac{\alpha k_B T}{V_{ap}} \ln\left(1+\frac{t}{c}\right), \tag{5.9}$$

where V_{ap} is the activation volume and c is a time constant.

In addition, using the successive relaxation procedure described in Refs. [28,29] the apparent activation volume (V_{ap}) and the effective activation volume (V) can be related according to $V_{ap} = \Omega V$, where Ω is a correction factor, i.e.

$$\Omega(n) = \left[1 - \frac{k_B T}{V_{ap}\sum_{i=1}^{n-1}\Delta\tau_i} \ln\left(\frac{\exp\left(-\frac{\Delta\tau_n V_{ap}}{k_B T}\right)-1}{\exp\left(-\frac{\Delta\tau_1 V_{ap}}{k_B T}\right)-1}\right)\right]^{-1}, \tag{5.10}$$

where n is the number of relaxations, V_{ap} is the activation volume of the first relaxation determined according to Eq. 5.9, and $\Delta\tau_i$ is the stress drop of the relaxation number i.

An example of two series of successive (compression) relaxation tests performed on a Vit105 specimen (right after yielding and after ~2 % plastic deformation) at $T = 77$ K is shown in Fig. 5.4. Fitting of the first relaxations of the two series according to Eq. 5.9 yields $V_{ap} = 70$ Å^3 and $V_{ap} = 121$ Å^3, respectively.

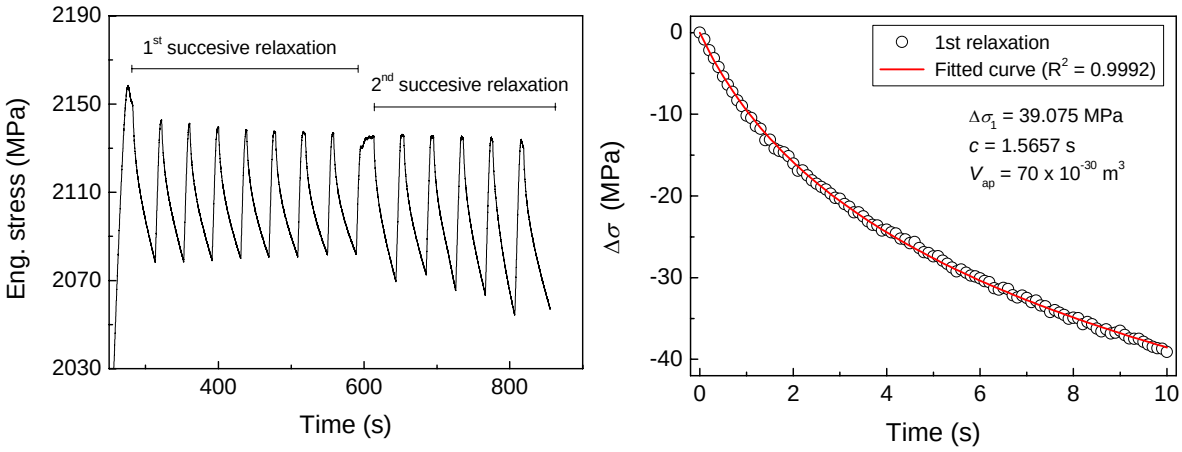

Fig. 5.4: Two successive stress relaxation tests on a Vit105 specimen at liquid-nitrogen temperature (loading at a strain rate of 3×10^{-4} s^{-1}) (left) and fitting of the initial 10 seconds of the first relaxation according to Eq. 5.9 (right).

The reason for the smaller apparent activation volume at yielding (70 Å^3) compared to the value of ~120 Å^3 during further deformation may be the slight overshoot (i.e. transient behaviour due to the formation of incipient shear bands) present at the beginning of the plastic deformation, while at higher plastic strains deformation may become easier due to (partial) reactivation of existing shear bands. Nevertheless, assuming a mean strain rate during stress relaxation in the specimen of $\dot{\varepsilon}_{mean} \approx \Delta\sigma / E\Delta t \approx 3.5 \times 10^{-5}$ s^{-1} the determined value of 70–120 Å^3 is in good agreement with the apparent activation volumes obtained from strain-rate change tests (cf. Fig. 5.1b) for such low strain rates. Note that this an important aspect because during shearing in strain-rate jump tests the shear band is activated, while during relaxation this is not necessarily the case.

Detailed analysis of the successive relaxation tests in Fig. 5.4 reveals that the correction factor (Eq. 5.10) is very close or equal to unity (i.e. $\Omega = 1.03$ and $\Omega = 1.00$, respectively) and therefore $V_{ap} \cong V$. Conclusively, this indicates that (at least at low temperature) stress changes upon strain-rate changes entirely reflect changes in the effective stress, and that the pre-exponential term in Eq. 5.2 can be considered as constant, indicative of a stable microstructure.

5.2.2 Thermal and athermal stress

In dislocation theories the shear stress necessary to deform a material is usually decomposed into a thermal component τ_{eff} and an athermal stress τ_{at} so that $\tau = \tau_{at} + \tau_{eff}$. The athermal long-range internal stress caused by grain boundaries and other obstacles should not depend significantly on temperature, but rather on strain [27]. Although the thermal component is usually a small fraction of the shear stress it entirely accounts for the strain-rate and temperature dependency of the latter. It arises from glide dislocations overcoming short-range obstacles by thermal activation processes involving only a small number of atoms. In literature various methods of determining the internal stress exist, such as stress-relaxation and stress-reduction experiments, and methods using estimates of the temperature dependence of the yield stress or the strain-rate dependence of the flow stress (a review of the most common methods can be found in Ref. [30]).

The situation in metallic glasses has not been so fully characterised and understood. It is generally assumed that the basic mechanism of deformation (i.e. STZ activity) is thermally activated. Experimental observations on colloidal glasses [31] and simulations on amorphous metals [21,23] have shown that highly-localised structural rearrangements can be induced by thermal fluctuations and consequently that under the application of shear STZs are caused by thermally induced strain fluctuations. The athermal stress component in metallic glasses might then be considered as originating from the long-range resistance of the microstructure to deformation, e.g. to the formation of shear bands. Experimental investigations on BMGs into this issue, however, are scarce, especially in the inhomogeneous deformation regime (i.e. at temperatures at or below room temperature). Therefore, in order to validate whether the flow stress of metallic glasses is composed of a thermal and an athermal component and to get an idea of the magnitude of the latter, stress

relaxation tests at different temperatures were performed. For this purpose cylindrical Vit105 specimens with diameters of 3 mm and heights of 5 mm were loaded at a constant strain rate of 3.3×10^{-4} s^{-1} until their flow stresses were reached. Deformation was then stopped and the stress relaxation measured for about 300 s. Note that the relaxation rate typically reached zero before 100 s. Fig. 5.5 summarises the total stress relaxation as a function of temperature, corrected for the relaxation of the testing machine. The stress relaxation is about 50 MPa at 77 K and decreases with increasing temperature, and at ~220 K it becomes negligibly small. Note that this is in good agreement with the transition temperature from serrated to non-serrated flow (cf. Fig. 4.12).

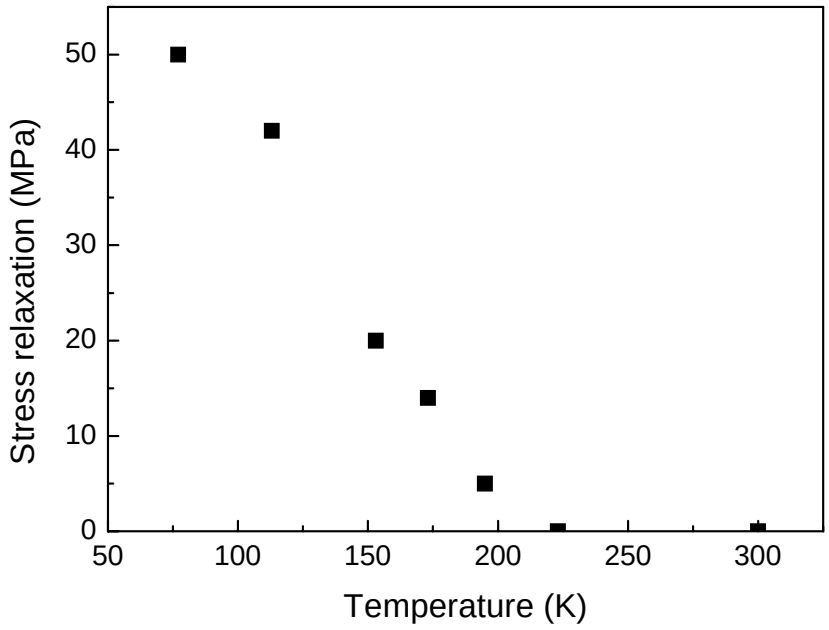

Fig. 5.5: Stress relaxation as a function of temperature for Vit105.

The results in Fig. 5.5 reveal that (i) the macroscopic flow stress of metallic glasses can be regarded as the sum of a thermal and an anthermal component; (ii) the thermal component is much smaller than the athermal stress; and (iii) the thermal component decreases with increasing temperature and flow becomes apparently athermal at temperatures above ~220 K. This apparently athermal behaviour, however, only arises due to inadequacies inherent in the test method. As pointed out e.g. in Refs. [32,33] stress relaxation tests only reveal accurate estimates of the thermal stress component if the microstructure does not change during the experiment. In our case it can be assumed that at

temperatures above ~200 K the microstructure evolves with time. This means that structural relaxation processes lead to a strengthening of the distorted structure and overlie the stress relaxation. Similarly, the structural relaxation leads to a negative asymptotic strain-rate sensitivity at temperatures above 200 K, as shown in Chapter 4.

Nevertheless, the stress relaxation experiments on Vit105 show that the treatment of composing the flow stress of an athermal and a thermal component seems justified.

5.3 Constitutive modelling

Based on the experimental findings presented in Chapter 4 and the preceding sections, this section summarises the similarities between the deformation characteristics of BMGs and crystalline alloys undergoing dynamic strain aging (DSA). Additional results on the deformation kinetics are presented, and finally a constitutive formalism is developed which enables a quantitative description of the (inhomogeneous) deformation characteristics of BMGs.

5.3.1 Deformation characteristics and similarities to the DSA effect

The change in the SRS from positive ($T < 195$ K) to negative values ($T > 195$ K) indicates a change in the micromechanism of flow, despite the fact that deformation still proceeds by shear banding. It also provides evidence that the disappearance of serrations at low temperatures or high strain rates is a true material response and does not result from instrumental artefacts (i.e. lack of resolution) or simply from the simultaneous activation of multiple shear bands. The correlation between the disappearance of serrated flow below a critical temperature and a change in the SRS from negative to positive values is also known from the dynamic strain aging (DSA) phenomena in crystalline metals, where macroscopically the flow instabilities are referred to as the Portevin-Le Châtelier (PLC) effect and associated with the formation of PLC- or Lüders bands [34,35,36].

According to the DSA model [34,37,38,39,40] the physical origin of such instabilities is in the dynamic interactions between fast-diffusing solute atoms and mobile dislocations. While a mobile dislocation is temporally arrested at localised obstacles (particularly forest dislocations), solute atoms diffuse along the core of the dislocations such that the obstacle strength increases as the waiting time increases, resulting in higher flow stresses at lower strain rates (i.e., negative SRS). The competing processes of aging (by solute atom diffusion) and thermally-activated unpinning of dislocations from their solutes manifests itself in the observable jerky flow behaviour. Typically, crystalline solids exhibiting the PLC effect show for the transition from serrated to non-serrated flow an activation energy (Q_{DSA}) that is less than the activation energy for volume diffusion (Q_D) of the alloying elements ($Q_{DSA}/Q_D \approx 0.3–0.7$). This discrepancy is explained by a pipe-diffusion process along the dislocation cores [41]. A similar trend was observed in the present study for Vit105: the activation energy derived for the onset of serrated flow ($Q = 0.37$ eV) is significantly lower than the activation energies for volume diffusion in Zr-based BMGs for a variety of the constituent elements (0.8–4.0 eV [42,43]). Note that despite the differences in the underlying mechanisms responsible for serrated flow behaviour, the activation energy, Q, derived in the present study for a metallic glass, represents a quantity comparable to Q_{DSA} for crystalline materials.

Other phenomenological similarities between the deformation behaviour of metallic glasses and crystalline materials displaying DSA can also be observed: for example, as quantitatively analyzed in Chapter 4, the magnitude of the stress drops and the waiting time between two serrations increase with increasing strain and decreasing strain rate, respectively. The increase in the stress drop accompanies a slight decrease in the SRS with strain at room temperature (see also Fig. 5.10a discussed later). In DSA-deforming alloys such behaviour was explained by considering the stress relaxation in the vicinity of a shear band [44]. An overview of the manifestations of dynamic strain aging in crystalline alloys is shown in Fig. 5.6 for comparison. The loss of ductility that usually accompanies the DSA is also observed in amorphous alloys: as shown in Fig. 5.7a, the plastic strain to failure of Vit105 is significantly reduced in the deformation regime (II) where serrated flow prevails. Additionally, DSA generates an increase in the flow stress, producing a deviation from the monotonically decreasing trend of the flow stress with increasing temperature [36,45] (“hump” in the temperature-dependence of the flow stress in the negative SRS regime). A similar trend is visible in Fig. 5.7b. Note that compared to Fig. 4.8b a larger temperature

range with more data points was measured in this series of experiments, revealing a clear deviation from the $T^{2/3}$ law as proposed for BMGs in Ref. [20]. As pointed out in Section 5.2.2, structural relaxation processes responsible for this deviation lead to the apparent athermal behaviour of Vit105 observed at temperatures between ~200–400°C (i.e. temperature-independent normalised stress in Fig. 5.7b). And finally, DSA produces a local maximum in the temperature dependence of the apparent activation volume for deformation [45], which is similarly observed for Vit105 in Fig. 5.2 (regime II).

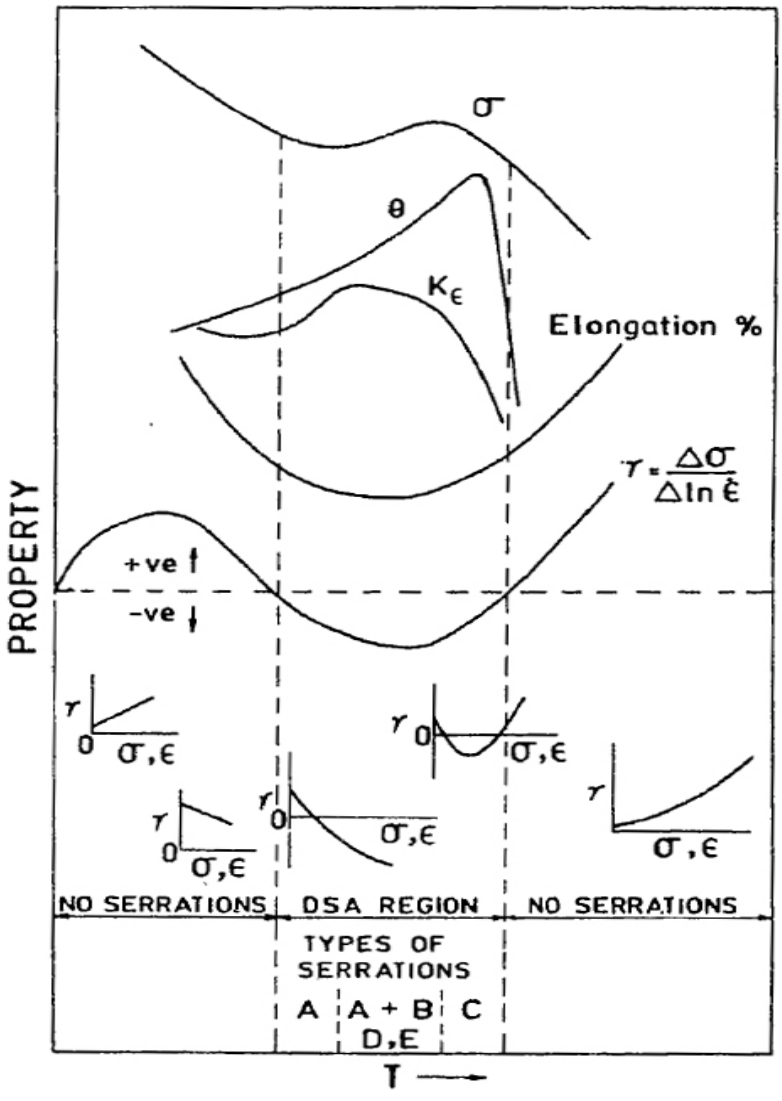

Fig. 5.6: Overview of dynamic strain aging effects in crystalline alloys. Schematically shown are the temperature dependence of the flow stress (σ), the work hardening (θ), the Hall-Petch slope (K_ε) and the strain-rate sensitivity (γ). The variation of γ with stress and strain at different temperatures, and the different types of serrations are also indicated. (Figure taken from [46].)

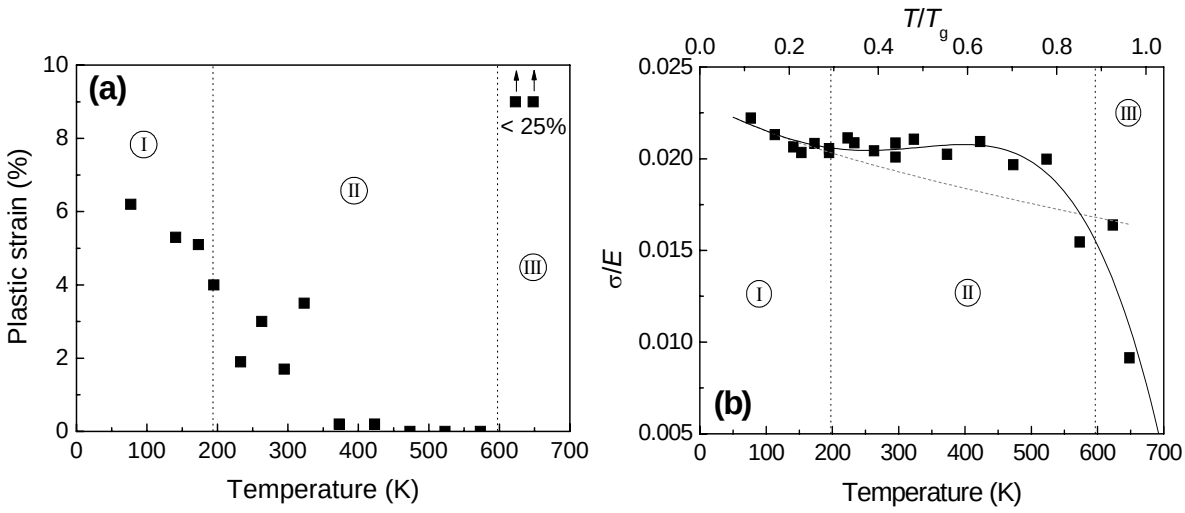

Fig. 5.7: (a) Plastic strain to failure and (b) normalised stress (i.e. maximum flow stress or fracture stress normalised to Young's modulus) for Vit105 at a strain rate $\dot{\varepsilon}_1 = 10^{-4}\,\mathrm{s}^{-1}$ as a function of temperature (and normalised temperature, respectively). I: spatially inhomogeneous deformation (non-serrated) and positive SRS; II: spatially and temporally inhomogeneous flow (serrated) and negative SRS; III: homogeneous deformation and positive SRS. The dashed line in (b) indicates the $T^{2/3}$-dependence of the stress; the solid line is a polynomial least squares fit of the data points.

In spite of the phenomenological analogies and the associated inhomogeneous deformation, the DSA model can obviously not be adapted to amorphous metals because it relies on dislocation-based mechanisms. Its framework, however, may provide a basis for refining the constitutive models of plastic flow in metallic glasses. As pointed out by Brechet and Estrin [47], strain-rate softening phenomena in short-range-ordered alloys may also occur in the absence of DSA. There, they can arise from the interplay between deformation-induced destruction of short-range order and diffusion-controlled re-ordering. Similarly, shear processes in BMGs are believed to increase the content of free volume [48,49,50] and locally destroy the short-range order within the shear bands, which makes them susceptible to preferential etching [2,51,52]. In this respect the disappearance of serrated flow and the observed change in the SRS value in BMGs can be explained by considering thermally-activated shear processes followed by time- and temperature-dependent relaxation or re-ordering, whose amount is determined by the time span (relaxation time) between two shear events in a shear band and the temperature, i.e. high strain rates and low temperatures favour the reactivation of existing shear bands. Similarly, the relaxation time or time required to rebuild stress and release it afterwards is lowered at high strain rates, and thus results in a smaller energy release during the shear event and

therefore a smaller stress drop. In contrast to the reasons proposed in Ref. [6] for the disappearance of pop-ins at high indentation rates, we show that the absence of serrated flow at high strain rates and/or low temperatures is caused by the inability of the shear band to relax (and thus to strengthen fast enough) rather than by the simultaneous activation of multiple shear bands.

5.3.2 Deformation kinetics, activation volume, and serration characteristics

While in crystalline solids plastic deformation processes such as dislocation glide/climb, diffusional creep and grain-boundary sliding are strongly influenced by the microstructure (grain size, dislocation density and impurities), the possibilities for varying the microstructure of BMGs are limited. Therefore the basic deformation mechanism can be anticipated to be the same for all temperatures and strain rates, namely STZ activity and redistribution of free volume [53]. The different macroscopic responses (e.g. anelasticity, homogeneous or inhomogeneous deformation and the varying strain-rate dependency of the flow stress) only arise because of different spatial distributions and temporal evolutions of these flow events.

At elevated temperatures (T close to T_g), where the characteristic period of structural relaxation (e.g., redistribution of free volume) is much shorter than the loading time, plastic flow is homogeneous (highly rate- and temperature-sensitive) and characterised by the strain accumulation of the stress-biased operations of local STZs [53]. The apparent activation volume V_{ap} of Vit105, derived in this study by strain-rate jump tests in the homogeneous flow regime, is on the order of $\sim 1 \times 10^{-28}$ m^3 (Fig. 5.2), resulting in a characteristic STZ volume of about 60 atoms. The value is in good agreement with other experimental measurements and simulations [16,20,22,23,54], where typical values between a few and roughly 100 atoms have been reported. The transient regime of stress overshoots/undershoots upon increasing/decreasing the strain rate (cf. Fig. 4.11) may be taken as an unbalanced condition of free-volume creation and relaxation. Steady-state deformation is only achieved after a transient structural evolution when the two rates have adapted to each other [53].

The apparent activation volume at 77 K (non-serrated regime) is on the same order of magnitude (1.5×10^{-28} m^3) as that of the homogeneous flow regime ($T > 600$ K), showing

the validity of the above-mentioned assumption that in metallic glasses there is only one single plastic flow mechanism (bearing in mind that the calculation of the activation volume assumes an exponential dependence of the strain rate on the activation volume according to Eq. 5.2. Increasing the temperature from 77 to 195 K (transition temperature from non-serrated to serrated flow) generates a significant increase in the apparent activation volume to $\sim 4 \times 10^{-27}$ m^3. At the same time the duration of a single serration significantly decreases with an increase in the temperature from 195 K to room temperature.

Table 5.1 summarises the characteristics of serrations that appear during deformation at different temperatures at strain rates of 10^{-4} s^{-1} (samples A and B) and 7×10^{-5} s^{-1} (sample C). While the amplitude of the stress drops decreases with decreasing temperature, both the duration and the size of the displacement bursts increase, as is similarly observed for the bulk metallic glass $Cu_{50}Zr_{50}$. It is worth noting that the duration of a shear event at 195 K, which for the applied strain rate is very close to the transition temperature from serrated to non-serrated flow for both Vit105 and $Cu_{50}Zr_{50}$, is on the order of 1–2 s and hence much longer than at room temperature. (Analogously, the smaller amplitude and longer duration of a stress drop at 195 K suggest a higher apparent viscosity during shearing in the shear band compared to the situation at room temperature [55].) The observations agree with the temperature dependence of the SRS in the temperature range of 195 K to room temperature (see Fig. 4.14). After the formation of an embryonic shear band, the negative SRS promotes the local strain rate in the fully operating shear band, since less stress is required to deform the material with increasing strain rate. This strain-rate softening instability results in a shorter shear event (e.g. 0.05–0.1 s at room temperature). Adjacent relaxation processes after the shear event then lead to a strengthening of the distorted structure and the material is strained elastically until the next shear event (serration) takes place. At temperatures below the transition from serrated to non-serrated flow (195 K), where the SRS becomes positive, the operation of an emerging shear band is impeded because higher stresses are required to deform the material at higher strain rates. Consequently an individual shear band evolves more continuously (longer times and smaller strain bursts) and no serrated flow is present. Our results also show clearly that a negative SRS is not imperative for the presence of shear bands. Shear banding can be regarded as a local *strain*-softening instability (i.e. due to the lack of strain hardening capacity of the material), whereas the presence of serrations is due to a *strain-rate*-softening instability.

Table 5.1: Serration characteristics of Vit105 specimens tested at different temperatures (T) at strain rates of 10^{-4} s^{-1} (samples A and B) and 7×10^{-5} s^{-1} (sample C). Δt is the duration, $\Delta\sigma$ is the stress drop and Δs is the displacement burst of a shear-banding event. The data acquisition rate was 20 Hz, and Δs was determined from the crosshead displacement.

Sample	T (K)	Δt (s)	$\Delta\sigma$ (MPa)	Δs (μm)
A	RT	0.05–0.1	20–40	0.35 ± 0.17
B	233	0.15–0.2	20–40	0.60 ± 0.19
C	195	1–2	10–20	0.71 ± 0.15

5.3.3 Constitutive model of inhomogeneous deformation

In the following a quantitative formalism describing the deformation behaviour is developed. Generally, the constitutive description relating the flow stress σ to the plastic strain ε and strain rate $\dot{\varepsilon}$ can be written in its differential form by [56]

$$\mathrm{d}\ln\sigma = \theta/\sigma\,\mathrm{d}\varepsilon + m\,\mathrm{d}\ln\dot{\varepsilon}, \tag{5.11}$$

where $\theta=(\partial\sigma/\partial\varepsilon)_{\dot{\varepsilon}}$ is the strain hardening coefficient and $m=(\partial\ln\sigma/\partial\ln\dot{\varepsilon})_{\varepsilon}$ is the strain-rate sensitivity. Eq. 5.11 implies that the flow stress responds instantaneously to changes in the strain rate. However, a strain-rate change is generally accompanied by stress transients (cf. Fig. 4.13). As discussed in Section 4.4 the instantaneous response of the flow stress upon an increase in strain rate is always positive, i.e., the instantaneous SRS $m_{\mathrm{i}}>0$ [40]. This is followed by an adjustment of the flow stress towards a new steady-state value where transients have died out and which is characterised by the asymptotic SRS m_{∞}. The transient behaviour can be taken into account by assuming that the flow stress depends on an additional variable, ϕ, describing the state of relaxation (or re-ordering) within the deformed material. A change in the order parameter, ϕ, results in a corresponding change in flow stress. However, ϕ cannot instantaneously assume its new steady-state value ϕ_0, but relaxes towards it within a characteristic time t_ϕ (see Fig. 4.12). Assuming that there is no strain hardening in metallic glasses (i.e. $\theta=0$), Eq. 5.12 can therefore be re-written as

$$\mathrm{d}\ln\sigma = m_i\,\mathrm{d}\ln\dot{\varepsilon} + \mathrm{d}\ln\sigma_\phi, \tag{5.12}$$

where $\mathrm{d}\ln\sigma_\phi$ accounts for the transient of the flow stress that results from the relaxation of ϕ. The asymptotic SRS is consequently

$$\mathrm{m}_\infty = m_i + \left.\frac{\partial \ln\sigma_\phi}{\partial \ln\dot{\varepsilon}}\right|_\varepsilon = m_i + \left.\frac{\partial \ln\sigma_\phi}{\partial \phi}\right|_{\varepsilon,\dot{\varepsilon}} \frac{\mathrm{d}\phi}{\mathrm{d}\ln\dot{\varepsilon}}, \tag{5.13}$$

i.e. the ϕ-dependence of the flow stress and the strain-rate dependence of ϕ determine whether the asymptotic SRS is positive or negative, as discussed in Chapter 4 and schematically depicted in Fig. 4.13.

Assuming that shearing in metallic glasses takes place via a thermally-activated operation of STZs, this structural relaxation towards ϕ_0 can equivalently be accounted for by incorporating an additional energy term Δg to the Arrhenius-type law for the plastic shear strain rate $\dot{\gamma}$ (cf. Eq. 5.2) [57,58], so that

$$\dot{\gamma} = \dot{\gamma}_0 \exp\left(-\frac{\Delta G_0 + \Delta g - V\tau_{\mathrm{eff}}}{k_\mathrm{B}T}\right), \tag{5.14}$$

with $\dot{\gamma}_0 = \alpha_0 \nu_0 \gamma_0$, where α_0 is a constant incorporating the fraction of material that is available to undergo shear transformation, ν_0 is a characteristic attempt frequency and γ_0 is the characteristic strain of a STZ. The free activation energy required for a shear transformation to occur (ΔG) is equal to the difference between the total energy barrier ($\Delta G_0 + \Delta g$) and the work performed by the effective shear stress τ_{eff} on the volume V, as shown in Fig. 5.8. In this framework the effective activation volume V is the product of the characteristic STZ volume times the shear strain assumed to be generated by one successful event, $\Omega_0\gamma_0$. The characteristic feature of this model approach is that the total energy barrier is considered as a dynamic variable: ΔG_0 is the total energy barrier of the unstressed system (e.g. Eqs. 5.3 and 5.4), and the internal variable Δg, which depends on temperature, strain and strain rate, accounts for the temporal evolution (structural relaxation) during the process of shearing and consequently for the presence/absence of serrations.

Serrated flow can be correlated with shear offsets of several hundred nanometres, while the shear of a single STZ is assumed to be on the order of nanometres. The process described here is believed to be a cooperative process where the operation of a single STZ creates an avalanche-type effect. The long-range elastic field of each STZ favours the activation of a new zone in its vicinity [31]. This finally adds up to (sub-)micrometer large

shear offsets and macroscopically results in shear bands with a different structure than the bulk. (Analogously, intermittent deformation phenomena such as spatial localisation of dislocation flow into slip bands are observed in single-crystal metals. Here for example, discontinuities (e.g. strain bursts) in stress-strain curves of single-crystal micropillars and resultant surface slip offsets [59] cannot stem from one single dislocation but might be perceived as a correlated event such as a collective motion of many dislocations [60]). For metallic glasses, at the moment where sufficient energy is provided (e.g. at yielding) autocatalytic/cooperative operation of numerous stress-assisted, thermally driven STZs may take place. This process results in a stress release, plastic strain and consequently the arrest of the shear band. The latter process triggers the annihilation of freshly produced free volume[2] and therefore causes a time-dependent hardening of the area in the vicinity of the shear band. The waiting time between two adjacent serrations causes the distorted structure, or macroscopically speaking the shear band, to recover and relax to a lower energy state (i.e. higher density due to free-volume annihilation), similar to the description in Refs. [61,,]. The rates of these counteracting processes, finally, determine the mechanical response of the metallic glass. Fig. 5.8a shows the energy barrier diagram for two successive shear events at low temperatures in the absence of relaxation (i.e. smooth deformation). It depicts the thermal energy barrier ΔG_0 which must be overcome with the help of the temperature- and strain-rate-dependent stress part $V\tau_{\mathrm{eff}}$ and the assistance of thermal agitation (grey and hatched areas in Fig. 5.8a). Here τ_{at} reflects the athermal stress contribution, which is equal to the internal stress. At $T = 0$ K all the energy would have to be provided by the applied stress in order to overcome ΔG_0, while at finite temperatures

[2] In the framework of the free-volume theory [62], for example, free volume is increased by a shear-stress-induced disordering process in which atoms squeeze into available free-volume sites and decreased by a diffusion-controlled reordering process in which the surrounding atomic cage collapses down on the newly open site. For applied shear stresses sufficiently large that the free-volume creation rate is greater than the annihilation rate, the net rate of change of the free volume, υ_{f}, can be expressed as [63]

$$\dot{\upsilon}_{\mathrm{f}} = \upsilon^{*} f \exp\left(-\frac{\Delta G^{\mathrm{m}}}{k_{\mathrm{B}}T}\right)\exp\left(-\frac{\alpha\upsilon^{*}}{\upsilon_{\mathrm{f}}}\right)\left\{\frac{2\alpha k_{\mathrm{B}}T}{\upsilon_{\mathrm{f}}S}\left[\cosh\left(\frac{\tau\Omega}{2k_{\mathrm{B}}T}\right)-1\right]-\frac{1}{n_{\mathrm{D}}}\right\},$$

where υ^{*} is the critical free volume required for an atomic jump, n_{D} is the number of jumps required to annihilate υ^{*}, ΔG^{m} is the activation energy for an atomic jump, τ is the applied shear stress, Ω is the atomic volume, f is the jump frequency, α_{g} is a geometrical factor on the order of 1, S is a material constant given by $(2/3)\mu((1+\nu)/(1-\nu))$, ν is Poisson's ratio, and μ is the shear modulus.
However, annihilation of free volume is only one manifestation and consequence of structural relaxation. In our model relaxation processes are considered to originate from structural ordering (i.e. enhanced local topological order and symmetry and local chemical order) as well as from the annihilation of free volume (i.e. small reduction in local atomic volume and increase in packing density).

thermal agitation contributes to the process. After a shear event has taken place, the configuration of the atomic structure in the shear band changes towards a less dense structure. This more disordered configuration reflects a structure of elevated potential energy and favours the reactivation of the same shear band. At higher applied strain rates the frequency of successful STZ activations must be higher and therefore for a given temperature the part provided by thermal agitation becomes smaller. This can be achieved only at the price of a higher flow stress (i.e. positive SRS). At higher temperatures > 200 K where relaxation processes are substantial (i.e. serrated flow) structural relaxation may alter the configuration of atoms in the shear band enough that the ground state of the energy barrier changes. Compared to the non-relaxed structure this generates a higher free energy for STZ activation and hence provokes a further increase in stress followed by stress drops (i.e. serrated flow behaviour). As shown in Fig. 5.8b, here an increase in the applied strain rate leads to both a decrease in the thermal agitation part and the total energy barrier. As a result, the flow stress is lower at higher strain rates (i.e. negative SRS).

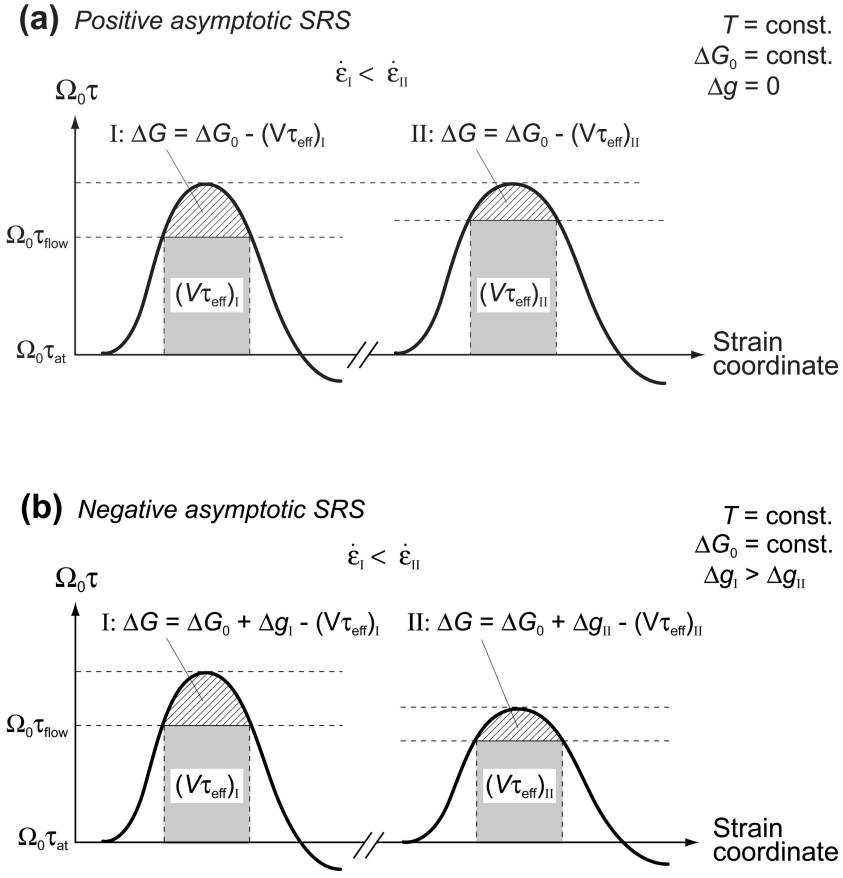

Fig. 5.8: Schematic energy barrier diagram for the activation of a STZ in the case of (a) a positive asymptotic SRS and (b) a negative asymptotic SRS for two different strain rates $\dot{\varepsilon}_{\mathrm{I}} < \dot{\varepsilon}_{\mathrm{II}}$.

Using $\sigma = \sigma_{\mathrm{at}} + \alpha\tau_{\mathrm{eff}}$ (where σ_{at} is the athermal stress, independent of temperature and strain rate) with τ_{eff} from Eq. 5.14 and the activation volume from Eq. 5.6, the asymptotic SRS yields

$$\mathrm{m}_{\infty} = m_i + \left.\frac{\partial \ln\sigma}{\partial \Delta g}\right|_{\varepsilon} \frac{\mathrm{d}\Delta g}{\mathrm{d}\ln\dot{\varepsilon}} = m_i\left(1 + \frac{1}{k_{\mathrm{B}}T}\frac{\mathrm{d}\Delta g}{\mathrm{d}\ln\dot{\varepsilon}}\right). \tag{5.15}$$

The similarity between Eq. 5.13 and Eq. 5.15 reveals that the introduced variable Δg indeed accounts for the state of relaxation and the dependence of the flow stress on the history of the plastic strain rate. Obviously the asymptotic SRS becomes negative if $\mathrm{d}\Delta g / \mathrm{d}\ln\dot{\varepsilon} < -k_{\mathrm{B}}T$.

The deformation process in metallic glasses is basically governed by thermally-activated shear transformations of atomic clusters (i.e. STZs) [16]. Its macroscopic appearance (temporal and spatial behaviour), however, is determined by the ratio between the rates of individual shear events and adjacent diffusive rearrangements within the dilated structure. The shear-induced disordering of the amorphous structure generates an increase in the free energy of the material, as schematically shown in Fig. 5.9. At low temperatures structural relaxations after a successful shear event are greatly hindered (i.e. Δg is equal/close to zero and hence the SRS is positive), and following shear transformations are favoured in the distorted zone, resulting in the formation of shear bands (since ΔG_0 of the following shear event is usually slightly reduced). The positive SRS retards the propagation of an operating shear band and consequently no abrupt strain bursts are present (non-serrated flow). At intermediate temperatures structural relaxations can take place, generating an increase in the height of the total energy barrier ($\Delta G_0 + \Delta g$) as shown in Fig. 5.9. A successful shear event causes a change in the configurational state within the shear band and hence lowers the instantaneous energy barrier for a successive shear event and Δg is reset to zero. Plastic deformation is then governed by the interplay of these counteracting effects, which lead macroscopically to serrated flow behaviour. In this respect, the transition from serrated to non-serrated flow (see boundary in Fig. 4.12) represents the lower energy limit for the onset of serrated flow where strain rate matches the rate of time-dependent relaxation. Hence, this transition is characterised by the two different states of Δg (either $\Delta g > 0$ or $\Delta g \to 0$) or consequently by a change of ΔG as a function of temperature and strain rate. Finally, at elevated temperatures where the characteristic rate of structural relaxation is much higher than the deformation rate (i.e. Δg

is independent of $\dot{\varepsilon}$), plastic flow can simply be regarded as structural relaxation governed by external stresses. The diffusive arrangements outweigh the free-volume accumulation, impede any strain localisations, and homogeneous deformation takes place.

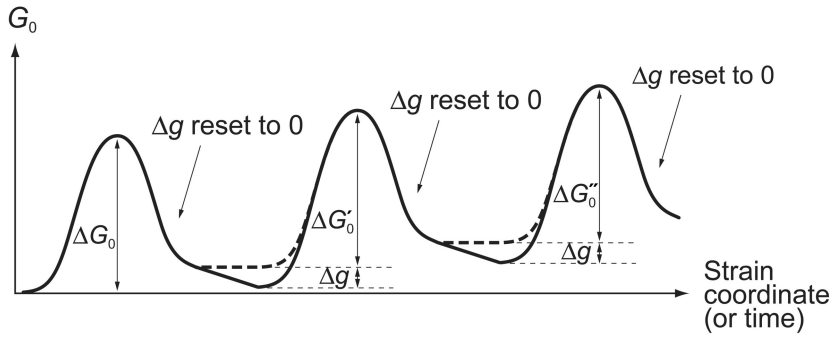

Fig. 5.9: Free energy diagram in the course of deformation for a shear event in the absence of structural relaxation (high $\dot{\varepsilon}$ or low T, dashed line) and in the presence of structural relaxation (low $\dot{\varepsilon}$ or high T, solid line). Note that the energy barrier ΔG_0 usually reduces slightly during the course of deformation (i.e. $\Delta G_0 \geq \Delta G_0' \geq \Delta G_0''$).

5.4 Implications and experimental validation

5.4.1 Influence of temperature and strain rate on the strain-rate sensitivity

Assuming that no geometrical changes in the sample occur (i.e. change in stress gradients), a progressive reactivation of an existing shear band is expected. Thus, a continuous propagation of microscopic shear events (i.e. STZs) increases the free volume or changes the atomic configuration within the shear bands, resulting in a lower-density structure compared to the undeformed material. The increase in the stress drop amplitude with increasing strain (see Fig. 4.6a) can be rationalised with this explanation. At low enough testing temperatures, where no serrations occur, fewer changes in the atomic structure within the shear bands can occur in the course of deformation due to reduced atomic mobility, i.e. the SRS is positive and remains constant with strain, as shown in Fig. 5.10a

for $Cu_{50}Zr_{50}$ BMG at $T = 77$ K. At room temperature, however, the SRS decreases slightly with strain, due to the fact that relaxation processes can take place more easily with proceeding plastic deformation. In Fig. 5.10b the average SRS is plotted as a function of temperature for different applied mean strain rates. A clear decrease in the SRS value from 0.008 at the slowest strain rate to values in the range of 0.002 at the highest strain rate is measured at $T = 77$ K. A similar, but much less pronounced, decrease in m with increasing $\dot{\varepsilon}$ can also be observed at $T = 153$ K. At room temperature and 195 K, in contrast, a change from negative values of m to slightly positive ones (at the highest strain rate) was measured, where the change in sign correlates with the disappearance of serrated flow, similar to the observations made on Vit105 (Fig. 4.14). At equal strain rates hardly any difference in m is measured for tests performed at 300 K compared to 195 K ($\Delta T \sim 100$ K), while a significantly larger difference in m is measured if tested at 77 K compared to 153 K ($\Delta T \sim 75$ K) for the same strain rates. This temperature dependence on the part of m at constant $\dot{\varepsilon}$ suggests (i) differences in the rate-dependent mechanisms governing shear banding at 300 K compared to 77 K, and (ii) a strongly time- and temperature-dependent process active at 77 K (in particular at low strain rates where differences are the highest), such as a diffusion-dependent mechanism that dominates the kinetic flow behaviour.

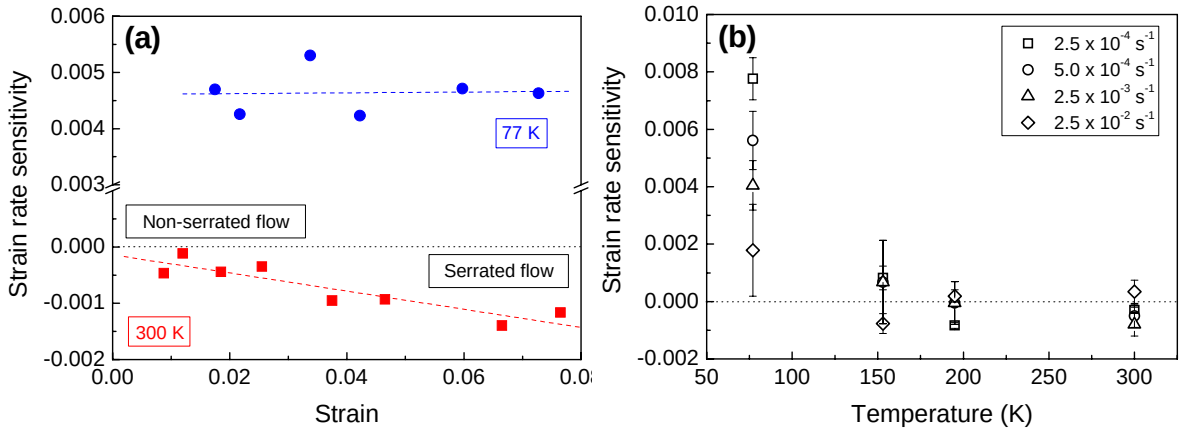

Fig. 5.10: Strain-rate sensitivity of $Cu_{50}Zr_{50}$ (a) as a function of strain for 300 K and 77 K measured at strain rates alternating between 10^{-3} and 10^{-4} s^{-1}, and (b) as a function of different mean strain rates applied for temperatures of 300, 195, 153 and 77 K. Note that at higher strain rates (>10^{-2} s^{-1}) data accuracy is lower due to the high speed of testing, which only allows one to two changes in the strain rate per test.

5.4.2 Shear band density measurements

A direct consequence of the model developed in Section 5.3.3 is that shear-band density should be lower at high strain rates and/or low temperatures because there no or little relaxation of the distorted structure in a shear band takes place and consequently the re-activation of an existing shear band is favoured. Indeed, optical microscopy analysis on the surface of compressed specimens (plastic deformation of ~1 %) confirms this. As shown in Fig. 5.11, at low temperatures ($T = 77$ K) only very few shear bands are present. At room temperature, however, significantly more shear bands are visible, and the density decreases with increasing strain rate. At the same time, analysis of the corresponding stress-strain curves indicate that at room temperature 25 ± 1 stress drops per 1 % plastic deformation are present, which implies an average displacement burst of 2 μm per serration. Quantitative measurements of the surface steps (i.e. shear offsets) on the deformed specimens by scanning laser profilometry confirmed the observations made: they revealed a decreasing number of shear bands (but with increased average shear offset) with decreasing temperature and/or increasing strain rate while the cumulative shear offset after 1 % plastic deformation remained roughly constant, irrespective of temperature and/or strain rate.

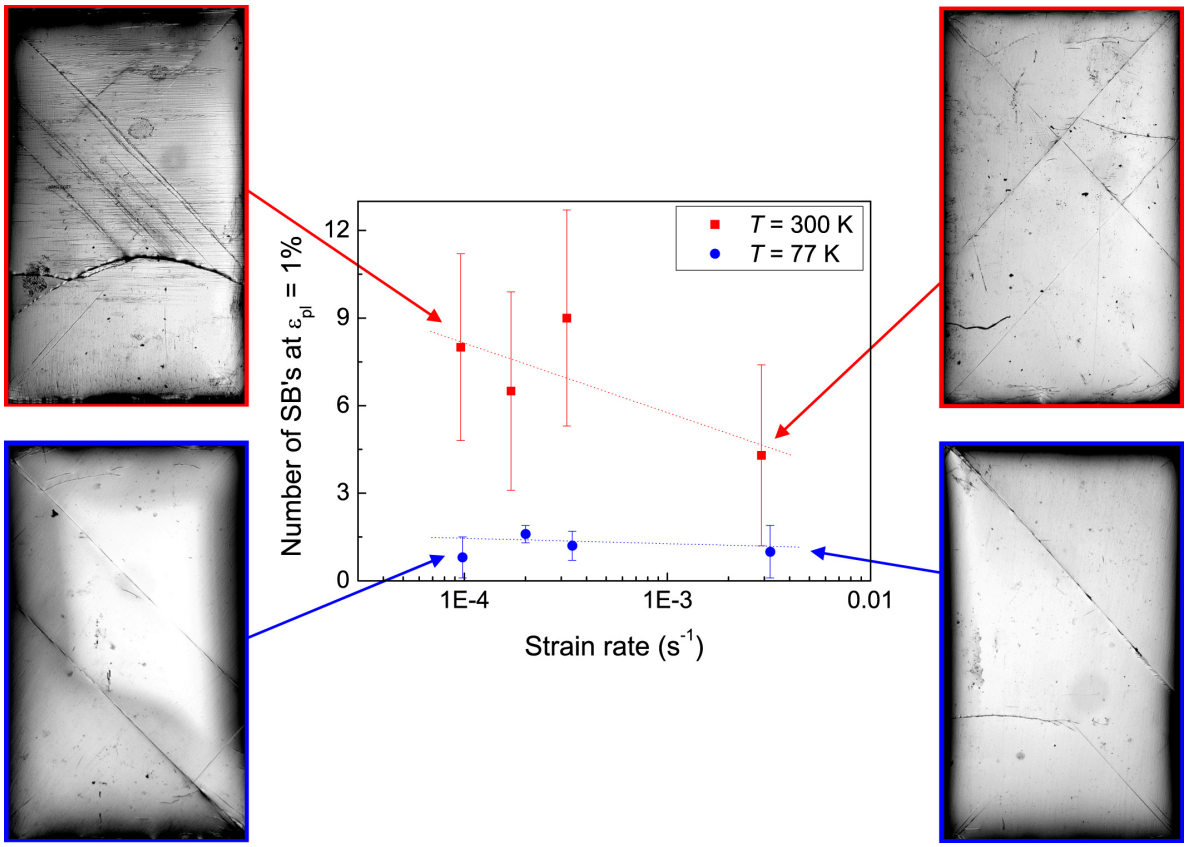

Fig. 5.11: Average number of shear bands measured by optical microscopy on the surface of Vit105 specimens ($3 \times 3 \times 5$ mm) deformed at room temperature and 77 K to a plastic strain of ~1 % at different strain rates. (The number is equal to the number of intersections of shear bands with an imaginary line in the middle of the surface that is parallel to the loading axis). The four optical microscopy images show characteristic shear-band appearances for the lowest and highest strain rates for the two temperatures.

Jiang *et al*. [64,65] observed the same behaviour in compression tests on Vit105 specimens with low aspect ratios (i.e. height/diameter < 1). Cyclic loading-unloading tests at different strain rates and temperatures showed lower flow stresses at high strain rates (i.e. a negative strain-rate sensitivity) and a decrease in the shear-band density with increasing strain rate and/or decreasing temperature.

5.4.3 Comparison with recent data from literature

Experimental work carried out by other research groups also provides further evidence in support of the findings presented in this thesis. Difficulties in comparing certain characteristics, however, arise when BMGs with different compositions are compared. A possible way to take into account the compositional dependence may be the scaling to the homologous temperature. By doing so, the transition from serrated to non-serrated flow for Vit105 at a strain rate of 10^{-4} s^{-1}, for example, takes place at $T/T_g \approx 0.29$. As mentioned briefly in Section 4.4.1 and shown in Fig. 5.12a, recent compression results [66] on a $Ti_{40}Zr_{25}Ni_3Cu_{12}Be_{20}$ BMG with comparable Young's modulus but a lower T_g (≈ 590 K) than Vit105 revealed that serrated flow at a strain rate of 4×10^{-4} s^{-1} disappears somewhere in the temperature range below 193 K and above 123 K (which corresponds to a homologous temperature of $T/T_g = 0.21$–0.33). Assuming a homologous temperature similar to that of Vit105 the transition for the Ti-based BMG can be expected at ~170 K. Similar to our observations, a decrease in the temperature leads to an increase in the plastic strain to failure (analogous observations were reported in Ref. [67] on a $Cu_{45}Zr_{45}Al_5Ag_5$ BMG). As shown in Fig. 5.12b the (normalised) strength also reveals a slight deviation from the linear temperature dependence in the temperature range where serrated flow prevails (hump around $0.7\,T/T_g$), similar to our observations made for Vit105. A maximum in the temperature dependence of the normalised stress around room temperature was also observed on La- and Zr-based BMGs [68]. By stopping the shear before fracture with a cylindrical stopper around the specimen, repolishing and reloading, the authors showed further that there is no change in the shear fracture stress. This observation indicates that the softening in the shear band is healed at room temperature by an annealing process or that the softening is largely dynamic in nature.

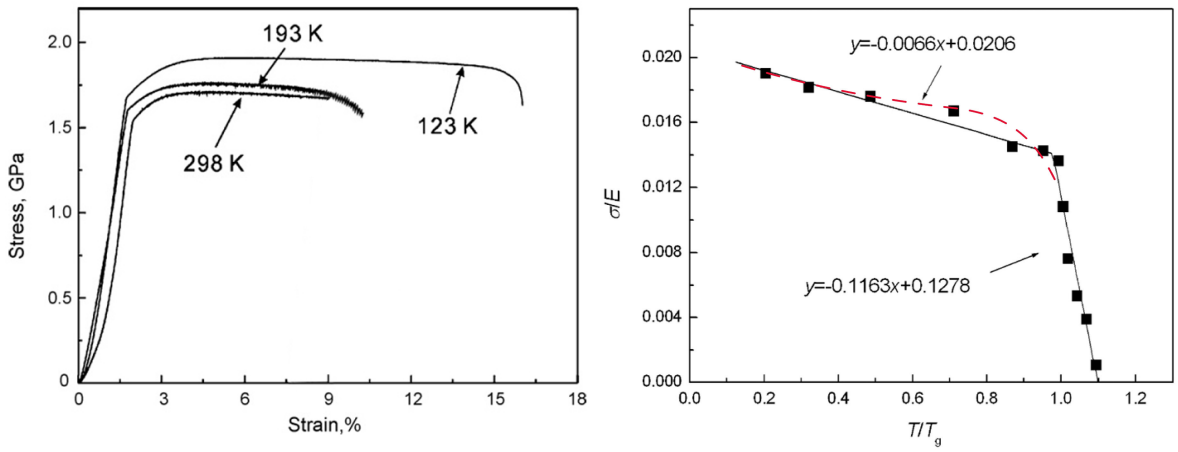

Fig. 5.12: (a) Compressive stress-strain curves for different temperatures and (b) the normalised temperature (T/T_g)-dependence of the normalised strength (σ/E) for $Ti_{40}Zr_{25}Ni_3Cu_{12}Be_{20}$. The dashed red line in (b) is a guideline for the eye revealing the deviation from the linear temperature dependence. (Reproduced from [66]).

Systematic investigations at subambient temperatures were also recently reported for a $Ni_{60}Pd_{20}P_{17}B_3$ bulk glassy alloy ($T_g = 605$ K) [69]. Compression tests at an initial strain rate of 5×10^{-4} s^{-1} showed an increase in the plastic strain to failure with decreasing temperature and a disappearance of serrated flow between 173 K and 223 K (which corresponds to $T/T_g = 0.29$–0.37). Interestingly, complementary measurements of the elastic constants showed a change in the temperature dependence of the ratio between shear and bulk modulus (μ/B) and Poisson's ratio (ν), respectively, in the same temperature interval. While μ/B (and ν) slightly decreased (increased) with decreasing temperature between 380 K and ~220 K, it significantly increased (decreased) with decreasing temperature below ~220 K. This behaviour reflects a hardening of the glassy phase (i.e. an increase in the bonding strength of atoms) and consequently explains the increased yield strength at cryogenic temperatures. However, the observation contradicts the theory that intrinsically ductile/tough BMGs have low μ/B [70,71] and the increased plastic strain at lower temperatures cannot be rationalised solely by a low μ/B.

Nevertheless, all the experimental results indicate that the disappearance of serrated flow at low temperatures is universal in metallic glasses. Whether the scaling of the transition temperature to the homologous temperature is oversimplified and other microstructural aspects have to be considered cannot be answered conclusively at the moment due to the lack of accurate measurements on different glass-forming alloys. As

pointed out in Ref. [1] the magnitude of the stress drops also depends on the compliance of the machine assembly. Therefore, additional caution is advised when comparing transition temperatures measured on different testing machines.

Following the cooperative shearing model of Ref. [20] the STZ volumes (Ω_0) of different bulk glass-forming alloys were recently investigated by means of rate-jump nanoindentation measurements at room temperature [24]. STZ volumes between 2.5 nm^3 and 6.6 nm^3 were determined and correlated with the Poisson's ratio (or ductility) of the various BMGs. The results, however, cannot be directly compared with the room-temperature results presented in this thesis. Due to the constantly changing stress gradient/state during indentation, new shear bands are continuously activated and the temporal evolution of the structure within a shear band (which in uniaxial compression experiments causes a negative SRS) does not show up, and the measured hardness reveals a positive strain-rate dependence. Therefore the STZ volumes presented in [24] should actually be compared with our values, $\Omega_0 = 1.5–2.5\ nm^3$, determined in the absence of relaxation (i.e. liquid nitrogen temperature), which agrees well and suggests that the assumption $V_{ap} \approx 0.1\ \Omega_0$ made in Section 5.2 is valid. Based on the correlation of STZ volume and ductility the authors of Ref. [24] concluded that STZs of large size reinforce the shear capability and promote the formation of multiple shear bands, which is consistent with our observation (see Figs. 5.2 and 5.11) that more shear bands are present on the surface of a specimen deformed at room temperature (large STZ volume) as opposed to liquid nitrogen temperature (small STZ volume). As shown in Table 5.1, similar apparent activation volumes have recently been obtained by room-temperature nanoindentation creep tests or in the supercooled liquid region (i.e. homogeneous flow around T_g) by tensile or compression tests on various BMGs, in excellent agreement with the activation volume determined in this study for Vit105 at elevated temperatures.

Table 5.1: Apparent activation volumes for flow in various BMGs at different temperatures T and strain rates $\dot{\varepsilon}$, experimentally determined either via n = nanoindentation, c = compression, t = tension, or to = torsion tests.

BMG	T_g (K)	Test	T (K)	$\dot{\varepsilon}$ (s^{-1})	V_{ap} (Å^3)	Ref.
$Zr_{56}Ni_{6.4}Cu_{23.5}Al_{6.2}Sn_{3.9}W_4$	660	n*	RT	-*	100–200	[72]
$Zr_{52.5}Ti_5Cu_{17.9}Ni_{14.6}Al_{10}$ (Vit105)	625	c	RT	6.7×10^{-5}–7.3×10^{-4}	~3600	This study
$Zr_{41.2}Ti_{13.8}Cu_{12.5}Ni_{10}Be_{22.5}$	628	c	628–646	2.5×10^{-4}–2.6×10^{-3}	160	[73]
$Zr_{52.5}Ti_{2.5}Cu_{22}Ni_{13}Al_{10}$	659	c	673–403	5×10^{-4}–2.5×10^{-3}	193–206	[54]
$Zr_{52.5}Ti_5Cu_{17.9}Ni_{14.6}Al_{10}$ (Vit105)	625	c	623–673	6.7×10^{-5}–1.3×10^{-4}	90–150	This study
$Pd_{80}Si_{20}$	673	to*	546–572	-*	105	[74]
$Pd_{40}Ni_{40}P_{20}$	577	t	556	10^{-5}–10^{-3}	80–180	[75]
$Pd_{41}Ni_{10}Cu_{29}P_{20}$	565	c*	550–565	-*	106	[76]
$Cu_{47.5}Zr_{47.5}Al_5$	702	c	703–733	10^{-6}–10^{-4}	~160	[77]
$Au_{49}Ag_{5.5}Pd_{2.3}Cu_{26.9}Si_{16.3}$	403	n	373–403	7.7×10^{-2}	155	[78]

* creep test, i.e. strain rate is stress-and time-dependent.

5.4.4 Implications on pressure sensitivity

Because STZ operation requires local dilatation of the surrounding matrix, metallic glasses exhibit pressure sensitivity. This manifests itself macroscopically for example in a tension-compression asymmetry, with higher yield strength and smaller fracture angles in states of net compression loading than in tension (e.g. according to the Mohr-Coulomb criterion). From the temperature dependence of the apparent activation volume and STZ volume in Fig. 5.2 a change of the pressure sensitivity with temperature can be expected: the local dilatation around a small STZ (at low temperatures) is larger than for a large STZ (at room temperature), suggesting an enhanced pressure sensitivity at low temperatures. As proposed in Ref. [79], a very straightforward way to characterise the pressure sensitivity is to measure the included angle or intersection angle (α) of mutually emanating shear bands that follow an outward logarithmic spiral pattern at the edge of a spherical/conical indent. For pressure-insensitive materials the included angle of conjugated shear bands is $\alpha = 90°$

and decreases below 90° for pressure-sensitive materials [80]. As shown in Fig. 5.13, the included angles are $\alpha = 84° \pm 2°$ and $\alpha = 80° \pm 2°$ for indentations at room temperature and $T = 77$ K, respectively, supporting the increased pressure sensitivity and hence the decrease in the STZ volume with decreasing temperature.

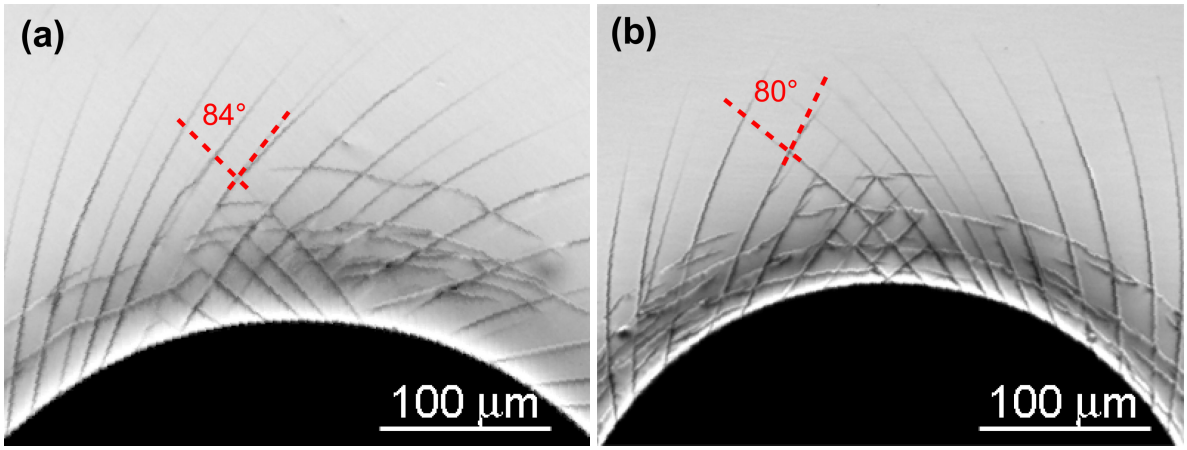

Fig. 5.13: Optical micrographs showing the intersecting slip lines emanating from the edge of a conical indent made at (a) room temperature and (b) liquid nitrogen temperature. The indents were made using a diamond cone tip (cone angle 120°, tip radius 0.2 mm) that is normally used for Rockwell hardness measurements with an applied load of 980 N

Support for the importance of structural relaxation processes in governing the inhomogeneous flow (i.e. shear banding) in amorphous solids proposed in this study also emerged from molecular dynamics simulations involving model glasses (e.g. Refs. [21,81,82,83]). For example, it was shown that more relaxed glasses (e.g., annealed or more gradually quenched ones) exhibit a higher degree of short-range order and consequently an increased yield strength. On the other hand, shear localisation is associated with the disruption of short-range order due to the extensive deformation inside shear bands (which would explain why shear bands are preferentially etched by chemical attack and why existing shear bands reactivate upon removal and reapplication of load). Within the framework of the potential energy landscape model Jagla [83] showed that when the energy landscape of the elemental constituents is kept fixed, the shear events (i.e. STZs) distribute uniformly throughout the sample, producing on average a uniform deformation. However, when the energy landscape at different spatial positions can be rearranged dynamically to account for structural relaxation, the system develops inhomogeneous deformation in the

form of shear bands at low shear rates, and stick-slip-like motion at the shear bands for the lowest shear rates. This means that the "amount" of strain localisation is a direct consequence of the ratio of applied strain rate and relaxation rate: for small shear rates, the system has enough time to relax and generate a more stable configuration, producing a larger value of stress than obtained at larger shear rates. If some region of the system shears more rapidly than another region, stress diminishes in the former and increases in the latter, producing the final result that shear is completely halted in some part of the system and becomes spatially localised. The elastic compatibility in the system causes the regions where shear is accumulated to take the form of narrow shear bands.

5.5 Conclusions

In conclusion, we have shown that despite fundamental differences in the underlying deformation mechanisms in amorphous and crystalline alloys there exist close phenomenological similarities between the inhomogeneous deformation of BMGs and crystalline solids (which deform via the DSA mechanism), such as strain-rate-dependent serrated flow, negative SRS, loss of ductility, etc. Based on a detailed micromechanical analysis of Zr-based BMGs at various temperatures and strain rates, a constitutive kinetic model for inhomogeneous flow was developed. Lowering the temperature generates a significant extension of the duration of a shear-banding event and at the same time an increase in the plastic strain to failure. The disappearance of serrated flow behaviour (temporal homogenisation) below a critical temperature (or above a critical strain rate) corresponds to a transition of the asymptotic SRS from negative to positive values. Since shear-band formation is related to a stress-driven structural disordering process, the temporal evolution of the deformation (and consequently also the strain-rate sensitivity) is quantitatively assessed by introducing a structural state variable in the classical, thermally-activated shear rate equations. The structural state variable accounts for the degree of structural relaxation after a shear event and hence governs the temperature and strain-rate dependence of the inhomogeneous deformation characteristics of BMGs, i.e. it reflects a strain-, strain-rate and temperature-dependent energetic quantity for the appearance and

disappearance of serrated flow in BMGs. The compositional dependence of serrated flow suggests the importance of local diffuse atomic rearrangements within shear bands. Such relaxation processes lead to a strengthening of the latter and lower the probability of reactivation of the same shear band. Therefore, more shear bands are present at higher temperatures and/or lower strain rates. Therefore, in contrast to the reasoning for the disappearance of pop-ins at high indentation rates proposed in Ref. [6], we explain the absence of serrated flow by the inability of the shear band to relax (and thus to strengthen fast enough) rather than by the simultaneous activation of multiple shear bands.

Preliminary observations of the angles between two different families of shear bands at the edge of a conical indent reveal an enhanced pressure sensitivity with decreasing temperature, in conjunction with the decrease in the STZ volume. (A detailed discussion of pressure sensitivity in BMGs and possible correlations with STZ size is provided in the next chapter.) Our results also indicate the importance of the (initial) condition of the material (introduced here as short-range order parameter ϕ), its influence on the deformation characteristics, and the necessity of accurately defining a general reference state of metallic glasses, in particular when comparing different alloys or differently processed samples.

5.6 References

[1] H.S. Chen, Scr. Mater. 7 (1973) 931.
[2] C.A. Pampillo, H.S. Chen, Mat. Sci. Eng. 13 (1974) 181.
[3] H. Kimura, T. Masumoto, Acta Metall. 28 (1980) 1663.
[4] H. Kimura, T. Masumoto, Acta Metall. 31 (1983) 231.
[5] H.J. Leamy, H.S. Chen, T.T. Wang, Met. Trans. 3 (1972) 699.
[6] Y.I. Golovin, V.I. Ivolgin, V.A. Khonik, K. Kitagawa, A.I. Tyurin, Scr. Mater. 45 (2001) 947.
[7] C.A. Schuh, T.G. Nieh, Acta Mater. 51 (2003) 87.
[8] W.H. Jiang, M. Atzmon, J. Mater. Res. 18 (2003) 755
[9] C.A. Schuh, T.G. Nieh, J. Mater. Res. 19 (2004) 46.
[10] B. Moser, J. Kübler, H. Meinhard, W. Muster, J. Michler, Adv. Eng. Mater. 7 (2005) 388.

[11] C.A. Schuh, A.C. Lund, T.G. Nieh, Acta Mater. 52 (2004) 5879.
[12] G. Schoeck, Phys. Stat. Sol. 8 (1965) 499.
[13] G.B. Gibbs, Phys. Stat. Sol. 10 (1965) 507.
[14] A.G. Evans, R.D. Rawlings, Phys. Stat. Sol. 34 (1969) 9.
[15] U.F. Kocks, A.S. Argon, M.F. Ashby, in *Thermodynamics and Kinetics of Slip*, Progress in Materials Science 19 (1975), Pergamon, New York.
[16] A.S. Argon, Acta Metall. 27 (1979) 47.
[17] A.S. Argon, L.T. Shi, Acta Metall. 31 (1983) 499.
[18] J.D. Eshelby, Proc. R. Soc. A 241 (1957) 376.
[19] F. H. Stillinger, Science 267 (1995) 1935.
[20] W.L. Johnson, K. Samwer, Phys. Rev. Lett. 95 (2005) 195501.
[21] M.L. Falk, J.S. Langer, Phys. Rev. E 57 (1998) 7192.
[22] M. Zink, K. Samwer, W.L. Johnson, S.G. Mayr, Phys. Rev. B 73 (2006) 172203.
[23] S.G. Mayr, Phys. Rev. Lett. 97 (2006) 195501.
[24] D. Pan, A. Inoue, T. Sakurai, M.W. Chen, Proc. Natl. Acad. Sci. U.S.A. 105 (2008) 14769.
[25] Z.F. Zhang, J. Eckert, L. Schultz, Metall. Mater. Trans. A 35 (2004) 3489.
[26] B. Lo Piccolo, P. Spätig, T. Kruml, J.L. Martin, J. Bonneville, Mater. Sci. Eng. A 309 (2001) 251.
[27] D. Caillard, J.L. Martin, in *Thermally activated mechanisms in crystal plasticity*, edited by R.W. Cahn, Pergamon Materials Series, Vol. 8, 2003.
[28] P. Spätig, J. Bonneville, J.L. Martin, Mater. Sci. Eng. A 167 (1993) 73.
[29] J.L Martin, B. Lo Piccolo, T. Kruml, J. Bonneville, Mater. Sci. Eng. A 322 (2002) 118.
[30] V.I. Dotsenko, Phys. Stat. Sol. B 93 (1979) 11.
[31] P. Schall, D.A. Weitz, F. Spaepen, Science 318 (2007) 1895.
[32] J.-P. Poirier, in *Creep of crystals*, edited by A.H. Cook, W.B. Harland, N.F: Hughes, A. Putnis, J.G. Sclater, M.R.A. Thomas, Cambridge University Press, 1985.
[33] T. Kruml, O. Coddet, J.L. Martin, Acta Mater. 56 (2008) 333.
[34] A. Portevin, F. Le Châtelier, C.R. Acad. Sci. Paris 176 (1923) 507.
[35] A. Portevin, F. Le Châtelier, Trans. Am. Soc. Steel Treat. 5 (1924) 457.
[36] J.M. Robinson, M.P. Shaw, Int. Mater. Rev. 39 (1994) 113.
[37] A.H. Cottrell, Philos. Mag. 44 (1953) 829.
[38] R.A. Mulford, U.F. Kocks, Acta Metall. 27 (1979) 1125.
[39] P.G. McCormick, Acta Metall. 36 (1988) 3061.
[40] M. Zaiser, P. Hähner, Phys. Stat. Sol. B 199 (1997) 267.
[41] P. Hähner, A. Ziegenbein, E. Rizzi, H. Neuhäuser, Phys. Rev. B 65 (2002) 134109.
[42] F. Faupel, W. Frank, M.P. Macht, H. Mehrer, V. Naundorf, K. Ratzke, H.R. Schober, S.K. Sharma, H. Teichler, Rev. Mod. Phys. 75 (2003) 237.
[43] A. Grandjean, P. Blanchard and Y. Limoge, Phys. Rev. Lett. 78 (1997) 697.
[44] F.H. Dalla Torre, E.V. Pereloma, C.H.J. Davies, Acta Mater. 54 (2006) 1135.
[45] S.I. Hong, Mater. Sci. Eng. 76 (1985) 77.
[46] P. Rodriguez, Bull. Mater. Sci. 6 (1984) 653.
[47] Y. Brechet, Y. Estrin, Scripta Mater. 35 (1996) 217.
[48] P. Asoka-Kumar, J. Hartley, R. Howell, P.A. Sterne, T.G. Nieh, Appl. Phys. Lett. 77 (2000) 1973.

[49] K.M. Flores, D. Suh, R.H. Dauskardt, P. Asoka-Kumar, P.A. Sterne, R.H. Howell, J. Mater. Res. 17 (2002) 1153.
[50] K.M. Flores, B.P. Kanungo, S.C. Glade, P. Asoka-Kumar, J. Non-Cryst. Solids 353 (2007) 1201.
[51] C.A. Pampillo, Scripta Mater. 6 (1972) 915.
[52] T. Masumoto, M. Maddin, Mater. Sci. Eng. 19 (1975) 1.
[53] C.A. Schuh, T.C. Hufnagel, U. Ramamurty, Acta Mater. 55 (2007) 4067.
[54] M. Bletry, P. Guyot, J.J. Blandin, J.L. Soubeyroux, Acta Mater. 54 (2006) 1257.
[55] F.H. Dalla Torre, D. Klaumünzer, R. Maaß, J.F. Löffler, submitted for publication in Acta Mater. (2009).
[56] Y. Estrin, L.P. Kubin, Mater. Sci. Eng. A 137 (1991) 125.
[57] T. Wutzke, C. Schwink, Phys. Stat. Sol. A 137 (1993) 337.
[58] F. Springer, A. Nortmann, C. Schwink, Phys. Stat. Sol. A 170 (1998) 63.
[59] D.M. Dimiduk, M.D. Uchic, T.A. Parthasarathy, Acta Mater. 53 (2005) 4065.
[60] D.M. Dimiduk, C. Woodward, R. LeSar, M.D. Uchic, Science 312 (2006) 1188.
[61] F. Shimizu, S. Ogata, J. Li, Acta Mater. 54 (2006) 4293.
[62] F. Spaepen, Acta Metall. 25 (1977) 407.
[63] P.S. Steif, F. Spaepen, J.W. Hutchinson, Acta Metall. 30 (1982) 447.
[64] W.H. Jiang, F.X. Liu, F. Jiang, K.Q. Qiu, H. Choo, P.K. Liaw, J. Mater. Res. 22 (2007) 2655.
[65] W.H. Jiang, F.X. Liu, D.C. Qiao, H. Choo, P.K. Liaw, R. Li, T. Zhang, Adv. Eng. Mater. 10 (2008) 1016.
[66] Y.J. Huang, J. Shen, J.F. Sun, Z.F. Zhang, Mater. Sci. Eng. A 498 (2008) 203.
[67] T. Okuno, A. Kawashima, H. Kurishita, W. Zhang, H. Kimura, A. Inoue, Mater. Trans. JIM 49 (2008) 513.
[68] S. Takeuchi, T. Kakegawa, T. Hashimoto, A.-P. Tsai, A. Inoue, Mater. Trans. JIM 41 (2000) 1443.
[69] A. Kawashima, Y. Zeng, M. Fukuhara, H. Kurishita, N. Nishiyama, H. Miki, A. Inoue, Mater. Sci. Eng. A 498 (2008) 475.
[70] J. Schroers, W.L. Johnson, Phys. Rev. Lett. 93 (2004) 255506.
[71] J.J. Lewandowski, W.H. Wang, A.L. Greer, Philos. Mag. Lett. 85 (2005) 77.
[72] S. Nowak, P. Ochin, A. Pasko, O. Maciejak, P. Aubert, Y. Champion, J. Alloys Compd. 483 (2009) 139.
[73] Q. Wang, J.M. Pelletier, J.J. Blandin, M. Suéry, J. Non-Crys. Solids 351 (2005) 2224.
[74] A.S. Argon, L.T. Shi, Acta Metall. 31 (1983) 499.
[75] P. De Hey, J. Sietsma, A. Van Den Beukel, Acta Mater. 46 (1998) 5873.
[76] M. Heggen, F. Spaepen, M. Feuerbacher, J. Appl. Phys. 97 (2005) 033506.
[77] K.S. Lee, H.J. Jun, S. Pauly, B. Bartusch, Y.W. Chang, J. Eckert, Intermetallics 17 (2009) 65.
[78] B. Yang, J. Wadsworth, T.G. Nieh, Appl. Phys. Lett. 90 (2007) 061911.
[79] G.R. Trichy, R.O. Scattergood, C.C. Koch, K.L. Murty, Scr. Mater. 53 (2005) 1461.
[80] G.S. Yu, J.G. Lin, M. Mo, X.F. Wang, F.H. Wang, C.E. Wen, Mater. Sci. Eng. A 460 (2007) 58.
[81] Y. Shi, M.L Falk, Scr. Mater. 54 (2006) 381.
[82] Y. Shi, M.L Falk, Phys. Rev. B 73 (2006) 214201.
[83] E.A. Jagla, Phys. Rev. E 76 (2007) 046119.

6 Deformation size effects and free-volume-dependent pressure sensitivity

This chapter summarises the results of micropillar compression tests[1] and investigations on the pressure sensitivity[2] of a Zr-based BMG with varying free-volume content. In the range of the tested sample dimensions the investigations show deformation behaviour that is independent of sample size and material condition. Hardness, however, is sensitive to the altered material conditions, indicating a change in the pressure sensitivity with free-volume content.

[1] A. Dubach, R. Raghavan, J.F. Löffler, J. Michler, U. Ramammurty, *Scripta Materialia* **60** (2009) 567.

[2] A. Dubach, K. Eswar Prasad, R. Raghavan, J.F. Löffler, J. Michler, U. Ramammurty, *Journal of Materials Research* **24** (2009), 2697.

6.1 Introduction

The intrinsic state variable that largely determines plastic deformation and toughness of bulk metallic glasses (BMGs) is the free volume [1]. Under the influence of external applied stress, regions with high free-volume content accommodate shear strains locally. These regions or clusters of atoms are referred to as shear transformation zones (STZs) [2,3]. Above the glass transition temperature, T_g, STZs operate everywhere and profusely, and hence plastic deformation is homogeneous. At relatively low temperatures and at high stresses, STZs coalesce along the maximum shear stress planes, localising flow into narrow shear bands. This results in inhomogeneous flow and imparts intrinsic instability to plasticity in BMGs. Several factors contribute to the latter: (i) large elastic strain energies stored in the material at the point of yield (by virtue of high yield strengths as well as yield strains); (ii) strain softening and concomitant localisation of flow into narrow bands; and (iii) lack of microstructure, which would otherwise hinder the propagation of shear bands. These issues complicate the measurement, and thus the understanding, of the mechanical behaviour of metallic glasses.

The focused ion beam (FIB) milling technique has recently been used in a wide variety of materials to micro-machine pillars, ranging in size from sub-microns to several microns, and to examine size effects on plasticity. Volkert *et al*. [4], who conducted such a study on sputtered amorphous $Pd_{77}Si_{23}$ films, showed that below a certain size (~400 nm) room-temperature plasticity is entirely homogeneous. They argued, by recourse to a Griffith-like model, that this transition is due to the lack of a critical driving force (stored elastic strain energy) for shear-band formation. Schuster *et al*. [5] examined the possibility of size-dependent strength in $Pd_{40}Ni_{40}P_{20}$ on micro-pillars ranging in size from 2 to 20 μm, and concluded that yield strength is insensitive to pillar size. Motivated by this work, we examined the influence of free volume on the compressive stress-strain response of micro-pillars of a Zr-based BMG, with the objective of examining (i) the (possible) transition from heterogeneous to homogeneous deformation as the specimen size is decreased and (ii) the effect of free volume on such a transition length scale. The results of these investigations are presented in Section 6.3.

Unlike conventional crystalline metallic alloys, whose plastic flow is only sensitive to shear, BMGs may also be sensitive to non-deviatoric parts of the stress tensor (e.g.

hydrostatic or normal stresses), as for instance shown in [6] and references therein. This difference in pressure dependence of flow (i.e. pressure sensitivity) is a simple consequence of the various underlying processes which govern plastic deformation. In contrast to crystalline metals, where plastic deformation is linked to the generally non-pressure-dependent motion of dislocations, shear in BMGs is accommodated through local atomic arrangements. Both the free-volume model (where deformation proceeds via diffusion-like atomic jumps and free-volume creation) and the STZ model (where a local cluster of atoms undergoes an elastic strain by crossing an activated configuration of higher energy and volume) are dilatational during deformation, so that pressure sensitivity can be expected. In addition, metallic glasses show very high macroscopic elastic strain limit of ~2% (as opposed to ~0.5% in crystalline metals), such that local dilatation becomes important. A direct consequence of this pressure sensitivity in metallic glasses manifests itself as a macroscopic yield asymmetry between compression and tension, which might be described by a Mohr-Coulomb criterion (cf. Section 4.3.2). Investigations into the pressure sensitivity of a Zr-based BMG and its dependence on the structural state of the glass (i.e., different free-volume content) are presented in Section 6.4.

6.2 Experimental

A 3-mm-thick amorphous $Zr_{41.2}Ti_{13.8}Cu_{12.5}Ni_{10}Be_{22.5}$ BMG (Vit1, $T_g \approx 625$ K) plate was investigated in three different conditions: as-cast (AC), structurally-relaxed (SR), and shot-peened (SP). The as-cast BMG was annealed at 563 K for 12 h to induce structural relaxation. Structural characterisation by means of DSC and XRD were performed on the relaxed material. Results of this and detailed analysis of free-volume reduction upon annealing can be found elsewhere [7,8]. Shot-peening was performed on polished surfaces of the as-cast BMG as per the AMS-S-13165 standard, using cast steel balls of 280 μm mean diameter as a shot-peening material. The deformed layer thickness due to shot-peening is ~40 μm, whereas the residual compressive stress field is much larger (~150 μm) [9]. The surfaces of the bulk specimens were polished to a mirror finish before micro-pillars with diameters of ~0.3, 1, and 3 μm and aspect ratio (i.e. height/diameter) of 2–2.5

were fabricated via focused-ion beam (FIB) technique using a Tescan Lyra instrument. First, rough cutting with a high Ga-ion beam current (30 keV and 4 nA) was used to mill a trench, leaving an island in the centre. Machining of the final pillar was performed by gradually reducing the beam current to 15 pA. The pillars were examined prior to and after deformation using a Leo 1530 scanning electron microscope (SEM). They were found to be slightly tapered with a convergence angle of between ~2° (larger pillars) and ~4° (0.3 μm pillars).

The micro-pillars were uniaxially compressed either in-situ inside a Zeiss DSM962 SEM or ex-situ. The ex-situ compression tests were performed on an MTS NanoXP indenter at constant loading rates (such that the initial nominal strain rate was in the $2 \times 10^{-4} - 4 \times 10^{-4}\ s^{-1}$ range) using a diamond flat punch. The in-situ compression experiments were performed using two different custom-built instrumented micro-indentation devices. Compression of the larger pillars was performed at constant displacement rates on a microindenter driven by a stack piezo with a built-in displacement measurement and equipped with a 0.5 N load cell. A piezo-actuated (stick slip) system allows exact positioning of the sample with respect to the flat punch. The 0.3 μm pillars were compressed at constant loading rates on a nanoindentation device based on a Hysitron PicoIndenter transducer. Further details of these instruments can be found in [10,11]. All the in-situ experiments were performed at a constant displacement rate using an initial strain rate of $8 \times 10^{-4}\ s^{-1}$. (Note that here the small strain-rate sensitivity of this BMG at room temperature was neglected and consequently that the different strain rates used, which fall into a relatively narrow range, do not affect the fundamental findings of this work.) The SEM images during the experiment were video-recorded (0.1 frames per second) and later synchronised with the load-displacement curve.

Additional hardness measurements of the material in its three conditions was performed on polished surfaces using an MTS NanoXP indenter at constant loading rates up to a maximum load of 500 mN using cube corner and Berkovich diamond tips. Cross-sections of particular indents were fabricated by FIB technique using a Tescan Lyra instrument. Post-compressed pillars, shear-band patterns around the indents and cross-sectional profiles were finally examined using a Leo 1530 FEG SEM.

6.3 Influence of sample size and structural state on micro-compression behaviour

6.3.1 Results

Figure 6.1 shows representative stress-strain responses of the three different-sized micro-pillars in the as-cast state. Yielding is defined at the stress where the first displacement burst is observed (see arrows in Fig. 6.1). The experiments were then stopped manually during the second displacement burst and then unloaded. Due to the slightly tapered shape of the pillars, engineering flow stresses were calculated using the diameter measured close to the top surface (at ~85% of the height of the pillar). The Young's modulus measured here is much lower (~50%) than the value of ~97 GPa reported in literature (e.g. [12]). Possible reasons are the taper, misalignment or imperfect contact between top surface and tip, and finally the effect of the base compliance (i.e. sink-in of the pillar), which, however, can be accounted for by correcting the measured Young's modulus by a factor of about 1.25 [13].

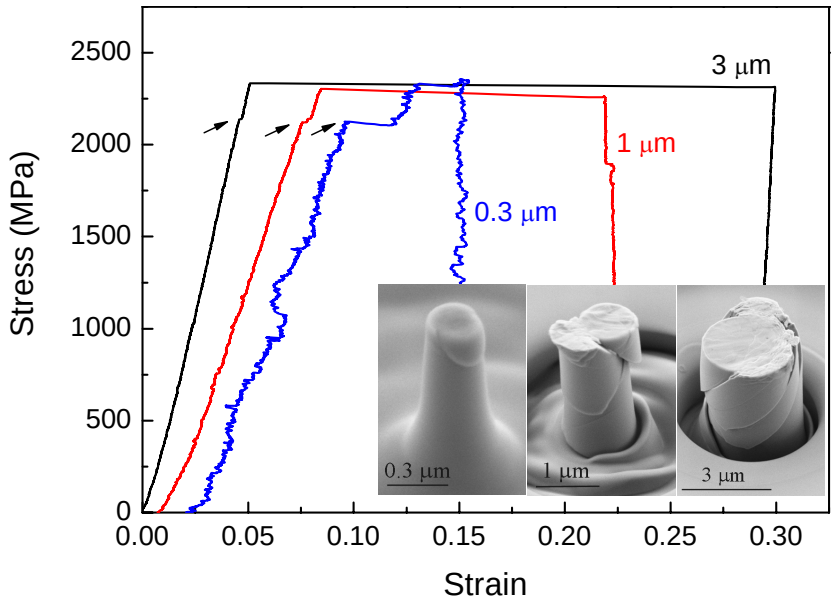

Fig. 6.1: Characteristic stress-strain curves for 0.3, 1, and 3 μm as-cast Vit1 pillars tested at constant loading rates of 0.05, 0.005, and 0.001 mN/s, respectively (generating initial strain rates of approximately $2\times10^{-4} - 5\times10^{-4}$ s^{-1}). The insets show the corresponding SEM images of the deformed pillars and the arrows indicate the first displacement burst (i.e. yield strain). The curves are shifted for better visibility.

The in-situ compression tests conducted at constant displacement rate typically show serrated stress-strain behaviour (Fig. 6.2). Synchronised SEM imaging allowed correlation of new shear-band appearance with the stress drops. Detailed analysis of the SEM images show that approximately two mature shear bands are present after a deformation of 12 % (bear in mind that only one side of the pillar is visible in the SEM) and that existing shear bands are preferentially reactivated (in agreement with [14] and observations made on "macroscopic samples" reported in Chapters 4 and 5). This is also supported by the fact that significantly more discrete stress drops are recorded than the number of shear bands observed after deformation. Therefore some of the stress drops are associated with the rigid slip of the top portion of the pillar with respect to the bottom part. Arrest of the shear band leads to build-up of load again, followed by another slip.

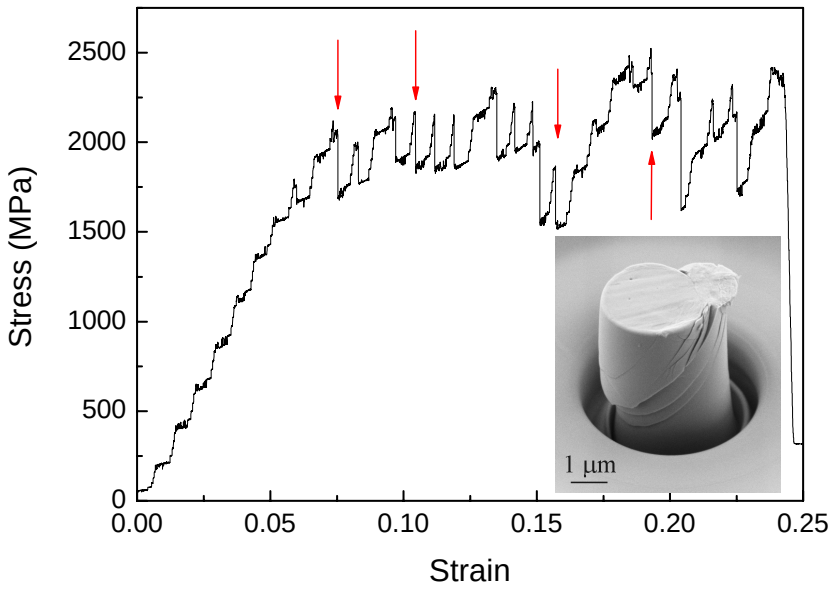

Fig. 6.2: Characteristic stress-strain curve of a 3 µm as-cast Vit1 pillar tested under displacement control (1 nm/s) at an initial strain rate of $\sim 2 \times 10^{-4}$ s^{-1}. The arrows indicate the appearance of a new shear band, i.e. the formation of a new shear step on the pillar surface. The inset shows the corresponding SEM image of the deformed pillar. (Note that the step-like behaviour in the "elastic" part of the loading curve is due to a problem with the used extensometer.)

As shown in Fig. 6.3, SEM images taken after deformation further confirm that plastic deformation proceeds via shear banding irrespective of material condition and pillar size (cf. also insets to Figs. 6.1 and 6.2). Other than that reported in Ref. [4], no change in the deformation mode is observed. Qualitatively, there is also no difference in shear-band density between the different conditions. However, it may be speculated that a transition to

homogeneous deformation could be observed at even smaller scales, where the sample dimensions are on the order of the shear band thickness (~20 nm) and the localisation of a shear band becomes extremely difficult. Recent experimental work on nanoscale metallic glasses has shown large tensile strains and possible size effects in plasticity, fracture behaviour and strength [15,16], and an inverse scaling of plastic strain (ε_p) to sample size (L) in the form of $\varepsilon_p \propto L^{-\alpha}$ has been suggested [17].

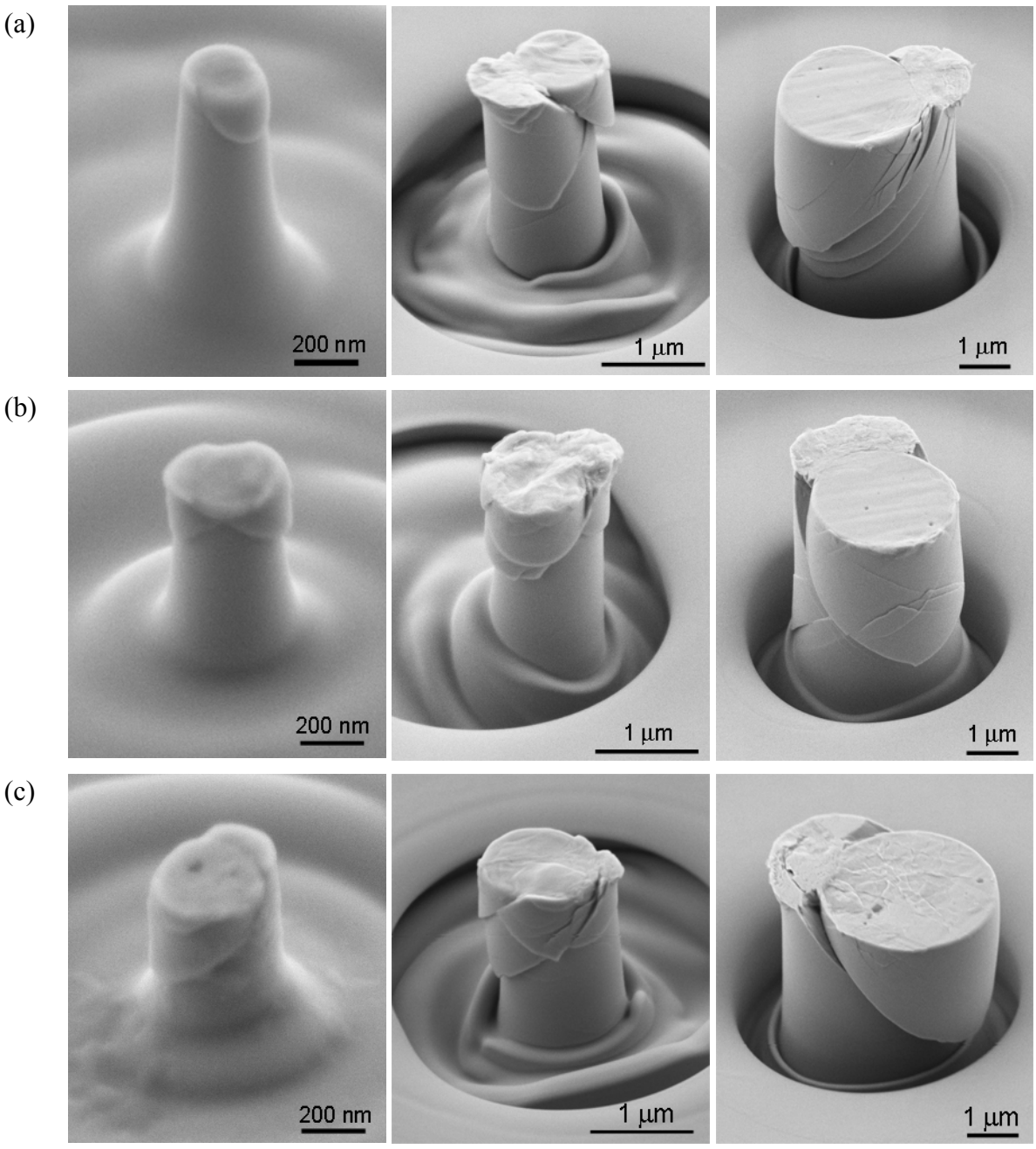

Fig. 6.3: SEM images of post-compressed Vit1 pillars with different diameters for (a) as-cast, (b) structurally-relaxed and (c) shot-peened conditions, respectively, revealing the inhomogeneous deformation by localised shear bands.

Figure 6.4 summarises the yield strengths measured as a function of the pillar diameter for the different conditions. (Here, yield strength is taken as the stress value at which the first stress drop or displacement burst occurs.) The scatter in the data appears to increase with decreasing pillar diameter. No size or condition dependence in strength was noted, with the data obtained on as-cast, relaxed, and shot-peened samples falling within a ~400 MPa scatter band. While the lowest of the yield strengths measured for all diameters is approximately equal to the bulk yield strength, the mean compressive yield strength of the micro-pillars is slightly higher (~7 %) than that reported for the bulk specimens [12]. A similar strength enhancement was reported for Pd-based micro-pillars in Refs. [4,5]. Possible reasons for this could be either experimental inaccuracies or intrinsic size scaling of strength. Note that the experimental errors increase with decreasing pillar size (which may arise e.g. from more difficult alignment of specimen and loading axis, increased taper angle or larger deviations in diameter determination in the SEM). For brittle materials, the strength variability and size scaling of strength is due to their flaw sensitivity. This is rationalised using Weibull statistics. Adapting the concept to BMGs and assuming that there is no change in the fundamental deformation mechanism, it has been suggested that the difference in strength is associated with the flaw sensitivity [18] or defect population that assists shear-band initiation [4,5,19,20]. Therefore the increase in strength with decreasing sample size appears to be a result of reduction in the critical flaw population in the tested sample volume. An additional influence may also be FIB damage (ion implantation) on pillar surfaces. Thickness estimations of the damaged layer on Zr-based BMG micro-pillars by Auger electron spectroscopy have revealed a thickness of ~4 nm [20], which for a 0.3 μm pillar results in an area contribution of the damaged layer of ~5 %. However, identifying the exact reason for the enhanced strength of micro-pillars is beyond the scope of this study.

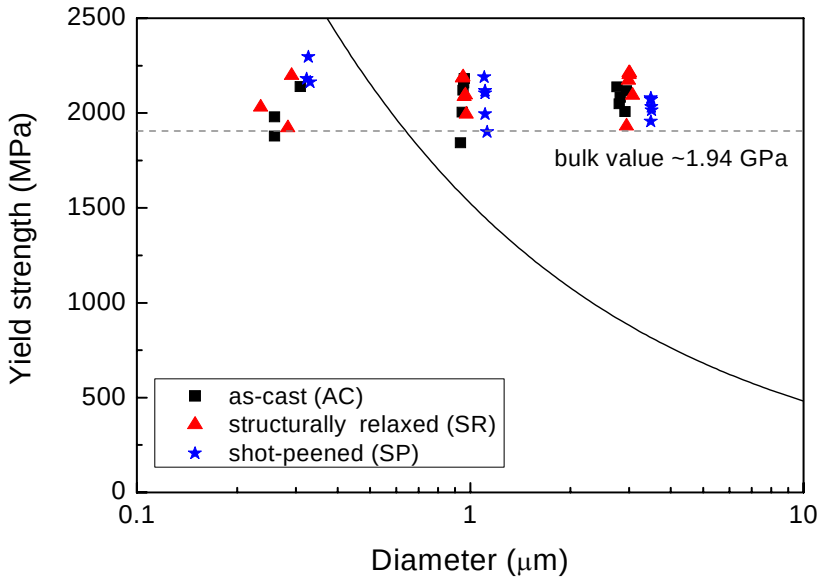

Fig. 6.4: Yield strength as a function of the pillar diameter (aspect ration $h/d \sim 2$) for the differently-treated Vit1 samples. The solid line shows the estimated minimum stress $\sigma = \sqrt{2Y\Delta E / Ad}$ required for shear-band formation (for details see text).

6.3.2 Energetic considerations

Figure 6.5 shows the stress drops, $\Delta\sigma$, of 1 and 3 μm pillars for the various material conditions up to a strain of 12 %.

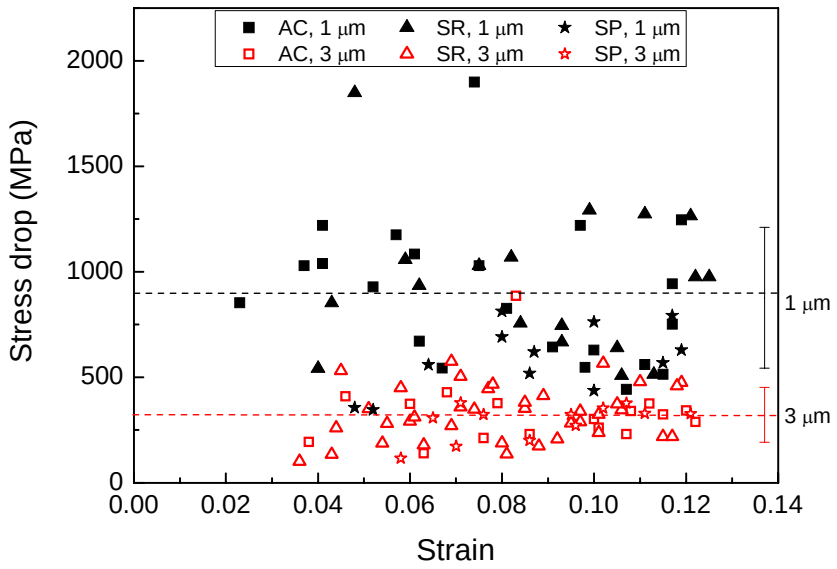

Fig. 6.5: Magnitude of the stress drops for the different pillar sizes as a function of strain during compression at constant displacement rate. The dashed lines are the mean values of the 1- and 3 μm pillars, respectively.

The first stress drop for the samples generally takes place at a strain of ~3.8 %, approximately twice that reported for bulk samples. This is because of the lower stiffness measured during micropillar compression. As shown by Kimura and Masumoto [21], the stress drop amplitude is also influenced by the compliance of the machine-sample assembly. Low compliances lead to smaller stress drops than would be observed in perfectly rigid machines. In this respect the measured stress drops are understood as the lower limit of the effective stress drops occurring in the pillars. The $\Delta\sigma$ measured on the 3 μm pillars (~300 MPa) are about one third of those measured on the 1 μm pillars (~880 MPa), suggesting a constant energy release per shear plane (i.e., energy density). Assuming that during a stress drop the whole elastic strain (i.e. elastic strain limit ε_e) is recovered locally in an operating shear band, the energy release ΔE during a stress drop can be written as

$$\Delta E = \frac{1}{2}\Delta F x = \frac{1}{2}\Delta\sigma\left(\frac{d}{2}\right)^2 \pi\varepsilon_e h, \tag{6.1}$$

where ΔF is the load drop, x is the displacement, and d and h are the diameter and height of the pillar, respectively. With a constant aspect ratio ($h = 2d$) and the shear plane area $A = \pi(d/2)^2 / \sin\theta$, where θ is the angle between shear plane and loading axis, the energy release per shear plane is $\Delta E / A = \varepsilon_e \Delta\sigma d \sin\theta$, i.e. $\Delta E / A \sim \Delta\sigma d$, as demonstrated experimentally for the differently-sized pillars. Using the measured $\Delta\sigma$ (Fig. 6.5) and the elastic strain limit $\varepsilon_e = 0.02$ yields $\Delta E / A \approx 12$ J/m^2, which is close to the approximated value of ~10 J/m^2 for a $Pd_{77}Si_{23}$ BMG [4] estimated from the maximum disordering possible in a shear band with a thickness of 10 nm. The value is also in very good agreement with the energy release per shear plane in macroscopic specimens (see Section 4.5: $d = 3$mm, $\Delta E \approx 10^{-4}$ J) which yields $\Delta E / A \approx 10$ J/m^2.

Following the analysis of the critical condition for shear-band formation proposed by Volkert *et al*. [4], the minimum stress required can be estimated as $\sigma = \sqrt{2Y\Delta E / Ad}$, where Y is the Young's modulus (~97 GPa). A plot of the critical stress as a function of the pillar diameter (Fig. 6.4) shows that a transition to homogeneous flow is expected at around $d \approx 0.62$ μm. However, our experimental results clearly show shear-band-mediated flow even in 0.3 μm pillars, in contrast to what was observed in Ref. [4].

6.3.3 Discussion

The observed stress drops (at constant displacement rate) and displacement bursts (at constant loading rate) are triggered by the formation and propagation of one (or multiple) shear band(s). The constancy of the stress during a displacement burst is a measure of the friction between the two shearing parts of the pillar. However, the measurement of the deformation behaviour (e.g. load-displacement curve) loses its proper physical significance at high strains as soon as the flat punch is pressed into the remaining, lower part of the pillar and a characteristic lip is formed, as shown in Fig. 6.6. The SEM images also reveal that shear-band initiation mostly takes place close to the corner of the top surface where the pillar, due to tapering effects, has the least cross-sectional area. This stress concentration is further intensified by possible frictional forces between the top surface of the pillar and the flat punch.

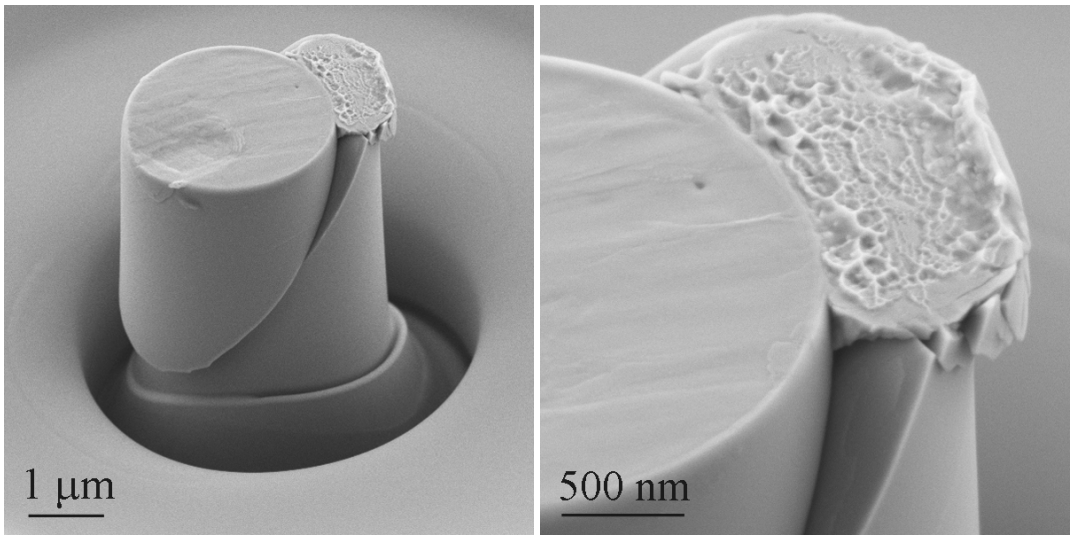

Fig. 6.6: Slipping of the upper part of the pillar and formation of a deformed lip at high strains where the flat punch hits the top of the lower part. (The right SEM image is a magnified view of the left one.)

The experimental micro-pillar compression results presented above show no discernible difference between the uniaxial compression responses of the BMG in the three different states. This contrasts with results of their toughness. The as-cast glass possesses sufficient free volume and hence reasonable toughness [8,22]. Structural relaxation leads to free-volume annihilation and hence imparts significant embrittlement [8,22,23]. This is reflected

in the experimentally-measured values of impact toughness for the as-cast and structurally-relaxed samples of 1.1 J and ~0 J, respectively [24]. Three-point flexure tests by Zhang *et al*. [25] on shot-peened BMG specimens showed that the latter exhibit pronounced plasticity. This is because shot-peening, which induces extensive plastic deformation, enhances the free-volume content in the deformed layer and hence makes shear-band initiation easier. Note that the largest pillar's height (~6 μm for the 3-μm-diameter pillar) is much less than the deformed layer thickness. Therefore the entire pillar consists of material that was extensively deformed during shot-peening. However, because of the small pillar size it is reasonable to assume that the residual stress field is completely relaxed during the micromachining process.

Despite significant differences in free-volume content, which in turn markedly affects plasticity and toughness, the micro-pillar compression experiments reveal no perceptible differences. This is because of the intrinsic limitations of compression testing, especially of materials susceptible to inhomogeneous flow. Friction between the loading plate and the specimen surface can induce plastic flow via shear-band nucleation, but the fact that the first and second shear bands initiate at the same stress level indicates that this may not be of major concern. However, relative shear displacement of one part of the specimen with respect to the other can lead to erroneous interpretation of plasticity. This is further complicated by the fact that the normal stress traction on the shear plane is negative (as opposed to the opening mode in uniaxial tension). As a result, the shear bands never become shear cracks and the shear bands propagate without reaching criticality. In fact, fracture toughness, which is highly sensitive to underlying structural features, is very appropriate for evaluating these quasi-brittle materials. This was recently demonstrated by Kim *et al*. [12], who examined the mechanical properties of several different compositional variants of Zr–Ti–Be–LTM (late transition metal) BMGs.

6.3.4 Microcompression tests on circular and square Vit105 pillars

In-situ SEM microcompression tests on Vit105 pillars with diameters of 0.3, 1 and 3 μm basically reveal the same size-independent behaviour as the Vit1 pillars in Section 6.3.1. As shown in Fig. 6.7a, deformation proceeds by shear banding, and no change of the deformation mode is observed with decreasing pillar size down to a diameter of 300 nm.

Similar to the observation on Vit1 the yield strength is size-independent and on average about 9 % higher than the measured bulk value.

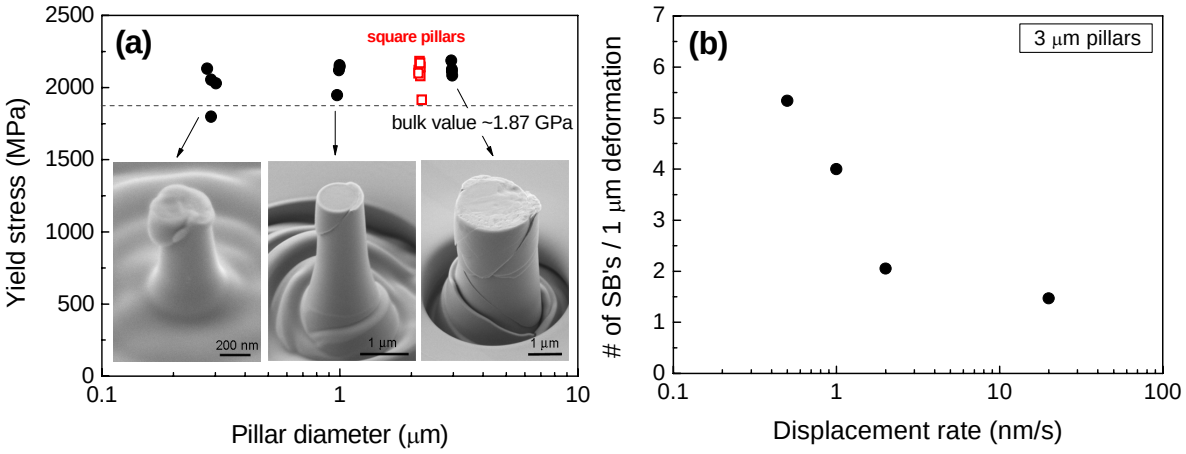

Fig. 6.7: (a) Yield stress of Vit105 as a function of the pillar diameter (at an initial strain rate of $\sim 2 \times 10^{-4}$ s^{-1}) and (b) number of shear bands visible on the surface of 3-μm pillars after a deformation of 1 μm for different deformation rates, determined by in-situ SEM compression tests. The red squares in (a) show the yield stresses measured on square pillars (for comparison with the circular pillars an "apparent circular diameter" was determined from their cross-sectional areas) and the inlets show SEM images of compressed pillars.

Detailed analysis of the in-situ SEM image sequences shows that the number of shear bands decrease with increasing displacement rate (Fig. 6.7b) as similarly observed on macroscopic samples in Section 5.4 (see Fig. 5.11). This is further evidence that high deformation rates generate preferential reactivation of existing shear bands. Time-dependent relaxation processes which are only substantial at lower strain rates (see also Section 5.3) lead to a strengthening of the distorted structure in shear bands, and consequently the probability of reactivation decreases and multiple shear bands are formed.

Preliminary microcompression tests on square pillars with a surface-area-to-volume ratio increased by a factor of $2/\sqrt{\pi}$ $(=1.128)$ compared to the circular pillars show no sample shape influence. As shown in Fig. 6.7a (red squares), no difference in yield strength between circular and square pillars can be observed or if present it lies within the experimental scattering. SEM observation (cf. Fig. 6.8) shows that during compression multiple shear bands are formed that mainly emanate from the upper corners of the pillar at ~45° to the loading axis. These experimental findings provide indirect evidence that FIB

damage on pillar surface has no or only marginal influence on the strength and deformation behaviour of amorphous micropillars.

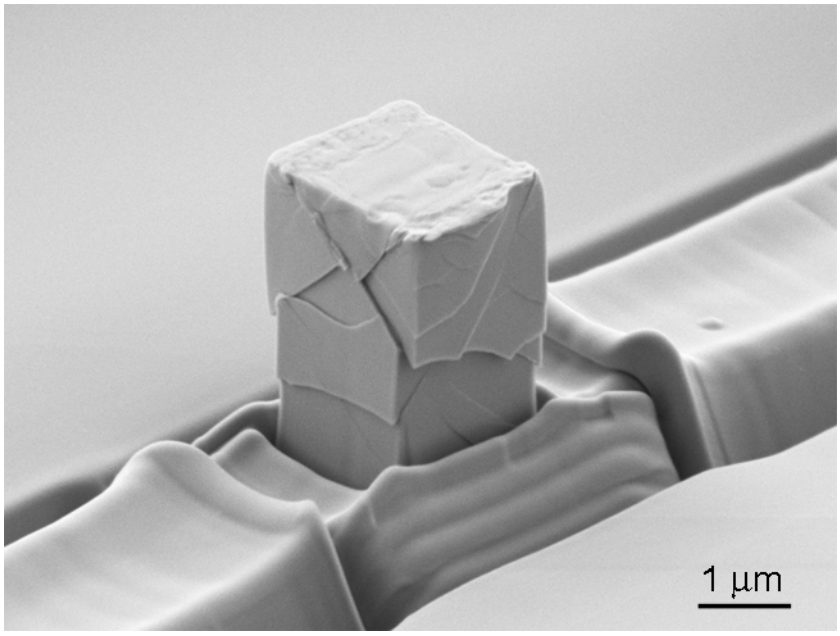

Fig. 6.8: SEM image of a deformed square pillar.

6.4 Free-volume dependent pressure sensitivity

The inhomogeneous nature of deformation in metallic glasses through shear banding as well as the mechanical instability associated with the strain softening post-yielding complicate the experimental assessment of plasticity in amorphous alloys. In addition, shear in BMGs may be sensitive to normal or hydrostatic stress components. This pressure sensitivity of plastic flow complicates the matter further, imparting tension/compression asymmetry. In uniaxial tension, fracture ensues almost immediately after yield due to mechanical instability. Hence, only the yield strength can be measured reliably by tension tests. Flexure tests, which apart from tensile testing are a common procedure for testing rapidly-quenched glassy ribbons [26,27], are not suitable for thicker plates of bulk metallic glasses (BMGs). The reason for this is that shear bands develop into shear cracks once they are allowed to traverse certain minimum distances, and the large elastic strain energy stored

in the specimen is released upon the initiation of shear cracks, leading to immediate fracture [26]. Also, accurate determination of the stress state under flexure loading is complicated by the tension-compression asymmetry that amorphous alloys exhibit. Therefore, uniaxial compression and indentation have been widely used testing techniques for characterising plasticity in BMGs.

As shown in Section 6.3 compression tests on micropillars in the as-cast (AC), structurally-relaxed (SR) and shot-peened (SP) state show no significant specimen-size- or specimen-condition-related differences either in their strength or plastic flow characteristics (i.e. shear banding), despite the fact that the toughness of the BMG is markedly different in the three different conditions investigated. This is primarily because of the intrinsic limitations associated with uniaxial compression testing of materials that undergo inhomogeneous plasticity, i.e, frictional contact at the platen-specimen surface initiating localised flow (shear bands) and subsequently, facilitation of relative sliding of one part of the specimen with respect to the other without ever reaching the critical condition for initiating fracture.

In this section, we examine whether instrumented indentation tests can reveal any distinct features associated with the plasticity of a Zr-based BMG, $Zr_{41.2}Ti_{13.8}Cu_{12.5}Ni_{10}Be_{22.5}$ (Vit1), in the three different conditions. The indentation method offers many advantages. These include (a) the relatively small material volumes necessary to conduct a large number of tests; (b) the relative ease with which these tests can be performed (only a flat surface of rigidly held specimens is required); and (c) the allowance of large plastic strain, mainly due to the constrained compressive stress state which imparts intrinsic stability to the deformation. In addition, hardness measurements can help to identify the extent of pressure sensitivity to plastic flow through the constraint factor, given by the ratio of hardness to yield strength [28,29,30,31].

6.4.1 Indentation curves

Figure 6.9 shows representative load, P, vs. displacement into the surface, h, curves obtained using a cube-corner indenter at a constant loading rate of 1.67 mN/s. Pronounced displacement instabilities (i.e., “pop-ins”) are visible during loading. The magnitude of the pop-ins (pop-in length) increases linearly with h as shown in Fig. 6.10. (For reasons of

clarity they are each averaged over 200 nm displacement intervals.) This linear relationship may simply be ascribed to the geometrical self-similarity of the sharp cube-corner tip and the associated deformation field [32]. No significant difference in the measured pop-in lengths between the AC and the SR material can be discerned (see also Table 6.1). However, the BMG in the SP condition shows relatively large (and consequently fewer) pop-ins than the AC sample. The onset of pop-ins in the load-displacement curve is also more pronounced in this case.

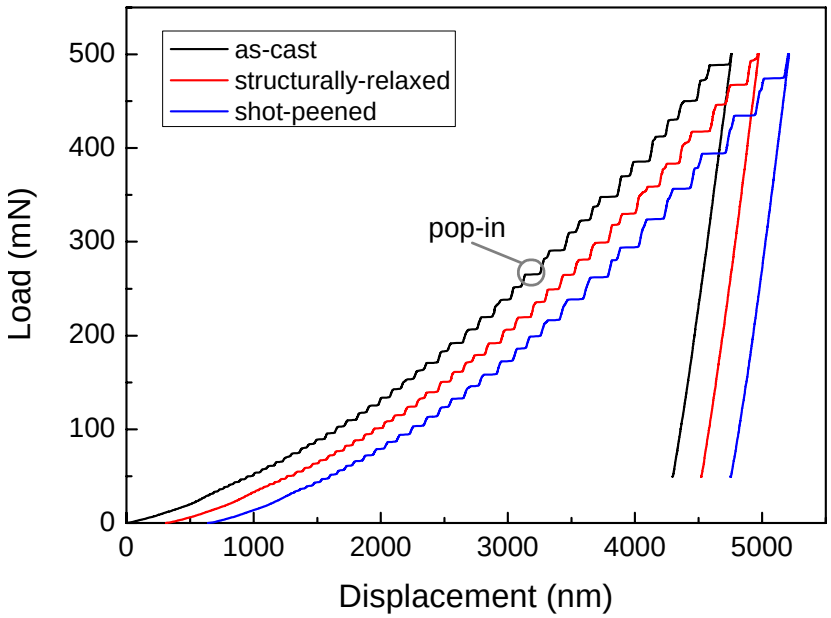

Fig. 6.9: Characteristic cube-corner indentation curves for the differently treated Vit1 samples at a loading rate of 1.67 mN/s. The curves are shifted relative to each other for better visibility.

Table 6.1: Pop-in length versus displacement ratio (see Fig. 6.10) of the differently treated Vit1 samples for the two loading rates applied.

Material condition	Low loading rate (1.67 mN/s)	High loading rate (16.7 mN/s)
as-cast	2.30 ± 0.08%	1.85 ± 0.03%
structurally-relaxed	2.38 ± 0.11%	1.76 ± 0.05%
shot-peened	4.04 ± 0.09%	2.59 ± 0.08%

Indentation at higher loading rates generates a decrease in the pop-in lengths (compare Figs. 6.10a and 6.10b) as well as a decrease of the number of pop-ins. As the loading rate is increased the nature of the pop-ins changes from discrete, horizontal stair-step-like displacement bursts to more blurred fluctuations or ripples. These observations are consistent with earlier indentation studies (e.g. [14,32]) which showed that the ratio of discrete plastic depth (i.e., individual pop-ins) to total plastic depth decreases with increasing indentation loading rate. Further, the apparent onset of pop-ins in the load-displacement curve is shifted to both higher loads and indentation depths with increasing loading rates. An increase in the applied loading rate from 1.67 to 16.7 mN/s shifts the apparent onset of pop-ins for each material's condition to higher values by approximately 40 mN and 700 nm, respectively.

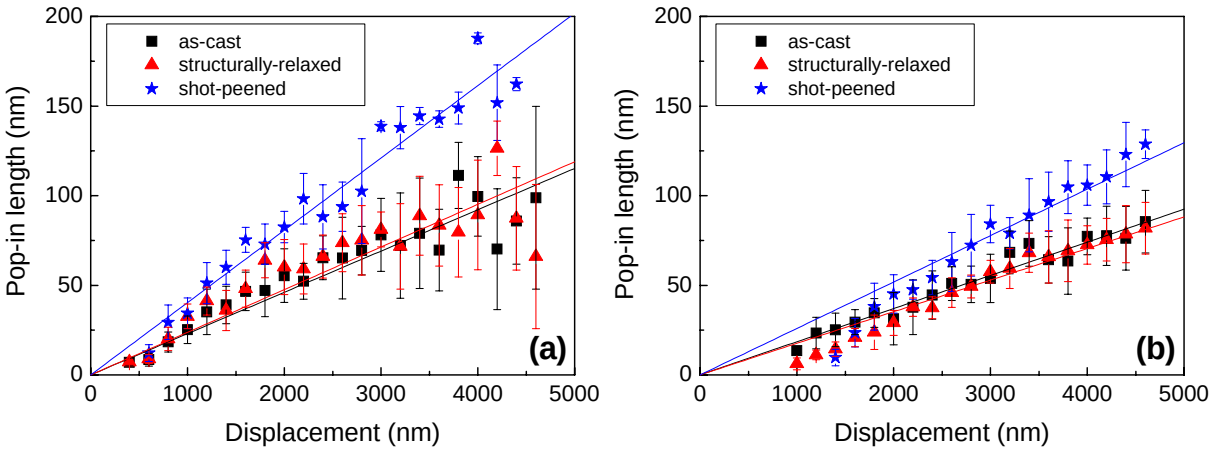

Fig. 6.10: Pop-in lengths for the differently treated Vit1 samples as a function of the displacement into the surface at a loading rate of 1.67 mN/s (a) and 16.7 mN/s (b), respectively. For reasons of clarity the pop-in lengths are averaged over 200 nm displacement intervals; the solid lines are linear fits of the data.

6.4.2 Shear-band morphology

Figure 6.11 shows the appearance of shear bands in the form of surface steps around the cube-corner indents for the three different material states. There is no discernible difference between the AC and SR state; the top view images of the indents show a rather triangular shear-band pattern. However, the shear-band appearance on the SP material is markedly different, and the shear bands form in a semi-circular pattern. A slightly lower number of

shear steps on the surface was observed on the SR sample compared to the AC sample, which is in agreement with the lower shear-band density on structurally-relaxed and partially-crystallised $Zr_{52.5}Ti_5Cu_{17.9}Ni_{14.6}Al_{10}$ samples reported in [14]. In contrast, significantly fewer shear bands are formed in the SP sample (see the inclined images of Fig. 6.11). Keryvin [33] showed that shear offsets on the surface are observed only when the indenter deployed induces strains large enough to reach the fully plastic regime. In this regard, the extremely sharp cube-corner indenter induces large indentation strains, and hence provokes a fully plastic regime for all three conditions of the Zr-based BMG used in this study. It is possible that great differences in shear-band number density and spacing among the AC, SR and SP specimens will be observed when blunt indenter tips are used. In fact, Murali and Ramamurty [8] reported such differences between AC and SR samples tested with spherical indenters, with the SR sample showing significantly fewer shear bands. The authors attributed this embrittlement upon structural relaxation to the inability of the SR BMG to mitigate the crack-tip stress concentration through shear-band induced plasticity.

The cross-sections of the cube-corner indents obtained by FIB machining are shown in Fig. 6.12. While the height of the shear offsets (Δs) increases, the angle of inclination with respect to the surface appears to decrease in the sequence AC, SR, and SP. In the SP case, the shear offsets have the appearance of wedge cracks.

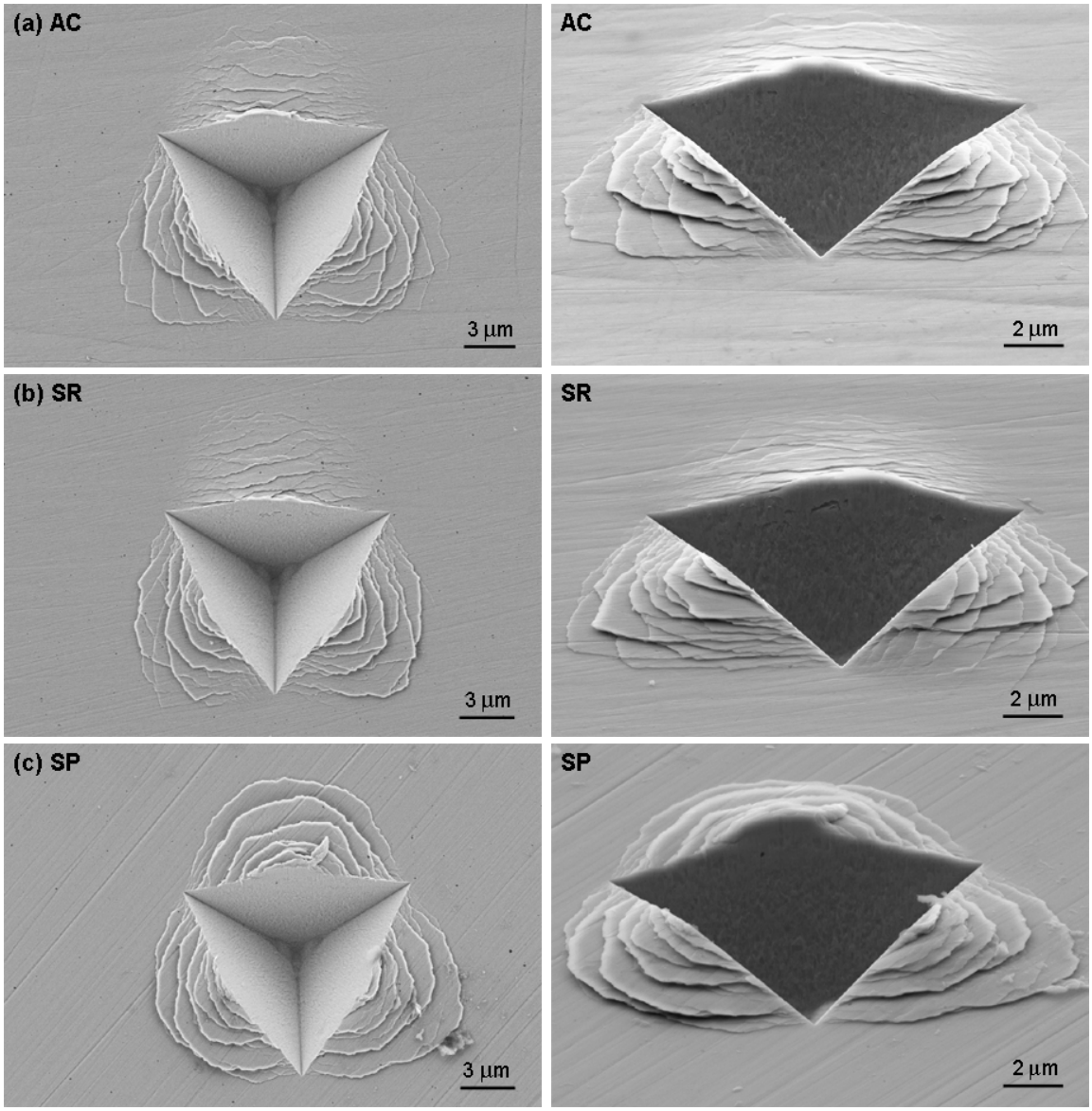

Fig. 6.11: SEM images (left: top view, right: inclined (60°) view) of cube-corner indents (loading rate of 1.67 mN/s) showing the appearance of shear bands in the form of surface steps for (a) as-cast, (b) structurally-relaxed, and (c) shot-peened Vit1 samples.

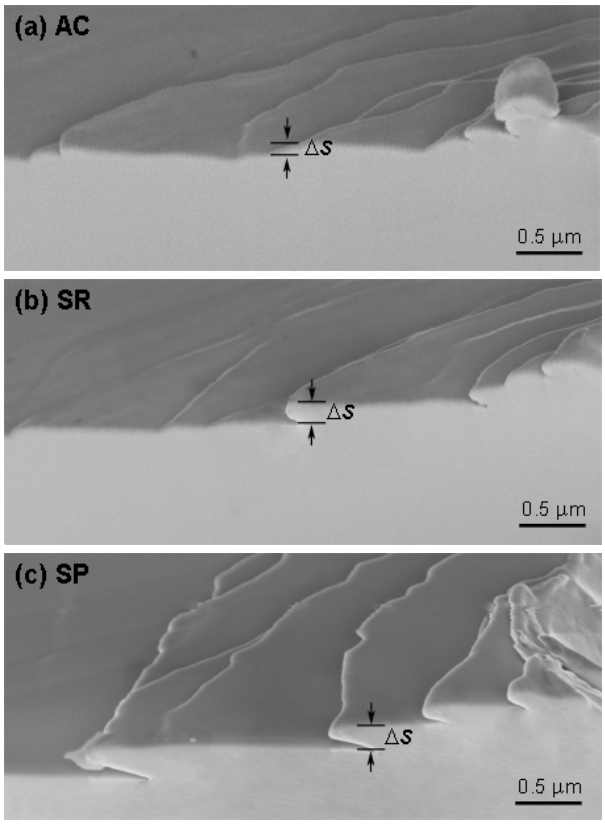

Fig. 6.12: FIB-cut cross-sections of the shear offsets (i.e. surface steps next to the cube corner indent, which is at the right image border) for (a) as-cast, (b) structurally-relaxed, and (c) shot-peened Vit1 samples. The figure also illustrates how the shear offset Δs (with additional tilt correction) was determined.

Schuh *et al*. [34] modelled the correlation between the pop-ins observed in the *P-h* curves and the shear offsets, which was verified by Moser *et al*. [14] with the help of in-situ indentation. Considering that the pop-in lengths of the AC and SR condition are similar (Fig. 6.10), the differences in the shear offset heights suggest a more prevalent reactivation of existing shear bands in the SR state. The observed large shear offset and low angle of inclination in the SP sample is associated with larger pop-in lengths and may be due to the biaxial compressive residual stresses that are present in the SP layer.

6.4.3 Hardness and pressure sensitivity

The hardness (mean contact pressure) was calculated as $H = P_{max}/A$, where P_{max} is the maximum applied load and A is the projected contact area of the cube-corner indenter (including the pile-up, whose area contribution is ~20 %), determined via SEM image analysis. The values are listed in Table 6.2. The biaxial compressive residual stress that exists in the peened layer of the SP sample, estimated to be ~1.9 GPa by Zhang *et al*. [25], elevates the flow stress, and in turn enhances the measured hardness [35]. Raghavan et al. [9], who measured the hardness on the transverse section of the peened layer using a nanoindenter with a Berkovich tip, found the hardness values of the peened layer to be actually lower than the bulk hardness. This is because the biaxial residual stress is relaxed due to sectioning and the "actual" hardness is lower because of deformation-induced softening [36]. However, it is well known that the Oliver and Pharr (OP) method [37] overestimates the hardness when there is substantial pile-up against the indenter due to plastic flow. Since the authors of Ref. [9] report significant pile-up in their cross-section indentations and have used the OP method, the hardness values reported by them cannot be used for further analysis here.

Therefore, cube corner nanoindentation was performed on the sectioned SP layer in this work and the mean contact pressure was accurately determined. The nanoindentation experiments were performed on a mirror-polished cross-section of the shot-peened layer ~5 μm from the surface using a Hysitron triboindenter with a cube-corner diamond tip (peak load of 5 mN, loading/unloading rate of 0.01 mN/s and peak load hold of 10 s). Imaging of the indents was performed by atomic force microscopy (AFM) using the same cube corner tip, and the projected area of the imprint was subsequently determined from these AFM images using the image analysis software *Sigma scanpro 4.0*. The average values of H, measured in this study, and the uniaxial compressive strengths, σ_y, determined on 3-μm micro-pillars in Section 6.3, are listed in Table 6.2. It is seen that H increases upon structural relaxation by ~6% whereas it decreases by ~14% upon shot-peening (the AC values are used as the reference for comparison). While σ_y can also be ranked in the same order as H, i.e., SP < AC < SR, the relative change is small and within the margin of experimental error.

Table 6.2: Yield strength, σ_y (data obtained by conducting uniaxial compression tests on 3-μm micropillars, cf. Section 6.3), hardness, H (using a cube-corner tip), constraint factor C ($=H/\sigma_y$), and intersection angle α of shear bands around a conical indent of the differently treated Vit1 samples. Data in parentheses indicate percentage change in property with respect to the as-cast state.

Material condition	σ_y (MPa)	H (GPa)	C	Intersection angle α (degrees)
as-cast	2079 ± 52	6.07 ± 0.04	2.92	80.9 ± 1.1
structurally-relaxed	2137 ± 110 (+2.8%)	6.45 ± 0.05 (+6.3%)	3.02 (+3.4%)	79.8 ± 1.2
shot-peened	2030 ± 49 (-2.4%)	5.22 ± 0.21 (-14%)	2.57 (-12%)	91.2 ± 3.2

During indentation, the matrix that surrounds the material underneath the indenter constrains the plastic flow. As a result, flow stress during indentation gets elevated significantly and is measured through the ratio of H/σ_y in the fully plastic regime of indentation. The ratio H/σ_y, therefore, is referred to as the constraint factor, C [30,31]. In crystalline metals $C \sim 2.6–2.8$, whereas $C \geq 3$ for metallic glasses, a reflection of the sensitivity of their plastic flow to pressure [28,38]. Further, the C of BMGs, as well as that of other amorphous materials like polymers, increases with increasing temperature [29,30,31]. The C values, estimated using H and σ_y and listed in Table 6.2, can also be organised in the ascending order of SP < AC < SR. Keryvin *et al*. [30] have shown a one-to-one correspondence between C and pressure sensitivity and hence C can be taken as the pressure-sensitivity index. Consequently, the experimental results of this work show that pressure sensitivity of the BMG increases modestly upon structural relaxation, whereas it decreases considerably upon shot-peening.

To further confirm these changes in pressure sensitivity due to changes in structural states, we conducted conical indentations and examined the intersection angles, α, between the two families of slip lines (here, shear bands) that emanate from the edge of contact. If the material obeys the Tresca or the von Mises yield criterion, applicable for pressure-insensitive plasticity, the slip lines follow the maximum shear directions with $\alpha = 90°$ [39,40,41]. For pressure-sensitive materials the intersection angles are smaller, i.e. $\alpha < 90°$. The conical indentations on the AC and SR specimens were performed using a diamond cone tip (cone angle 120°, tip radius 0.2 mm) that is normally used for Rockwell hardness

measurements with an applied load of 980 N. Smaller indents were performed on the cross-section of the peened layer of the SP specimen using the MTS NanoXP indenter with a conical tip (cone angle 84.6°, tip radius 1 μm) and a maximum load of 100 mN. The morphology around conical indents (i.e. the intersection angle of different families of shear bands) was examined by optical microscopy and SEM.

Figure 6.13 shows representative micrographs with families of shear bands intersecting each other, for the three structural states examined. The average α values measured from such micrographs are listed in Table 6.2. For the AC condition $\alpha = 80.9°$, close to that of ~79° reported by Patnaik *et al*. [28] for the same alloy, which is representative of a material that obeys the Mohr-Coulomb yield criterion with a friction parameter of 0.19. Upon structural relaxation, α decreases marginally to 79.8°. This observation is in excellent agreement with the reduction in α (for similar temperature and time of annealing) upon structural relaxation reported by Yu *et al*. [40]. The reduction in α suggests slightly enhanced pressure sensitivity with relaxation, which is consistent with the small increase in *C*.

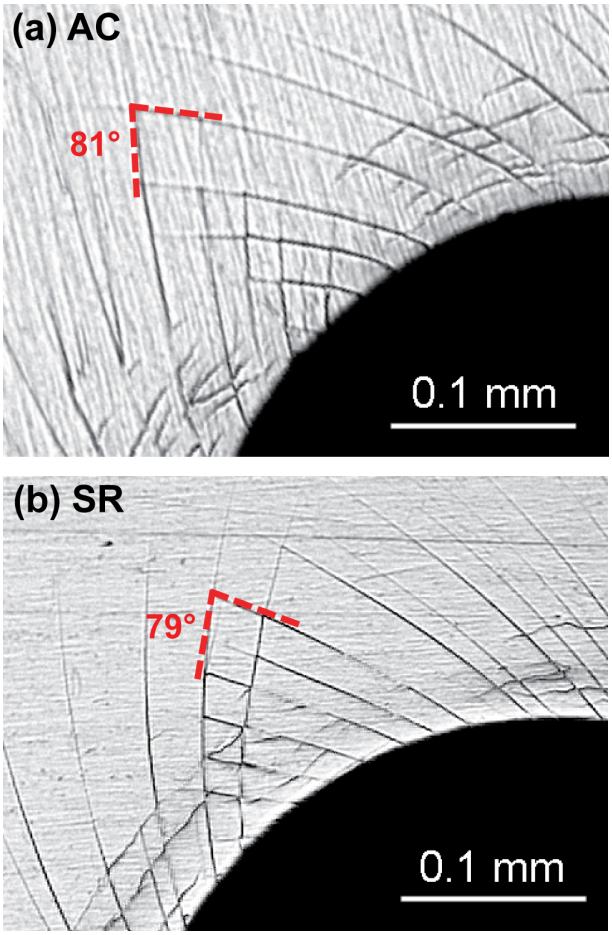

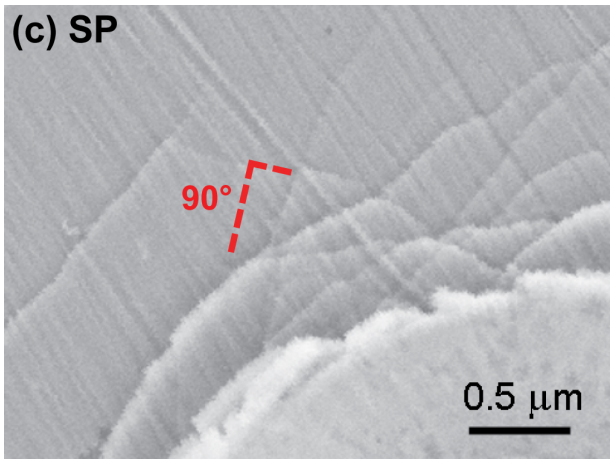

Fig. 6.13: Optical micrographs and SEM image showing the intersecting slip lines (with the intersection angle α) emanating from the edge of a conical indent, performed on (a) as-cast and (b) structurally-relaxed Vit1 samples, and (c) on the cross-section of the shot-peened layer.

6.4.4 Discussion

The mechanistic origin of the enhanced σ_y, H and pressure sensitivity upon structural relaxation can be understood as follows. The primary carriers of plasticity in amorphous materials are the shear transformation zones (STZs) [2,3]. Since STZ operation requires significant dilatation of the matrix that surrounds it, availability of free volume is critical for the STZs to occur in a given volume of material. Therefore, STZs occur preferentially in those regions which are less densely packed (i.e., have higher free-volume content), because relatively less dilatation of the matrix is required. It is well known that annealing leads to a reduction/annihilation of free volume [8], which in turn results in a densification of the BMG [42]. This makes the operation of STZs difficult (due to "higher atomic friction"), which results in an increased resistance to plastic deformation and therefore enhancement of yield strength and hardness of the BMG upon structural relaxation. This is consistent with other studies that report an enhancement in hardness upon structural relaxation [43,44].

Turning our attention to the SP condition, the measured α is ~90°, indicating that the BMG in this structural state obeys Tresca or von Mises yield criteria, which rely only on the deviatoric component of the stress tensor, as in crystalline metals. Also, the $C = 2.57$ obtained for the SP case is close to that obtained in crystalline metals [45], confirming that

the BMG indeed becomes pressure-insensitive upon exposure to severe plastic deformation. The free-volume model by Cohen and Turnbull, and adapted for plastic flow in metallic glasses by Spaepen [46], implies the creation of free volume during the deformation, which in turn leads to local reduction in viscosity. Such free-volume enhancements were confirmed experimentally in Refs. [36,47], among others. However, the excess free volume generated during plastic deformation may not be stable [48] and it coalesces to form nanovoids once the externally applied stress is removed, as experimentally verified by Li *et al*. [49] and Flores *et al*. [50]. Nanoindentation of ball-indented plastic regions showed that these nanovoids act as sites for the initiation of shear bands [36]. Since the shot-peening process involves repeated indentations that induce successive plastic strains in the surface layers, it is likely that the effective free volume in those layers increases considerably. In contrast to that seen in SR samples, where reduction in free volume enhances hardness and also pressure sensitivity, increase in free volume due to shot-peening decreases the flow stress and hardness. It is interesting to note that the free-volume increase is so significant that pressure sensitivity completely vanishes, which implies that in this case the operation of STZs does not involve any dilatational component.

Finally, the results presented in the preceding sections show clearly that the indentation method exposes additional, critical information about plasticity in amorphous alloys. It seems that hardness is more sensitive to the structural state of the BMG than the uniaxial compressive yield strength. Often the yield stress in uniaxial compression is equated with the onset of shear banding, although a considerable amount of homogeneous deformation through uncorrelated STZ operation (i.e. “anelasticity”) may have taken place before that. Unless careful experiments such as acoustic emission spectroscopy are performed, such STZ activity is difficult to reveal (see e.g. [51]). Indentation tests, on the other hand, seem to be more sensitive to this anelasticity. At large depths of penetration deformation occurs through shear bands, amply reflected by the pop-ins in the *P*-*h* curves in Fig. 6.9 as well as by the observation of indents in Fig. 6.11. This observation suggests that plasticity that occurs through inhomogeneous flow (i.e. shear banding) during sharp indentation may be similar to that seen in uniaxial compression tests, while plasticity that occurs through uncorrelated STZ operation is affected by the large hydrostatic compressive stress that is present underneath the indenter. This hydrostatic stress makes the STZ operations difficult, and consequently elevates their shear stress. Thus critical examination of indentation test on amorphous alloys can reveal vital information about the underlying physics of deformation.

6.5 Conclusions

Detailed micro-pillar compression experiments on a Zr-based BMG with varying amounts of free volume reveal that yield strength remains unchanged with varying pillar size or free-volume content. No influence on the part of sample shape (i.e. increased surface-area-to-volume ratio) was observed, either. Plastic flow remains invariant with size, contradicting suggestions that it becomes homogeneous below some critical size in the sub-micron range. The experimental findings also highlight some of the limitations of the uniaxial compression testing technique in evaluating the plasticity of BMGs whose deformation is inhomogeneous in nature.

Instrumented indentation tests on Vit1 reveal significant differences in hardness and slight changes in the shear-band morphology around the indents, depending on the structural state of the BMG, while its yield strength remains roughly invariant. The different behaviour can be rationalised in terms of a free-volume dependent pressure sensitivity, quantified by the constraint factor (i.e., hardness-to-yield strength ratio) and the intersection angle of emanating shear bands at the edge of conical indents. While structural relaxation leads to an enhanced pressure sensitivity compared to that seen in the as-cast state, pre-deformation by means of shot-peening results in a pressure-insensitive deformation response of the BMG. The microscopic origin of this behaviour is the ease of STZ operation, which requires local dilatation and can hence be activated more easily in less dense glassy structures. In consequence, it would be interesting to study whether the changes in pressure sensitivity with varying amounts of free volume are also reflected in changes in the STZ volume and activation volume, respectively.

6.6 References

[1] C.A. Schuh, T.C. Hufnagel, U. Ramammurty, Acta Mater. 55 (2007) 4067.
[2] A.S. Argon, Acta Metall. 27 (1979) 47.
[3] M.L. Falk, J.S. Langer, Phys. Rev. E 57 (1998) 7192.
[4] C.A. Volkert, A. Donohue, F. Spaepen, J. App. Phys. 103 (2008) 083539.
[5] B.E. Schuster, Q. Wei, T.C. Hufnagel, K.T. Ramesh, Acta Mater. 56 (2008) 5091.
[6] V. Keryvin, J. Phys.: Condens. Mater. 20 (2008) 114119.
[7] R. Raghavan, P. Murali, U. Ramamurty, Intermatallics 14 (2006) 1051.
[8] P. Murali, U. Ramamurty, Acta Mater. 53 (2005) 1467.
[9] R. Raghavan, R. Ayer, H.W. Jin, C.N. Marzinsky, U. Ramamurty, Scr. Mater. 59 (2008) 167.
[10] R. Rabe, J.M. Breguet, P. Schwaller, S. Stauss, F.J. Haug, J. Patscheider, J. Michler, Thin Solid Films 469 (2004) 206.
[11] K.A. Rzepiejewska-Malyska, G. Bürki, J. Michler, R.C. Major, E. Cyrankowski, S.A.S. Asif, O.L. Warren, J. Mater. Res. 23 (2008) 1973.
[12] P.C. Kim, J.Y. Suh, A. Wiest, M.L. Lind, R.D. Conner, W.L. Johnson, Scr. Mater. 60 (2008) 80.
[13] H. Zhang, B.E. Schuster, Q. Wei, K.T. Ramesh, Scr. Mater. 54 (2006) 181.
[14] B. Moser, J.F. Löffler, J. Michler, Philos. Mag. 86 (2006) 5715.
[15] Y.M. Wang, J. Li, A.V. Hamza, T.W. Barbee, Proc. Natl. Acad. Sci. U.S.A. 104 (2007) 11155.
[16] H. Guo, P.F. Yan, Y.B. Wang, J. Tan, Z.F. Zhang, M.L. Sui, E. Ma, Nat. Mater. 6 (2007) 735.
[17] Z.W. Shan, J. Li, Y.Q. Cheng, A.M. Minor, S.A. Syed Asif, O.L. Warren, E. Ma, Phys. Rev. B 77(2008) 155419.
[18] W.F. Wu, Y. Li, C.A. Schuh, Philos. Mag. 88 (2008) 71.
[19] C.J. Lee, J.C. Huang, T.G. Nieh, Appl. Phys. Lett. 91 (2007) 161913.
[20] Y.H. Lai, C.J. Lee, Y.T. Cheng, H.S. Chou, H.M. Chen, X.H. Du, C.I. Chang, J.C. Huang, S.R. Jian, J.S.C. Jang, T.G. Nieh, Scr. Mater. 58 (2008) 890.
[21] H. Kimura, T. Masumoto, Acta Metall. 31 (1983) 231.
[22] C.J. Gilbert, R.O. Ritchie, W.L. Johnson, Appl. Phys. Lett. 71 (1997) 476.
[23] A. Castellero, D.I. Uhlenhaut, B. Moser, J.F. Löffler, Philos. Mag. Lett. 87 (2007) 383.
[24] R. Raghavan, P. Murali, U. Ramamurty, Intermetallics 14 (2006) 1051.
[25] Y. Zhang, W.H. Wang, A.L. Greer, Nat. Mater. 5 (2006) 857.
[26] R.D. Conner, W.L. Johnson, N.E. Paton, W.D. Nix, J. Appl. Phys. 94 (2003) 904.
[27] A. Castellero, D.I. Uhlenhaut, B. Moser, J.F. Löffler, Philos. Mag. Lett. 87 (2007) 383.
[28] M.N.M. Patnaik, R. Narasimhan, U. Ramamurty, Acta Mater. 52 (2004) 3335.
[29] K. Eswar Prasad, R. Raghavan, U. Ramamurty, Scr. Mater. 57 (2007) 121.
[30] V. Keryvin, K. Eswar Prasad, Y. Gueguen, J.-C. Sangleboeuf, U. Ramamurty, Philos. Mag. 88 (2008) 1773.
[31] K. Eswar Prasad, V. Keryvin, U. Ramamurty, J. Mater. Res. 24 (2009) 890.
[32] C.A. Schuh, T.G. Nieh, Acta Mater. 51 (2003) 87.
[33] V. Keryvin, Acta Mater. 55 (2007) 2565.
[34] C.A. Schuh, A.C. Lund, T.G. Nieh, Acta Mater. 52 (2004) 5879.

[35] L.Y. Chen, Q. Ge, S. Qu, J.Z. Jiang, Scr. Mater. 59 (2008) 1210.
[36] R. Bhowmick, R. Raghavan, K. Chattopadhyay, U. Ramamurty, Acta Mater. 54 (2006) 4221.
[37] W.C. Oliver, G.M. Pharr, J. Mater. Res. 7 (1992) 1564.
[38] U. Ramamurty, S. Jana, Y. Kawamura, K. Chattopadhyay, Acta Mater. 53 (2005) 705.
[39] A. Nadai, *Theory of Flow and Fracture of Solids*, Vol. 1, McGraw-Hill, New York, 1950.
[40] W. Johnson, R. Sowerby, R.D. Venter, *Plane-Strain Slip-Line Fields for Metal-Deformation Processes*, Pergamon Press, 1982.
[41] G.S. Yu, J.G. Lin, M. Mo, X.F. Wang, F.H. Wang, C.E. Wen, Mater. Sci. Eng. A 460 (2007) 58.
[42] D.I. Uhlenhaut, F.H. Dalla Torre, A. Castellero, C.A.P. Gomez, N. Djourelov, G. Krauss, B. Schmitt, B. Patterson, J.F. Löffler, Philos. Mag. 89 (2009) 233.
[43] S. Xie, E.P. George, Acta Mater. 56 (2008) 5202.
[44] B.-G. Yoo, K.-W. Park, J.-C. Lee, U. Ramamurty, J.-I. Jang, J. Mater. Res. 24 (2009) 1405.
[45] M. Dao, N. Chollacoop, K.J. Van Vliet, T.A. Venkatesh, S. Suresh, Acta Mater. 49 (2001) 3899.
[46] F. Spaepen, Acta Metall. 25 (1977) 407.
[47] K. Hajlaoui, T. Benameur, G. Vaughan, A.R. Yavari, Scr. Mater. 51 (2004) 843.
[48] W.J. Wright, T.C. Hufnagel, W.D. Nix, J. Appl. Phys. 93 (2003) 1432.
[49] J. Li, Z.L. Wang, T.C. Hufnagel, Phys. Rev. B 65 (2002) 144201.
[50] K.M. Flores, E. Sherer, A. Bharathula, H. Chen, Y.C. Jean, Acta Mater. 55 (2007) 3403.
[51] A.Y. Vinogradov, V.A. Khonik, Philos. Mag. 84 (2004) 2147.

7 Summary and outlook

This chapter gives a summary of the most important results of this thesis and gives an outlook on future mechanical and structural investigations of BMGs.

7.1 General summary

In this study we performed compression tests on millimetre-sized Zr-based BMG samples over a wide range of temperatures and strain rates. Based on the resulting experimental findings we developed a constitutive framework of (inhomogeneous) flow of BMGs and determined kinetic state variables, such as activation volume, shear transformation zone (STZ) volume and strain-rate sensitivity. We complemented these investigations with in-situ compression of micrometre-sized pillars inside a scanning electron microscope (SEM) and instrumented indentation tests on a BMG in various structural states. The results revealed size-independent yield strength and deformation behaviour, but free-volume-dependent pressure sensitivity.

7.1.1 Influence of temperature and strain rate on inhomogeneous flow

Detailed mechanical investigations on millimetre-sized Zr-based BMGs at various temperatures (77–623 K) and strain rates (3×10^{-5}–2×10^{-1}) revealed accurate information on the inhomogeneous flow kinetics. Serrated flow in conjunction with a negative strain-rate sensitivity was observed at temperatures around room temperature. The serrated flow behaviour disappears below a critical temperature and/or above a critical strain rate, indicating that the underlying processes are thermally-activated. The results suggest a micromechanical deformation mechanism based on (i) shear displacement through the operation of STZs, and (ii) subsequent relaxation of the distorted structure. The latter vanishes below a critical temperature (or above a critical strain rate), resulting in the measured change in the strain-rate sensitivity and the disappearance of serrated flow. The crucial factor determining serrated flow in BMGs is the ratio between the (cooperative) shearing of STZs and the rate of adjacent diffusive rearrangements. In contrast to fracture surfaces the shear surfaces exhibit closely-spaced shear striations, and only a few areas reveal typical vein pattern structures, but of more limited thickness than those resulting at the moment of fracture. These observations, combined with estimates of the energy release, suggest that the heat release during plastic deformation is not sufficient to melt the entire shear surface. Melting only takes place locally due to friction and bursts in energy release at the moment of stress drops.

7.1.2 Constitutive modelling of the inhomogeneous flow of BMGs

Despite fundamental differences in the underlying deformation mechanisms in amorphous and crystalline alloys, there exist close phenomenological similarities between the inhomogeneous deformation of BMGs and of crystalline solids which deform via a dynamic strain-aging mechanism, such as strain-rate-dependent serrated flow, negative strain-rate sensitivity and loss of ductility. The disappearance of serrated flow, i.e. temporal homogenization, below a critical temperature and above a critical strain rate corresponds to a transition of the asymptotic strain-rate sensitivity from negative to positive values. Based on thermally-activated shear processes, a temperature and strain-rate-dependent deformation model was presented that includes a time-varying state variable which represents the local degree of relaxation in the shear band after a shear event has taken place. The model makes possible a theoretical description of the observed strain-rate sensitivity and the spatio-temporal evolution of plastic deformation in metallic glasses. The compositional dependence of serrated flow implies importance on the part of local diffuse atomic rearrangements within shear bands. Such relaxation processes lead to a strengthening of the shear bands and lower the probability of their reactivation. Therefore, more shear bands are present at higher temperatures and/or lower strain rates.

Preliminary observations of angles between two different families of shear bands at the edge of a conical indent reveal enhanced pressure sensitivity at low temperature (77 K), in conjunction with a decrease in the STZ volume. Our results also point to the importance of the (initial) condition of the material, its influence on the deformation characteristics, and the necessity to accurately define a general reference state for metallic glasses, in particular when comparing different alloys or differently-processed samples.

7.1.3 Deformation size effects and influence of free volume on plasticity

Detailed micro-pillar compression experiments on a Zr-based BMG with varying amounts of free volume revealed that yield strength is size-independent (at least down to pillar diameters of 300 nm) and remains unchanged if free volume content is varied. Deformation always proceeds via the formation and propagation of shear bands and no change in the mechanism (e.g., a shift to homogenous flow) was observed. The results suggest that homogenization, if present, would only take place at substantially smaller dimensions, e.g.

in the range of the shear-band thickness (~20 nm). Complementary instrumented indentation tests showed significant differences in hardness and slight changes in the shear-band morphology around the indents depending on the structural state of the BMG. The varying hardness (but constant yield strength) suggests a free-volume-dependent pressure sensitivity, quantified by the constraint factor (i.e. hardness-to-yield strength ratio). Further evidence for the changing pressure sensitivity was provided by the measured intersection angles of emanating shear bands at the edge of conical indents. While structural relaxation (i.e., decrease in free volume) generates pressure sensitivity which is enhanced compared to the as-cast state, pre-deformation by means of shot-peening (i.e. increase in free volume) causes a pressure-insensitive deformation response in the BMG. The microscopic origin of this behaviour is the ease of STZ operation, which requires local dilatation and hence is prone to easier activation in less-dense glassy structures.

7.2 General outlook and future work

The picture we have obtained so far on the temperature-dependent inhomogeneous deformation of Zr-based BMGs is only partially complete. Due to the spontaneous embrittlement of the alloys in the temperature range between ~0.5–0.8 T_g the deformation characteristics could not be assessed experimentally in this temperature range. Possibilities for avoiding the problem of limited plasticity may be mechanical testing under geometrically confined conditions, such as the use of low-aspect-ratio samples or nanoindentation techniques. Further information may also be gained by extending the mechanical characterization to temperatures below liquid nitrogen temperature (77 K).

Since our deformation model is based primarily on experimental findings using Zr-based BMGs (with some support, however, from own and literature results on other alloy systems), it is essential to systematically study the deformation kinetics of other (non-Zr-based) glass-forming alloy systems (which, as a matter of fact, is currently being done in a follow-up Ph.D. thesis [1]). Such investigations will further validate our constitutive model and show the extent to which our findings represent fundamental characteristics of BMGs

and how far they can be generalized, for example by scaling to the homologous temperature in a generalized deformation map.

More detailed study of the structure-property relationships is required in order to understand the influence of potential inhomogeneities (impurities, nanocrystals, voids, etc.) and to clarify why certain monolithic BMGs are tough while others are completely brittle. Transition electron microscopy (TEM) on as-cast and deformed specimens may provide some insight into microstructural effects and shed light on why deformation behaviour differs between room temperature and liquid-nitrogen temperature. The major difficulty in answering the question about structural evolution in shear bands is their spatial limitation and dynamic nature. As pointed out in a recent study [2], the structural difference between shear bands and the undeformed matrix is very small. Only by using pair distribution functions derived from energy-filtered nanobeam electron diffraction were the authors able to reveal a slight difference in packing density and short-range order. Further evidence on structural changes and subsequent relaxation processes during shear banding might be observed by electron energy loss spectroscopy, and would clarify whether the mechanical distortion of the structure leads to an accumulation/depletion of certain constituent elements in or around a shear band. Detailed analysis of the chemical etchability of shear bands upon annealing at various temperatures and times (see Ref. [3]) or internal friction measurements (e.g. Ref. [4]) are complementary methods for gaining information (e.g. apparent activation enthalpy) about structural relaxation processes in shear bands and thermal relaxation of free volume.

At present it seems that STZs act as “basic deformation units” governing the mechanical behaviour of metallic glasses. However, more work needs to be done to understand the composition-, strain rate- and temperature-dependent size and shape of STZs as well as the transition from individual STZs to fully-developed shear bands. Prominent approaches in this context are, for example, in-situ acoustic emission tests at different temperatures and strain rates to reveal STZ and shear band activity [1], or the experimental determination of STZ volumes (as carried out in this study, via indentation creep [5] or strain-rate change nanoindentation tests [6]) on metallic glasses of varying compositions and structural conditions. Corresponding measurements of pressure sensitivity may clarify whether changes in the structural condition (e.g. with varying free volume content, as shown in this thesis) are reflected in a different STZ volumes, similar to the observations made on nanocrystalline materials where an increase in the pressure sensitivity correlates with a

decrease in the activation volume [7]. Obviously, detailed atomistic simulations can also help to improve the microstructural description and understanding of deformation in amorphous alloys. For example, the activation energy of STZs in simulations were determined to be 0.34 eV [8] and 0.31 eV [9] for a CuTi and a NiZr model glass, respectively. In order to verify these values experimentally, the activation enthalpy ΔH could be determined by measuring the slope of an Arrhenius plot of steady-state creep-rates at different temperatures, i.e.,

$$\Delta H = k_{\mathrm{B}} T^2 \left(\frac{\partial \ln \dot{\varepsilon}/\dot{\varepsilon}_0}{\partial T} \right)_{\sigma} . \tag{7.1}$$

By using the relation $\Delta H = \Delta G + T\Delta S = \Delta G_0 - \tau V + T\Delta S$ conclusions on the free activation energy ΔG and the total energy barrier ΔG_0 would then be possible. Assuming that the evolution of the shear modulus with temperature is the main component of ΔS the following relation between ΔG and ΔH was derived [10,11]

$$\Delta G = \frac{\Delta H + (T/\mu)(\mathrm{d}\mu/\mathrm{d}T)\tau V}{1 - (\mathrm{T}/\mu)(\mathrm{d}\mu/\mathrm{d}T)} \tag{7.2}$$

which would then enable quantitative estimates of the experimentally derived ΔG and ΔG_0 and their comparison with values obtained from simulations.

While plastic zone size and toughness of metallic glasses are seemingly correlated, fracture criteria necessarily involve certain length scales above which stress and/or strain reach a critical value. Our micropillar compression tests revealed a size-independent yield strength down to a sample size of 300 nm. Systematic studies of the deformation behaviour of metallic glasses in the nanometre range, however, are scarce and questions about possible size effects in plasticity are not yet fully resolved. We speculate that a transition to homogeneous deformation may be observed at smaller scales, where sample dimensions are on the order of the shear band thickness and shear-band localization becomes extremely difficult. In compression it is also generally observed that macroscopic specimens break into pieces, while corresponding microscopic samples can deform without catastrophic fracture, suggesting a possible transition from brittle behaviour to malleability. Unfortunately experimental data in the interesting, intermediate size range is lacking, but this deficiency might be addressed by compression tests on intermediate-size pillars ($10\ \mu\mathrm{m} < d < 1$ mm, fabricated e.g. by electrical discharge machining where the wire is kept

parallel to the surface and subsequently polished by focused-ion beam technique or by micro-ultrasonic machining) or by tensile tests on wires with equivalent diameters [12].

An issue that has hardly been touched upon is the influence of the specimen surface area on its mechanical behaviour. The fabrication of pillars by focused-ion beam technique offers a relatively straightforward way to obtain specimens with different geometries and surface-area-to-volume ratios. An example of a rectangular specimen is shown in Fig. 7.1. Testing of such structures could demonstrate the influence of an increased surface-area-to-volume ratio on the deformation behaviour of metallic glasses and, for instance, show to what extent outer surfaces act as initiation sites for shear bands.

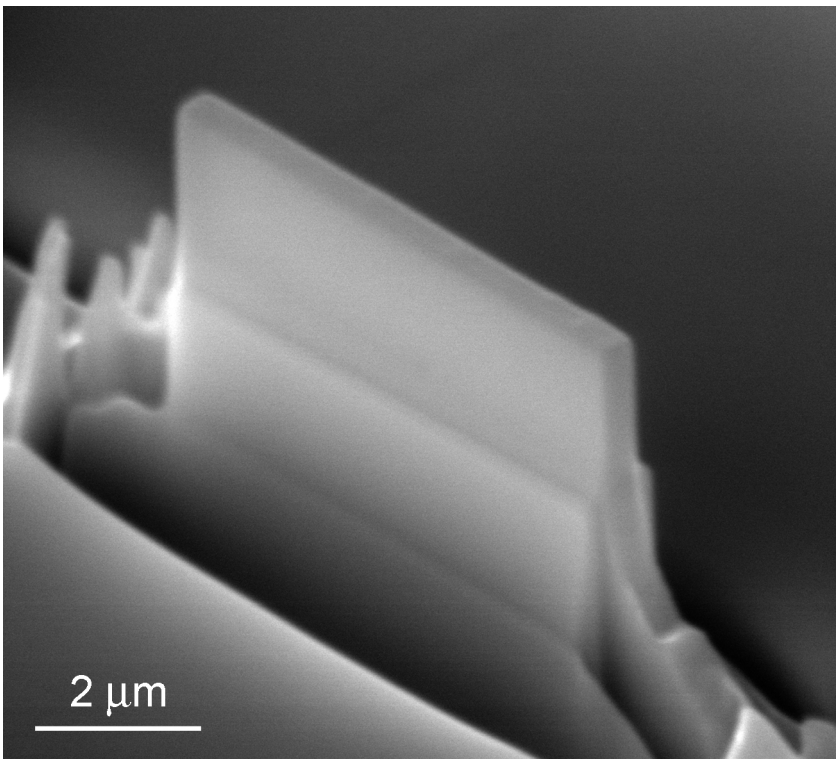

Fig.7.1: SEM image of a rectangular wall-structure produced by the focused-ion beam technique.

As follow-ups to this thesis project the following specific tasks should be addressed:

(a) Determine the strain-rate sensitivity and activation volume for Vit105 in the temperature range between 300–600 K by using high-temperature instrumented indentation.

(b) Compare the strain-rate sensitivities and activation volumes measured via uniaxial compression tests with those obtained by indentation techniques.

(c) For various BMGs, investigate in more detail the deviation of the normalized flow stress (σ/E) from the generalized $T^{2/3}$ dependence. (Besides the measurement of the flow stress at different temperatures this also requires accurate determination of the temperature dependence of the elastic modulus).

(d) Extend the investigations on the transition from serrated to non-serrated flow to amorphous alloys with glass transition temperatures and shear moduli different from those of Vit105.

(e) Perform detailed transmission electron microscopy studies on specimens deformed at different temperatures to reveal possible differences in the shear-band microstructure.

(f) Measure internal friction spectra to obtain information about temperature- and time-dependent structural relaxation processes and mechanisms of anelasticity.

(g) Study the correlation between atomic processes (i.e., STZs) and the initiation and propagation of shear bands which occur on two different length scales, for example via acoustic emission measurements or in situ deformation experiments inside an SEM or TEM.

(h) Investigate possible size effects in the deformation behaviour of intermediate-size ($1\mu m < d < 1mm$) and very small ($d < 300$ nm) pillars.

In conclusion, despite great efforts made in metallic glass research over the last few decades, a fully comprehensive understanding of glass deformation is still lacking. Novel future insights gained from both experiments and simulations are eagerly anticipated which will pave the way for metallic glasses designed with specific properties in mind and thus further the innovative application of this interesting class of material.

7.3 References

[1] D. Klaumünzer, Ph.D. thesis, ETH Zürich (work in progress).
[2] Y.M. Chen, T. Ohkubo, T. Mukai, K. Hono, J. Mater. Res. 24 (2009) 1.
[3] P.T. Vianco, J.C.M. Li, J. Mater. Sci. 22 (1987) 3129.
[4] M. Fukuhara, X.M. Wang, A. Inoue, F.X. Yin, Phys. Stat. Sol. (RRL) 1 (2007) 220.
[5] S. Nowak, P. Ochin, A. Pasko, O. Maciejak, P. Aubert, Y. Champion, J. Alloys Compd. 483 (2009) 139.
[6] D. Pan, A. Inoue, T. Sakurai, M.W. Chen, Proc. Natl. Acad. Sci. U.S.A. 105 (2008) 14769.
[7] J.R. Trelewicz, C.A. Schuh, Acta Mater. 55 (2007) 5948.
[8] S.G. Mayr, Phys. Rev. Lett. 97 (2006) 195501.
[9] F. Delogu, Intermetallics 16 (2008) 658.
[10] G. Schoeck, Phys. Stat. Sol. 8 (1965) 499.
[11] D. Caillard, J.L. Martin, in *Thermally activated mechanisms in crystal plasticity*, edited by R.W. Cahn, Pergamon Materials Series, Vol. 8, 2003.
[12] B. Zberg, E.R. Arata, P.J. Uggowitzer, J.F. Löffler, Acta Mater. 57 (2009) 3223.

Appendix

Curriculum vitae

Personal data

Name:	Alban Dubach
Date of birth:	December 14th, 1979
Nationality:	Swiss
Email:	alban.dubach@gmail.com
Mobile:	+41 (0)78 870 06 50

Education

Oct. 2005 – present	Ph.D. candidate at the Laboratory of Metal Physics and Technology, Department of Materials, ETH Zurich and the Laboratory of Materials Technology, Department of Advanced Materials and Surfaces, EMPA Thun
Nov. 2004 – Apr. 2005	Diploma Thesis "*Microwave heating of silicon powder – the influence of grain size and doping*" at the Laboratory of Materials Technology, Department of Advanced Materials and Surfaces, EMPA Thun
Oct. 1999 – Apr. 2005	Studies in Materials Science at ETH Zurich, including 2 exchange semesters at EPF Lausanne (2002/2003)
Sept. 1995 – Apr. 1999	Matura Typus C, Deutsches Gymnasium Biel

Work experience

Apr. 2005 – Jul. 2005	Research assistant at the Institute of Nonmetallic Inorganic Materials, ETH Zurich *(Synthesis and characterization of thin films for SOFC applications)*
Jan. 2002 – Jul. 2002	Practical training at ContravesSpace, Zurich *(Technology: autoclave-free curing of CFR-prepreg)*
Feb. 2001 – Jun. 2001	Tutorial assistant at the Institute for Mechanical Systems, ETH Zurich *(Revision of lecture manuscripts and drawing of figures)*
Feb. 2000 – Apr. 2000	Practical training at Stahl AG, Gerlafingen *(Basic skills in metal working)*

Publications

Journal publications based on thesis work

F.H. Dalla Torre, A. Dubach, M.E. Siegrist, J.F. Löffler, "*Negative strain-rate sensitivity in bulk metallic glass and its similarities with the dynamic strain-aging effect during deformation*", Appl. Phys. Lett. 89 (2006) 091918.

F.H. Dalla Torre, A. Dubach, A. Nelson, J.F. Löffler, "*Temperature, strain and strain rate dependence of serrated flow in bulk metallic glasses*", Mater. Trans. JIM 48 (2007) 1774.

A. Dubach, F.H. Dalla Torre, J.F. Löffler, "*Deformation kinetics in Zr-based bulk metallic glasses and its dependence on temperature and strain rate sensitivity*", Philos. Mag. Lett. 87 (2007) 695.

F.H. Dalla Torre, A. Dubach, J. Schällibaum, J.F. Löffler, "*Shear striations and deformation kinetics in highly deformed bulk metallic glasses*", Acta Mater. 56 (2008) 4635.

A. Dubach, F.H. Dalla Torre, J.F. Löffler, "*Constitutive model for inhomogeneous flow in bulk metallic glasses*", Acta Mater. 57 (2009) 881.

A. Dubach, R. Raghavan, J.F. Löffler, J. Michler, U. Ramamurty, "*Micropillar compression studies on a bulk metallic glass in different structural states*", Scr. Mater. 60 (2009) 567.

A. Dubach, K. Eswar Prasad, R. Raghavan, J.F. Löffler, J. Michler, U. Ramamurty, "*Free-volume dependent pressure sensitivity of Zr-based bulk metallic glass*", J. Mater. Res. 24 (2009) 2697.

F.H. Dalla Torre, A. Dubach, J.F. Löffler, "*Deformation kinetics of Zr-based bulk metallic glasses – Temperature and strain rate influences on shear banding*", J. Alloys Compd. (2009), doi:10.1016/j.jallcom.2009.10.015.

Other journal publications

D. Beckel, A. Dubach, A.R. Studart, L.J. Gauckler, "*Spray pyrolysis of $La_{0.6}Sr_{0.4}Co_{0.2}Fe_{0.8}O_{3-\delta}$ thin film cathodes*", J. Electroceram. 16 (2006) 221.

S. Leparoux, C. Diot, A. Dubach, S. Vaucher "*Synthesis of silicon carbide coating on diamond by microwave heating of diamond and silicon powder: A heteroepitaxial growth*", Scr. Mater. 57 (2007) 595.

D. Beckel, A. Dubach, A.N. Grundy, A. Infortuna, L.J. Gauckler, "*Solid-state dewetting of $La_{0.6}Sr_{0.4}Co_{0.2}Fe_{0.8}O_{3\pm\delta}$ thin films during annealing*", J. Eur. Ceram. Soc. 28 (2008) 49.

Conference contributions

A. Dubach, F.H. Dalla Torre, M. Siegrist, J.F. Löffler, "*High compression strain in bulk metallic glass composites containing low fraction of nanocrystals*", Spring Meeting of the Division of Condensed Matter of the German Physical Society, Dresden, Germany, March 2006. *(Talk)*

A. Dubach, J.F. Löffler, "*Mechanical properties of bulk metallic glasses*", 1st MRC graduate symposium, Zurich, Switzerland, June 2006. *(Poster)*

A. Dubach, F.H. Dalla Torre, J.F. Löffler, "*Low-temperature strain rate sensitivity measurements of a Zr-based bulk metallic glass*", 13th International Symposium on Metastable and Nano Materials (ISMANAM), Warsaw, Poland, August 2006. *(Talk)*

A. Dubach, J.F. Löffler, "*Mechanical properties of a Zr-based bulk metallic glass*", Sino-Swiss Cooperation Symposium, Zurich, Switzerland, November 2006. *(Poster)*

A. Dubach, F.H. Dalla Torre, J.F. Löffler , "*Deformation kinetics in Zr-based bulk metallic glasses*", Spring Meeting of the Division of Condensed Matter of the German Physical Society, Regensburg, Germany, March 2007. *(Talk)*

A. Dubach, J.F. Löffler, "*Les métaux amorphes et leur usages*", Conférence de l'Association Suisse pour la Recherche Horlogère (ASRH), Neuchâtel, Switzerland, October 2007. *(Talk)*

A. Dubach, F.H. Dalla Torre, J.F. Löffler, "*Temperature and strain-rate dependence of deformation kinetics in Zr-based bulk metallic glasses*", 2007 MRS Fall Meeting, Boston (MA), USA, November 2007. *(Poster)*

A. Dubach, F.H. Dalla Torre, J.F. Löffler, "*Inhomogeneous flow characteristics of bulk metallic glasses*", Spring Meeting of the Division of Condensed Matter of the German Physical Society, Berlin, Germany, February 2008. *(Talk)*

A. Dubach, D. Klaumünzer, B. Zberg, F.H. Dalla Torre, J.F. Löffler, "*Constitutive model for inhomogeneous flow in bulk metallic glasses*", Materials Day, Zurich, Switzerland, March 2009. *(Poster)*

A. Dubach, J. Michler, U. Ramamurty, J.F. Löffler, "*In-situ SEM micropillar compression of Zr-based bulk metallic glasses with different free volume content*", Spring Meeting of the Division of Condensed Matter of the German Physical Society, Dresden, Germany, March 2009. *(Talk)*